



Kent Academic Repository

Everson, Michael (2021) *Optimising a Polygon Mirror-based Spectral Filter for Swept Source Optical Coherence Tomography*. Doctor of Philosophy (PhD) thesis, University of Kent,.

Downloaded from

<https://kar.kent.ac.uk/90828/> The University of Kent's Academic Repository KAR

The version of record is available from

<https://doi.org/10.22024/UniKent/01.02.90828>

This document version

UNSPECIFIED

DOI for this version

Licence for this version

CC BY (Attribution)

Additional information

Versions of research works

Versions of Record

If this version is the version of record, it is the same as the published version available on the publisher's web site. Cite as the published version.

Author Accepted Manuscripts

If this document is identified as the Author Accepted Manuscript it is the version after peer review but before type setting, copy editing or publisher branding. Cite as Surname, Initial. (Year) 'Title of article'. To be published in *Title of Journal*, Volume and issue numbers [peer-reviewed accepted version]. Available at: DOI or URL (Accessed: date).

Enquiries

If you have questions about this document contact ResearchSupport@kent.ac.uk. Please include the URL of the record in KAR. If you believe that your, or a third party's rights have been compromised through this document please see our [Take Down policy](https://www.kent.ac.uk/guides/kar-the-kent-academic-repository#policies) (available from <https://www.kent.ac.uk/guides/kar-the-kent-academic-repository#policies>).

UNIVERSITY OF KENT

DOCTORAL THESIS



Optimising a Polygon Mirror-based Spectral Filter for Swept Source Optical Coherence Tomography

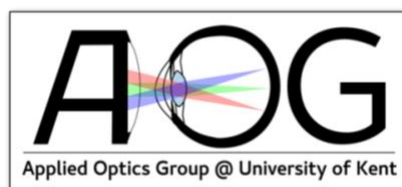
Author:
Michael James
EVERSON

Supervisor:
Dr George
DOBRE

*A thesis submitted in fulfilment of the requirements
for the degree of Doctor of Philosophy
in the*

Applied Optics Group

School of Physical Sciences



Submission: 12th October 2021

249 pages / 80,400 words

Declaration of Authorship

I, Michael EVERSON, declare that this thesis titled, “Optimising a Polygon Mirror-based Spectral Filter for Swept Source Optical Coherence Tomography” and the work presented in it are my own. I confirm that:

- This work was done wholly or mainly while in candidature for a research degree at this University.
- Where any part of this thesis has previously been submitted for a degree or any other qualification at this University or any other institution, this has been clearly stated.
- Where I have consulted the published work of others, this is always clearly attributed.
- Where I have quoted from the work of others, the source is always given. With the exception of such quotations, this thesis is entirely my own work.
- Where the thesis is based on work done by myself jointly with others, I have made clear exactly what was done by others and what I have contributed myself.

Signed:



Date: Thursday 12th October 2021

UNIVERSITY OF KENT

Abstract

Faculty of Science

School of Physical Sciences

Doctor of Philosophy

Optimising a Polygon Mirror-based Spectral Filter for Swept Source Optical Coherence Tomography

By Michael James EVERSON

Optical Coherence Tomography (OCT) is a non-invasive, depth-scan imaging modality with proven applications in medical physics. The benefits of this modality, combined with the range of possible techniques that can be employed, continue to stimulate research and development within this field. One such technique uses a polygon mirror-based spectral filter as a swept light source, and is particularly useful when conducting OCT experiments in a laboratory setting due to its low cost and high versatility. The development of these swept sources has resulted in a variety of experimental designs, however research into the most suitable design needed to fully optimise every aspect for OCT imaging is rarely reported. Ideally, these systems must provide a broad swept bandwidth and produce narrowband, instantaneous laser linewidths, whilst maintaining sufficient optical power levels across the entire spectrum, but it was found that these features can be significantly limited by the design of the spectral filter. The research presented in this thesis is a detailed, multi-parameter analysis of system operation and has resulted in the identification of various techniques that can be applied to improve overall system performance. The polygon mirror-based swept source was studied theoretically, experimentally and using Zemax™ ray tracing simulation software to minimise the effects of mechanical vignetting and maximise the optical power transmission. A design hierarchy was also developed which can be used to determine the most suitable combination of component parameters and the best construction methods needed to optimise the design.

Acknowledgments

Firstly, I would like to say how grateful I am to the Engineering and Physical Sciences Research Council (EPSRC) for funding this project. Secondly, I would like to thank my friends and family for their constant support and belief in my ability to finish the PhD. I would like to acknowledge and express my deepest appreciation to all of the academics and fellow researchers at the University of Kent for their help and support throughout my undergraduate and postgraduate studies. More specifically, I would like to thank the following academic members of the Applied Optics Group (AOG); Dr Adrian Bradu for his extensive knowledge and excellent diagnostic abilities on the laboratory workbench, Dr Ramona Cernat for always offering her time to help me even when she had none of her own, Dr Manuel Jorge Marques for his over complicated explanations of relatively simple operations, Dr Mike Hughes for his kind understanding of my ignorance with LabVIEW coding software, Professor David Jackson for sharing his office with me, as well as many interesting and lengthy conversations, and finally to Professor Adrian Podoleanu, the passionate and ambitious leader of the AOG, for supporting and encouraging all of the members in the group and for making each and every one of us feel part of a family, no matter how short our stay might be. I would also like to thank; Felix Fleischhauer, Magalie Bondu, Adrian Fernández Uceda, Andy Thrapp and Giannis Nteroli for all of their help in the laboratory but more importantly for their friendship outside of it. Further recognition goes to; Dr Sally Marques for kindly reading through my work and offering valuable feedback and helpful advice, and to my second supervisor, Professor Virgil Duma, for inspiring the direction of the research and allowing me to participate in a number of conferences, as well as being my guide in unfamiliar territories. Extra special thanks must go to my supervisor and friend, Dr George Dobre, who provided the opportunity for me to start this postgraduate research project in the first place, allowing me to become part of the AOG and giving me the experience of participating in a large number of events including conferences and training exercises both at home and abroad. Finally, I would like to thank my fiancé, Dr Sophie Caujolle, without whom I'm quite sure this thesis would never have been finished. Her love, support, kindness and patients throughout has been far greater than I could ever have asked for. I love you to the moon and back, Niggle Snush, xXx.

TABLE OF CONTENTS

Chapter 1	10
1.1 Introduction to the Thesis.....	10
1.1.1 About the Project and its Contributions.....	15
1.2 Organisation of the Thesis.....	18
1.3 Optical Coherence Tomography (OCT)	19
1.3.1 OCT Operation.....	19
1.4 Spectral Domain OCT	23
1.4.1 SS-OCT Operation.....	25
1.4.2 Sample Penetration Depth.....	26
1.4.3 Axial Scanning Range.....	26
1.4.4 Sensitivity – Fringe Visibility	27
1.5 Image Resolution and Scanning Methods.....	28
1.5.1 Transverse Resolution.....	29
1.5.2 Axial Resolution	31
1.5.3 Scanning Methods.....	33
1.6 OCT Requirements	34
1.6.1 Operating Wavelength	34
1.6.2 Total Swept Bandwidth (TSB).....	35
1.6.3 Polygon Mirror-Based Spectral Filter Requirements	36
Chapter 2	37
2.1 Chapter Introduction.....	37
2.2 Experimental Setup.....	37
2.3 The Swept Source	39
2.3.1 Ring Laser Cavity	40
2.3.1.1 Optical Fibres	42
2.3.2 Light Source – Semiconductor Optical Amplifier (SOA)	43
2.3.2.1 SOA Parameters	44
2.3.2.2 Optimising Linewidth Amplification in the Ring Laser Cavity.....	46
2.3.2.3 SOA Temperature Control	47
2.3.3 Polygon Mirror-Based Spectral Filter.....	48
2.3.3.1 Spectral Filter Experimental Setup	51
2.3.4 Spectral Filter Stabilisation.....	53
2.3.4.1 Windage	54
2.3.4.2 Vibration Reduction	55
2.4 Interferometric, Optical Fibre-based Array.....	58
2.4.1 Object Arm & Reference Arm.....	60
2.4.2 Transverse Resolution Measurements	62
2.5 Signal Processing and Image Creation.....	62
2.6 Simulations in Ray Tracing Software.....	64
2.7 Vignetting.....	67
2.7.1 Primary Vignetting.....	68
2.7.2 Secondary Vignetting.....	69
2.8 Discussion.....	71
Chapter 3	73
3.1 Chapter Introduction.....	73
3.2 The Spectral Filter	73
3.3 Collimators.....	74
3.4 Diffraction Gratings.....	77
3.4.1 Instantaneous Laser Linewidth	80
3.4.2 Divergence Angle	83
3.4.3 Spectral Energy Distribution.....	84
3.5 Telescope	86

3.5.1 Aberrations.....	89
3.6 Polygon Mirror.....	90
3.6.1 Polygon Parameters	93
3.7 Discussion.....	94
Chapter 4	96
4.1 Chapter Introduction.....	96
4.2 Acceptance Angle	96
4.3 Duty Cycle.....	98
4.3.1 Central Wavelength and the Optical Axis	98
4.3.2 Low Duty Cycles	99
4.4 Polygon Eccentricity	100
4.5 Visible Facet Width.....	102
4.5.1 Sweeping Facet Width	106
4.5.2 Final Visible Sweeping Facet Width	110
4.6 Simultaneous Tuning	112
4.6.1 Secondary Simultaneous Tuning	115
4.6.2 Optimising Eccentricity	118
4.7 Instantaneous Wavelength With Respect To PM Rotation Angle.....	120
4.8 Beam Width Analysis.....	122
4.8.1 Beam Width Calculations	126
4.9 Total Swept Bandwidth Equation (TSB)	128
4.9.1 Design Hierarchy	131
4.10 Discussion.....	133
Chapter 5	137
5.1 Chapter Introduction.....	137
5.2 Experimental Work.....	137
5.3 Collimator Comparison	138
5.3.1 Collimator Analysis	138
5.3.2 Experimental Comparison	140
5.4 Telescope Design Considerations.....	143
5.4.1 Telescope and Lens Parameters	144
5.4.2 Short Focal Length Simulation	147
5.5 1-inch Verses 2-inch Diameter Lens Experiment.....	150
5.5.1 Lens Aberration Analysis	150
5.5.2 Telescope Comparison Setup.....	152
5.5.3 Simulation and Experimental Results	154
5.6 On-Axis Verses Off-Axis Polygon Mirror Experiment	159
5.7 Above-Axis Verses Below-Axis Polygon Mirror Experiment	163
5.8 Polygon Mirror Translation Experiment.....	170
5.8.1 Consequences of Polygon Translation.....	175
5.9 Discussion.....	177
5.9.1 Collimator Analysis	177
5.9.2 Telescope Design.....	179
5.9.3 1-inch Versus 2-inch Diameter Lenses	180
5.9.4 On-Axis Versus Off-Axis	181
5.9.5 Above-Axis Versus Below-Axis.....	182
5.9.6 Polygon Mirror Translation	182
5.9.7 Final Conclusion	183
Chapter 6	184
6.1 Chapter Introduction.....	184
6.2 Parabolic Mirrors.....	184
6.3 Zemax™ Simulation Methods.....	185
6.3.1 On-Axis Simulation Setup	186

6.3.2 On-Axis Simulation Results	189
6.3.3 Off-Axis Simulation Results.....	193
6.4 Experimental Setup.....	198
6.4.1 On-Axis Experimental Results	200
6.4.2 Off-Axis Experimental Results.....	202
6.4.3 Experimental Images	207
6.5 Discussion.....	208
6.6 Further Work	210
Chapter 7	212
7.1 Chapter Introduction.....	212
7.2 Specifications For Individual Components In The Spectral Filter.....	213
7.2.1 Light Source – Semiconductor Optical Amplifier	213
7.2.2 Collimators.....	214
7.2.3 Diffraction Grating.....	214
7.2.4 Two-Lens Telescope.....	214
7.2.5 Polygon Mirror.....	215
7.2.6 Summary.....	216
7.3 Further Steps On The Path To Optimisation	217
7.3.1 Wavelength Dependent Path Lengths.....	217
7.3.2 General Design and Construction Methods for the Spectral Filter.....	218
7.3.3 Maximising The Visible Facet Width.....	219
7.3.4 Simultaneous Tuning	220
7.3.5 Realignment of the Non-Linear Wavelength Distribution.....	220
7.3.6 Summary.....	221
7.4 Grand Optimisation And Component Interconnectivity	222
7.4.1 Polygon Mirror Constraints	223
7.4.2 Collimator Constraints	225
7.4.3 Diffraction Grating Constraints	225
7.4.4 Telescope Constraints	226
7.5 Example Using The Design Hierarchy	228
7.6 Parabolic Mirrors.....	231
7.7 Final Design Considerations.....	232
7.7.1 Ring Laser Cavity Modular Design	234
7.7.2 Parabolic Mirrors With A Twist	235
REFERENCES.....	237

List of Abbreviations

PM	Polygon Mirror
TG	Transmission Grating
RG	Reflection Grating
SS	Swept Source
OCT	Optical Coherence Tomography
TD-OCT	Time Domain OCT
SD-OCT	Spectral Domain OCT
SS-OCT	Swept Source OCT
FWHM	Full Width at Half Maximum
RM	Retroreflector Mirror
SMF	Single Mode Fibre
cMSI	Complex Master-Slave Interferometry
FSR	Free Spectral Range
TSB	Total Swept Bandwidth
SST	Secondary Simultaneous Tuning
TF	Target Facet
RFL	Reflected Focal Length (parabolic mirrors)
FDML	Fourier Domain Mode Locked

Nomenclature

γ	incidence angle on diffraction grating
δ	diffraction angle
λ	wavelength
N	number of facets (polygon mirror)
G	line/groove density (diffraction grating)
E	eccentricity (polygon mirror)
m	diffraction order
φ	acceptance angle (polygon mirror)
ψ	convergence angle
λ_c	central wavelength
f	focal length
r	apothem (polygon mirror)
R	radius (polygon mirror)
Ω	retro angle
W	beam width
L	facet width
l	visible facet width
θ	polygon rotation angle

Conferences and Publications

- **SPIE. Optical Systems Design, Frankfurt, Germany, May 2018**
Oral Presentation and Manuscript Publication (Section 5.5)

Everson, M., Duma, V.F. and Dobre, G., “Performance enhancements from telescope optics in a polygon mirror-based, spectral filter for Swept Source-Optical Coherence Tomography (SS-OCT)”. *Optical Instrument Science, Technology, and Applications* (Vol. **10695**, p. 1069507) (May 2018). International Society for Optics and Photonics.

- **Frontiers in Optics & Laser Sciences (FiO&LS), Student Leadership Conference, Washington DC, USA, September 2017**
Participant
- **2nd Canterbury Conference on OCT with emphasis on Broadband Sources, Canterbury, UK, September 2017**
Oral Presentation and Manuscript Publication (Section 5.3)

Everson, M., Duma, V.F. and Dobre, G., “Optimisation of a polygon mirror-based spectral filter for swept source optical coherence tomography (SS-OCT)”. *2nd Canterbury Conference on OCT with Emphasis on Broadband Optical Sources* (Vol. **10591**, p. 105910V) (March 2018). International Society for Optics and Photonics.

- **SPIE. 7th International Conference on Lasers in Medicine, Timisoara, Romania, July 2017**
Oral Presentation and Manuscript Publication (2nd Prize for best oral presentation) (Sections 0, 4.4, 4.5 & 4.8)

Everson, M., Duma, V.F. and Dobre, G., “Aspects of vignetting in a polygon mirror-based spectral filter for swept source optical coherence tomography (SS-OCT)”. *Seventh International Conference on Lasers in Medicine* (Vol. **10831**, p. 108310L) (August 2018). International Society for Optics and Photonics.

- **European Conference on Biomedical Optics (ECBO), Laser World of Photonics, Munich, Germany, June 2017**
Poster Presentation and Manuscript Publication

Everson, M., Duma, V.F. and Dobre, G., “Optical power transmission in a polygon mirror-based swept source optical coherence tomography system”. *Digital Optical Technologies 2017* (Vol. **10335**, p. 1033520) (June 2017). International Society for Optics and Photonics.

- **International School of Light Science & Technology (ISLiST), Santander, Spain, June 2016**
Participant & Honorary Diploma Recipient

- **TIM 15-16 Physics Conference, Timisoara, Romania, May 2016**
Oral Presentation and Peer Reviewed manuscript publication

Everson, M., Duma, V.F. and Dobre, G., “Geometric & radiometric vignetting associated with a 72-facet, off-axis, polygon mirror for swept source optical coherence tomography (SS-OCT)”. *AIP Conference Proceedings* (Vol. **1796**, No. 1, p. 040004) (January 2017). AIP Publishing.

CHAPTER 1

INTRODUCTION

The work presented in this Thesis was carried out in the Applied Optics Group, School of Physical Sciences, University of Kent, from October 2015 to February 2019. All of the theoretical, experimental and simulation work was geared towards developing a full model, analysing the capabilities and optimising the performance, of a polygon mirror-based spectral filter for swept source optical coherence tomography (SS-OCT) systems.

1.1 Introduction to the Thesis

Mechanically-swept lasers, utilising a multi-faceted, rotating polygonal mirror, provide an alternative spectral filtering method that could play an important role in the high-resolution imaging modality known as Swept Source Optical Coherence Tomography (SS-OCT). A swept source (SS) fulfils the role of rapid and sequential, instantaneous laser linewidth selection from across the broad spectral range of an input laser source. High sweeping speeds, narrowband laser linewidths and a broadband spectral sweeping range, as well as a sufficiently high optical power output and overall system stability, are the key properties required of SSs employed in producing high-resolution SS-OCT images. Successful SS-OCT imaging relies upon having a long axial scanning range (imaging depth) and a high axial resolution, which are fundamentally linked to the narrowness of the linewidths and the broadness of the swept bandwidth respectively. A polygon mirror (PM)-based spectral filter has the ability to satisfy these requirements whilst also providing a versatile and stable platform for further experimentation that could lead to additional developmental paths.

The concept of using a PM to create a SS was first realised in the late 1990's [1] and was followed up in the early 2000's with a surge of research. A number of studies in the literature have successfully demonstrated the application of PM-based spectral filters in SS-OCT [2] [3] [4] [5] [6] including *in-vivo*, human retina and choroid imaging [7] and spectrally encoded confocal microscopy [8]. There have also been various attempts to improve particular aspects of these filters – for example; increasing the sweeping speed by counterintuitively minimising the duty cycle [9], or minimising the narrowband laser linewidths through the application of multiple, light-interactions with a diffraction grating [10]. Yet few have reported in detail the factors and trade-offs that govern their overall

performance or which methods produce the best results. Any improvements that are found are usually shown to have an impact on another property of the filter.

Figure 1.1. shows the instantaneous laser linewidth and the total swept bandwidth achieved by researchers using a PM-based spectral filter. The majority of publications measured a linewidth of less than 0.20 nm and a bandwidth less than 150 nm . Several publications managed to achieve larger bandwidths but did so at the cost of sacrificing other parameters. For example, the telescope-less spectral filter designs employed by Y.Mao 2011 [11], S.M.R.M.Nezam 2008 [12] and A.Morosawa 2007 [13] all produced total swept bandwidths $\geq 160\text{ nm}$ but had relatively large linewidths and/or suffered from less than ideal duty cycles. A 150 nm bandwidth with a 0.24 nm linewidth was demonstrated by W.Y.Oh 2005 [14], although the method used to achieve it required two spectral filters and two semiconductor light sources, working in tandem whilst operating on a single PM.

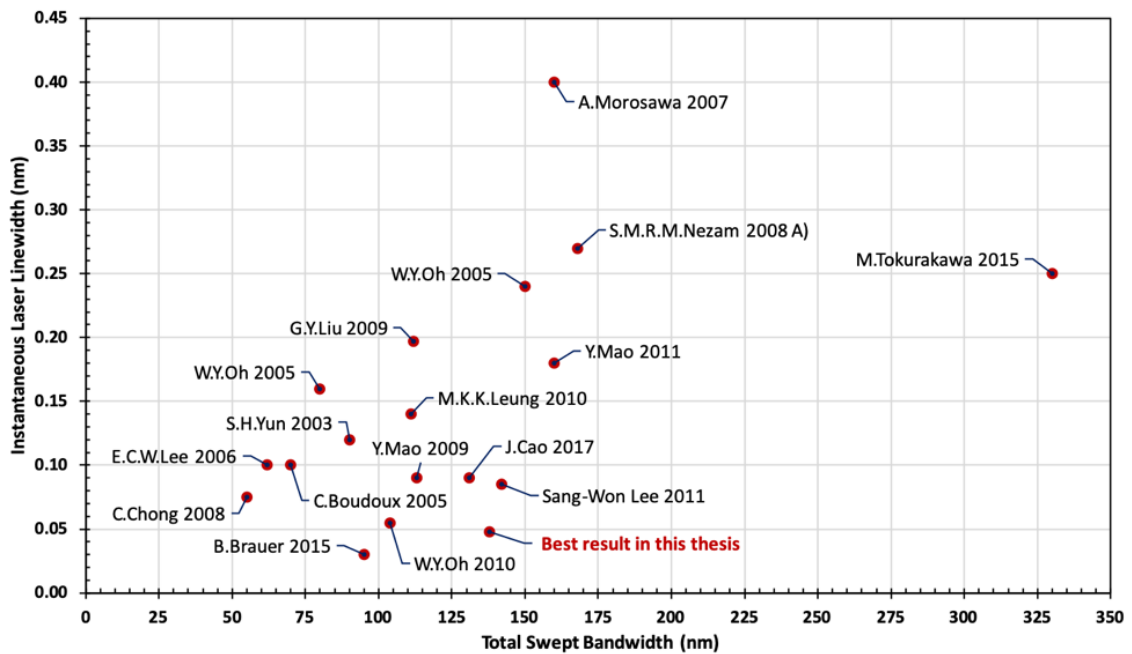


Figure 1.1. Instantaneous laser linewidth and total swept bandwidth achieved by researchers using a PM-based spectral filter. The general trend shows that larger bandwidths are produced at the cost of wider linewidths. Maintaining a narrow linewidth ($<0.05\text{ nm}$) over a wide spectral range ($>150\text{ nm}$) is generally regarded as one of the most desirable features for SS-OCT imaging.

M.Tokurakawa 2015 [15] produced the largest bandwidth at 330 nm but this was achieved at a much longer wavelength ($\sim 2\text{ }\mu\text{m}$) and suffered from a low sweeping speed (340 Hz) and gave less than ideal linewidths (0.25 nm). The most comparable result to that presented later in this thesis came from Sang-Won Lee 2011 [16] who produced a

142 nm bandwidth and 0.085 nm linewidths. The main disadvantage of this system came from a poor duty cycle and a less than ideal sensitivity. The smallest linewidth (0.03 nm) was produced by B.Brauer 2015 [10], who specifically designed their system to meet this objective, and was achieved through multiple diffraction grating interactions in order to minimise the spectral resolution, however the bandwidth was less than 100 nm.

There are three key advantages for using a PM-based spectral filter as a SS. These are:

- Speed – suitable for rapid data acquisition
- Cost – less than commercially available systems
- Versatility – highly customisable, wavelength independent operation

The speed is related to the rate of image generation in the SS-OCT system. High speed operation is desirable because it reduces motion artefacts in functional, real-time imaging. For PM-based SSs, the rate of image generation is fundamentally linked to the rotational speed of the PM through the bandwidth sweeping frequency, whereby a large facet count (e.g. >50) and a high rotational speed will improve the rate of data acquisition. Basic PMs have a minimum rotational speed of several thousand RPM [17], allowing them to achieve kHz sweeping frequencies (depending on the number of facets). By targeting specific parameters, scanning speeds in excess of 115 kHz have been achieved [18] and by applying additional delay line techniques (buffering) the sweeping frequency was successfully increased from 258 kHz [5] to > 400 kHz [9]. Alternative spectral sweeping methods, such as Micro-Electro-Mechanical Systems (MEMS) [19] and Fourier Domain Mode-Locked (FDML) SSs [20], [21], [22], can achieve considerably higher sweeping frequencies (> 1 MHz) [23], and have been successfully packaged into commercially available systems (< 300 kHz) [24], but they are typically limited in their ability to operate in separate wavelength bands using a single actuator. Their total swept bandwidth range, which is gradually increasing [25], is another limitation. Although PM-based systems are currently unable to compete with these speeds, they are still able to achieve modest tuning frequencies that are fast enough to perform real-time, *in vivo* studies, with full volumetric scanning capabilities. Progress in PM technology continues to push operating frequencies further [17], but if higher speeds are desired, then certain technological challenges must first be overcome, which will always be constrained by the fundamental physical limitations of the mechanical design [26].

Another advantage is that the cost of the PM-based spectral filter, and that of all its associated operating systems (power supply, motor and drivers), remains relatively low in comparison to commercially available SS systems [24]. A complete, PM-based SS, including all of the necessary optical components and alignment stages, can be purchased and assembled for ~15,000 Euros (depending on the design specifications) whereas commercial systems can exceed 50,000 Euros. The freedom of experimentation when using a PM in a laboratory setting allows a range of modifications to be made to its design, at relatively low cost, that greatly alter the properties of the SS and therefore offers significant leveraging capabilities from only a single component.

The most attractive feature of the PM-based SS is that it can operate at any wavelength (within reasonable limits). The instantaneous linewidth tuning process is carried out through angular selection, facilitated by the reflection of light off of a mirrored surface. A PM can therefore be used to create a SS that operates at more exotic, non-conventional wavelengths, which is of particular interest to SS-OCT since shorter wavelengths ($< 800\text{ nm}$) generally achieve longer axial scanning depths. Although non-PM-based SSs can be found that operate at these shorter wavelengths, they typically lack the necessary power output and/or they are limited by their swept bandwidth range [27]. If designed correctly, the PM-based spectral filter has the ability to deliver a sufficient power output and a broad sweeping bandwidth at any selected wavelength.

With a PM-based SS, experimenting with different wavelengths essentially only requires changing the light source input, which is significantly cheaper than purchasing an entirely new SS system. Indeed, some of the optical components would still need to be changed (e.g. optical fibres, diffraction grating, etc.) but the cost of these changes can be effectively minimised by selecting wavelength independent components (within limits) such as using reflective instead of refractive focusing optics to guide and shape the light beams (explored in Chapter 6). Furthermore, a PM-based SS can also be designed to operate at several wavelengths simultaneously by building multiple spectral filters that each utilise their own light source but interact with a single PM. This can either be used to broaden the total swept spectrum of the SS output, as shown by W.Y. Oh *et al* who combined two light sources to create a 145 nm bandwidth [11], or it can be used to provide dual-wavelength-band operation, as shown by Y. Mao *et al* who simultaneously performed SS-OCT imaging at 1310 nm and 1550 nm [14]. It is therefore entirely

feasible to envisage a single, low cost system, capable of high-speed operation, working at any desired wavelength range, whilst having a level of performance sufficient for SS-OCT imaging.

PM-based spectral filters also provide the advantage of sweeping through the spectral bandwidth continuously in a single direction of motion called unidirectional scanning. This is unlike the back and forth, bidirectional scanning of galvanometer scanners, piezoelectric actuators and MEMS-based systems [28]. Bidirectional sweeping can have a significant impact on the data acquisition speed of the OCT imaging system since it generates dead-time between the sweeps of the spectrum, realised by a poor duty cycle. The unidirectional sweeping provided by a PM-based spectral filter allows the duty cycle to be maximised (under the right conditions), leading to a more efficient SS. Furthermore, this feature also allows the spectrum to be swept either from short-to-long wavelengths (forward sweep) or from long-to-short wavelengths (backward sweep), depending on the arrangement of the components, which is advantageous since the typical light sources used in these spectral filters (semiconductor optical amplifiers – Section 2.3.2) operate more efficiently when the bandwidth is swept in one particular direction [19]. However, the unidirectional scanning of PMs can allow the mirrored facets to sweep across the path of the incident beam of light (termed ‘beam walk-off’ [13]) rather than pivoting underneath them, about an axis at the centre of their surface (like a galvanometer scanner). This allows some of the light to momentarily interact with an adjacent facet, which is then reflected in an undesired direction due to the incorrect angle of incidence. This form of light loss is one of the primary concerns in this research project and shall be discussed in greater detail in Section 2.7.1.

There is a current demand for improving the phase-stability in SS-OCT technology [29], which is important for maintaining the precise measurement of different features, in depth, along the optical scanning axis. The mechanical operation of the spectral filter relates the sweeping wavelength to the rotational angle of the PM, which may provide a more accurate method of establishing the timing signal of each sweep through the spectrum. A theoretical approach to this problem, discussed later in Section 1.6.1, may improve the phase-stability. However, this may be difficult since the mechanical nature of the PM can affect the dynamic tracking [26] which can cause the light to reflect in the wrong direction and decrease the optical power transmission (although this is usually

within acceptable tolerances ≤ 15 arcsec, see Appendix B). PMs also tend to be noisy when operating at high speeds, which makes them less desirable in a commercial setting. The sound is caused by the high velocity of the facet tips passing through the surrounding air. It is possible however to significantly reduced the amplitude of the sound by isolating the PM inside a closed chamber, with a partial vacuum, and using a glass window to transmit the light to and from the reflecting facets (~ 60 dB working at 70,000 RPM [17]).

1.1.1 About the Project and its Contributions

The work in this thesis is focused on the optimisation of a PM-based spectral filter for SS-OCT imaging systems. The intention is to deliver a stable platform that can be applied to multi-spectral, SS devices that allow operation at much shorter wavelengths which are currently not yet commercially available. Given the paramount importance of the aforementioned parameters (axial scanning range and axial resolution), the main objectives of this research project were to maximise the swept bandwidth and minimise the instantaneous laser linewidths. This was achieved by identifying the factors that had the biggest impact on these properties and was carried out by rigorously exploring and testing various spectral filter designs, both experimentally and theoretically, and by performing numerous software simulations, before constructing the real-life setup. All areas of the spectral filter design have been explored including the component choice, the construction methods and the detailed interaction of the light with each of its components.

Due to the freedom in designing a wide variety of different experimental arrangements, and the interconnectivity of the large number of parameters, finding a suitable method that achieves these goals requires multiple iterations through an assortment of methods. A judicious design approach is therefore required in order to simultaneously maximise the swept bandwidth and obtain reproducible and unambiguous, narrowband, instantaneous linewidth selection, whilst also maximising the power output and the stability of the system. Among the aspects selected for consideration, the following four fundamental factors were found during the analysis to significantly impact the spectral filter's performance. These are:

- Component Parameter Selection – limiting the swept bandwidth
- Simultaneous Tuning – due to filter design and setup
- Primary Vignetting – due to beam walk-off on the PM facets
- Secondary Vignetting – on the optical fibre exit aperture

The swept, spectral bandwidth can be physically restricted if care is not taken when selecting the components of the spectral filter, which must accommodate as much as possible the full spectrum provided by the laser source. It is entirely feasible to select components whose combined operation enables light to fall outside of the filter's physical sweeping range, producing an un-swept portion of the available bandwidth. The light undergoes multiple interactions with a number of components in the spectral filter and therefore a fully comprehensive study was required. Examination of each component's properties, and the geometry of their arrangement, led to a better understanding of their combined operation and the physical limitations that can be expected. This rigorous approach also resulted in the derivation of several new theoretical formulae that can be used to make predictions about the system's performance or to provide the operator with a guide to the precise location of each component needed to prevent unnecessary losses or unwanted effects such as simultaneous tuning.

Simultaneous tuning describes the unwanted selection and detection of two or more laser linewidths, at a particular instant in time, during a single sweep of the spectrum. This leads to ambiguity between the instantaneous wavelength measurements and their timing signatures, which generates unwanted noise in the OCT images. Although evidence of this can be found in the literature [30], the reasons why it occurs and the consequences it has on the system are not discussed in any detail. This thesis attempts to address this issue by demonstrating, using the derived formulae, how it occurs and how it can be prevented, and has been achieved by considering the properties of the components in the spectral filter as well as their precise arrangement and orientation with respect to one another.

Primary and secondary vignetting describe the two most important ways that optical power can be reduced in the spectral filter. Primary vignetting occurs when the light interacts with the rotating PM (sometimes referred to as 'beam walk-off') and secondary vignetting occurs when the light attempts to leave the spectral filter through the optical fibre exit aperture. Both forms of vignetting have already been shown to significantly reduce the amount of optical power transmission [31] [32] [33] and are therefore highly undesirable. Many publications attribute the shortcomings of their spectral filter to one or both forms of vignetting, however they are rarely explored in any detail and no solution to this problem has ever been presented. Therefore, the work in this thesis has made a

considerable effort to understand how vignetting occurs and shall demonstrate several novel ways to minimise these effects or even prevent them from happening altogether.

The most significant contribution in this thesis came from understanding the main cause of secondary vignetting, which can be largely attributed to the refractive optical components (lenses) and the aberrations that occur when using them. Although these effects are small, they are still able to prevent a large proportion of the light from following its intended path through the spectral filter, decreasing the optical power as a result. To remedy this problem, a novel filter design is presented that uses 90 degree, off-axis parabolic mirrors, instead of a two-lens telescope design, which removes the majority of aberrations and guides the light rays more successfully through the spectral filter. This design is shown to significantly improve the optical power transmission and can also help to maximise the swept bandwidth.

The SS-OCT imaging modality shall be introduced shortly in Section 1.3, since it is the intended application of the PM-based spectral filter. However, very applied and detailed aspects of OCT are not covered extensively here since the method was only used sporadically for capturing images from particular spectral filter designs that were significant to the overall goals of the project. A secondary consideration of the project was to minimise the overall experimental footprint. This would provide easier storage and transportation, as well as lending itself more conveniently to commercialisation. The footprint is directly related to the properties of the components, which therefore influences their choice. However, this consideration was not prioritised if it meant sacrificing the performance of the system. Maximising the sweeping speed of the spectral filter was also not prioritised since it requires either a faster PM or the application of techniques that were not covered in this research.

1.2 Organisation of the Thesis

The chapters in this thesis are organised as follows:

- Chapter 1 introduces the fundamental principles and requirements of OCT imaging, with a focus on Swept Source OCT (SS-OCT).
- Chapter 2 is a rigorous explanation of the experimental setup and reviews several assembly techniques and design considerations that can be applied to improve the overall performance of the spectral filter. The simulation software and the concept of mechanical vignetting are also discussed in detail.
- Chapter 3 introduces each of the components used in the spectral filter, describing their properties and fundamental operating principles including the most relevant equations.
- Chapter 4 applies a fully comprehensive theoretical treatment to the combined workings of all the components in the spectral filter and highlights the most important parameters that have the biggest impact on its performance.
- Chapter 5 presents the experimental and the simulation results to support the theoretical work from Chapter 4 and draws conclusions about the specific design being used.
- Chapter 6 uses the results from Chapter 5 to introduce the novel approach of using two 90 degree, off-axis parabolic mirrors instead of a two-lens telescope design.
- Chapter 7 is the final discussion of the thesis including recommendations based on the findings of the research.

1.3 Optical Coherence Tomography (OCT)

Optical Coherence Tomography (OCT) is a non-invasive imaging modality, capable of producing high-resolution, cross sectional scans through several millimetres of tissue depth. OCT allows real-time, *in-vivo* examinations of micron scale structures beneath the surface layers of a sample [34]. It has been used to non-destructively investigate a wide variety of objects, including paintings and historical artefacts [35], but it most commonly serves as an analytical and diagnostic tool in the field of biomedical imaging, specifically ophthalmology [36]. OCT provides an alternative imaging modality that conveniently bridges the gap between confocal microscopy and ultrasound imaging, offering additional image penetration depth over confocal microscopy, combined with an image resolution several orders of magnitude higher than conventional ultra-sound (Figure 1.2).

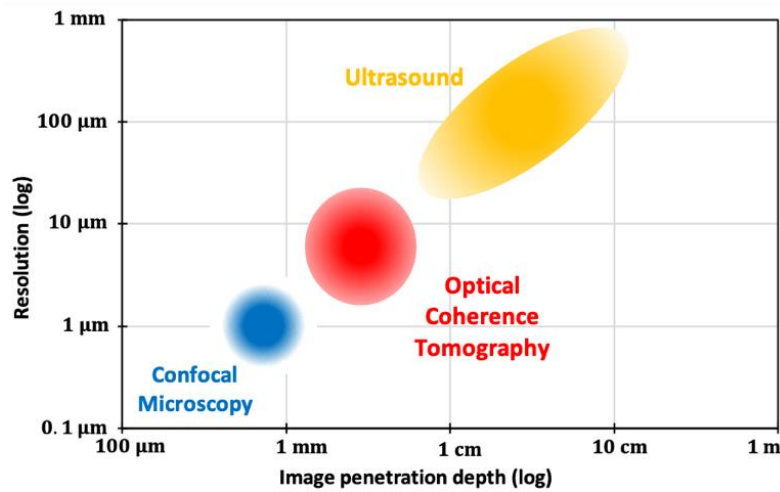


Figure 1.2. Penetration depth versus image resolution for three medical imaging modalities (adapted from Fujimoto et al. [37]). OCT conveniently bridges the gap between microscopy and ultrasound imaging.

Although the experimental work presented in this thesis included the design and construction of all the necessary equipment required to capture OCT images, this report does not emphasise the aspects of OCT imaging, nor the specifics of the software and the code used to generate the images. Images will be shown if a clear comparison can be made but the work is more exclusively concerned with the operation of the spectral filter and the goal of maximising its performance.

1.3.1 OCT Operation

A complete theoretical description of OCT goes beyond the scope of this thesis but the fundamental concepts shall be introduced and discussed with respect to the specific imaging modality that was used in this research project (Swept Source OCT – Section

1.4). OCT takes advantage of the wave properties of electromagnetic radiation and uses the interference between two overlapping wave-trains to identify the location of different structures within a sample. The interference is generated using an interferometer, which is the fundamental component at the heart of every OCT system. Most interferometers utilise (at least partly) optical fibres to guide the light to its destination (in this case, to the sample being imaged). The light from the source must also be divided and then later recombined, which is more conveniently achieved using fibre-based coupling methods. A diagram of a simple optical fibre-based interferometer is shown in Figure 1.3. The interferometer receives light from a partially coherent source and then uses an optical fibre-based coupler to split and guide the light along two paths. A proportion of the light is sent to the sample along an Object Arm and the rest is sent to a mirror along a Reference Arm. The light then reflects back from both arms and is recombined in the fibre coupler before being sent to a photodetector.

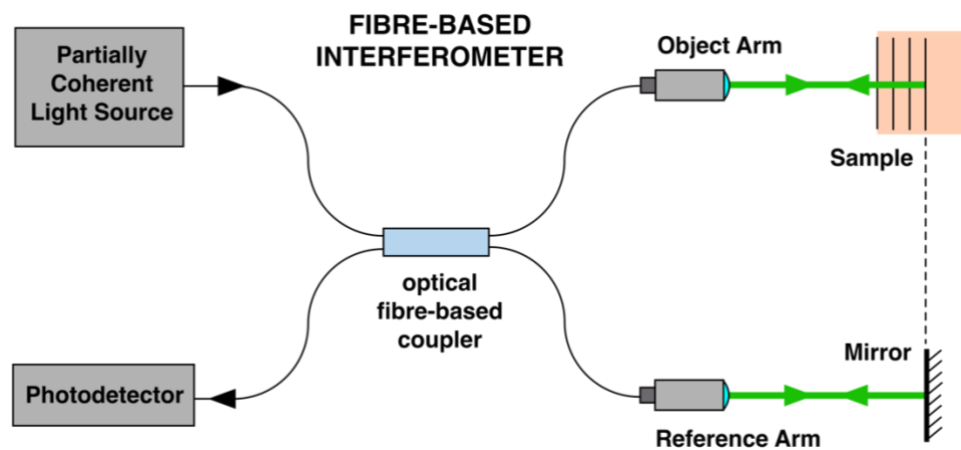


Figure 1.3. Simple representation of an optical fibre-based interferometer. Light from a partially coherent source is split by the fibre-based coupler and sent to the object arm and the reference arm. The light reflects off the various layers in the sample and mirror in either arm respectively. The returning light is recombined in the fibre coupler and a fraction of that is sent to the photodetector to measure the intensity of the interference pattern.

The echo time delay between the two signals returning from the object arm and the reference arm is linearly related to the optical distance in the axial direction (along the z-axis) to the various structures in the sample (depth). Interference between these two signals can therefore be linked to the Optical Path Difference (OPD), which describes the relative change in length between the two arms of the interferometer. For a partially coherent source, the interference pattern has a maximum signal amplitude when the two arms are of equal length ($OPD = 0$), since there will be no difference in phase between

the two returning wave-trains. As the OPD increases, the two returning wave-trains go out of phase and the signal amplitude decays. The amplitude of the light for each spectral component returning from each depth in the sample is measured with a photodetector as a time encoded signal and digitally processed to produce a depth resolved, axial reflectivity profile (or A-scan). Multiple A-scans carried out across the sample can then be stitched together to create a two-dimensional image of the sample in depth (see Section 1.5.3 for more detail). If the recombined interfering light is spectrally resolved (spectrally encoded signal), the interference pattern appears as peaks and valleys in the spectrum, which gives rise to the concept of a channelled spectrum. Only mutually coherent wave-trains returning from the object arm and the sample arm with at least a partial overlap will combine coherently to produce an interference pattern, placing a limit on the maximum path imbalance that still gives rise to interference.

The equations that describe the instantaneous electric field of each wave returning from: 1) a single depth location, z , in the object arm (E_{obj}) and 2) the reference arm (E_{ref}) can be written respectively as [38].

$$E_{obj}(z_{obj}) = A_{obj} \cos(kz_{obj} - \omega t) \quad \text{Eq. 1.1}$$

$$E_{ref}(z_{ref}) = A_{ref} \cos(kz_{ref} - \omega t) \quad \text{Eq. 1.2}$$

Where A is the (complex) amplitude of the wave (taking into consideration the amplitude transmission and reflection coefficients [37]), k is the wavenumber (where $k = 2\pi/\lambda$, with λ being the wavelength), z_{obj} and z_{ref} are the optical propagation distances along the object and reference arms respectively, $\omega = 2\pi\nu$ is the angular frequency (with ν being the frequency) and t is time. The two waves are recombined after travelling back through the arms of the interferometer and the superposition gives the amplitude of the electric field at the photodetector, $E_D = E_{obj} + E_{ref}$. However, the photodetector measures the intensity modulation, I_D , of the interference pattern, rather than the amplitude of the electric field, which must be time-averaged and squared before giving

$$I_D(OPD) = A_{obj}^2 + A_{ref}^2 + 2|A_{obj}||A_{ref}|\cos(k \cdot OPD) \quad \text{Eq. 1.3}$$

In the expression above, the first two terms (usually called the DC terms) produce unwanted background signals whilst the third term provides the required interference fringes. The OPD is also defined here as the difference between the total optical path lengths of the object and reference arms, i.e.:

$$OPD = z_{obj} - z_{ref} \quad \text{Eq. 1.4}$$

OCT imaging with partially coherent light relies on the relatively broad nature of the illuminating source spectrum, which preferably would have a Gaussian power spectrum, as depicted in Figure 1.4, that is described by the cross-correlation function, $\zeta(z)$ (or fringe visibility function) [37].

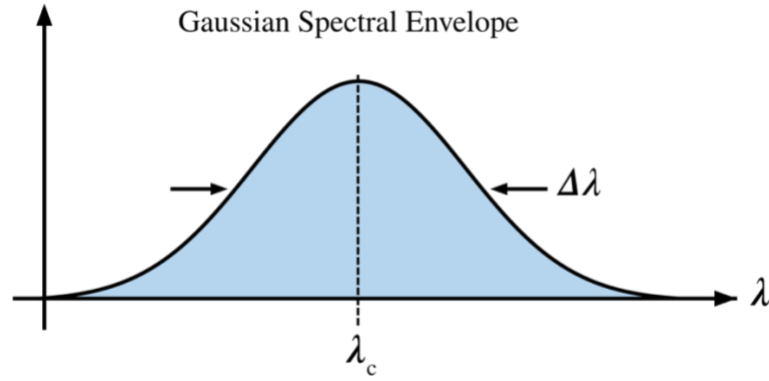


Figure 1.4. Gaussian power spectrum of the light source output. $\Delta\lambda$ is the FWHM bandwidth and λ_c is the central wavelength.

The coherence length, l_c , describes the mutual degree of coherence between the wave-trains, which gets smaller at distant wavelengths and therefore makes the FWHM of the source spectrum, $\Delta\lambda$, a useful measure of the spectral integral for which there is still coherence/cross-correlation. The coherence length as a function of source bandwidth is given by [37]

$$l_c = \frac{2 \ln 2}{\pi} \frac{\lambda_c^2}{n \Delta\lambda} \quad \text{Eq. 1.5}$$

where λ_c is the central wavelength and n is the refractive index of the medium. The optical path lengths of the two interferometer arms must be matched to within the coherence length in order to create an interference pattern. It is therefore advantageous for l_c to be as small as possible, which requires $\Delta\lambda$ to be as large as possible.

The unambiguous detection of peaks in OCT is intrinsically linked to the limited spatial extent of l_c . Since the instantaneous interference signal is the superposition of all interference signals I at all k values, the OPD must be less than l_c , in order to generate an interference pattern for a particular layer at a particular depth in the sample. This is called the coherence gate condition, $OPD < l_c$. Beyond that depth the fringe patterns, $I(t)$, combine increasingly less coherently due to the lack of correlation between their maxima and minima. Eq. 1.3 ($I_D(OPD)$) must change to incorporate the coherence gate condition at a given depth z , which for convenience is used instead of OPD.

$$I_D = A + 2|A_{obj}||A_{ref}|\zeta(z)\cos(2kz) \quad \text{Eq. 1.6}$$

The expression in Eq. 1.6 above assumes a single scattering event in the object arm. In reality multiple scattering events can be expected, particularly from multi-layered objects. As the wave-train (with wave number k) penetrates the sample, it undergoes a number of such scattering events, N , along the z -axis, from discrete scatterers at depths, z_n , away from $OPD = 0$. This gives a different wave-train for each scattering event. The superposition of all wave-trains from all scattering events simultaneously makes up the final modulated signal. The intensity measured at the detector, I_D , is then given by the previous formula adapted for N scatterers.

$$I_D = A + \sum_{n=1}^N 2|A_{obj}||A_{ref}|\zeta(z_n)\cos(2kz_n) \quad \text{Eq. 1.7}$$

where A is a constant incoherent term and $2z_n$ is the OPD due to the double pass in the object arm. Different depths into the sample, z_n , contribute to the signal at the detector only when $\zeta(z_n)$ is sufficiently greater than zero, i.e. when the coherence gate condition has been met, where the spatial extent of the superposed wave-trains, emitted by the source, maintain a constant phase relationship. This sets a limit on the axial scanning range, as will be shown shortly.

1.4 Spectral Domain OCT

The first OCT systems were designed to operate in the Time Domain (TD-OCT) but were limited in their data acquisition speed due to the necessity to modulate the length of the reference arm in order to take measurements over a range of depths in the sample [34].

As the science and technology advanced over time, this necessity was removed after OCT operation in the Spectral Domain (SD-OCT) was demonstrated [39], which allowed data to be collected from all depths simultaneously, leading to much faster data acquisition rates, higher sensitivity and more versatility in real-time imaging [40] [41].

Section 1.3.1 showed how a broadband light source with a time-invariant spectrum can be used with scanning the OPD to generate TD-OCT images. On the other hand, in SD-OCT, either Spectrometer Based (SB-OCT) or Swept Source (SS-OCT), the reference arm path length is fixed and instead the signal is built from the interference of spectral components, across a broad spectrum, returning from the various structures at different depths in the sample (and therefore each component has a different OPD). The two modalities, SB-OCT and SS-OCT, exhibit several hardware differences, but both use a broadband source to image the sample and separate the different frequency modulations using a Fourier transform in order to retrieve the structural information from different depths simultaneously, all whilst maintaining a constant path difference, Δz , in the arms of the interferometer.

In SB-OCT, the illuminating beam contains the entire spectrum of the broadband light source and the interference signals from across the entire broadband spectral envelope are detected simultaneously. All wavelengths, from λ_{min} to λ_{max} , penetrate into the sample simultaneously and are returned to combine with light from the reference arm on a spectrometer, which uses a CCD camera with a linear pixel array to record the interference signal such that the k values are spatially encoded to pixel numbers. Maxima arise at pixel locations (wavelength) where the OPD fulfils the maximum interference condition, and minima arise at locations fulfilling the minimum interference condition, giving rise to a channelled spectrum as a function of k (wavenumber). The camera measures each pixel sequentially in order to build up the one-dimensional reflectivity profile. Usually signal resampling is needed to make k linear prior to performing the Fourier transform. The speed of the camera determines the scanning speed of the accompanying OCT system. In SS-OCT, the interference signals at each depth are generated and detected sequentially by scanning a narrowband window across the broadband spectral envelope, such that the k values are spatially encoded in time on a balanced photodetector [42], [43], [44].

1.4.1 SS-OCT Operation

SS-OCT on the other hand, illuminates the sample with a source of much narrower bandwidth than those described in TD-OCT and SB-OCT. Such a source has a laser-like linewidth, $\delta\lambda$, selected from a broad overall spectrum, $\Delta\lambda$, by a tuning process. This tuning process performs a sweep through the broadband source, i.e. a selection from λ_{min} to λ_{max} in a continuous sequence before repeating the cycle. At any instantaneous moment in time, the tuned spectral component will penetrate into the sample and return from a given scatterer with information that is depth and wavelength specific. This information is encoded into the interference signal, which is retrieved by measuring the intensity of the signal on a balanced photodetector. Every spectral component in the bandwidth completing this operation contributes a narrow range of depth towards the one-dimensional reflectivity profile (A-scan). In contrast with SB-OCT, k is now a function of time, $k(t)$, rather than pixel number on the line camera.

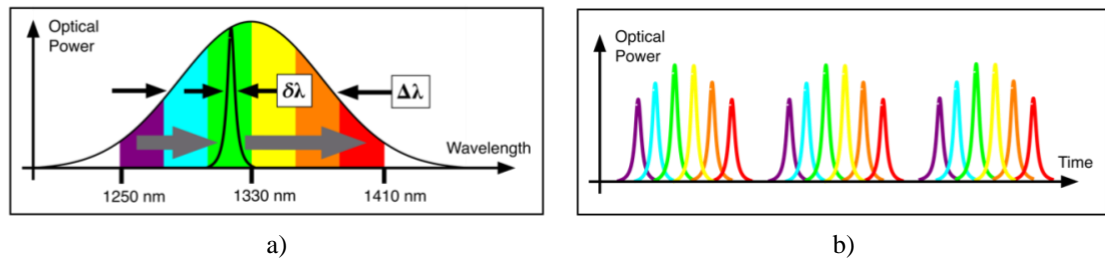


*Figure 1.5. Example of the SS sweeping process and the output generated. **a)** shows the selection of a narrowband, laser linewidth, $\delta\lambda$, from a broadband source with a spectral bandwidth, $\Delta\lambda$. The SS scans through the bandwidth, sequentially selecting a narrow component from across the entire spectral range, which constitutes a single sweep of the spectrum. **b)** represents three consecutive output sweeps of the spectrum over time. Individual linewidths are coloured to indicate which region of the spectrum they came from and the order they were tuned in. The lateral extent of the spectrum is typical of the range found in many optical amplifiers.*

The linewidth selection is carried out sequentially and continuously as the bandwidth is swept from one side of the spectrum to the other – left to right in Figure 1.5 a) (short-to-long wavelength). At the end of the sweep, the process is repeated and the linewidth selection starts again. An example of the swept spectrum output is demonstrated in Figure 1.5 b), which shows the individual linewidths with respect to time. The bandwidth sweeping frequency (or tuning speed) of the SS determines the scanning speed of the accompanying OCT system. The fringe signal is now measured by a photodetector, where the intensity is a function of k rather than z . As the reference arm is fixed, the OPD, z_n , between a given scatterer and the reference mirror is time-invariant. The fringe visibility

function, $\zeta(z_n, \delta\lambda)$, is also time-invariant. Due to the narrower range of wavelengths, ζ is much broader in SS-OCT than TD-OCT and SB-OCT.

$$I_D(k(t)) = DC \text{ terms} + \sum_{n=1}^N 2|A_0||A_R| \zeta(z_n, \delta\lambda) \cdot \cos(2k(t)z_n) \quad \text{Eq. 1.8}$$

The DC term at the beginning of the function contains the sum of mutually incoherent signals. This term is removed at the output of the balanced photodetector due to the anti-phase of optical signals in the final fibre coupler. Apart from the DC term cancellation, the balanced photodetector also has the effect of doubling the second term (the AC term) containing the desired SS-OCT signal.

1.4.2 Sample Penetration Depth

As described in Section 1.3, OCT provides high-resolution, cross sectional depth scan images of the surface layers in a tissue sample. The maximum penetration depth along the scanning axis is limited by three factors: light attenuation of the investigating beam through scattering and absorption (discussed immediately below), the limited mutual coherence between the interfering wave-trains (Section 1.4.3) and limited depth of field of the objective lens in the object arm (Section 1.5.1). For all OCT methods (TD and SD-OCT), a percentage of light is lost due to absorption and scattering (typically Mie scattering in biological tissue). Progressive attenuation with depth decreases the signal returned from deeper layers, which is related to the properties of the tissue being examined (see Section 1.6.1). After a certain depth, the amount of light returned is reduce to zero. The strongest signals are returned from the surface of the sample, since the relative change in the refractive index is typically an order of magnitude greater for the transition at the boundary between air and the sample, compared to the difference between the various layers beneath. Increasing the optical power on the surface of the sample will increase the amount of light recaptured from greater depths, but the power incident on *in vivo* targets must conform to the maximum permissible exposure (MPE) limits for eye and skin (w.r.t wavelength) in order to avoid the risk of damaging the tissue [45].

1.4.3 Axial Scanning Range

The requirement for mutual coherence between the returning wave-trains, from the object arm and the reference arm, results in a limitation on the maximum axial scanning range due to the fact that the reference arm is fixed in SD-OCT. In SB-OCT, the limitation is

caused by the finite nature of the sampling performed by each pixel on the spectrometer CCD line camera, but in SS-OCT the limitation is caused, in a somewhat analogous way, by the instantaneous laser linewidths, which cannot be infinitely narrow.

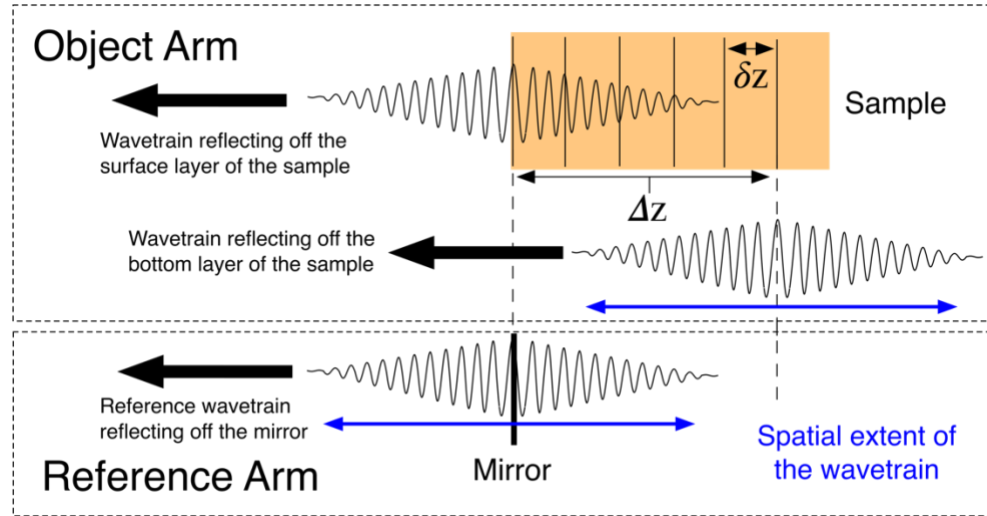


Figure 1.6. Reflected wave-trains from the sample in the object arm and the mirror in the reference arm using either SB-OCT or SS-OCT imaging modalities. The spatial extent of the wave-trains and their overlap determine the visibility of the structures at different depths. It is useful to identify the imaging depth, Δz , and the spacing, δz , between layers that are just resolved. The deeper into the sample the light penetrates, the less the wave-trains overlap, which reduces the sensitivity.

This maximum range can be defined in a similar way to the TD-OCT coherence length, using Eq. 1.5. In SS-OCT however this coherence length should be thought of as an axial coherence imaging range, which should be as large as possible (Eq. 1.9). Consequently, this means that the instantaneous laser linewidths, $\delta\lambda$, should be as small as possible.

$$\Delta z < \frac{\lambda_c^2}{2\delta\lambda} \quad \text{Eq. 1.9}$$

Finally, even if the losses from scattering and attenuation were not the limiting factor, the axial range also depends upon the numerical aperture of the objective lens in the object arm, which should ideally be selected to provide a long depth of field in order to maximise the confocal gate. However, this requirement will also have an impact on the transverse resolution (see Section 1.5.1).

1.4.4 Sensitivity – Fringe Visibility

Sensitivity is essentially a description of the system's ability to discern the usable signal from the inherent background noise. The discernibility of the signal depends on the properties described in Section 1.4.2 above but also adheres to fundamental theoretical

limitations. In TD-OCT, the sensitivity is the same for all of the layers interrogated in the sample, since the detection process is carried out around $OPD = 0$, but in SD-OCT systems (both SB-OCT and SS-OCT) the sensitivity decays with depth (also known as signal drop-off). The detection process of SD-OCT depends on the mutual overlap between the two interfering wave-trains returning from the object arm and the reference arm. The fringe visibility decreases with increasing sample depth and is an inherent feature of systems with a fixed path length in the reference arm [46]. The axial distance at which the signal intensity reduces by half, $z_{half\ max}$, is related to the FWHM of the instantaneous laser linewidth, $\delta\lambda_{FWHM}$, given by [37]

$$z_{half\ max} = \frac{\ln(2)}{\delta k_{FWHM}} = \frac{\ln(2)}{2\pi} \frac{\lambda_c^2}{\delta\lambda_{FWHM}} \quad \text{Eq. 1.10}$$

There is a 20-30 dB sensitivity advantage from using SD-OCT over TD-OCT [40], which can be explained by the fact that TD-OCT systems exclude light from outside the narrow coherence gate condition, removing it from the detection process (only a small fraction of $l_c/2z_{max}$ contributes towards the instantaneous signal), whilst the signal generation in SD-OCT systems comes from the combined backscattered light from all depths simultaneously [47].

In both SD-OCT methods, it is important to maintain a stable phase relationship between the interfering wave-trains. Instabilities can arise if the sample moves during the data acquisition (counteracted by using faster SS) or if the swept spectrum suffers from inconsistent wavelength tuning. In SB-OCT, poor phase stability results in signal loss of the fringes, leading to a necessity to increase the power [48], but in SS-OCT the inconsistent wavelength sweeping effects the location of the fringes, leading to ambiguity in the depth measurements, which introduces noise to the images.

1.5 Image Resolution and Scanning Methods

The transverse resolution and the axial resolution of an OCT system are decoupled from one another, which means they can be optimised independently. The transverse resolution (Section 1.5.1) is determined by the focusing properties of the interrogating optics, which follow the laws of confocal microscopy and Gaussian beam theory, but the axial resolution (Section 1.5.2) is determined by the properties of the investigating light source.

1.5.1 Transverse Resolution

The transverse (or lateral) resolution of the OCT imaging system is determined by the diffraction limited spot size of the focused beam produced by the objective lens in the object arm (Figure 1.7).

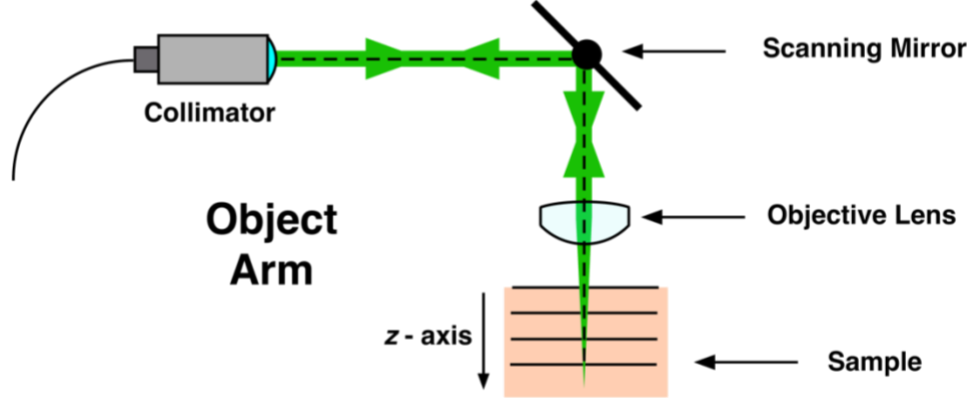
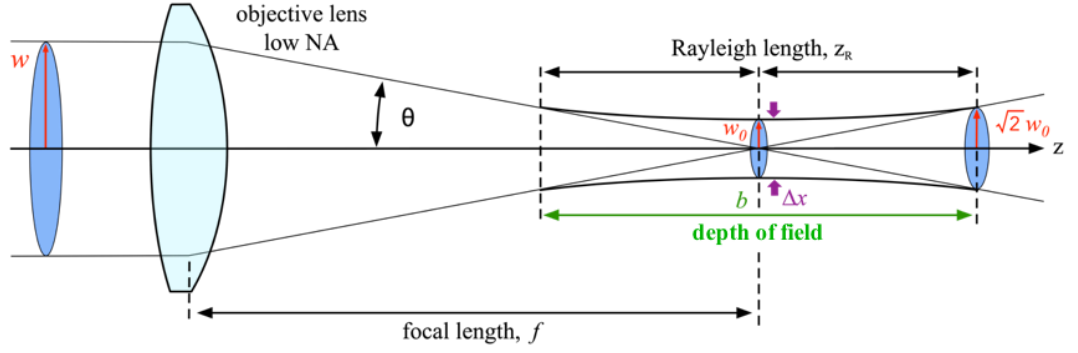


Figure 1.7. Object arm scanning optics indicating the direction of propagation of light into the sample (z-axis). Light from the optical fibre enters the free-space path through a collimator directed onto a galvanometer scanning mirror which reflects and scans the beam over an objective lens before penetrating into the sample.

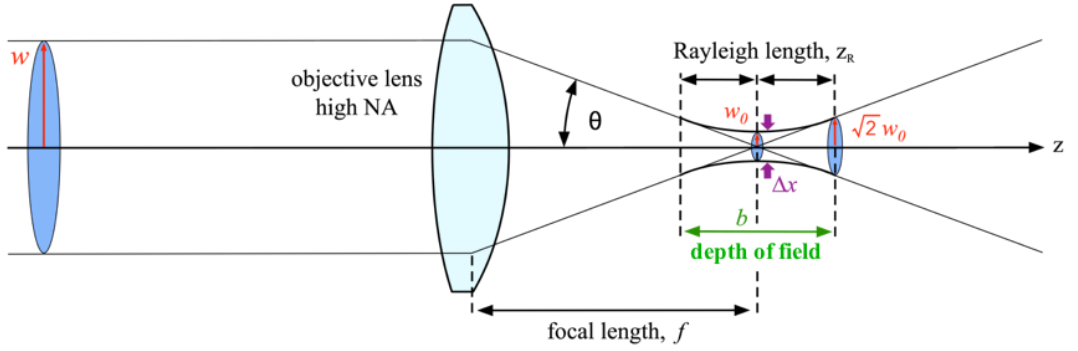
The spot size, Δx , is inversely proportional to the numerical aperture, NA , of the objective lens and directly proportional to the operating wavelength, λ_c . The NA of the lens can be approximated by $D/2f$, where f is the focal length and D is the diameter of the beam incident on the lens or the diameter of the objective lens itself, whichever is smaller [49]. The transverse resolution, Δx , is therefore given by [49].

$$\Delta x = \frac{2}{\pi} \frac{\lambda_c}{NA} = \frac{4}{\pi} \frac{f \lambda_c}{D} \quad \text{Eq. 1.11}$$

Increasing the NA of the objective lens increases the transverse resolution, as shown in Figure 1.8 a) and b). However, this also shortens the depth of field, b , which can have an impact on the axial scanning range, Δz , discussed shortly.



a) Low NA objective lens – large spot size, lower transverse resolution, long depth of field



b) High NA objective lens – small spot size, higher transverse resolution, short depth of field

Figure 1.8. Objective lens NA comparison and their focused beam spot size, Δx (assuming a Gaussian beam). a) Low NA lens (long focal length) providing a large spot size. b) High NA lens (short focal length) providing a small spot size and an improved transverse resolution. The depth of field, b , is determined by the Rayleigh length, z_R , defined as the axial distance from the focused spot to the point where the beam's radius, w_0 , increases to $\sqrt{2}w_0$ (or where the cross-sectional area doubles).

In Gaussian beam theory, the focused spot has a radius, w_0 , defined by the radial distance at which the irradiance is equal to $1/e^2$ (13.5 %) of its initial value at the centre of the beam. The Rayleigh length, z_R , is determined by the axial distance from the focused spot to the point where the beam radius has increased by a factor of $\sqrt{2}$, or where the cross-sectional area of the beam has doubled. The depth of field (or confocal parameter), b , is given by twice the Rayleigh length of the Gaussian beam and describes the axial range (confocal gate) within which the transverse resolution is approximately maintained.

$$b = 2z_R = \frac{\pi \Delta x^2}{2 \lambda_c} \quad \text{Eq. 1.12}$$

Eq. 1.12 demonstrates that the depth of field increases with the square of the transverse resolution – the smaller the spot size of the focused beam, the shorter the axial range. Selecting a high NA objective lens will improve the axial resolution but at the cost of

having a short depth of field. Since OCT is concerned with imaging in depth, the axial scanning range, Δz , described in Eq. 1.9, should ideally be shorter than the depth of field ($\Delta z < b$) to ensure that the transverse resolution is maximised throughout the scanning range. Typically, $\Delta z > b$, although this can be solved by selecting a low NA objective lens with a long depth of field, but at the cost of worsening the transverse resolution. The only way to maintain a high transverse resolution throughout the entirety of the scanning range is to use a high NA lens with dynamic focusing along the optical axis [50].

1.5.2 Axial Resolution

The axial resolution, δz , refers to the shortest distance between two features within a sample that can be successfully resolved along the light propagation axis (z-direction). In OCT, it is independent from the imaging optics and only depends upon the properties of the swept light source. The axial resolution is defined as half the coherence length, since the optical path between two scattering events is double the physical separation between scatterers.

$$\delta z = \frac{l_c}{2} = \frac{2 \ln(2)}{\pi n} \cdot \frac{\lambda_c^2}{\Delta \lambda} \quad \text{Eq. 1.13}$$

The theoretical axial resolution, δz , for a Gaussian source, is proportional to the square of the central wavelength, λ_c , and inversely proportional to the FWHM of the SS bandwidth, $\Delta \lambda$, and the group refractive index, n , of the medium (Eq. 1.13). Therefore, a swept light source with a short central wavelength value and a wide spectral bandwidth will increase the ability of the system to resolve finer details (depending on the sample). The benefits from using such parameters are demonstrated in Figure 1.9, which shows the theoretical axial resolution for three central wavelength values; 600 nm (red), 1000 nm (green) and 1400 nm (blue). A refractive index value $n = 1$ was used in Eq. 1.13 to plot each of the three curves.

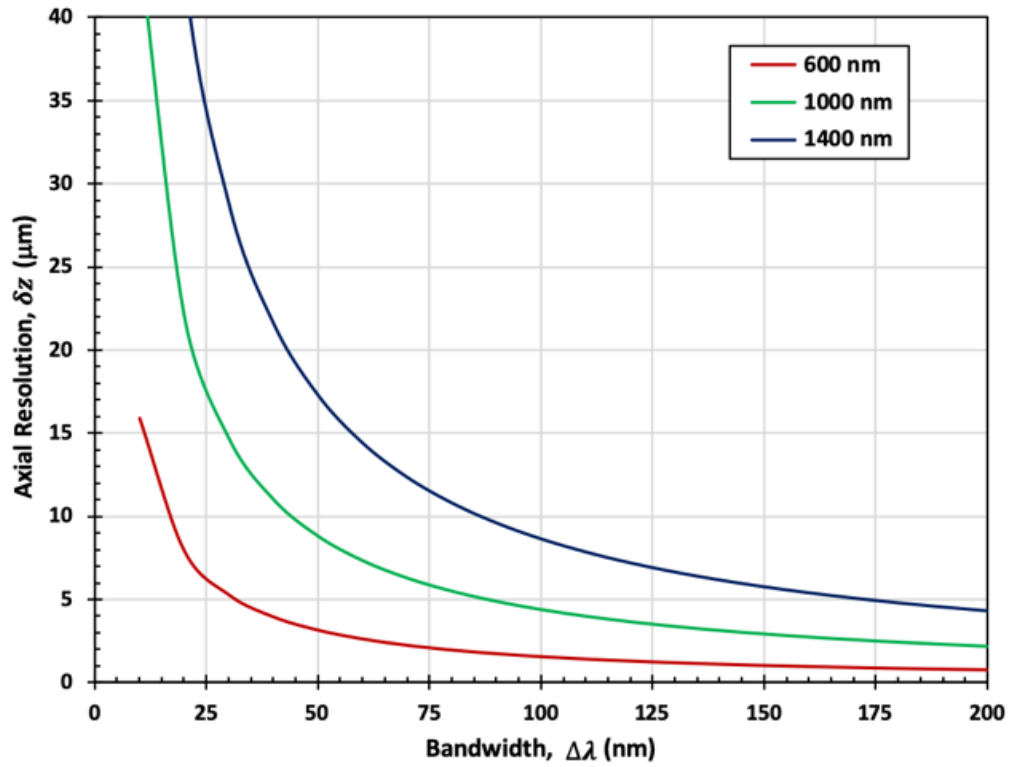


Figure 1.9. Theoretical axial resolution for three central wavelength values - 600 nm (red), 1000 nm (green) and 1400 nm (red). The difference in axial resolution between the two extreme wavelengths decreases with increasing bandwidth.

The axial resolution is shown to improve considerably when the bandwidth is increased around values $< 100 \text{ nm}$. After this point, the biggest impact to the axial resolution comes from changing the central wavelength value. However, a much wider bandwidth is required for longer central wavelengths in order to achieve the same resolution as a system using a shorter central wavelength. For example, sub $5 \mu m$ resolution can be theoretically achieved with bandwidths as narrow as 35 nm when using a central wavelength value $\lambda_c = 600 \text{ nm}$, but an equivalent resolution at $\lambda_c = 1400 \text{ nm}$ requires a bandwidth of around 200 nm , which is 5.7 times larger. However, the central wavelength depends upon the application (Figure 1.11), which may require a larger value in order to penetrate deeper into the sample (Eq. 1.9) or to minimise the risk of tissue damage (Section 1.4.2). Therefore, an important goal when designing a SS is to ensure that it provides the widest swept bandwidth possible.

1.5.3 Scanning Methods

The advantage of OCT is that it allows the exploration of a sample in three dimensions. This is due to the method of extracting information from the sample. OCT images are obtained in reflection by focusing light through an objective lens onto a tissue sample. The illuminating light penetrates into the sample and scatters off the various structures at different depths. The reflected light is collected via the same imaging optics and contains the path length information to the various structures along the z-axis. Each one-dimensional depth profile is called an A-scan, shown by the vertical red lines in Figure 1.10. Two-dimensional depth profiles are created by performing multiple A-scans across the surface of the sample and stacking them together to form a B-scan (blue box).

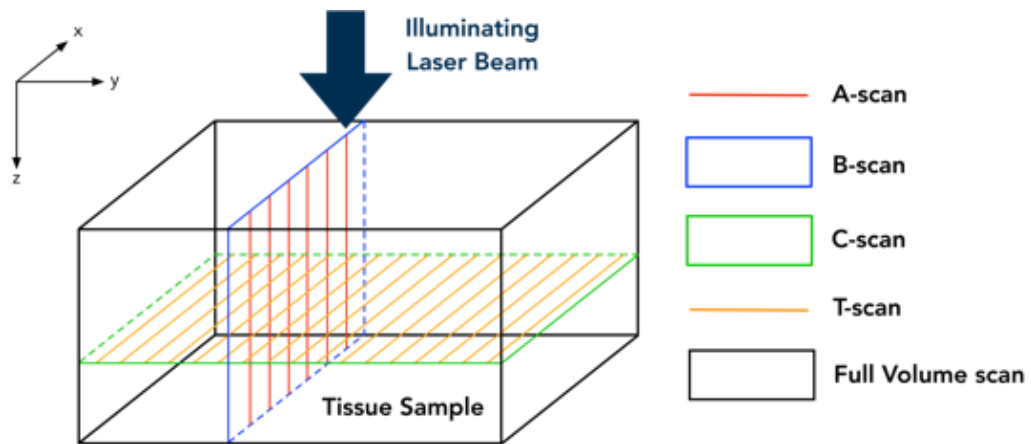


Figure 1.10. Sample scanning methods. All OCT images are constructed by first performing an A-scan (red line) which is a two-dimensional line scan that contains the depth location of the various structures in the sample. Stacking A-scans gives a B-scan (blue box) and, if two scanning mirrors are used, a Full Volume scan can be produced by stacking B-scans. C-scans and T-scans can also be selected after constructing the Full Volume scan.

Multiple A-scans are produced by scanning the laser beam across the object in the lateral (or transverse) direction, which is typically carried out with a galvanometer scanning mirror. If two scanning mirrors are used, both orthogonal directions can be scanned to sample an area in the x - y plane, which allows multiple B-scans to be collected and stacked together to construct a Full Volume scan (black box). The information used to create the Full Volume scan can also be used to create a T-scan (orange lines) or a C-scan (green box) from any depth desired. Every OCT image presented in this Thesis is a B-scan (blue box) since only a single galvanometer scanning mirror was used in the object arm.

1.6 OCT Requirements

The current research in OCT is divided along two paths; either improving the resolution in both the axial and the transverse directions (in order to supersede confocal imaging) or by enhancing the image penetration depth and the data acquisition speed of the devices. The main factor involved with improving these features is the light source, more specifically several of its properties: the operating wavelength, the total spectral range and, in the case of SSs, the bandwidth sweeping frequency.

1.6.1 Operating Wavelength

The operating wavelength (or central wavelength, λ_c) of the OCT system is generally chosen as a function of the sample intended to be imaged. The objective is to minimise the amount of light absorption in the sample, which depends upon the properties of the tissue. The graph in Figure 1.11 displays the known absorption of light (cm^{-1}) for a selection of biological material [34]. The wavelength region with the least absorption is between roughly 600 – 1400 nm and is called the optical (or therapeutic) window. Typical SS-OCT systems, especially those used in biomedical imaging, function somewhere in this wavelength range, although there are some non-biological OCT systems that operate at longer wavelengths for alternative applications [51].

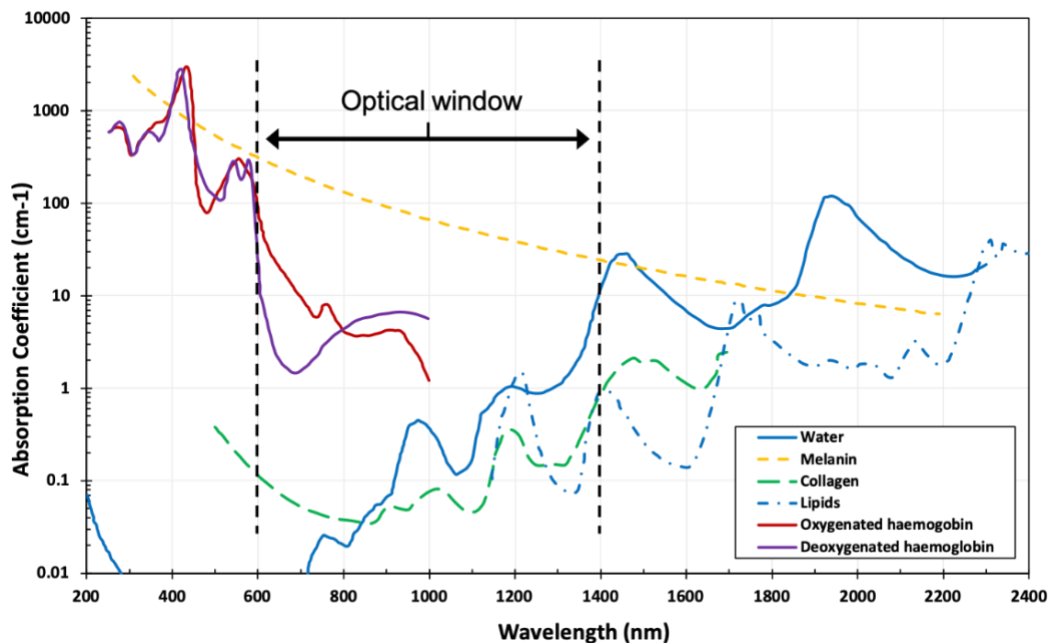


Figure 1.11. Absorption coefficient (cm^{-1}) for biological tissues at different wavelength values, adapted from Huang et al. [34]. The optical (or therapeutic) window is the wavelength range that is least absorbed by the various substances in the tissue and sits approximately between 600 nm to 1400 nm.

However, the operating wavelength is limited by the availability of optical amplifiers, which were primarily developed for telecommunication systems and are therefore not so readily available at all wavelengths in the optical window or whilst simultaneously providing a sufficiently large bandwidth. Progress in optical amplifier technology, with an emphasis on shorter wavelengths (500 – 800 nm), would benefit OCT imaging of biological tissue with high water content, such as the eye. This could be combined with the PM-based SS, which has the ability to operate at any of the wavelengths in the optical window and therefore would enable advances in OCT imaging.

1.6.2 Total Swept Bandwidth (TSB)

Many publications typically discuss the free spectral range (FSR) of their spectral filter [52], however this can be misleading since the theoretical values they predict in their calculations are often much higher than the system is actually capable of providing. This is usually due to a limited bandwidth but it can also be due to the properties and combined operation of the components used. For this reason, this thesis refers to the total swept bandwidth (TSB) of the spectral filter, which is a more accurate prediction (or measurement) of the actual SS bandwidth output and therefore can be used to predict the coherence length (Eq. 1.5) or the axial resolution (Eq. 1.13) of the accompanying OCT system.

The TSB of the SS should be as wide as possible in order to minimise the coherence length and approach the theoretical maximum axial resolution. However, broadband laser sources such as supercontinuum lasers are technologically difficult to create, making them expensive to produce [53]. Progress in ultra-wideband sources has also been hampered by the need to manufacture components that can accommodate such a wide range of wavelengths, e.g. diffraction gratings and spectrometers. For this reason, and taking into account the variation in tissues and their transparency at different wavelengths (Figure 1.11), most OCT systems so far have opted to restrict the TSB, with commercially available SSs claiming the widest. Wider bandwidths also increase the effects of dispersion, which prevents all the different wavelengths of light from reaching their destination simultaneously. This causes unwanted time-delays in the returning signals and therefore reconstructs the depth of the various structures in the sample incorrectly. These dispersion effects can be mitigated through dispersion compensation software [54], [55] (cMSI takes care of some dispersion – see Section 2.5) and hardware [56].

1.6.3 Polygon Mirror-Based Spectral Filter Requirements

In order to maximise performance, the SS must be designed in accordance with the operating principals of OCT imaging, presented in Sections 1.4, 1.5 and 1.6. The PM-based spectral filter has the biggest influence on the performance of the OCT system since it is responsible for providing all of the properties of the light required of the SS. The operating wavelength of the light source is determined by the nature of the sample (Section 1.6.1) and has an effect on the transverse resolution (Eq. 1.11). The light source provides the total available bandwidth; however, the design of the spectral filter plays a significant role in how efficiently this bandwidth is maintained whilst sweeping through it. As was discussed in Section 1.6.2, the TSB of the SS should be as wide as possible in order to minimise the coherence length and approach the theoretical maximum axial resolution (Eq. 1.13). The light source is also responsible for the initial optical power amplitude, which must be preserved by the spectral filter to avoid under illuminating the sample (Section 1.4.2). Another important parameter of the spectral filter is the width of the instantaneously swept, narrowband laser linewidths, which must be as small as possible in order to maximise the axial scanning range (Eq. 1.9) and the sensitivity (Eq. 1.10). In general, optimising the SS involves maximising the light transmission through the spectral filter, whilst simultaneously ensuring that the smallest linewidths are selected from the maximum swept bandwidth possible. As will be shown in this thesis, this task is less than trivial and requires approaching the problem from multiple directions to find an acceptable solution.

CHAPTER 2

EXPERIMENTAL SETUP & METHODS

2.1 Chapter Introduction

This chapter introduces the entire experimental setup and the methods that were used in its design and construction. For completeness, all aspects of the OCT system have been included, providing a suitable level of detail for each, but the most attention will be given to the PM-based spectral filter and how it has been used to create a swept source for OCT imaging. The primary goal of this chapter is to become familiar with the general operation of the spectral filter in order to progress into a more detailed discussion of its components in Chapter 3, before exploring their combined operation in the theoretical work that follows in Chapter 4.

Section 2.2 provides an overview of the entire experimental setup. This includes all of the essential equipment used to build the system, analyse the SS output and generate the OCT images. The setup is then broken down into sub-systems where each one is introduced separately in its own section. Each section highlights the most relevant details of the system's function, design and construction and is presented in the same order as the sequence of operations required for performing OCT imaging. The light generation method of the SS is introduced in Section 2.3. This section forms the main body of work in this chapter since it includes the PM-based spectral filter, which is the primary area under investigation in this research project and the subject of extensive simulation, experimental and theoretical work. The two subsequent sections introduce the rest of the OCT imaging system, which includes the interferometer (Section 2.4) and the signal processing and image creation stage (Section 2.5). Section 2.6 introduces the ray tracing software used for the simulations and Section 2.7 uses the simulations to explain two of the key processes involved with light loss in the spectral filter. This chapter ends with a short reiteration of the most significant features of the system, which are considered to be important aspects of the design method for optimising the performance of the SS.

2.2 Experimental Setup

The entire layout of the SS-OCT system can be seen illustrated in Figure 2.1. This diagram shows all of the equipment used for creating the SS, scanning the sample and

generating the OCT images. The diagram also illustrates all of the power supplies, as well as both data analysis instruments (Oscilloscope and Optical Spectrum Analyser (OSA) (yellow boxes)), and shows all of the necessary connections that link them together (optical fibres, electrical cables and free space laser paths – see legend).

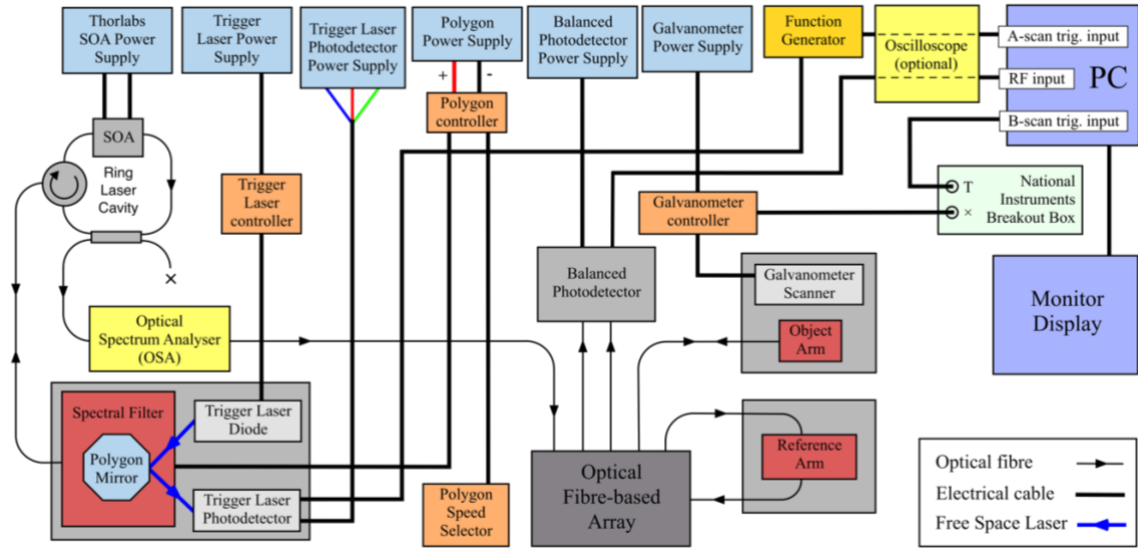


Figure 2.1. An image of the entire SS-OCT experimental setup showing all of the components and data analysis devices including their power supplies and all of their connections. When the SS output is being examined, the optical fibre from the ring laser cavity is removed from the array and inserted into the OSA to measure the optical power and the TSB.

Several of the components had additional controllers (orange boxes) that could be used to adjust their operation. For example, the PM used an external selector to change between the various speed settings. A trigger laser and a photodetector were used to obtain the timing signal of each sweep through the spectrum and a function generator (dark yellow box) was also needed to amplify this signal to the correct operating voltage (0.5 volts) and to synchronise the start of each sweep through the spectrum with the correct wavelength. The performance of the spectral filter was continuously monitored by referring to traces of the SS output on the OSA, which simultaneously assessed the bandwidth and the optical power being sent to the interferometer.

A better understanding of the SS-OCT system can be achieved by breaking down the experimental setup into three separate sub-systems. The diagram presented in Figure 2.2 shows the separation between the SS, the interferometer, and the signal processing & image creation stages and includes all of the relevant coaxial electrical cables (brown lines) and optical fibres (black arrows) that link them together.

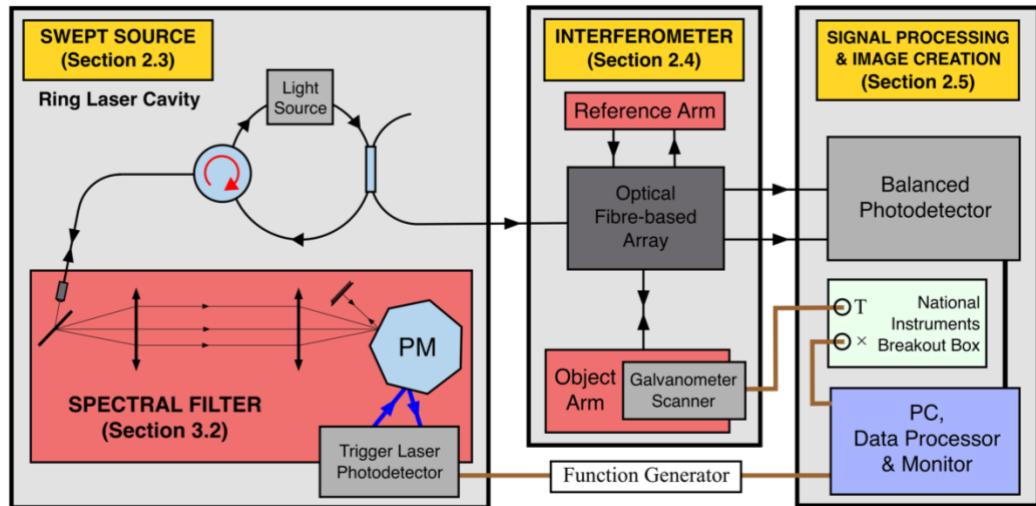


Figure 2.2. Simplified layout of the experimental setup in Figure 2.1 grouped into its three constituent systems. These are the; swept source (Section 2.3), interferometer (Section 2.4) and signal processing & image creation (Section 2.5). The black arrows (outside the spectral filter) are the optical fibres and the brown lines are the electrical cables. PM is the polygon mirror.

The SS generates the swept spectrum that is sent via optical fibre to the interferometer and contains the light source and the spectral filter. A more rigorous explanation of this system follows shortly in Section 2.3. The interferometer is constructed around a custom built optical fibre-based array, which has an object arm, containing the scanning optics for imaging the sample, and a reference arm, providing the reference optical path length. This stage is discussed in Section 2.4 and did not require any significant experimental work (outside of aligning the object and reference arms for maximum performance). The signal processing & image creation stage acquires the interference signal from the interferometer through a balanced photodetector and processes the data via a PC before displaying the images on a monitor. This stage is briefly discussed in Section 2.5 but was not the subject of any experimental work, although several different data processing setups were tested before a suitable method was found to generate the images. The resolution target used for some of the images is also presented in Section 2.4.2.

2.3 The Swept Source

The fundamental operating principles of SSs were introduced in Section 1.4, which defined the essential features needed to perform SS-OCT imaging. The SS must provide a wide bandwidth envelope that is continuously swept through in rapid succession to generate narrowband instantaneous laser linewidths. The following sections describe the operation, design and construction methods of the PM-based, SS system used in this research project and how it has been used to achieve these goals.

The SS is composed of a semiconductor laser light source, several optical fibre-based components and the spectral filter. These components are connected together to form a ring laser cavity (see Figure 2.2), which consists of an optical fibre pathway and the free space length of the spectral filter, all of which are necessary for creating the swept laser source. The ring laser cavity is therefore introduced first in Section 2.3.1. The following sections then sequentially address each component of the SS in the same order as the path the light follows around the ring laser cavity, starting with the laser generation in the semiconductor light source, followed by the sweeping method of the spectral filter.

Section 2.3.2 introduces and explains the operation of the semiconductor light source inside the ring laser cavity and then specifies the parameters of the laser light that are essential for providing context in the studies presented in the rest of the thesis (Section 2.3.2.1). This section also highlights the necessity to control the temperature settings of the light source in order to maximise the optical power output and the total bandwidth before being used in the spectral filter (Section 2.3.2.3).

Section 2.3.3 introduces the PM-based spectral filter, providing a detailed explanation of its operation, design and the methods that were used in its construction. This section addresses the challenges that were faced when assembling and aligning the spectral filter and suggests several preliminary design considerations that can be used to overcome these challenges. Certain component settings and alignments have also been suggested that are relatively simple to apply or install but are considered essential for achieving the maximum performance of the SS. These settings were employed throughout the project and are strongly recommended in any future assemblies of a similar nature.

2.3.1 Ring Laser Cavity

Typical Fabry-Pérot lasers use highly reflective mirrors at either end of a linear, optical cavity to generate stimulated emission. Amplification occurs as the light bounces back and forth multiple times through a gain medium between the two mirrors. The amplified laser light then exits the linear cavity into free space (e.g. through a partially transparent mirror). In this project however, the laser operates by guiding the light through a semiconductor chip (gain medium) in one direction only.

A diagram of the ring laser cavity is shown in Figure 2.3. The light source can be seen at the top of a circular, fibre optic path (black arrows) with polarisation controllers (PC) placed on either side. It has an entrance and an exit optical fibre on either side of the chip

so that light exiting from one side of the chip can be delivered to the other. This creates a loop that allows the light to repeatedly pass through the chip and build up the stimulated emission. The semiconductor light source creates a broadband spectrum, which is sent via single mode optical fibre around the ring laser cavity towards the spectral filter. The spectral filter produces the swept laser light, which is then amplified before exiting the cavity and entering the interferometer to image the sample in the OCT system.

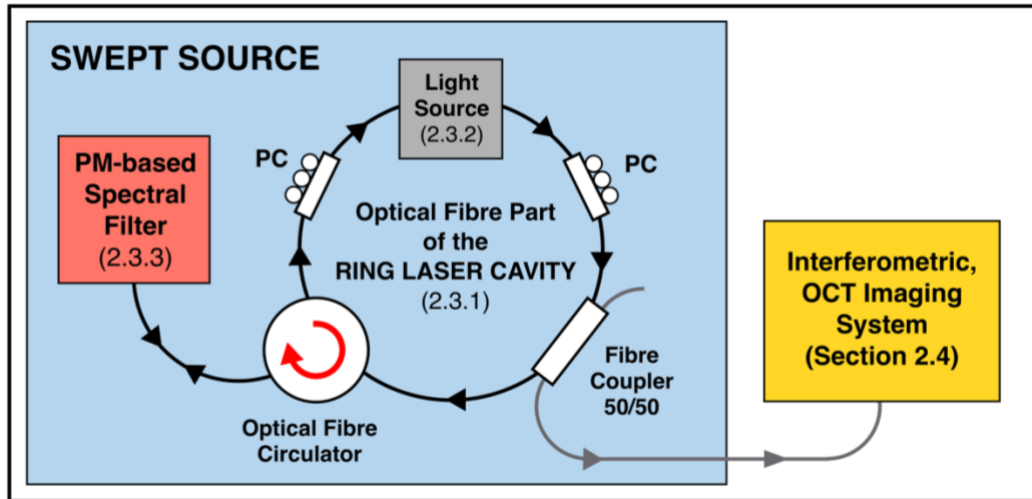


Figure 2.3. Swept Source, optical fibre-based ring laser cavity. Light from the laser source travels clockwise around the fibre loop to the optical fibre circulator, which sends it to the spectral filter. The returning swept laser light is then guided back to the laser source for amplification, completing a single cavity round trip. Half of the amplified light exits the ring laser cavity via the 50/50 fibre coupler and goes towards the interferometer and the OCT imaging system. Polarisation controllers (PC) are also placed on either side of the laser source to maximise the output signal.

Laser light exits the source and proceeds to travel clockwise around the fibre part of the ring laser cavity, through a 50/50 fibre coupler (discussed shortly) until it reaches an optical fibre quasi-circulator with three input/output fibres. This circulator is needed to ensure that light propagates in one direction through the SOA while allowing the back-and-forth pass through the spectral filter, and is necessary in this SS design since there is only one path leading into, and away from, the spectral filter (Section 2.3.3). Thus, the circulator simultaneously delivers the broadband spectrum to the spectral filter and collects the returning, narrowband swept laser linewidths through the same optical fibre. The circulator is designed to only allow light to pass through from one fibre to the next adjacent fibre in a clockwise direction (indicated by the red arrow). The filtered light is then sent back to the semiconductor light source for amplification, which occurs each time it circulates around the ring laser cavity and passes through the gain medium of the

semiconductor chip. During each round trip, the 50/50 fibre coupler allows close to half of the swept, amplified laser light to exit the cavity and enter the interferometer to be used in the OCT imaging system (grey arrows).

2.3.1.1 Optical Fibres

Optical fibres are used to transmit the light around the experimental setup - towards the spectral filter and the reference and object arms of the interferometer. All optical fibres in the setup are single mode fibre (SMF-28e) with a $9\ \mu\text{m}$ core, $125\ \mu\text{m}$ cladding and a $900\ \mu\text{m}$ jacket (Figure 2.4 a). Some fibres also possess an additional sleeve, over the top of the jacket, whenever extra protection is required. All fibres terminate with a fibre connector (FC) that have an angled physical contact (APC) of 8 degrees, which are used to eliminate back reflections between two connected fibres. The mode field diameter (MFD) inside the optical fibre is the diameter of the beam at which the optical power per unit area reduces to a value $1/e^2$ of its peak amplitude (for a Gaussian power distribution). It is a function of wavelength, core radius, and the refractive indices of the core and cladding (since the MFD is slightly larger than the diameter of the core).

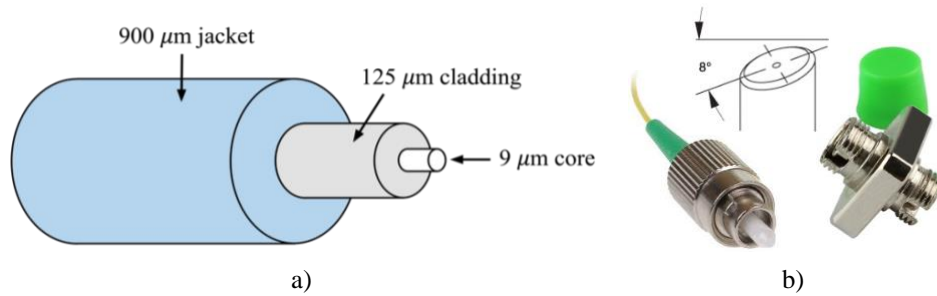


Figure 2.4. **a)** An example of the optical fibre used throughout the experimental setup (not to scale), consisting of a $9\ \mu\text{m}$ core, $125\ \mu\text{m}$ cladding and a $900\ \mu\text{m}$ jacket. **b)** FC/APC male and female optical fibre mating connectors with 8° angled physical contact, used throughout the experimental setup. Picture credit: Thorlabs online catalogue [57].

The entire ring laser cavity shown in Figure 2.3 contains over 10 meters of single mode optical fibre. This is made up of around 20 separate lengths (depending on the study being carried out), the majority of which were joined together by FC/APC mating connectors (Figure 2.4 b). Some fibres were spliced together while others were used to project light onto the lens of a collimator to initiate the propagation of light into a region of free space. All extended lengths of optical fibre were attached to circular fastening cards and every FC/APC mating sleeve was carefully oriented and secured in place on the optics bench. This was necessary to avoid twisting the fibres and causing torsional stresses that reduce the optical power by introducing unwanted states of polarisation.

2.3.2 Light Source – Semiconductor Optical Amplifier (SOA)

The light source used in the ring laser cavity is generated by a semiconductor optical amplifier (SOA) (Figure 2.5). This component provides the total available broadband spectrum (shown shortly in Figure 2.6) and the amplification of the filtered, narrowband laser linewidths before they are sent to the interferometer and the OCT imaging system. SOAs are highly efficient and can operate with both monochromatic and multi-wavelength signals but they are also polarisation sensitive and therefore require external polarisation controllers to maximise their output (seen earlier in Figure 2.3).

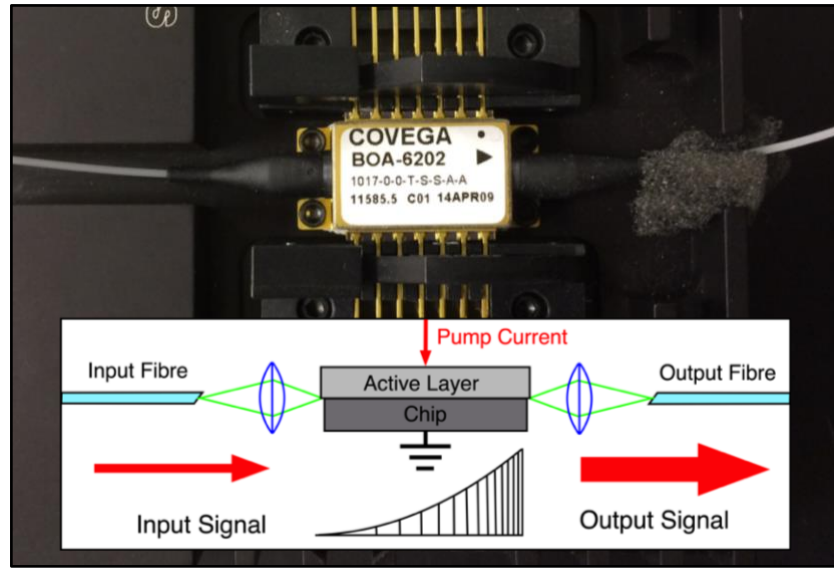


Figure 2.5. Covega BOA1017 Semiconductor Optical Amplifier (SOA) used as the light source and the amplifier in the ring laser cavity. Directionality is indicated by the small black triangle on the right-hand side of the chip and the optical fibre input and output are seen entering and exiting the chip on the left and right respectively.

Optical fibres allow light to enter the SOA on one side of the semiconductor chip and exit on the other. Therefore, SOAs are travelling-wave amplifiers that operate by allowing light to continuously pass through the semiconductor chip. The circulating light is assisted by having anti-reflective coatings at either end of the chip to reduce optical feedback. This results in light passing through in one direction and prevents light from resonating inside the chip. For the SOA module used in this research, input and output coupling efficiency, between the fibre-to-chip and the chip-to-fibre interface, have typical losses between 1.5 and 2.5 dB respectively, which affects the gain, noise and saturation power. The amplification depends upon the properties of the semiconductor gain medium (e.g. amplified stimulated emission (ASE) intensity, time constant, saturation power, gain etc.) as well as the properties of the spectral filter and the ring laser cavity. Each narrowband

laser linewidth, instantaneously produced by the filter, must complete a number of cavity round-trips in order to achieve sufficient laser intensity build-up. This is directly linked to the cavity path length (including the spectral filter) and the rotational speed of the PM, which shall be discussed shortly in Section 2.3.2.2. Firstly however, it is necessary to introduce the parameters of the SOA.

2.3.2.1 SOA Parameters

The SOA used in this research was a Covega BOA1017 (Thorlabs), which has a documented central wavelength of 1332.8 nm and a FWHM of 75.8 nm (using an operating current $I_{op} = 600 \text{ mA}$, seed wavelength $\lambda = 1312 \text{ nm}$ and a temperature, $T = 25^\circ\text{C}$ according to the manufacturer datasheet provided in Appendix A). The spontaneous emission output spectrum of the SOA was measured in the laboratory under the same conditions to have a central wavelength of approximately 1330 nm and the FWHM was measured slightly wider at 81 nm (Figure 2.6).

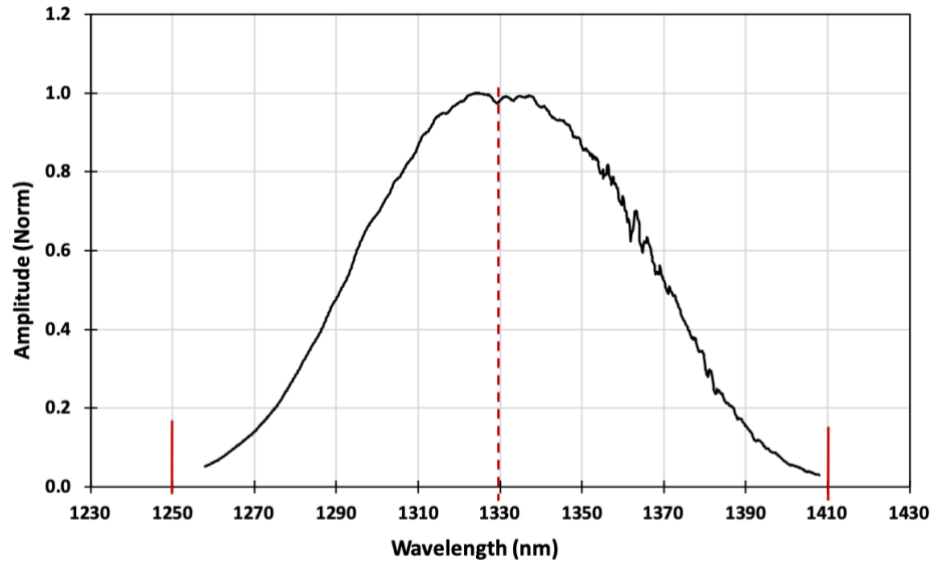


Figure 2.6. The spontaneous emission output spectrum of the Covega BOA1017 as measured by an optical spectrum analyser in the laboratory using an operating current of 600 mA at a temperature of 25°C . Central wavelength $\lambda_c \cong 1330 \text{ nm}$, FWHM $\Delta\lambda_{FWHM} \cong 81.1 \text{ nm}$ and the total spectral range $\Delta\lambda_T \cong 160 \text{ nm}$. The two vertical red lines, indicating the extent of the total spectral range, were selected based on the equidistant location from the measured central wavelength and the amplitude, which was approximately 5% of the maximum value.

It is also important to note the total spectral range, $\Delta\lambda_T$, of the SOA, which was approximately 160 nm and has been indicated in Figure 2.6 by the two vertical red markers. Selection of these boundary marker values were guided by considering a minimum amount of measured light, typically around 5% of the maximum recorded

amplitude, and by the desire to arrange an equal distribution of wavelengths, on either side of the measured central wavelength value, that could then be used in the simulation work and the theoretical analysis. For convenience, the central wavelength, λ_c , and the total spectral range, $\Delta\lambda_T$, shall be applied continuously throughout the rest of the thesis in order to have consistent values for the three most significant wavelengths of the input spectrum. These are: the shortest wavelength, $\lambda_{0_{min}} = 1250 \text{ nm}$, the central wavelength, $\lambda_c = 1330 \text{ nm}$ and the longest wavelength, $\lambda_{0_{max}} = 1410 \text{ nm}$. Note that these wavelength values are constants of the SOA output and that all subsequent measurements of the maximum and minimum swept wavelengths will simply be referred to as λ_{max} and λ_{min} respectively.

The total spectral range, $\Delta\lambda_T$, represents the maximum bandwidth of laser light that is available for use by the spectral filter. Even if the spectral filter is capable of accommodating and filtering a wider spectral range of wavelengths, the final, swept output will always be limited by the bandwidth of the input light source. Therefore, the input bandwidth from the SOA places an upper limit on the theoretical axial resolution of the OCT system. If the spectral envelope of the SS matches the spontaneous emission output of the SOA (and assuming ideal conditions), the theoretical axial resolution will be ~ 9.6 microns (Eq. 1.13, $n_{air} = 1$, $\lambda_c = 1330 \text{ nm}$, $\Delta\lambda_{FWHM} = 81 \text{ nm}$).

However, maintaining this resolution largely depends upon the spectral envelope of the SS output, which must have a Gaussian profile in order to remain Gaussian after performing the Fast Fourier Transform (FFT). The SS output is typically not Gaussian and can have a FWHM that is larger than the SOA output. The nature of the spontaneous emission occurring within the SOA introduces noise to the SS output, whilst the signal gain of the SOA (Appendix A), which is a function of wavelength, will modify the shape of the spectrum if the wavelength sweeping is not constant or repeatable. The SS output therefore requires apodization, prior to the FFT, which was carried out using a Hamming window at the signal processing stage (see Section 2.5). Unfortunately, this apodization reduces the effective bandwidth. The majority of work in this thesis is therefore dedicated to optimising the performance of the spectral filter in order to maximise and homogenise the SS output.

2.3.2.2 Optimising Linewidth Amplification in the Ring Laser Cavity

The spectral filter sweeps through the available spectrum of the broadband light source to sequentially select instantaneous, narrowband laser linewidths. The swept laser linewidths spend a brief moment of time circulating around the ring laser cavity and passing through the SOA chip for amplification before exiting the SS. The maximum amplification is essentially achieved by passing through the chip a sufficient number of times and the number of passes depends on the total length of the cavity and the bandwidth sweeping frequency of the PM. Long cavity lengths and high PM speeds will limit the number of passes through the SOA, which reduces the amount of light amplification and therefore lowers the optical power of the system. Therefore, since a high-speed sweeping frequency is desirable for OCT, it is recommended that the length of the cavity is kept short to encourage as many round trips as possible [58].

The amount of amplification on each linewidth can be considered by using the properties of the SS and making several common assumptions. The pre-existing optical track of the ring laser cavity in the SS (including the SOA, optical fibres and the components of the spectral filter) was measured to have a total length of approximately 8.68 m. Using the speed of light, c , and an average value for the index of refraction, $n = 1.47$, the cavity round trip travel time is approximately 42 ns. A 72-facet PM, operating at 12 kHz, will give a bandwidth sweeping period of 83.33 μ s (individual facet period). Assuming that the spectral filter can select 1 nm laser linewidths from a 160 nm bandwidth, each linewidth will spend 521 ns circulating around the ring laser cavity. If the light takes 42 ns to travel once around the cavity, each of the 160 linewidths will make roughly 12 cavity round trips per sweep. When the polygon operates at 48 kHz (4 times faster), this value reduces to just 3 cavity round trips. In reality, the laser linewidths are typically around ten times smaller and therefore make far fewer trips around the cavity, which provides less time to build up the necessary amplification.

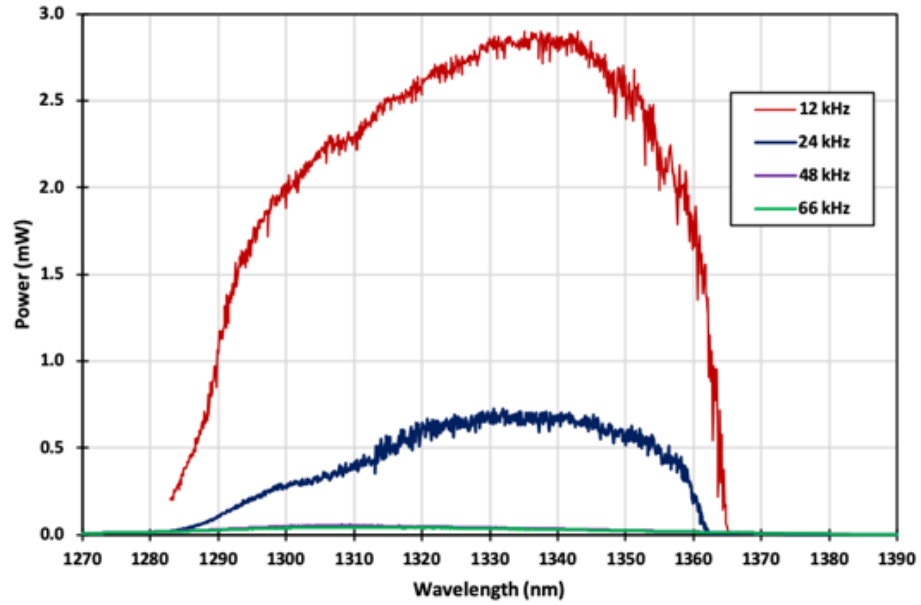


Figure 2.7. Swept bandwidth amplification for each PM operating speed; 12 kHz, 24 kHz, 48 kHz and 66 kHz. After 24 kHz, the number of passes through the SOA decreases to zero (following the assumptions made in the analysis above) and amplification no longer takes place.

This amplification deficiency is demonstrated in Figure 2.7, which shows the amplitude of the SS output on the optical spectrum analyser in peak hold mode for four different PM speed settings; 12 kHz, 24 kHz, 48 kHz and 66 kHz. Operating the PM at the two highest speed settings does not provide any signal strength greater than the background output. This simple analysis, strongly suggests that the cavity length should be reduced as much as possible in order to maximise the number of cavity round trips per unit time to supplement the amplification of each linewidth, especially when high sweeping frequencies are required (> 20 kHz).

2.3.2.3 SOA Temperature Control

The SOAs power supply (ITC4001, Thorlabs, USA) provides multi-parameter adjustability of the current running through the chip and its temperature. These parameters influence the total power output and modulate the spectral profile respectively. The benefits of controlling the SOA temperature were demonstrated by Sang-Won Lee *et al.* who observed an ~ 23 nm increase to the FWHM of their swept bandwidth when the temperature was decreased from 30°C down to 9°C [16]. It was therefore considered advantageous to perform the same experiment to establish the correct settings that delivered the best performance from the SOA before sending the light into the spectral filter.

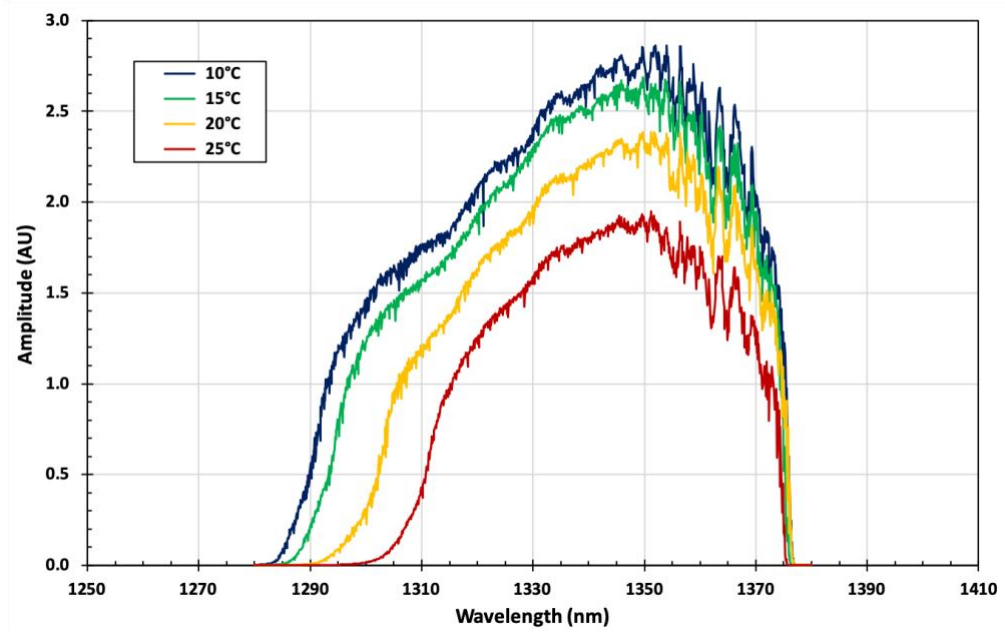


Figure 2.8. Swept bandwidth as a function of SOA temperature at 300 mA. ~ 20 nm is gained when the temperature is reduced to 10°C . The increase was produced on the left-hand side of the spectrum only, which was the consequence of using a particular filter design (see Chapter 5).

Figure 2.8 shows the result of decreasing the temperature from 25°C to 10°C , in steps of 5°C , whilst using a constant current of 300 mA. The results showed an extra ~ 20 nm of bandwidth, which also increased the amplitude by $\sim 50\%$. However, the increase in bandwidth was only seen occurring on the left-hand side of the spectrum, whilst the maximum wavelength value on the right-hand side remained relatively unchanged ($\lambda_{\text{max}} \sim 1375$ nm). This result was caused by using a particular filter design – one that physically prevented light with a wavelength longer than 1375 nm from being tuned by the filter – and highlights the necessity to understand the best way to build and optimise the spectral filter to prevent light from being lost in this way. Nevertheless, lowering the temperature of the SOA chip does indeed provide a wider spectral output and increases the optical power. Controlling the current and the temperature settings of the SOA are simple, preliminary adjustments that can be made to ensure that the maximum amplitude and the widest spectral range are used in the spectral filter. Therefore, throughout all of the experimental work that follows in this thesis, the SOA chip was controlled to maintain a constant temperature of 10°C and an operating current of 600 mA.

2.3.3 Polygon Mirror-Based Spectral Filter

The spectral filter is a multi-parameter optical system whose operation is based on carefully calibrated reflections of broadband light off the active facet of a rotating

polygonal mirror. The purpose of the filter is to sweep through the spectrum of light (produced by the SOA) and sequentially return narrowband, instantaneous laser linewidths. Only one facet at a time is expected to interact with the incident spectrum of light. A single sweep of the spectrum occurs on each facet of the PM as it moves into the position of the active facet. This results in repeated sweeps of the spectrum, one from each facet on the PM.

The light is injected into the spectral filter through a single optical fibre, which also recaptures the swept laser linewidths and delivers them back out of the filter. In order for the wavelength selection to be successful, the tuned wavelengths must propagate back along exactly the same path they took when going into the filter. Only the light rays that have reflected at normal incidence on the final mirrored surface of the filter will achieve this and exit through the optical fibre. The spectral filter built in this research project uses a diffraction grating to spatially separate the spectrum. Each wavelength in the spectrum is therefore assigned to a different angular displacement, which is the key operation that allows for wavelength tuning. The diverging spectrum, emerging from the diffraction grating, is captured by a telescope and inverted into a converging spectrum incident on the polygon. This particular arrangement constitutes what is known as a '*Littman*' configuration, rather than a '*Littrow*' configuration whereby the injected light interacts with the PM before the diffraction grating [59]. The Littman configuration was chosen for its higher spectral resolution, which therefore produces narrower laser linewidths [13]¹.

The converging spectrum is then swept via angular selection, facilitated by the rotation of the PM. As the polygon rotates, each wavelength, from λ_{0min} to λ_{0max} (or vice versa, depending on the polygons' direction of rotation), sequentially fulfils the normal incidence angle condition on a single mirrored facet and is reflected back through the spectral filter. At any instant during a single sweep of the spectrum, only a very narrow portion of the light will be reflected at the correct angle of incidence and be tuned by the filter. These tuned portions of light constitute the narrowband, instantaneous laser

¹ The Littrow configuration (diffraction angle equal to the incidence angle) also constitutes the telescope-less design of spectral filter, which has been discussed in a number of publications but will not be the subject of any exploration in this thesis.

linewidths required of the SS. This process then repeats itself on every facet, creating continuous sweeps of the spectrum as the polygon rotates.

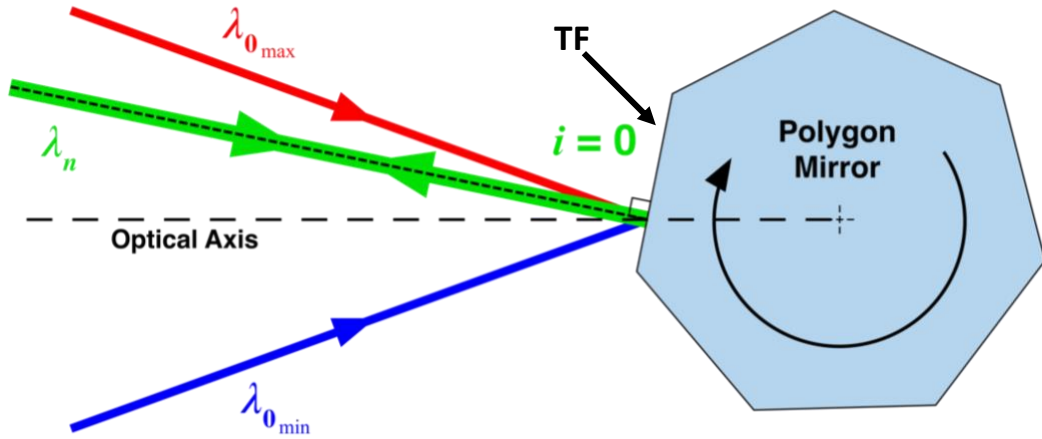


Figure 2.9. Example of spectral sweeping using a PM. Each wavelength meets the normal incidence condition sequentially on the target facet, TF, as the polygon rotates. The diagram depicts the instantaneous moment when λ_n reflects off the TF at normal incidence and returns exactly along the same path. $\lambda_{0_{max}}$ and $\lambda_{0_{min}}$ can be seen striking the TF at non-zero incidence, which do not reflect back along their incident paths (not shown). The same is true for every other wavelength apart from λ_n .

The diagram in Figure 2.9 shows the PM, mid-rotation, selecting an arbitrary, narrowband laser linewidth, λ_n , from the converging spectrum, between $\lambda_{0_{min}}$ and $\lambda_{0_{max}}$. This wavelength has met the normal incidence angle condition, $i = 0$, required to retroreflect the light back through the filter along the same path. The diagram has been simplified for the purpose of this introduction since it shows the light directly retroreflecting off the Target Facet (TF) of the PM. In the experimental setup, described shortly in Section 2.3.3.1, an additional retroreflector mirror is used as the final surface in the sequence of operations, although the basic principle is still the same. Also, the diagram only shows seven facets, whereas this project used a 72-facet PM.

The efficiency of the spectral filter partly depends upon successfully returning a high proportion of the injected light back to the optical fibre, which can be affected by poor component choice and alignment or by the aberrations introduced from having refractive optics. However, the performance can also be affected by vibrations or by light propagating through areas of highly turbulent air flow [26]. These last two causes are discussed shortly in Section 2.3.4 since they are both undesirable consequences of using a mechanical, high speed PM and must be minimised whenever possible.

Successfully operating the spectral filter requires precise control over every component's position and orientation and also resistance to vibrations produced by the active polygon mirror which can spin at speeds up to 55,000 RPM. High precision adjustment and structural resilience made competing demands on the design and, as a result, the construction method went through many revisions before an acceptable solution was found. The following section describes in detail the experimental operation of the spectral filter and the methods that were used to build it, as well as offering solutions to the challenges that were faced along the way.

2.3.3.1 Spectral Filter Experimental Setup

The experimental setup of the SS spectral filter is shown in Figure 2.10. The central wavelength beam (green arrows) can be seen propagating through the optical components, towards an off-axis PM (positioned above-axis), and terminating on the retroreflector mirror, RM. The red arrows show the path of the trigger laser, TL, which reflects off the PM and terminates on the trigger laser photodetector, TL-PD, and is used to provide the initial timing signal.

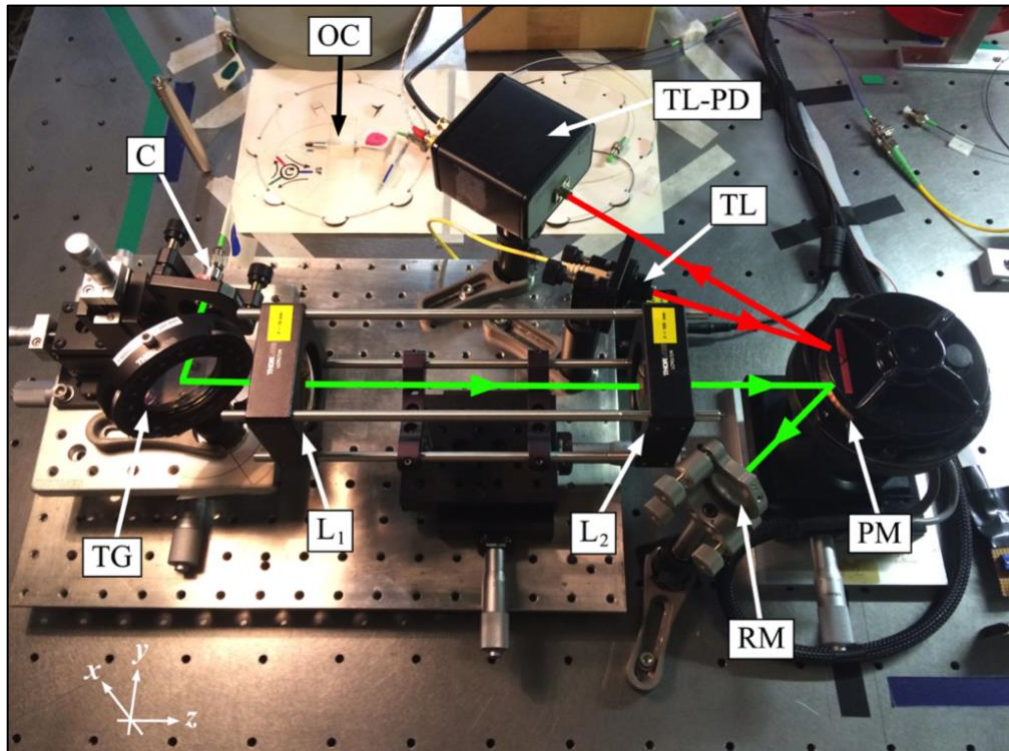


Figure 2.10. Full setup using an optical circulator, OC, collimator, C, transmission grating, TG, telescope with lenses L1 & L2, Polygon mirror, PM, retroreflector mirror, RM, trigger laser, TL, and the trigger laser photodetector, TL-PD. The green arrows trace the path of the central wavelength through the filter and the red arrows trace the path of the trigger laser. This particular setup shows the PM orientated 'above-axis' (Section 4.4).

Light produced in the SOA (not shown) proceeds to circulate around the ring laser cavity until it reaches the optical fibre-based circulator, OC. The circulator then guides the light into the spectral filter, where it enters through a collimator, C, mounted to a kinematic mount (KM100, Thorlabs, USA) used to adjust the angle of the beam in the x - z plane. This mount was also fixed to a stage with three translational planes of motion (x , y & z), which gave complete control over the direction of the beam. The need to precisely adjust every plane of motion on every component was essential for successfully guiding the light through the filter and recoupling it back into the optical fibre.

The height of the collimator must be equal to the height of the PM facets (from the surface of the optics bench) to prevent the beam from unnecessarily tilting away from the horizontal. Matching these two elevations was the initial challenge of the construction design since it needed to be carried out first whilst also considering the dimensions and construction of the other components. This is because the translation stages had a limited amount of vertical travel and because every sheet of stacked metal plating, used to match the heights, had to be firmly attached to the component, the optics bench and to each other in order to prevent them from introducing unnecessary inclines or unwanted vibrations caused by the active PM (see Section 2.3.4). The more sheets of stacked metal used, the greater the risk of misalignment and transmitting vibrations.

The collimated beam then falls incident on the transmission, diffraction grating, TG. This was a 6 mm thick, circular disk fixed inside a continuous rotation mount (RSP2, Thorlabs, USA), which allowed the grooves/lines to be orientated vertically to ensure the emerging spectrum continued in the horizontal, y - z plane. The grating was also free to rotate around the x -axis to establish the correct angle of incidence. The collimator and the grating were both mounted to a single optical breadboard with y - z directional translation mounts, which joined the two components together and guaranteed their fixed alignment.

The divergent spectrum, emerging from the grating, then enters the telescope lenses, L_1 and L_2 , before converging onto the PM. Initially, post mounts were used to hold each lens independently but these were soon identified as insufficient for achieving a consistently accurate alignment. Instead, a cage assembly was employed, mounted to another y - z translation stage, that provided extra stability and ensured that the location of the focal plane was fixed between the two lenses, regardless of how the other components were moved. Two vertically adjustable post mounts supported the cage assembly on top of the

translation stage and allowed for all three directions of adjustability as well as the freedom to fine tune the tilt of the telescopes' sagittal plane along the telescope optical axis (z).

The PM was also mounted to its own y-z translation stage, which meant that the spectral filter was constructed in three sections: the launching collimator and the diffraction grating, then the telescope and finally the PM and the retroreflector mirror. All three sections could be moved and aligned to each other whilst independently maintaining their own alignment. This design provided a much more consistent way of aligning the setup and allowed components to be exchanged quickly with minimal realignment required during the experimental comparison stages of the research (Chapter 5).

After the light has travelled through the telescope, the converging spectrum in the image plane of the second lens either retro-reflects off the polygon facets (when the polygon is on-axis – not shown) or is guided towards a planar mirror, RM, for retro-reflection (when the polygon is off-axis – shown in Figure 2.10). The tuned wavelengths then begin their return journey back through the filter. A more detailed discussion of the on-axis/off-axis PM arrangements are presented in Section 4.4 and is the subject of experimentation in Section 5.7.

2.3.4 Spectral Filter Stabilisation

Despite utilising air bearings to reduce friction and maximise speed, the rotational motion of the PM introduces unwanted vibrations that are difficult to eliminate. They are often attributed to defects within the PM, either by microscopic inhomogeneity's in the material or imperfections on the surface of the facets. The vibrations cause the surface plane of the TF to periodically deviate away from its natural, vertical orientation (dynamic tracking). When this happens, the light rays, which ordinarily approach the TF at normal incidence, will interact with the TF at an angle, reflecting them back in a different plane of propagation and preventing them from returning along the same path through the spectral filter.

The vibrations are also transmitted to the other components in the spectral filter, which oscillate with similar frequencies that are influenced by their own resonant properties. Under these conditions, the precise knowledge of the lights' path through the refracting and diffracting optics becomes less predictable and the amount of ray deflection increases. Although the magnitude of these deflections is relatively small, it is still large enough to have an effect on the recoupling process at the entrance aperture of the optical

fibre since it is only a few microns in diameter (Section 2.3.1.1). This leads to inconsistent wavelength sweeping with respect to time, which introduces phase instabilities in the interference signal, causing ambiguity in the depth measurements and manifesting as noise in the images (Section 1.4.4). It is vital, therefore, to prevent these affects as much as possible.

Consider the following example. If the return path through the spectral filter, from the PM to the launching collimator, is assumed to be a straight-line path with a length of 400 *mm* and that there are no other components in between, the angular displacement of the active facet, needed for the chief ray (travelling along the optical axis) to miss the entrance aperture of the optical fibre, is approximately one thousandth of a degree (3.6 *arcsec*). The dynamic tracking measurement of the PM facets is stated to be ≤ 15 *arcsec* (Appendix B). This is over 4 times greater and therefore demonstrates the necessity to minimise the cavity length of the spectral filter.

The high rotational speed of the active PM also generates significant amounts of turbulent air flow surrounding the access window of the PM casing, even when running at the minimum speed setting (12 kHz). It is suspected that this turbulent air flow also contributes towards deflecting the rays from their intended paths (see Section 2.3.4.1), which will gradually worsen with increasing speed. Although a full tribological analysis is beyond the scope of this thesis, time and effort was spent trying to find an easy to implement solution that could sufficiently dampen the vibrations and reduce the impact of the turbulent air flow.

2.3.4.1 Windage

Aside from vibrations, another potential cause of power loss in the system comes from having the light travel through a region of highly turbulent air flow ('Windage'). Micro changes in air density will affect the local refractive index, which is thought could be enough to deflect the light away from its intended path and therefore prevent it from returning to the optical fibre tip. Such a region exists next to the window in the casing that surrounds the PM and the rays must travel through this region twice in order to be tuned by the filter. However, observations using streamers placed in various locations around the casing of the polygon showed that more turbulent air flow occurred on one side of the window than on the other and was independent of the PM's speed (Figure 2.11).

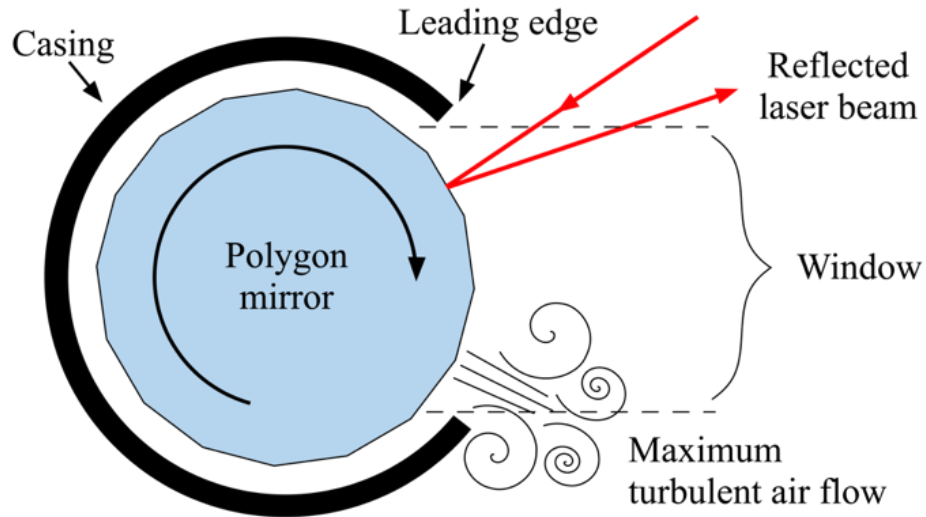


Figure 2.11. Top down, cut-away view of the PM inside its casing plus the window that allows the laser light to interact with the facets. Also depicted is the rotational direction of the polygon and the location of the highest observed turbulent air flow. Avoiding using this region by making the laser light interact with the opposite side of the window may reduce unwanted disturbances to the path of the rays and improve total power transmission.

In order to avoid any potential losses due to this effect, the components were aligned such that the incident light and the trigger laser were both guided towards the polygon through the least turbulent region of air flow, which occurred next to the leading edge of the casing window. Alternatively, these disturbances might be eliminated altogether by employing a PM enclosed within a vacuum chamber that uses a glass window to transmit the light from the polygon facets to the external components [17]. It is reasonable to assume that this would also reduce the amount of vibration produced and therefore provide a more stable filter for achieving maximum power output.

2.3.4.2 Vibration Reduction

A frequency analysis was carried out to examine the signal modulation of the PM when operating at 667 Hz (40,000 RPM or a facet frequency of 48 kHz). This was achieved using the trigger laser and the signal registered by the trigger laser photodetector (see Figure 2.10). Periodic peaks with varying amplitudes were recorded for every full revolution of the PM (Figure 2.12 a). A secondary, underlying signal was also observed repeating every twelve revolutions, corresponding to a frequency of ~8 kHz (Figure 2.12 b). The first signal suggests that imperfections exist within the PM whilst the second signal is more likely to be some form of mechanical resonance caused by the motor or the turbulent air flow in the vicinity of the PM casing access window.

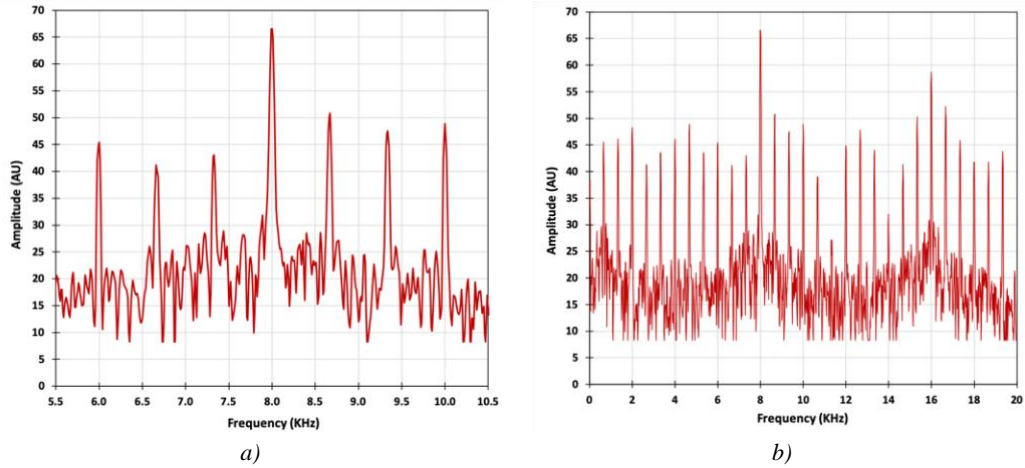


Figure 2.12. *a)* Frequency measurements showing a peak at 667 Hz for every full rotation of the polygon when operating at 40,000 RPM. *b)* The same frequency measurements were taken over an extended viewing range of 20 kHz to show an underlying frequency of 8 kHz, corresponding to every 12 rotations of the polygon. The facet frequency of 48 kHz cannot be seen in these graphs.

Vibrations in the telescopic cage assembly were observed to limit the performance of the SS. These vibrations could be dampened by applying a small amount of pressure to the top of the lens mounts, which instantly increased the output signal on the spectrum analyser. Adding an equivalent weight on top of the mounts also had the same positive effect. The cause of the reduction could only have come from the vibrations since it was not possible to achieve the same improvement to the signal by fine tuning the alignment alone. It was therefore necessary to isolate the PM from the rest of the components in order to reduce the transmission of the vibrations.

The filter was rebuilt multiple times using a variety of techniques in order to achieve the best performance. Isolating the PM was achieved by placing all of the other components onto a single optical breadboard supported by soft rubber feet, which can be seen in the photograph of Figure 2.10. The polygon itself was mounted to the optics bench using a combination of robust translation stages and a thin sheet of hard rubber to reduce the amount of vibration transmission. Other components on the optical breadboard were also given rubber bases to isolate them from the vibrations. The result of the reconstruction can be seen in the graph of Figure 2.13.

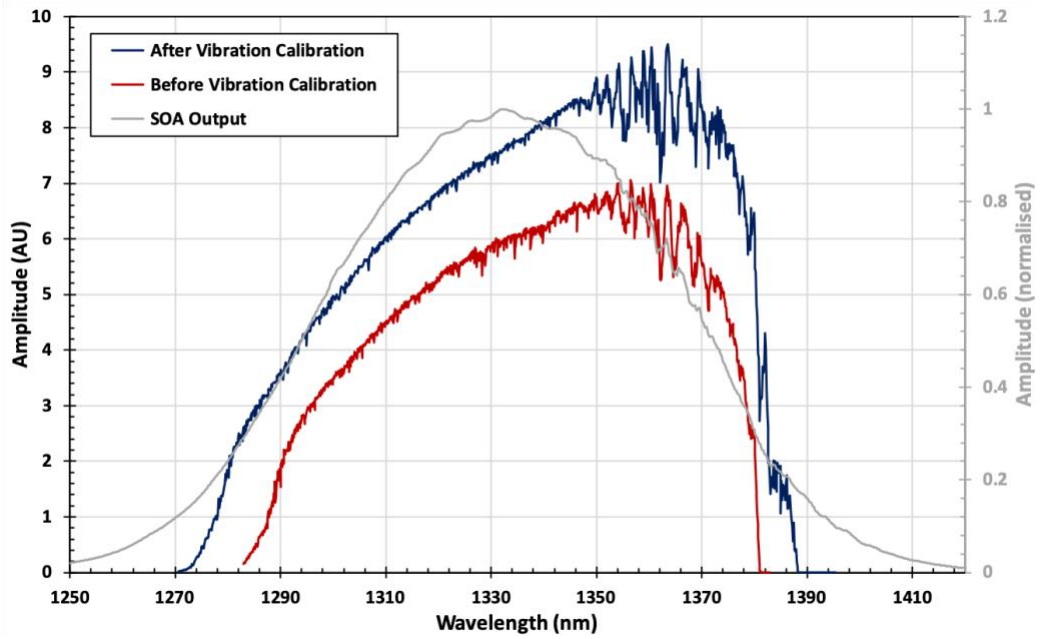


Figure 2.13. Vibration damping of the spectral filter. The two traces compare the performance of the filter before (red) and after (blue) introducing the various dampening techniques to isolate the vibrations and improve the output signal. The FWHM widened by ~ 7 nm and the peak power increased by 36%. The grey trace of the SOA output is also provided for comparison.

Both the power output and the swept bandwidth of the spectral filter increased after isolating the components from the vibrations of the polygon. The FWHM widened from 77 nm to 84 nm and the peak output power increased by approximately 36%. It could be argued that this improvement was not necessarily the result of isolating the components from the vibrations of the polygon and that the second alignment was simply more successful than the first. However, the methods used to align the setup were essentially the same in both cases, which was helped by the fact that certain components weren't necessary to realign (for the reasons discussed above) and that the experimental output could be observed in real time on the OSA. The second, more successful assembly also did not produce the same effect when applying pressure to the lens mounts – no improvement was seen on the spectrum analyser and only signal loss was observed. This was a good indication that the new assembly was more successful at dampening the majority of the vibrations.

Although the final assembly of the spectral filter was not necessarily the best design that could be envisaged, the extra effort put into the construction method resulted in a significant improvement to the output signal and, based on the number of attempts to overcome these issues, it is a reasonably confident assumption that it is close to the optimum setup achievable. This rigorous approach was continued throughout the rest of

the subsequent experimental work, whenever a new setup was assembled and tested, and consideration of these effects comes highly recommended in any future builds of a similar design.

2.4 Interferometric, Optical Fibre-based Array

OCT relies upon the phenomenon of wave interference to extract information on the depth location of different features within a sample. The interference is generated using an interferometer, which directs the swept light from the spectral filter along a pair of carefully measured path lengths and recombines them to produce fringe patterns that correspond to specific features in the sample at particular depths. The interferometer used in this research employed an optical fibre-based array (AFW Technologies), which was specifically designed for this project and the task of performing SS-OCT.

The interferometric, optical fibre-based array contains two directional couplers, which act as a beam splitter, and six input/output ports, which are used to implement the four arms of a Michelson interferometer (the reference arm and the detector arm both employ two ports each). All six ports exit the array housing via optical fibres and terminate with FC/APC connectors. Each optical fibre was specified in the design to be as short as possible whilst still offering sufficient length to be repaired in the event of becoming damaged. However, the total fibre-based path lengths in the object arm and the reference arm needed to be approximately equal due to the assumption that the combined, free-space path length within each arm would also be equal in length (including accommodating for the thickness and refractive properties of the lenses, etc.). Pairing the two path lengths in both interferometer arms allows the system to meet the requirements for interference to occur, and the fringe signal that is created can then be measured by the balanced photodetector and sent to the PC for signal processing and image creation.

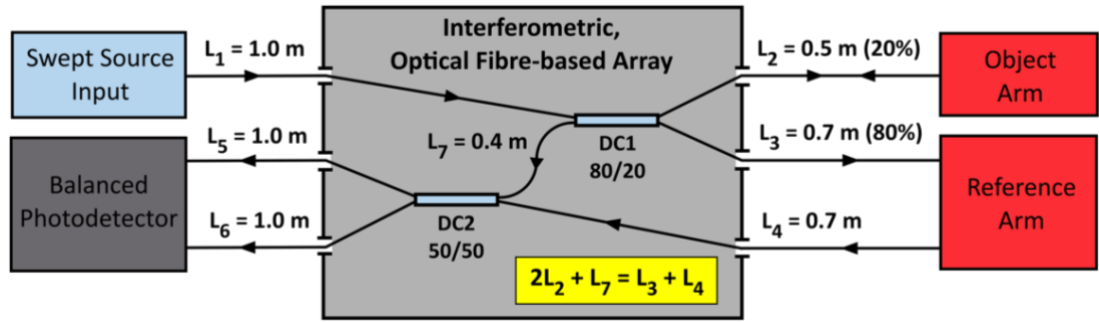


Figure 2.14. Interferometric, optical fibre-based array. The input light source enters through L_1 and is split by the first directional coupler, DC1, where it is then sent to the Object and Reference arms through fibres L_2 and L_3 respectively. Scattered light returns through L_2 and progresses through L_7 towards DC2 where it is recombined with light returning from the reference arm via L_4 . DC2 splits the light again and guides it towards the balanced photodetector through L_5 and L_6 . An interference signal is achieved if $2L_2 + L_7 = L_3 + L_4$ (assuming that the total free space path lengths in the object and reference arms are equal to each other).

Figure 2.14 shows all of the optical fibres used in the array, which have been labelled from L_1 to L_7 . The first optical fibre port (L_1) accommodates the input SS from the ring laser cavity and is connected to the first directional coupler (DC1 - 80/20 split ratio). L_2 is used to send 20% of the swept light to the object arm and collect the scattered light returning from the sample. L_3 is used to send 80% of the swept light to the reference arm, which is collected by L_4 and sent back into the array to be recombined with the light from L_2 . The light is then split via the second directional coupler (DC2 - 50/50) and the outputs L_5 and L_6 terminate on a balanced amplifier, photodetector (PDB460C, 800 – 1700 nm, DC - 200 MHz, 2014, S/N.: M00265309, Thorlabs). The seventh length, L_7 , is the short piece of optical fibre inside the array that joins the two directional couplers together and is considered to be part of the object arm. The electrical output signal is then sent to the processing software in the PC to be turned into an image. The 80/20 split on DC1 ensures that a strong interference signal amplitude is generated for each of the relevant reflectors in the sample whilst the majority of unwanted signals that do not correlate with any of the reference signals are minimised.

The total, optical fibre path lengths of the object and reference arm must be approximately equal in order to obtain an interference pattern (assuming equal, free-space path lengths as stated above). Therefore, the total length along L_3 and L_4 should be equal to twice the length of L_2 plus L_7 since the light travels back and forth along the same path in the object arm ($2L_2 + L_7 = L_3 + L_4$). This condition was specified in the design when ordering the array but can only be guaranteed to within $\pm 5 \text{ mm}$, due to manufacturing tolerances.

2.4.1 Object Arm & Reference Arm

The object arm made use of a pre-existing handheld assembly, *H*, that was fabricated by the 3OM Optomechatronics Group, Aurel Vlaicu University of Arad, Romania. This was designed to accommodate a collimator, *C*, and a single galvanometric scanning mirror, *GS*, to create a handheld scanner (Figure 2.15). However, a mounting stage, *HM*, also needed to be designed and fabricated to hold the scanning assembly securely in place for imaging when not in use as a handheld device.

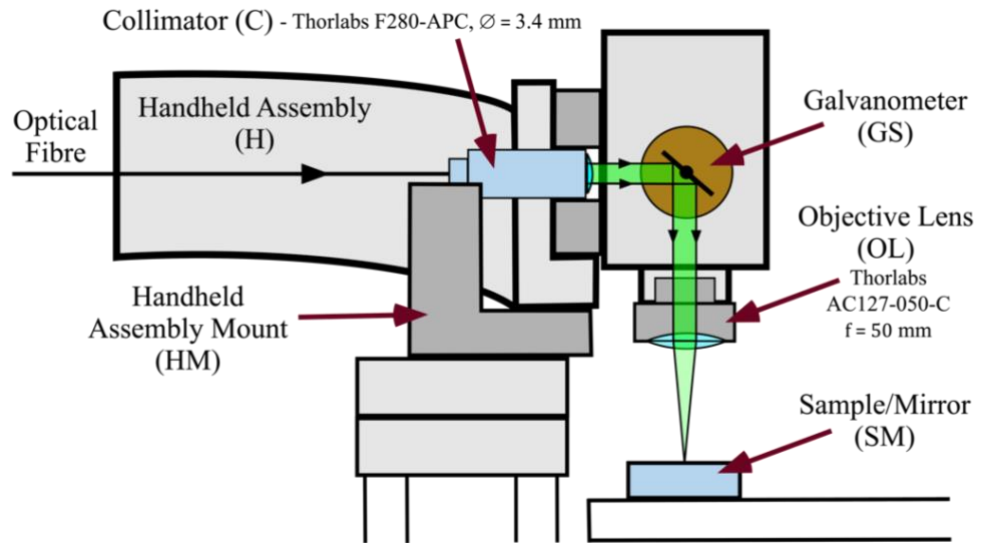


Figure 2.15. Handheld scanner design showing the insertion collimator, galvanometer scanner mirror and objective lens with a beam focussing light onto a sample (or mirror). An assembly mount was also designed to hold the scanner when not in use as a handheld device. The back and forth, free-space path length of the light in the object arm is indicated by the green beam exiting the collimator and falling incident on the sample mirror, via the galvanometer.

The handheld scanner in the object arm directs light from a collimator (F280-APC, $\varnothing = 3.4\text{ mm}$, Thorlabs) onto the galvanometer scanning mirror (GVS001 TS21099-X, Thorlabs), which then scans the beam through an objective lens, *OL*, (AC127-050-C, 12.7 mm diameter, 50 mm focal length, Thorlabs) before striking the sample, *SM*. However, the sample was often replaced by a mirror to calibrate the interferometer. A National Instruments 6110 with a BNC 2110 Shielded Connector Block/Breakout Box (185124F-01) was employed to drive the galvanometer. Using a single scanning mirror meant that only B-scan images could be produced.

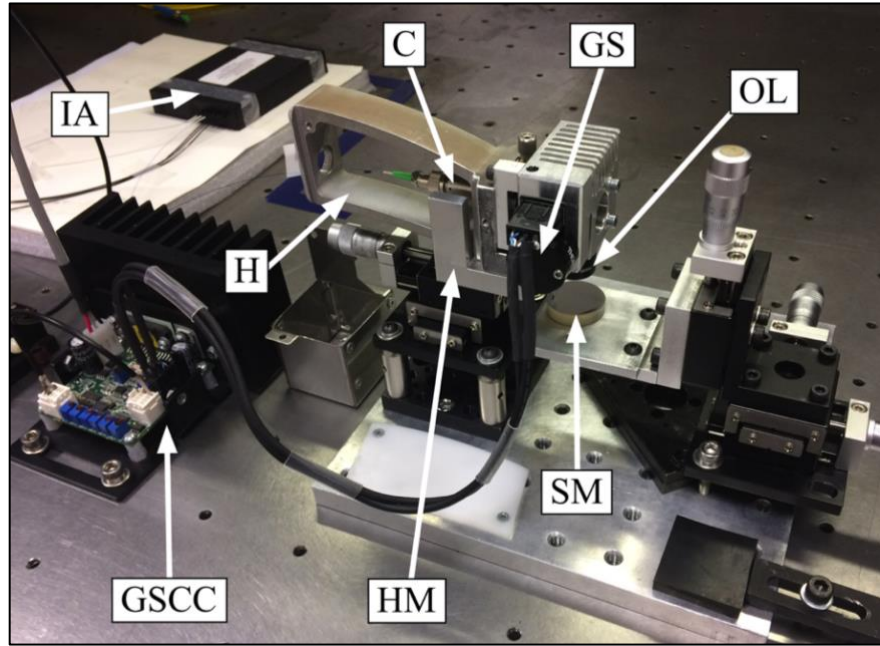


Figure 2.16. Object arm. The handheld scanner, *H*, is shown fixed to a bespoke mounting stage, *HM*, with its handle covers removed, exposing the optical fibre connected to a collimator, *C*. The galvanometer scanner, *GS*, and the objective lens, *OL*, direct the light onto the sample, which in this case is a planar mirror, *SM*, used to maximise the returning signal during the alignment process. The optical fibre interferometer array, *IA*, and galvanometer signal control circuit, *GSCC*, are also visible. The back and forth, free-space path length between *C* and *SM* is approximately equal to the path length inside the reference arm (Figure 2.17).

The object arm (Figure 2.16) and reference arm (Figure 2.17) were both constructed on optical breadboards to allow free movement around the optics bench and were connected directly to the interferometric, optical fibre-based array, *IA*. An adjustable aperture (not shown) was frequently used in the reference arm to attenuate the optical power and avoid over saturating the balanced photodetector, which incidentally also provided some control over the exposure of the images.

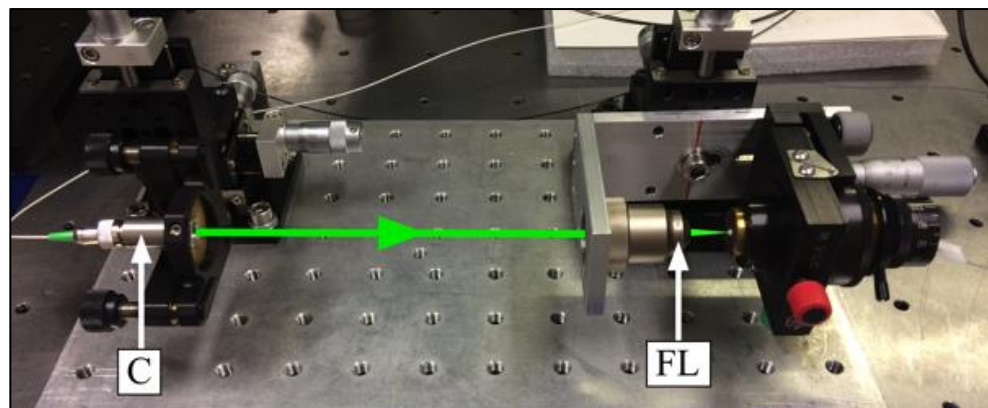


Figure 2.17. Reference arm. A collimator, *C*, delivers light (green arrow) into the free-space path of the reference arm, and a focusing lens, *FL*, injects the light back into the optical fibre. The free-space path length between *C* and the receiving optical fibre is approximately equal to the back and forth, free-space path length inside the object arm (Figure 2.16).

2.4.2 Transverse Resolution Measurements

The transverse resolution, Δx , of the handheld scanner in the object arm is given by Eq. 1.11 using the parameters of the collimator ($D = 3.4 \text{ mm}$), objective lens ($f = 50 \text{ mm}$) and the central wavelength of the light source ($\lambda_c = 1330 \text{ nm}$). The calculated value was $\Delta x = 23.86 \text{ }\mu\text{m}$. This was then confirmed using the lateral resolution test pattern on an OCT validation phantom from Arden Photonics (APL-OP01) [60], shown in the photograph of Figure 2.18 a) next to a finger for scale. A B-scan image of the target is shown in Figure 2.18 b), which shows 3 groups of 11 horizontal lines (along the y-axis) that are separated by a known line spacing. The lines begin to be consistently resolvable in the third group, which has a minimum line spacing of $23 \text{ }\mu\text{m}$ (red circle).

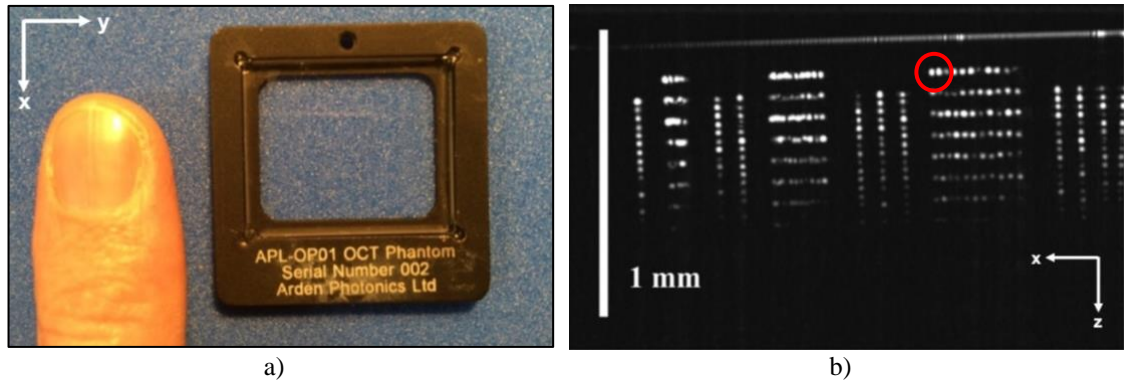


Figure 2.18 **a)** Arden Photonics OCT validation phantom (APL-OP01). **b)** B-scan image of the lateral resolution test pattern, showing consistently resolvable lines (along the y-axis) at approximately $23 \text{ }\mu\text{m}$ for the beginning of the third group of lines (red circle).

2.5 Signal Processing and Image Creation

After the optical interference signals have been collected by the balanced photodetector, the DC and AC component, analog information is delivered to a computer and digitised for processing. The computer used an Alazartech ATS 9350 data acquisition card (DAQ) to digitise the data, allowing up to 500 MS/s. The typical processing method for FD-OCT is to perform a fast Fourier transform (FFT) on the spectral frequency modulations [42]. The depth locations of the features in the sample are frequency-encoded into the spectra, which are then demodulated using the FFT after some prior signal conditioning is carried out. However, this research project had the advantage of using an alternative method called Complex Master-Slave Interferometry (cMSI), developed in 2016 by A.G. Podoleanu and A. Bradu *et al.* from the Applied Optics Group (AOG), University of Kent, UK, who were originally motivated by the desire to produce faster *en-face* images [61].

The Master-Slave process is two-fold; ‘Master’ refers to the preliminary calibration method, which takes several experimental measurements to establish the system’s characteristic parameters, and this information is used in the ‘Slave’ stage to produce the images. The process begins by replacing the sample in the object arm with a planar mirror and recording two or more channelled spectra corresponding to different, equidistantly spaced OPD values between the two arms of the interferometer. These few experimental channelled spectra (termed ‘masks’ in CMS publications) are used to generate a large number of theoretically inferred masks which fully characterise the system (Master), specifically the encoded chirp modulation generated by the non-linearity of the SS output, as well as any unbalanced dispersion between the object and reference arms of the interferometer. The number of theoretical masks is chosen such that it sufficiently covers the axial range required to scan through a particular depth (typically 512 but should be at least equal to the axial range divided by the axial resolution). Then, after the set of theoretical masks is generated, the planar mirror is replaced by the sample and the imaging process begins. As each lateral point (x,y) within the sample is explored, the experimental channelled spectra produced are compared with an equivalent theoretical mask from the same depth (Slave). Matrix multiplication (dot product) is used to carry out the comparison against the set of pre-generated masks and extract the depth information, which is the equivalent step of using the FFT operation. If the SS system or the interferometer setup is changed in any way, the experimental masks must be re-measured, and the theoretical masks re-generated, before successful imaging can continue.

The advantage of using cMSI is that it reduces the signal processing time (under certain conditions, e.g. using a small number of axial depths). It does this by removing the need to perform prior signal conditioning operations on the channelled spectra, such as resampling [62] or dispersion compensation [55], which allows cMSI to attain the maximum theoretical axial resolution [63]. Another key advantage is that cMSI is highly suited to non-linear scanning and does not require separate linearisation. A judicious choice of the window size means that the algorithm is faster than FFT based SD-OCT [64]. This unique method of extracting the depth information from the channelled spectra allows a particular axial location within the sample to be selected and processed independently from any other depth, removing the requirement to process a full volume

of data in order to produce a single *en-face* image² and thus delivering them faster. The mathematical algorithms used to carry out cMSI were set up in LabVIEW™ using the standard development suite package from National Instruments. All of the images in this thesis were captured using the same LabVIEW™ software package and adjustments were only made to the imaging session parameters on the graphical user interface, which provided full control over the whole OCT system including the galvanometer mirror in the handheld scanner (Section 2.4.1).

2.6 Simulations in Ray Tracing Software

Zemax™ Optics Studio is a fully comprehensive ray tracing software package that can accurately simulate the propagation of light rays through a variety of optical surfaces. The simulation software has the ability to perform diffraction limited ray tracing and successfully incorporates the effects of aberration with respect to wavelength. The simulations can also apply apodization, which is an efficient way to model optical beams that exhibit a non-uniform illumination, such as a Gaussian power distribution, along their cross section, and is therefore appropriate to use for beams that originate from single mode fibres. All of the components in the spectral filter could be modelled in the simulations, which made Zemax™ a valuable tool for studying the filter's operation. Zemax™ was used to visually and analytically explore a variety of spectral filter designs and establish the properties that had the greatest impact on the filter's performance. Simulation images and measurements are provided throughout this thesis to accompany the theoretical and experimental studies, which help to either confirm or refute the arguments put forward.

² Although in this research project only a single galvanometer scanner was used so only B-scan image generation could be achieved.

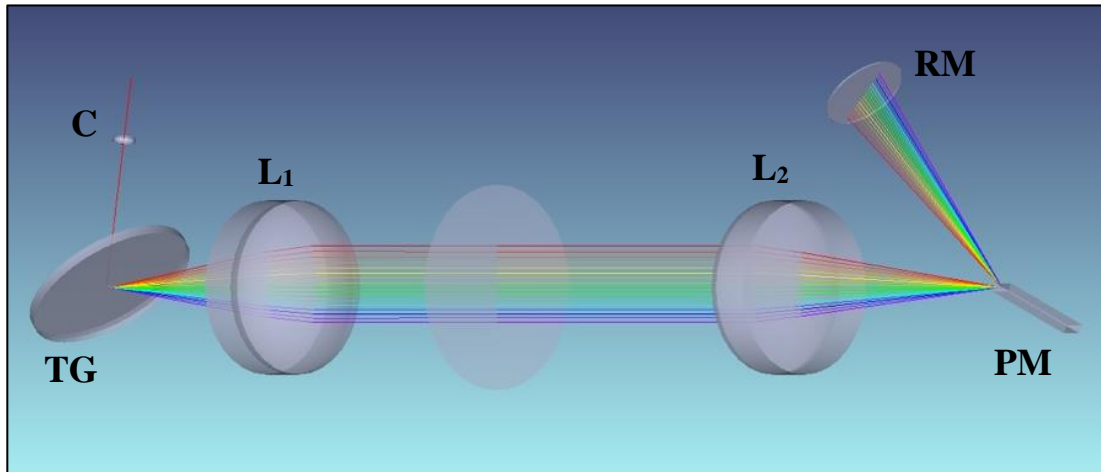


Figure 2.19. Zemax™ Optics Studio ray tracing simulation software - 3D shader model example. Light rays originate from the surface acting as the optical fibre tip (top left) and travel through each component in sequence; collimator lens, C, transmission grating, TG, two-lens telescope, L₁ & L₂, polygon mirror, PM, and retroreflector mirror, RM.

Zemax™ simulates an optical component by specifying the properties of each boundary (or surface) that light interacts with. An aspheric doublet lens modelled in Zemax, for example, requires three surfaces, each of a particular size and shape, and with a certain distance (or thickness) between them. Thickness is a surface parameter, i.e. represents “thickness to the next surface” in the medium between surfaces (such as air or various glasses), whose index can also be specified to simulate the refractive properties of the material. Each surface in the simulation is added sequentially into a lens data editor (see Appendix D) and the software traces the light rays through each surface in the same order as they are listed (sequential mode). A wide range of other surface properties can be inserted into the lens data editor including; radius, semi-diameter, glass type, surface coating and higher order terms for precisely replicating the curvature of a lens. With the exception of the RM, every component in the simulation is modelled twice – once to represent the forward path through the filter and then a second time, in reverse order, to represent the path back. The two sets of components perfectly overlap each other, and accommodate any changes made to the angle of the PM, and therefore can be viewed simultaneously without confusion.

Zemax™ also has a non-sequential mode which can be employed to simulate light interactions with a variety of non-elementary surfaces. The non-sequential mode was used to build a three-segment (three-facet) portion of the PM. This model was then

inserted into the sequential mode editor as a polygon object³. As described in Section 2.3.3, the facet rotation angle needs to be matched to a particular wavelength in order to return it successfully. A multi-configuration editor was therefore used to simulate the rotation angle of the PM, by attributing a specific angle to each wavelength in the simulation. The actual broadband spectrum of light propagating through the filter was simulated by activating a number of discrete wavelength inputs (11-17, depending on the simulation). The wavelength values were equidistantly spaced to model the full spectral range of the input light source used in the experimental setup. Throughout the rest of this thesis, the term ‘configuration’ shall refer to the individual wavelength and polygon angle combinations.

In reality the spectrum is of course continuous and a single ray of light with a finite wavelength value does not accurately represent the real life narrowband laser linewidths that are instantaneously tuned by the filter and emerge at its output. An approximation to the linewidth can be approached if the equidistant spacing between the wavelength values is suitably small (e.g. $\leq 0.25 \text{ nm}$). However, this would require several hundred individual wavelength inputs to span the breadth of the light source ($> 100 \text{ nm}$), which is neither practical, from a computational point of view, nor are there this many wavelength inputs available in Zemax™. Therefore, only a small fraction of the total spectrum can be selected whenever the narrowband laser linewidth are simulated. Weight was also given to each wavelength in the simulation to approximate the Gaussian shape of the input bandwidth.

One final comment should be made regarding the light rays propagating through the simulated filter. As with a stationary PM, it is assumed that no change in rotation occurs during the tuning of a single wavelength (or narrowband laser linewidth). This is due to the speed of light being many orders of magnitude above the rotational speed of the PM and the short path length between the components, i.e. there is no change in the position of the PM (whilst tuning an arbitrary wavelength) because the time of flight into and out of the filter is vanishingly small.

³ The polygon mirror was also simulated as a single facet in some of the simulations due to compatibility issues across the various versions of Zemax™ that were used.

The work that follows in Section 2.7 introduces the concept of vignetting. This term is used to describe a particular type of light loss through an aperture mismatch and was already recognised, before the project began, as having a significant impact on the amount of successfully transmitted light through the filter [32], [33]. The concept of vignetting therefore became one of the initial foundations of this project, establishing a clear objective and motivation to explore how it occurs and how it can be reduced to maximise the filters performance.

2.7 Vignetting

All optical systems suffer from light loss but the magnitude of the loss depends upon many factors. In the SS, a small fraction of light is lost through back reflections and low coupling efficiency in the free space and fibre based sections of the experimental setup. Their effects are unwanted but minimised wherever possible using, for example, antireflection (AR) coatings on the surfaces of lenses or in fibre based connectors with angled physical contacts (FC/APC). However, even if the system suffers significantly from these losses, their impact is still negligible in comparison to the potential loss that can occur from vignetting in the PM-based spectral filter.

Vignetting most commonly refers to the reduction of light or reduced brightness towards the periphery of a photographic image. It occurs naturally when light rays enter an aperture from the extremes of a wide Field of View (FOV), e.g. when light rays land on an optical sensor with a large angle of incidence. In this research, however, vignetting is caused by physically preventing the light rays from reaching their destination or missing it altogether. The consequences of vignetting are highly detrimental to the systems performance and are therefore entirely undesirable and should be removed, or at least minimised, wherever possible. A conscious effort was made to consider these effects throughout the project and to explore any options that may prevent vignetting at key surfaces. Unfortunately, not all of the solutions that were found could be applied without introducing additional detrimental consequences to the system. Finding a suitable balance between the various parameters of the system became one of the primary objectives in this project.

There are two key instances of vignetting that occur in the PM-based SS. These two instances shall be referred to as primary and secondary vignetting throughout this research. The filter experiences each of them sequentially and both can have a significant impact on the optical power output and the TSB of the SS. Primary vignetting occurs when the light interacts with the PM and secondary vignetting occurs when the light returns to the aperture of the launching fibre. These topics are explored in depth below, since the majority of theoretical work that follows is geared towards minimising or eliminating both forms of vignetting.

2.7.1 Primary Vignetting

The first instance of vignetting occurs when the light interacts with the facets on the PM. The simplest example is when the width of an incident beam is larger than the size of an individual facet. The beam will over illuminate the facet and the light falling outside of its surface aperture will be lost to primary vignetting. A more complex form of primary vignetting occurs when the PM is in operation. The rotation of the PM inevitably causes the boundary between two adjacent facets to pass through the incident beams of light. If this happens during the tuning process, i.e. when one of the wavelengths has satisfied the normal incidence condition, primary vignetting will occur for that wavelength. This beam ‘walk-off’ issue was first highlighted (w.r.t. OCT) by Morosawa *et al* in 2007 [13], yet very little has been done since to address the issue.

Figure 2.20 a) is a 3D shader model simulation image showing a three-facet segment of the PM intercepting a single-wavelength beam of light (red rays) with an elliptical cross-section. The majority of the beam can be seen striking the central, target facet, TF, but there is also a semi-circular section of the beam that can be seen overlapping onto the adjacent facet below. In this example, the light rays striking the TF meet the normal incidence condition and retro-reflect back successfully in the correct direction to exit the filter and contribute towards the SS output. The light rays that strike the adjacent facet will reflect back along a different path and be lost due to primary vignetting.

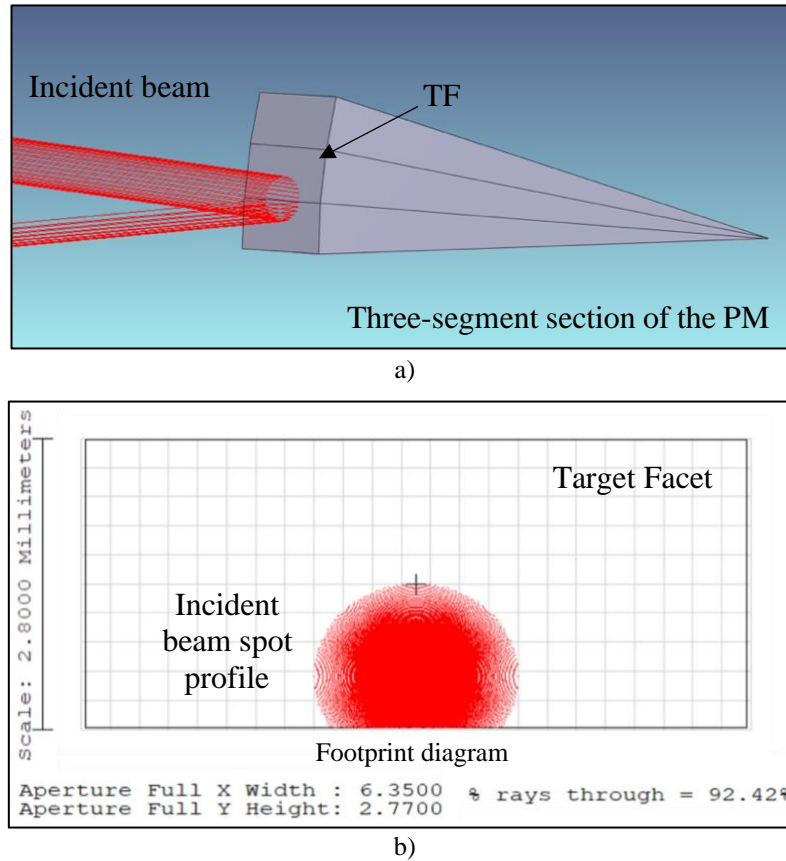


Figure 2.20. Primary vignetting. *a)* A three-segment portion of the PM is shown with a beam of light (red rays) falling incident on the TF and overlapping onto the adjacent facet below. *b)* Footprint diagram of the PM TF and the beam that has been cut at the bottom edge ('delete vignetting' option) to create a small, semi-circular segment that will be lost to primary vignetting.

Figure 2.20 b) is a specific Zemax report known as a footprint diagram, showing the location of 200 individual light rays striking the surface of the TF. The footprint diagram can be used to measure the percentage of rays that successfully arrive on any surface by using the report option to 'delete vignetting', which removes the rays that fall outside of the relevant aperture (used here). The percentage value is indicated in the bottom right of the diagram. This form of vignetting analysis was carried out frequently throughout the project to approximate the total optical power of the spectral filter. An estimation of the TSB can also be made by measuring the percentage of rays for each wavelength that successfully strike a surface.

2.7.2 Secondary Vignetting

The second instance of vignetting occurs when the light rays, having propagated back and forth through the telescope, attempt to exit the filter through the entrance aperture of the optical fibre. The vignetting occurs due to a mismatch between the fibre tip's mode field

diameter (MFD) and the spot shape of the returning light beam. The change in the spot shape is mostly caused by lens-induced aberrations, which are wavelength-dependent. Although these aberrations only deviate the rays by a small fraction of an arcsecond, the double-pass through the spectral filter means that the amount of ray deflection adds up, causing some of the rays to miss the $9\ \mu\text{m}$ diameter aperture of the optical fibre tip. The consequence of these ray deflections results in poor coupling efficiency and reduces the total optical power of the SS. This is mentioned throughout the literature [65] but never explored in any detail.

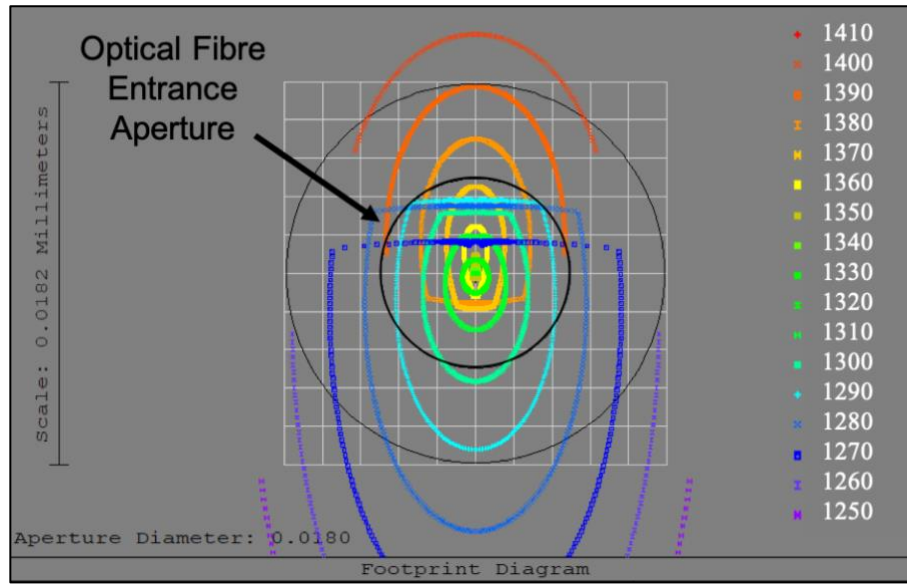


Figure 2.21. Secondary vignetting. Footprint diagram of the optical fibre aperture (black circle) and a selection of wavelength spot shapes represented by different coloured rings (the wavelength selection process was described in Section 2.6). A significant portion of the beams do not terminate inside the entrance aperture and therefore do not contribute towards the SS output. Primary vignetting is also demonstrated by the abrupt cuts across the elliptical shape of several wavelength beams from the margins of the spectrum.

The footprint diagram in Figure 2.21 shows the optical fibre entrance aperture (black circle) and the spot shape outline of individual wavelengths (coloured rings) from across the entire spectrum (the wavelength selection process was described in Section 2.6). In this example, many of the beams overlap the boundary of the aperture, preventing a significant portion of the rays from making it back into the optical fibre. The greater the mismatch of incoming light with this circular area, the greater the fibre coupling losses. This was first mentioned in the literature by Y. Mao *et al.* who carried out their own simulation analysis on a similar spectral filter design and reported a change in the focal spot at the image plane from circular to elliptical for the marginal wavelengths and a

lower coupling efficiency this caused as a result [21]. The abrupt horizontal lines, cutting across the elliptical shaped beams, indicates that primary vignetting has already occurred on the PM. The primary vignetting is more commonly associated with wavelengths from the margins of the spectrum, rather than from the central region, due to the movement of the TF as it sweeps across the incident spectrum (see Section 4.5.1). Although Zemax™ does take the diffraction limit into consideration, the footprint diagrams used throughout this thesis are not necessarily indicative of diffraction limited performance and are used for illustrative purposes only.

2.8 Discussion

This chapter has introduced the entire experimental setup as well as the methods that were used to construct and align the spectral filter. This included highlighting the most important features that should be considered during the design process. The following discussion is a short reiteration of these features and the techniques that were used, which are strongly recommended when attempting to optimise any PM-based SS system.

Several early conclusions were drawn from studying the components in the SS. Some of them can be optimised independently of one another, which should be established before any other assembly is carried out. For example, the SOA power supply controller settings should be adjusted to minimise the temperature and maximise the current running through the semiconductor chip. This was shown to widen the input bandwidth by 20 *nm* and also increased the optical power output by ~50 % (Figure 2.8). Both of these improvements are beneficial for OCT imaging but they are also helpful for setting up the simulations and constructing the theoretical framework since they provide the maximum and minimum wavelength values of the source bandwidth entering the spectral filter and suggest how each wavelength should be weighted in the simulations.

The SOA also amplifies the laser linewidths every time they pass through the semiconductor chip. The speed of the PM determines how long each linewidth spends oscillating around the cavity, whereby higher speeds (preferable for OCT) reduce the number of cavity round trips and therefore decrease the amount of amplification. The number of cavity round trips can be increased by having a short path length in the ring laser cavity, which can be achieved by minimising the length of the optical fibres. Although this modification is highly recommended, it was not practical to reduce the optical fibre lengths in this project since it was important to maintain flexibility in the

experimental setup. Any extensive lengths of optical fibre remaining in the ring laser cavity should be securely fastened, and every FC/APC connector used should also be oriented correctly to avoid causing a polarisation mismatch and accidentally reducing the optical power. The ring laser cavity length is considered an important design parameter and shall be revisited again in the discussion of Chapter 7.

The construction method of the spectral filter also has an impact on the filter's performance. Maintaining good relative alignment is easier if the filter is assembled in sections, e.g. mounting the collimator and diffraction grating onto their own optical breadboard or containing the telescope within its own cage assembly. This helped with the alignment since previously aligned components can be moved together instead of having to move each one separately. Ease of relative movement of the two interferometer arms is an additional advantage. Having the object arm and the reference arm mounted onto their own optical breadboard means that they can be moved more freely around the optics bench.

Isolating the vibrations caused by the active PM was shown to be an important design consideration. An increase in the total spectral bandwidth and the optical power output was recorded after rebuilding the spectral filter with more robust components and additional dampening techniques to counteract these effects. Air turbulence was also observed to contribute towards worsening the output of the SS by creating a localised refractive index variation in the vicinity of the PM. This was remedied by guiding the light through the region with the least turbulent air flow. It is recommended that the construction methods discussed in Section 2.3.3.1 and Section 2.3.4 are employed when building a PM-based SS in order to maximise filter performance before being used in any accompanying OCT system.

CHAPTER 3

SPECTRAL FILTER COMPONENTS PARAMETERS AND OPERATION

3.1 Chapter Introduction

This chapter explores the components used in the spectral filter. They shall be introduced sequentially, for convenience, in the same order that the light interacts with them, and their fundamental operating principles shall be explained in detail. This is necessary for understanding the theoretical work that follows in Chapter 4, which examines the components' combined operation and how their specific properties can influence the filters performance.

3.2 The Spectral Filter

Figure 3.1 shows a diagram of the PM-based spectral filter that was constructed and explored in this research. The laser light from the SOA enters the spectral filter through an optical fibre collimator, C , and the collimated beam produced is directed towards a dispersive element, which in this case is a diffraction grating working in transmission, TG . A two-lens confocal telescope, with lenses L_1 and L_2 (and focal lengths f_1 and f_2), collects the light and directs it onto the polygon mirror, PM . From here, the light is either directly retro-reflected off the polygon (not shown), or sent to an additional retroreflector mirror, RM , used when the polygon is positioned 'off-axis' (Section 4.4).

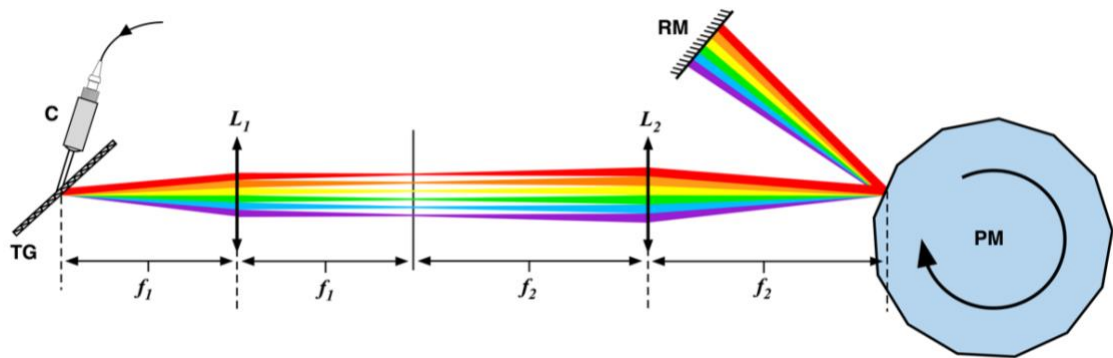


Figure 3.1. Spectral filter consisting of a fibre collimator, C , transmission grating, TG , two lens telescope, L_1 & L_2 , with focal lengths f_1 and f_2 respectively, polygon mirror, PM , and retroreflector mirror, RM . As the facet sweeps through the spectrum, only those wavelengths of light at normal incidence on the RM will retroreflect back along exactly the same path to be captured by the collimator and reinjected back into the optical fibre.

Retroreflection describes the instantaneous moment when the light rays strike a mirrored surface at normal incidence, which indicates the final surface of the filter, and the moment when the rays begin to trace their initial inbound paths back through the filter to exit via the same collimator they arrived from. The broadband, infra-red, laser light source is depicted by a visible coloured spectrum and can be seen terminating on the RM. The light reflects back off the RM in multiple directions but only the rays that retro-reflect at normal incidence will return along exactly the same path and be successfully reinjected back into the optical fibre. Each component will now be explored in more detail.

3.3 Collimators

Fixed focus collimators are used to transfer light from an optical fibre into a free-space region. Collimation is achieved by placing a lens (or lenses) in front of an optical fibre tip. This can be done with a single aspheric lens, when the collimated beam is to have a small diameter, or by using multiple element doublet (or even triplet) aspheric lenses, which are designed to provide diffraction limited performance when the beam diameter is much larger (e.g. $> 5\text{ mm}$). The beam exiting the collimator, W_0 , can be considered to have a circular cross section and a light intensity distribution described by the Gaussian $1/e^2$ MFD. All the collimators used in the experiments in this project accommodate FC/APC connectors and have anti-reflection surface coatings to reduce back-reflections for their specific wavelength operating range. An example of the fixed-focus, single aspheric lens collimators used in this project is shown in Figure 3.2 [57].

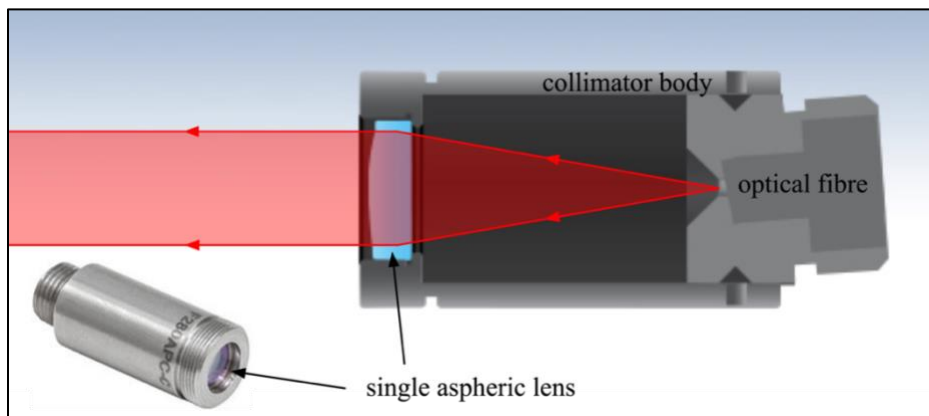


Figure 3.2 Example of a fixed-focus, single aspheric lens collimator. All of the collimators used in the experimental setup employ this type of collimation process. Images courtesy of Thorlabs [57].

The entire experimental setup employs four collimators (APC-C, Thorlabs, USA). Two of them are used in the interferometer, constituting the start of the free space regions of the reference and object arms. A third collimator is used to accommodate the trigger laser (Section 2.2) and the fourth is used to launch and capture light going into and out of the PM-based spectral filter. The trigger-based and interferometer-based collimators (F280APC-C) do not change throughout the experiments but the collimator used in the spectral filter will be the subject of subsequent experimentation in order to assess its effect on the filters performance (Section 5.3).

Precise control over the rays' direction and collimation is required to successfully recouple the maximum amount of light back into the optical fibre after travelling through the free-space regions of the interferometer and spectral filter. The efficiency of collimation is given by the full-angle beam divergence, which describes the angle that widens the diameter of the beam over distance. This angle can be approximated with Eq. 3.1 using the MFD of the optical fibre core and the focal length of the lens inside the collimator, f_c [57].

$$\text{Full-angle beam divergence (degrees)} = \frac{180}{\pi} \cdot \frac{\text{MFD}}{f_c} \quad \text{Eq. 3.1}$$

The graph in Figure 3.3 presents the beam divergence for a selection of single lens collimators (Thorlabs). In order of increasing beam diameter, these are; F230 (0.83mm), F110 (1.15mm), F240 (1.5mm), F220 (2.04mm), F260 (2.8mm), and F280 (3.4mm) [57]. The smaller beam diameter collimators use short focal length, singlet lenses with high numerical apertures (NA). The consequence of this arrangement increases the amount of refraction for the marginal rays in the beam, making their collimation more difficult to control. The results from Figure 3.3 suggest that the widest beam collimator (F280APC-C, Thorlabs) should have the highest coupling efficiency, since its low NA and longer focal length will reduce the amount of refraction the rays experience. Therefore, collimation is maintained over a longer distance, encouraging more light to arrive back into the entrance aperture of the optical fibre.

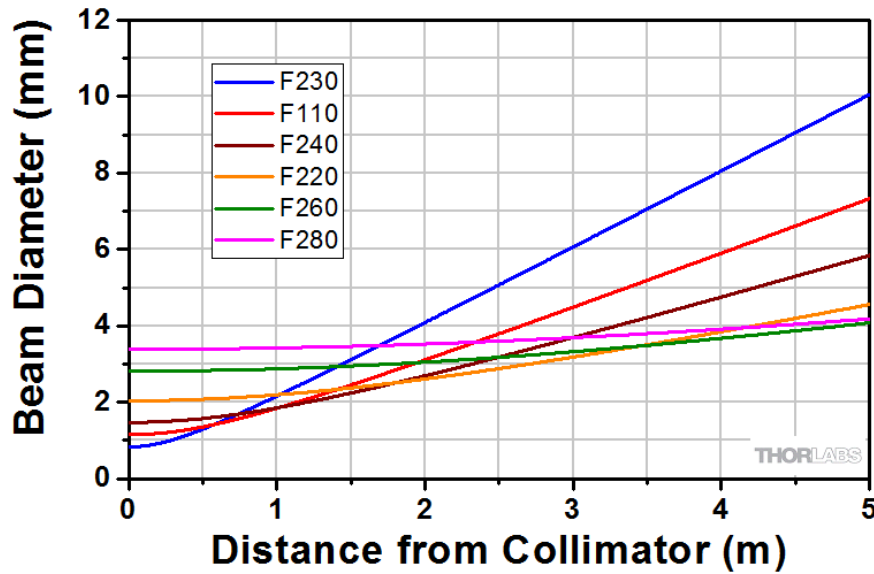


Figure 3.3. Beam diameter vs distance for a selection of collimators (Thorlabs; F230, F110, F240, F220, F260 and F280), central wavelength of 1310 nm using SMF-28-J9 fibre. The largest beam diameter collimator (F280) experiences 4 mm less beam divergence over a 5-meter distance than the smallest beam diameter collimator (F230), making them ideal for maximising the amount of recaptured light when using longer, free-space path lengths. Image – Thorlabs [57].

The free-space path lengths in the arms of the interferometer are relatively short (< 0.5 m) and the light only has two-to-three interactions with optical elements (excluding the complex interactions that occur inside the sample). Therefore, the effect of beam divergence in this area of the experiment is minimal. However, the free-space path length in the spectral filter is longer (~ 1 m, depending on the design) and the light executes multiple interactions with optical elements, all of which will contribute towards deflecting the rays away from their intended paths. The beam divergence may be relatively small but it should not be considered negligible, particularly for small beam diameter collimators as shown in Figure 3.3, since it may lead to a small loss.

The coupling efficiency of the SS is maximised when the rays follow the same path out of the filter as that going into it. Although the interaction of the light with the other optical components should also be investigated, a significant beam divergence will certainly limit the filter's ability to do this efficiently as it would reduce the number of successfully recaptured rays at the optical fibre entrance aperture (Section 2.7.2). The length of the path through the spectral filter is governed by the design of the optical elements and their properties, e.g. telescope magnification, however some components can and should be placed in close proximity to each other in order to help reduce the final path length. For example, the launching collimator can be placed almost directly in contact with the

dispersive element without causing any detrimental effects to the ray recapture. It is therefore preferable to select a wide-beam diameter collimator to minimise the free-space path length and avoid any losses caused by beam divergence.

3.4 Diffraction Gratings

The SS filters light through angular selection, which is facilitated by the rotation of the PM. To carry out this process, the different wavelengths within the spectrum must first be distributed over a range of angles. The angular displacement is enabled in this case by a diffraction grating, which operates either by illuminating a number of equidistantly-spaced lines (transmission grating, *TG*) or grooves (reflection grating, *RG*), but both will achieve the desired spectral distribution. The angular dispersion is the result of each wavelength in the spectrum diffracting off of these lines/grooves by different amounts (e.g. Figure 3.4).

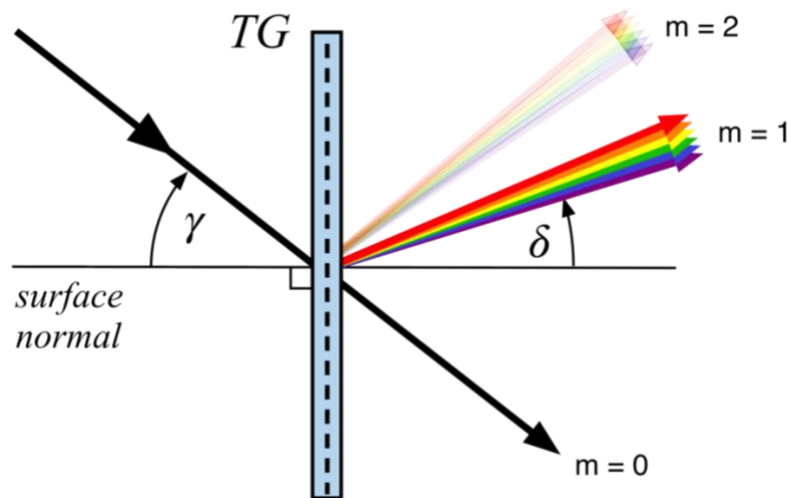


Figure 3.4. Diagram of a transmission grating, TG, and the diverging spectrum it creates. γ is the incidence angle from the surface normal (n) and δ is the diffraction angle w.r.t wavelength, λ_n . Each wavelength is diffracted by a different amount, which produces the angular distribution necessary for the filtering to occur.

The output is a continuous range of wavelengths, distributed over a continuous range of angles. Diffraction gratings also have surface coatings that maximise their efficiency at a specific operating wavelength range, and attenuate the transmission of light outside that range. Both reflection and transmission gratings were used in this research as well as different line/groove densities.

The grating equation (Eq. 3.2) provides the relationship between the incidence angle, γ , and the diffraction angle, δ_n , (both measured from the surface normal, n) for an arbitrary

wavelength, λ_n , between $\lambda_{0_{min}}$ and $\lambda_{0_{max}}$ of a multi-chromatic light source and is applicable to both types of diffraction grating [66].

$$Gm\lambda_n = \sin \delta_n + \sin \gamma \quad \text{Eq. 3.2}$$

Here, G is the line/groove density (or pitch, $p = 1/G$) and m is the diffraction order, which has a value of 1 throughout this research⁴. Gratings with higher values of G (shorter pitch) disperse the spectrum over a wider angular range, leading to higher grating resolution. The spectral resolution is attributed to the narrowband laser linewidths that the SS produces, $\delta\lambda$, which is a function of wavelength, λ_n , and the number of lines/grooves illuminated on the grating, N_0 .

$$\delta\lambda = \frac{\lambda_n}{mN_0} = \frac{\lambda_n \cos \gamma}{GW_0} \quad \text{Eq. 3.3}$$

The substitution $N_0 = \frac{GW_0}{\cos \gamma}$ is due to the beam's incidence angle on the grating, γ , and depends on the beam width, W_0 , at the collimator output. This makes the resolution of the grating inversely proportional to the line/groove density and the width of the incident beam, and therefore encourages the use of wide beam collimators to illuminate a high line/groove density diffraction grating. To emphasise this fact, Eq. 3.3 has been graphed in Figure 3.5 for three different incident beam widths (1 mm, 2 mm and 3 mm) and demonstrates how the spectral resolution narrows as a consequence of increasing the incident beam width by only a few millimetres⁵.

⁴ Higher diffraction orders ($m > 1$) do not exist for the transmission grating used in this research [78].

⁵ The incidence angle, $\gamma = 48.6^\circ$, is typically unique for each diffraction grating and depends on its operational wavelength range. Therefore, the graph in Figure 3.5 is only an example of the typical spectral resolutions that might be produced over the range of line/groove densities shown. At the least, it does categorically show the change in spectral resolution for the grating used in the majority of this research ($G = 1145 \text{ l/mm}$).

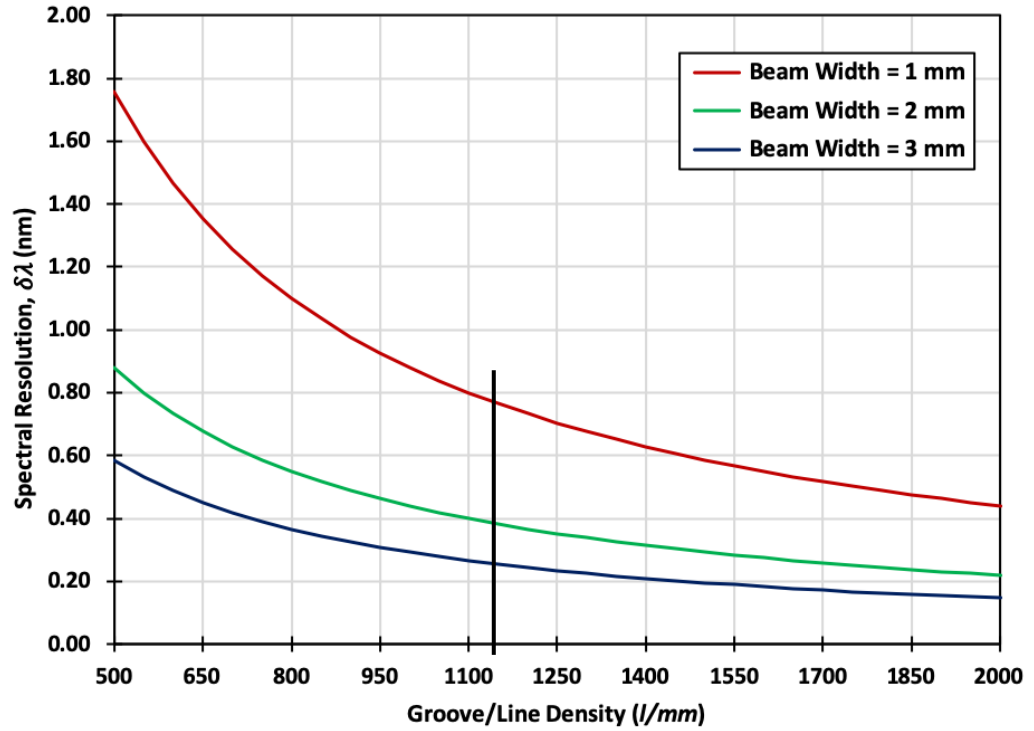


Figure 3.5. Spectral resolution (linewidth, $\delta\lambda$) as a function of grating line/groove density (Eq. 3.3) for three different incident beam widths; 1 mm (red), 2 mm (green) and 3 mm (blue). A diffraction grating with a high line/groove density combined with large beam diameter collimator will improve the spectral resolution and therefore produce narrower laser linewidths. This analysis assumes that the incidence angle remains constant over the total range of line/groove densities, which is not correct, but it does accurately display the difference when $G = 1145 \text{ l/mm}$, $\gamma = 48.6^\circ$ and $m = 1$ (vertical black line).

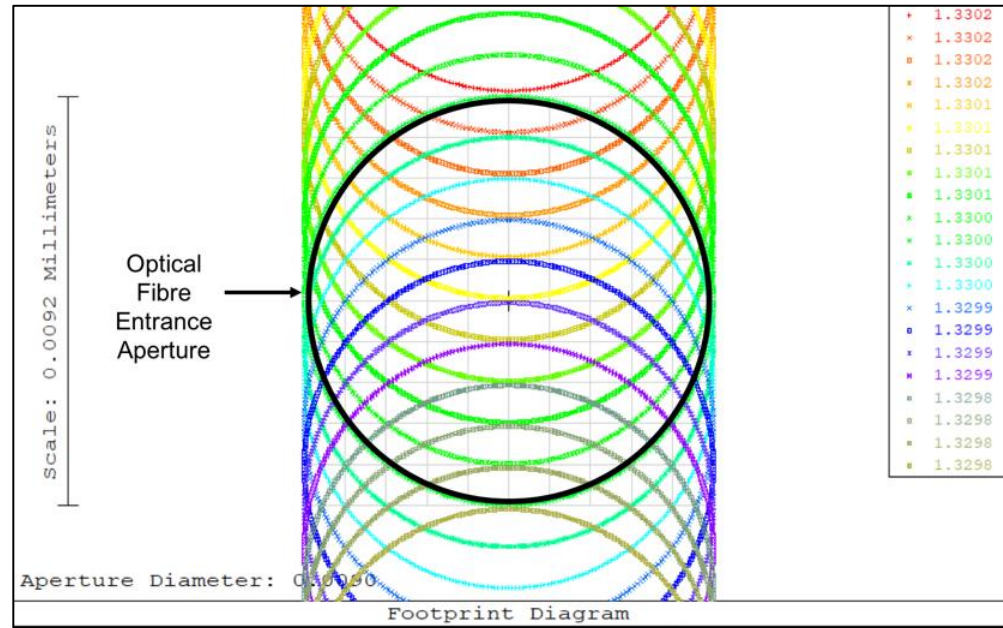
The vertical black line indicates the grating used throughout the majority of this project ($G = 1145 \text{ l/mm}$, $\gamma = 48.6^\circ$ and $m = 1$) and the improvement to the spectral resolution that is achieved from using a wider beam width collimator. Incidentally, if the properties of the diffraction grating are fixed and the incident beam width is maintained at 1.5 mm, the spectral resolution can be expected to gradually worsen with increasing wavelength, which is due to the linear proportionality between the linewidth and the wavelength in Eq. 3.3. In general, narrower linewidths will be produced for shorter wavelengths and wider beam diameter collimators, which are preferable for maximising the axial scanning range (Section 1.4.3).

3.4.1 Instantaneous Laser Linewidth

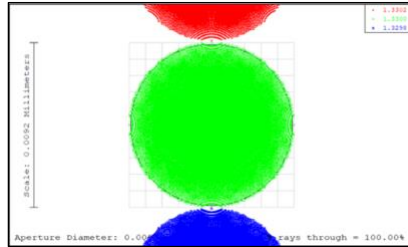
The axial scanning range of the OCT system depends upon the size of the instantaneous laser linewidths delivered to the sample being imaged (Section 1.4.3 and Section 1.4.4). The theoretical maximum scanning range can be approached if these laser linewidths are suitably narrow ($< 0.1 \text{ nm}$). Linewidth selection is carried out by the spectral filter but their FWHM is fundamentally determined by the spectral resolution of the diffraction grating (Eq. 3.3). The spectral filter design used in this research causes the light rays to interact with the diffraction grating twice before exiting the filter and entering back into the optical fibre-based, ring laser cavity. This occurs once during the inbound journey, after emerging from the collimator, and once again during the outbound journey, after passing back through the two-lens telescope. The second pass through the diffraction grating provides an extra contribution towards narrowing the filtered linewidths (see example in Figure 3.7), which approximately halve in size for every additional pass through the grating, according to the factor $2\sqrt{\ln 2}/\pi \sim 0.53$ [30].

The calculated spectral resolution of the diffraction grating used throughout the majority of this research⁶ has a single-pass linewidth of 0.51 nm (Eq. 3.3) but after applying the double-pass factor the linewidth reduces to 0.27 nm . ZemaxTM ray tracing software was used to simulate and verify these linewidth calculations. The simulation used a stationary PM, aligned to reflect the central wavelength ($\lambda_c = 1330 \text{ nm}$), and paraxial surfaces for the lenses and diffraction grating to demonstrate the ideal case. A narrow spectral region of the bandwidth, centred on λ_c and propagating along the telescope optical axis, was simulated using 21 individual wavelengths, separated by 0.025 nm and spanning a total range of 0.50 nm (from 1329.75 nm to 1330.25 nm). The linewidth of the central wavelength can then be approximately determined by counting the number of rays in each wavelength beam that successfully return to the optical fibre entrance aperture.

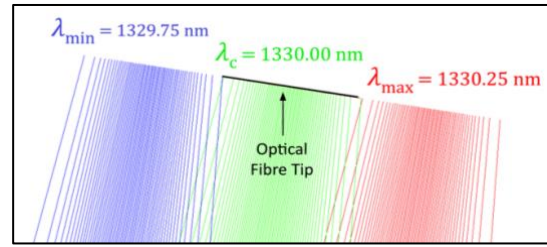
⁶ Wasatch transmission grating: $G = 1145 \text{ l/mm}$, $\gamma = 48.6^\circ$, and $m = 1$. The calculation in Eq. 3.3 also used an incident beam width $W_0 = 1.5 \text{ mm}$ and a central wavelength $\lambda_c = 1330 \text{ nm}$.



a)



b)



c)

Figure 3.6. Simulation images for examining the instantaneous linewidth of the system. **a)** shows the 21 wavelengths, represented by coloured rings, incident on the optical fibre entrance aperture. The rings overlap the aperture and a percentage of light from each wavelength is coupled back into the fibre, which contributes towards the linewidth. **b)** shows the same view but only the central and marginal wavelengths are visible; 1329.75 nm (blue), 1330.00 nm (green), 1330.25 nm (red), span = 0.50 nm. **c)** shows a side view of the same three wavelengths terminating in the plane of the optical fibre tip.

Figure 3.6 presents a collection of images from the simulation showing filtered light returning to the optical fibre entrance aperture. In the footprint diagram of Figure 3.6 a), the 21 individual wavelengths described above (represented by coloured rings) can be seen terminating in the plane of the optical fibre tip. The difference between each wavelength value (0.025 nm) is small enough to allow the majority of the beams to overlap one another on the entrance aperture and simultaneously send light from each wavelength back into the optical fibre. Only the two marginal wavelengths (1329.75 nm and 1330.25 nm) terminate completely outside of the entrance aperture. This is highlighted more clearly in Figure 3.6 b) and c), which show the footprints of the two marginal wavelengths and the central wavelength only, as well as a side-on view of the same interaction respectively. The total number of rays captured at each wavelength can

then be counted and the FWHM can be measure directly from the curve in Figure 3.7 to give the instantaneous laser linewidth for a double-pass (blue curve). The linewidth produced by a single-pass (red curve) through the diffraction grating was also measured by simulating a second fibre optic collimator, placed directly after the diffraction grating and aligned with the telescope optical axis, and repeating the same method described above.

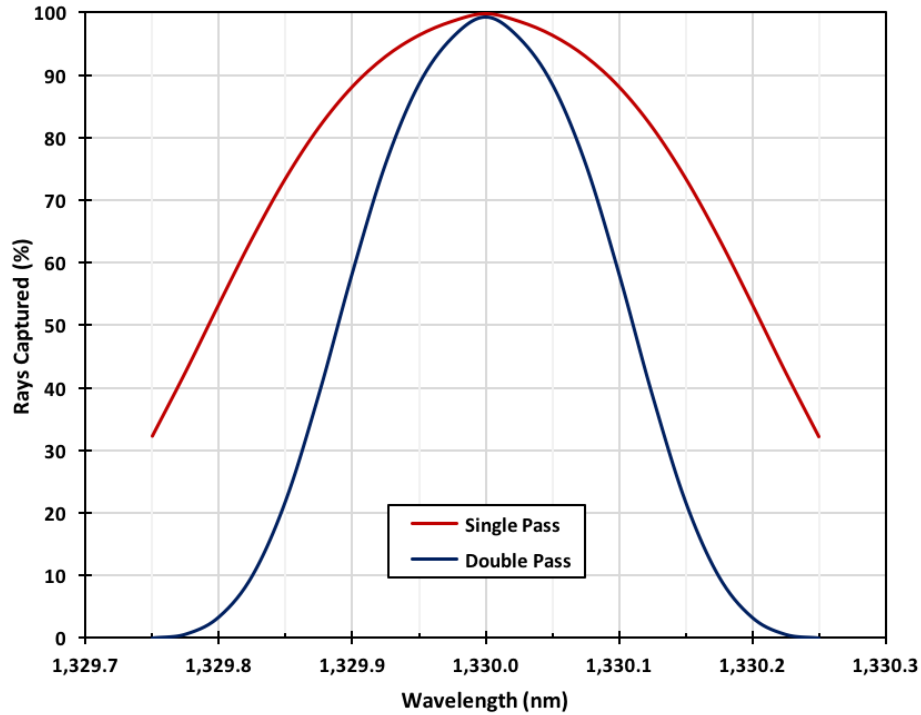


Figure 3.7. Simulation results of the instantaneous laser linewidth produced by a single-pass (red curve) and a double-pass (blue curve) through a transmission diffraction grating. Both terminate on 9 μm optical fibre entrance apertures and produced FWHMs of 0.42 nm and 0.20 nm respectively.

The FWHM of the single-pass linewidth was recorded in the simulation to be 0.42 nm and the FWHM of the double-pass linewidth was 0.20 nm. These are 0.09 nm and 0.07 nm smaller than the predicted values respectively, and a factor of 0.48 narrower than the single-pass value compared to the factor of 0.53 given earlier in this section. These results were generated using an ideal setup but in reality, dispersion and aberration will be present in the system and therefore the linewidths could be expected to broaden.

The instantaneous laser linewidths can be narrowed by increasing the beam diameter, increasing the diffraction grating line/groove density or by having multiple passes through the grating. A double-pass through the grating is equivalent to increasing the

beam width from 1.5 mm to 2.8 mm for a single-pass through the grating. The advantage of the double pass is that it allows the resolution of the filter to improve whilst maintaining a narrow beam width, which is of particular importance later when considering the interaction between the beam and the PM facets (Section 4.5). Multiple interactions with the grating are therefore welcome in these systems, especially if the grating has a poor spectral resolution. For example, Bräuer et al. were successful at incorporating four interactions with a reflection grating in order to minimise the instantaneous laser linewidth (0.03 nm) and maximise the axial scanning range (18 mm) of their SS [10].

3.4.2 Divergence Angle

The diffraction grating is placed into the setup such that the longest wavelength in the spectrum, $\lambda_{0_{max}}$ (diffracted the most), is positioned above the telescope optical axis, and the shortest wavelength, $\lambda_{0_{min}}$ (diffracted the least), is positioned below the telescope optical axis (Figure 3.8). The angular displacement between these two wavelengths is called the divergence angle, $\Delta\delta$, and is given by the difference between the maximum and minimum diffraction angles, $\Delta\delta = \delta_{0_{max}} - \delta_{0_{min}}$.

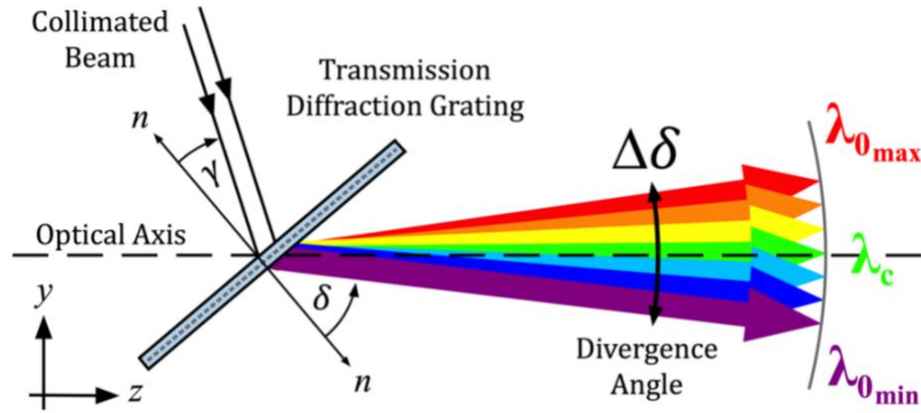


Figure 3.8. Transmission diffraction grating with incident collimated beam and diverging spectrum. The central wavelength, λ_c , is aligned to the optical axis and the angular displacement between the two marginal wavelengths, $\lambda_{0_{min}}$ and $\lambda_{0_{max}}$, gives the divergence angle, $\Delta\delta$.

Rearranging Eq. 3.2 for $\delta(\lambda)$, and substituting for the maximum and minimum wavelengths, provides the divergence angle as a function of spectral bandwidth (Eq. 3.4).

$$\Delta\delta = [\sin^{-1}(Gm\lambda_{0_{max}} - \sin\gamma)] - [\sin^{-1}(Gm\lambda_{0_{min}} - \sin\gamma)] \quad \text{Eq. 3.4}$$

The divergence angle is an important feature of the setup because the numerical aperture of the first lens in the telescope needs to accommodate the emerging spectrum from the

grating. If the diameter of the lens is too small or the focal length is too long, the marginal wavelengths will fail to propagate through the aperture of the lens, which will gradually worsen as the focal length increases. Therefore, the choice of grating somewhat restricts the parameters of the telescope that follows and, if these components are not chosen carefully, light from the margins of the spectrum will be lost and the TSB will decrease.

3.4.3 Spectral Energy Distribution

The diffraction angle of the central wavelength, δ_c , was chosen to align with the optical axis of the telescope (Figure 3.8) since it corresponds to the centre of the total, edge-to-edge bandwidth emitted by the SOA light source, $\Delta\lambda_T = \lambda_{0_{max}} - \lambda_{0_{min}}$ (Section 2.3.2.1). The central wavelength is simply the mean value between the maximum and minimum wavelengths in the spectrum, which satisfies either form of Eq. 3.5 below.

$$\lambda_c = \lambda_{0_{max}} - \frac{\Delta\lambda_T}{2} = \lambda_{0_{min}} + \frac{\Delta\lambda_T}{2} \quad \text{Eq. 3.5}$$

However, the diffracted spectrum does not sit equidistant on either side of the telescope optical axis because the grating equation is a non-linear, trigonometric function and the mean diffraction angle, δ_m , halfway between the two marginal angles, is not equal to the diffraction angle of the central wavelength, $\delta_m \neq \delta_c(\lambda_c)$.

$$\delta_m = \delta_{0_{max}} - \frac{\Delta\delta}{2} = \delta_{0_{min}} + \frac{\Delta\delta}{2} \quad \text{Eq. 3.6}$$

Table 3.1 lists the diffraction angles of the three most significant wavelengths in the SOA light source, which were calculated using a rearranged version of Eq. 3.2 ($\delta_n(\lambda_n)$) and the wavelengths given by the graph in Figure 2.6 respectively. The values used in the calculation are associated with the parameters of the diffraction grating that has been employed in the majority of the experiments; diffraction order, $m = 1$, incidence angle, $\gamma = 48.6^\circ$ and line/groove density, $G = 1145 \text{ l/mm}$.

Table 3.1. Diffraction angles for each of the three significant wavelengths from the light source bandwidth ($\Delta\lambda$); shortest (λ_{0min}), central (λ_c) and longest (λ_{0max}), including the magnitude of the angles between them, δ_+ and δ_- (see Figure 3.9 b). Values and figures are based on the 1145 l/mm transmission grating with a 48.6° incidence angle.

Wavelength	Diffraction Angle
$\lambda_{0min} = 1250 \text{ nm}$	$\delta_{0min} = 42.93^\circ$
$\lambda_c = 1330 \text{ nm}$	$\delta_c = 50.60^\circ$
$\lambda_{0max} = 1410 \text{ nm}$	$\delta_{0max} = 59.81^\circ$
$\Delta\lambda = 160 \text{ nm}$	$\Delta\delta = 16.88^\circ$
$\lambda_c \text{ to } \lambda_{0max}$	$\delta_+ = 9.21^\circ$
$\lambda_c \text{ to } \lambda_{0min}$	$\delta_- = 7.67^\circ$

The non-linear, asymmetric wavelength distribution has been plotted using the rearranged version of Eq. 3.2 and is shown in Figure 3.9 a). Displayed in this way the effect is subtle but still noticeable and therefore non-negligible (see red dashed linear trend line). A scale representation has been drawn in Figure 3.9 b) and Figure 3.9 c) is an example of the spectral energy density gradient, which is highest for the shorter wavelength region of the spectrum and decreases with increasing wavelength.

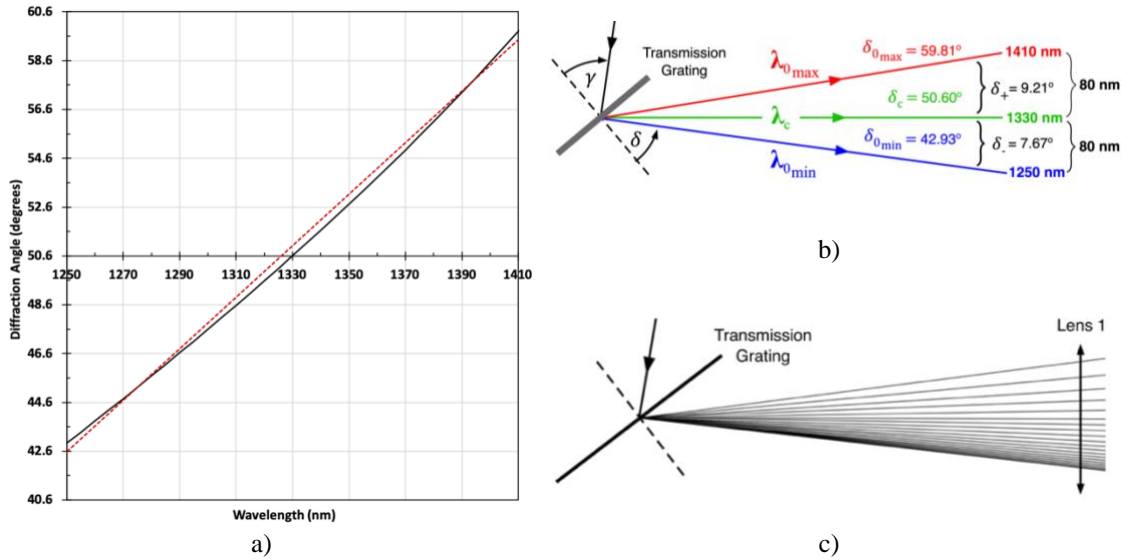


Figure 3.9. **a)** Non-linear spectral energy density distribution (black curve), generated using the grating equation (Eq. 3.2) and compared with a linear trendline (red dashed line). A scale diagram of the three significant wavelengths is shown in **b)** whilst **c)** gives an example sketch depicting the spectral energy density gradient. Values and figures are based on the 1145 l/mm transmission grating with a 48.6° incidence angle.

The rate of change of wavelength with respect to the diffraction angle is given by the derivative shown in Eq. 3.7.

$$\frac{d\lambda}{d\delta} = \frac{\cos \delta}{Gm} \quad \text{Eq. 3.7}$$

This non-linear spectral distribution has an impact on the wavelength selection with respect to time, $\lambda(t)$, which must be taken into account at the signal processing stage (Section 2.5). This property of the grating has various implications for the spectral filter, particularly the beam width, and shall be referenced throughout the thesis.

3.5 Telescope

The diverging spectrum from the diffraction grating is considered to consist of adjacent, collimated beams, differentiated by wavelength and diffraction angle. The spectral filter employs a two-lens telescope to capture these beams and convert the diverging angular dispersion into a converging angular dispersion incident onto the facets of the PM (Figure 3.10). This allows the wavelength selection to occur, either by directly reflecting off the polygon's facets or, by extension, off an additional retroreflector mirror (Section 4.4). Throughout the rest of this thesis, the converging angular dispersion incident on the PM shall be referred to as the converging spectrum. The magnification of the telescope simultaneously controls the converging spectrum and the size of the collimated beams as they arrive at the PM, both of which play an important role in optimising the spectral filter.

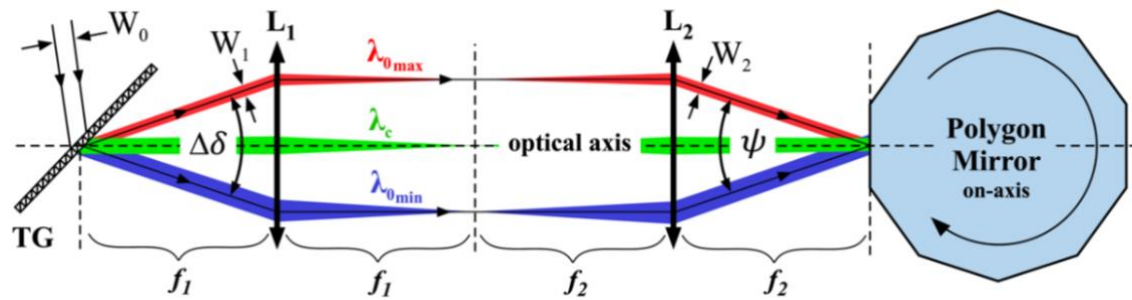


Figure 3.10. Spectral filter with transmission grating, TG, two-lens telescope, L_1 & L_2 and polygon mirror, PM. The central wavelength is aligned with the optical axis and the diffraction grating produces the divergence angle, $\Delta\delta$, which is inverted by the telescope, to produce the convergence angle, ψ , incident on the on-axis PM. The initial beam width, W_0 , originating from the collimator, changes to W_1 after going through the grating, which then changes again to W_2 due to the magnification of the telescope (f_1 and f_2).

The telescope consists of two achromatic doublet lenses, L_1 and L_2 (Thorlabs), placed in a $4f$ system configuration ($2f_1 + 2f_2$). Each lens has a numerical aperture, NA, given by the sine of the half-angle, θ_{half} , for a marginal ray measured from the optical axis, which can be assumed to be approximately equal to $\theta_{half} = \frac{\Delta\delta}{2}$.

$$NA = \sin \theta_{half} \quad \text{Eq. 3.8}$$

The focal length combination changes two important features of the filter; the convergence angle, ψ , which is the magnitude of the angular displacement of the converging spectrum, and the final beam width, W_2 . The former will have a negative impact on the TSB if it is too large (see Section 4.2) and the latter can affect the optical power transmission through the filter if it is too wide (see Section 4.8). Unfortunately, there is an inverse relationship between these two parameters, e.g. when a specific pair of lenses are used to decrease the final beam width (Eq. 3.9), the convergence angle will increase and vice-versa (Eq. 3.10).

$$W_2 = W_1 \frac{f_2}{f_1} \quad \text{Eq. 3.9}$$

$$\psi = \Delta\delta \frac{f_1}{f_2} \quad \text{Eq. 3.10}$$

As previously discussed in Section 3.4, there is an incentive to increase the size of the beam incident on the diffraction grating but also a requirement to ensure it will be fully accommodated by a single mirrored facet on the PM. The focal lengths of the telescope can be altered to achieve this but at the cost of enlarging the convergence angle. If too much attention is given to either one of these parameters, the other may suffer as a consequence and limit the filter's performance, which will be expanded upon theoretical in Chapter 4. Three possible focal length combinations exist; $f_2 = f_1$, $f_2 > f_1$ and $f_2 < f_1$. The convergence angle, ψ , and the final beam width on the facets of the polygon, W_2 , will change inversely with respect to one another as the magnification of the telescope satisfies each of these three possible configurations. For example, when $f_2 > f_1$, the final beam width on the facets will be larger than the initial beam width emerging from the grating, $W_2 > W_1$, but at the same time the convergence angle will have become smaller than the divergence angle, $\psi < \Delta\delta$. This example is illustrated in Figure 3.11 c) & d) respectively, alongside the two-other possible focal length combinations.

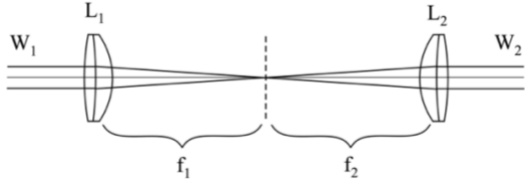
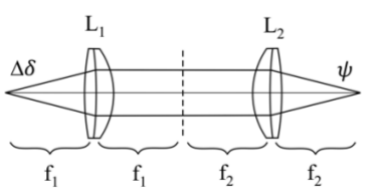
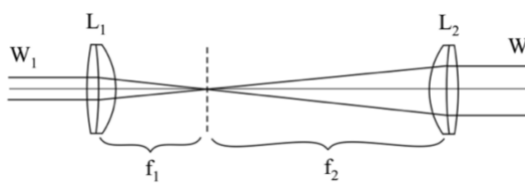
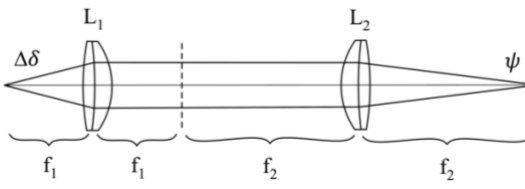
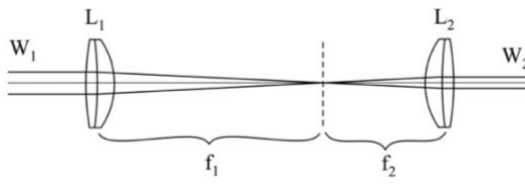
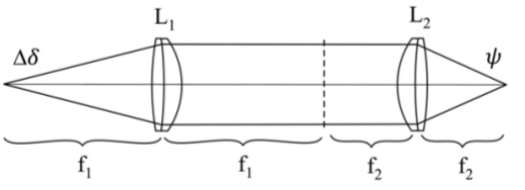
Beam Width, W_2	Convergence Angle, ψ
 <p>a) $f_2 = f_1, W_2 = W_1$</p>	 <p>b) $f_2 = f_1, \psi = \Delta\delta$</p>
 <p>c) $f_2 > f_1, W_2 > W_1$</p>	 <p>d) $f_2 > f_1, \psi < \Delta\delta$</p>
 <p>e) $f_2 < f_1, W_2 < W_1$</p>	 <p>f) $f_2 < f_1, \psi > \Delta\delta$</p>

Figure 3.11. Three diagram pairs showing how to control the size of the exiting beam width, W_2 , and the convergence angle, ψ , using a two-lens telescope. Three rays are shown passing through the telescope in each of the three diagram pairs, constituting the chief ray and the two marginal rays for a single beam in a), c) & e) but demonstrating the central wavelength, λ_c , between λ_{max} and λ_{min} at the edges of the spectrum in b), d) & f). Three distinctive focal length combinations exist, which change the incoming beam width, W_1 , and divergence angle, $\Delta\delta$. When $f_2 = f_1$, a) $W_2 = W_1$ and b) $\psi = \Delta\delta$. When $f_2 > f_1$, c) $W_2 > W_1$ and d) $\psi < \Delta\delta$. When $f_2 < f_1$, e) $W_2 < W_1$ and f) $\psi > \Delta\delta$.

Therefore, the combination and properties of the collimator and PM influence the choice of focal lengths used in the telescope when considering the width of the beam. However, the combination and properties of the diffraction grating and the PM also influence the choice of focal lengths but with respect to the converging spectrum. Focusing on just one of these relationships could significantly impact the other, whereby the power transmission or the TSB will be affected as a consequence. The correct combination of these parameters must be carefully selected for each spectral filter design, which will predominantly depend upon the choice of PM. This establishes an initial hierarchy to the design choices that must be made in the creation of any optimised, PM-based SS spectral filter (see Section 4.9.1 for a full discussion of the design hierarchy).

3.5.1 Aberrations

The incorporation of the two-lens telescope carries with it the unavoidable consequence of introducing various forms of aberration. The emerging spectrum from the grating is distributed across the surface of the first lens, which means that each wavelength has its own unique angle of incidence on the lens surface. Off-axis propagation of a collimated beam of a single wavelength results in a small range of incidence angles on the lens surface. This combination of interactions introduces spherical and chromatic aberration, field curvature, coma and oblique astigmatism that are more significant for some wavelengths than others, depending on their location in the spectrum and their incidence coordinate on the first lens of the telescope.

Spherical and chromatic aberrations are minimised by using achromatic doublet lenses in the two-lens telescope. Field curvature, coma and oblique astigmatism are more difficult to uniformly mitigate against due to the unique propagation of each wavelength through the filter. They have a greater impact for the most extreme, off-axis wavelengths and the cumulative effect of propagating back and forth through the telescope becomes significant to the filter's performance when it stops the light from returning to the $9\ \mu\text{m}$ aperture of the optical fibre tip. An example of this is shown in Figure 3.12.

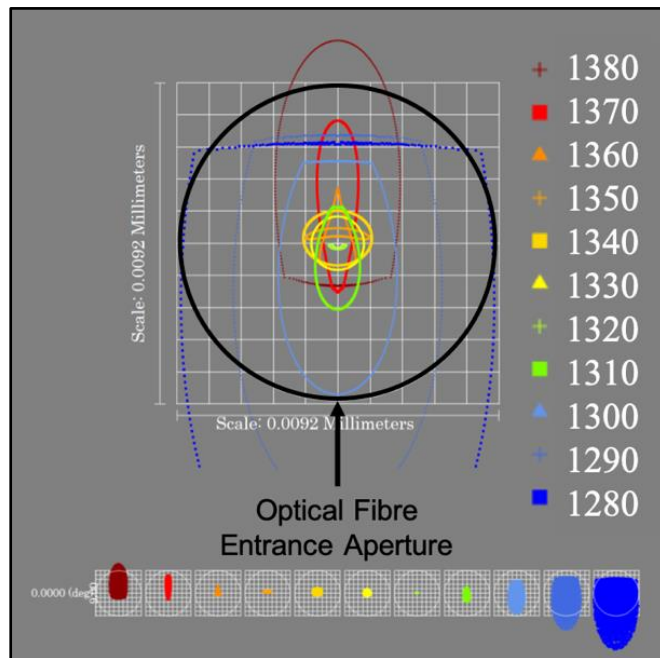


Figure 3.12. An example of the aberrations occurring as a result of the light propagating through the telescope. This spot diagram of the returning light on the optical fibre tip shows how the beams have been deformed by the various aberrations they experience as they traverse through the experimental setup. In this example, the mid-to-long wavelengths (1323 nm - 1363 nm) are particularly effected by coma and oblique astigmatism.

The unusual shapes of the spot profiles on the fibre tip demonstrate various forms of aberration occurring. For example, the teardrop shape of the 1310 *nm* wavelength (lime green) is indicative of coma whilst the saddle shaped spots of the 1320 *nm* (green) and 1350 *nm* (orange) wavelengths are caused by the combination of field curvature and astigmatism. In this example, the greatest impact on the spot profiles is seen occurring for the marginal wavelengths (1280 nm, 1290 nm and 1380 nm), whose footprints have increased in size to the point where they overlap the entrance aperture of the optical fibre tip. The light rays that fall outside of the optical fibre aperture will not be recaptured back into the optical fibre. Light rays that are lost in this way are described in this thesis as having been affected by secondary vignetting (Section 2.7.2).

Since the operation of the filter's telescope is unconventional compared to that of a typical magnifying telescope, the aberrations that occur cannot simply be resolved by using more sophisticated lenses (e.g. achromatic triplets) whose significantly higher cost may not justify the minor improvement they provide. An alternative and novel solution to these problems will be presented in Chapter 6, which introduces 90 degree, off-axis parabolic mirrors (instead of a two-lens telescope) to reducing the amount of aberration and therefore decrease the amount of secondary vignetting.

3.6 Polygon Mirror

The PM is the primary component of the SS spectral filter and is simultaneously responsible for the wavelength selection and the speed of data acquisition. The polygon itself consists of a narrow aluminium disk attached to a friction-limited, high speed electric motor, contained within a heavy-duty casing (Figure 3.13). The outside edge is occupied by a number of mirrored facets, N , all of which have a gold surface coating to maximise the reflectivity over a wide range of wavelengths. They are typically employed as laser scanners, although the polygon in this research is used to filter the spectral components of a broadband light source via angular selection.

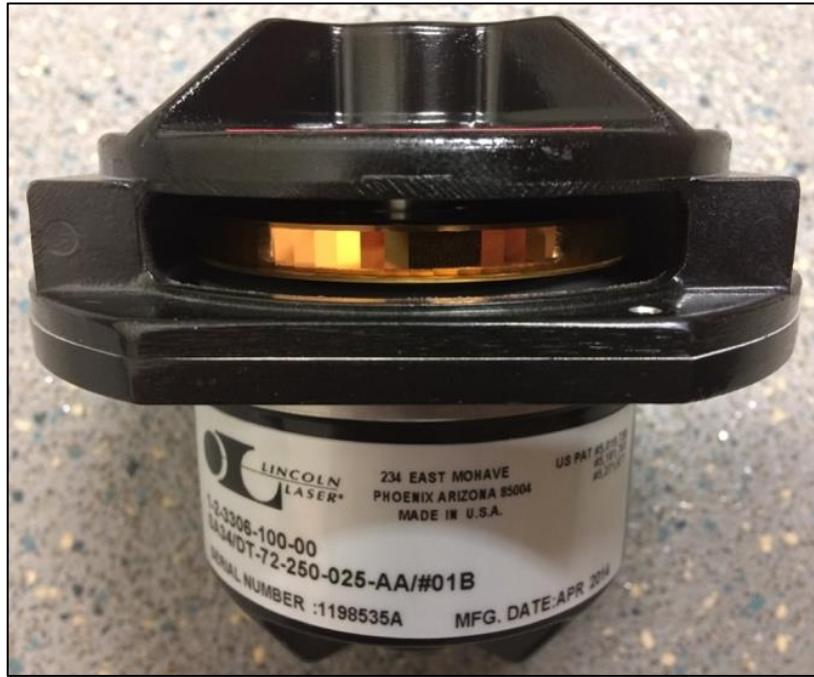


Figure 3.13. Lincoln Laser SA34 polygon mirror from Cambridge Technology. The 2.77×4.80 mm gold-coated facets (72) can be seen through the access window. The polygon rotates clockwise as seen from above. See Appendix B for more details.

Wavelength selection occurs every time a single mirrored facet sweeps across the path of the incident spectrum – as each facet passes, its surface normal aligns with the converging wavelengths and reflects each component sequentially before repeating the process for the following facet. When the PM is stationary, the active facet will successfully reflect only the rays that meet the alignment condition for a specific wavelength and facet angle, recorded as a narrowband instantaneous laser linewidth. The polygon’s direction of rotation is clockwise, as seen from above, which is important in this type of spectral filter since it determines the sweeping direction of the spectrum – the experimental setup used in this research has short-to-long wavelength sweeping due to the relative position between the grating and the PM (Figure 3.1).

As discussed in Section 1.4, while the speed of SD-OCT is limited by the detector, the speed of PM-based SS-OCT is fundamentally limited by the rotational speed of the PM or the sweeping facet frequency. The spectrum is swept through once for each pass of a single facet. The wavelength tuning speed, however, is the range of wavelengths swept per unit time, typically in nm/ms , and depends on the telescope magnification and how the spectrum is distributed within the convergence angle (Section 3.5). A fixed range of wavelengths within a small convergence angle will be tuned faster than if the same

wavelength range were distributed over a wider convergence angle. Several tens of kilohertz sweeping speed is sufficient to provide real time, B-scan images although higher frequencies are more desirable for reducing motion artefacts when performing full volume scans on *in-vivo* tissue samples.

Table 3.2. Polygon operating parameters. The maximum A-scan rate of the accompanying OCT system is approximately 66 kHz (setting 4) but the experimental work in this thesis mostly used the 12 kHz operating speed.

Setting	Polygon RPM	Polygon Frequency (Hz)	Facet Frequency (kHz)	Facet Period (μs)
1	10,000	166.67	12.00	83.33
2	20,000	333.33	24.00	41.67
3	40,000	666.67	48.00	20.83
4	54,945	915.75	65.93	15.17

The PM used throughout this entire body of research was a Lincoln Laser SA34 (Cambridge Technology), which had 72 gold coated facets and four operating speeds (Table 3.2). The maximum tuning speed (facet frequency) of this polygon is approximately 66 kHz (Setting 4), which is the maximum acquisition rate of a single A-scan in the accompanying OCT system (without applying additional techniques). However, the majority of experiments in this research use only the 12-kHz operating speed (Setting 1), since higher speeds have little-to-no effect on the operation of the other components in the filter (ignoring vibrations), which were the primary focus of investigation. Running the polygon at its slowest speed is also known to prolong its lifespan, as well as minimise the noise pollution in the laboratory and maximise healthy relationships with co-workers. The maximum tuning speed is also a consequence of the number of facets, since a higher facet count will result in a greater number of spectral sweeps for every full rotation of the polygon. However, opting for a polygon model with a higher number of facets will reduce the facet width (at a fixed radius) and this will restrict the diameter of the beams that can be successfully accommodated by the polygon facet without primary vignetting occurring (Section 2.7.1). Additional techniques can be employed to increase the functional speed of the filter which will be briefly discussed later in Section 4.3.2.

3.6.1 Polygon Parameters

The choice of PM has a significant impact on the performance of the SS. Its fundamental parameters influence the design of the filter by establishing one of the first steps in the design hierarchy of the component selection, which is necessary for maximising the swept bandwidth and the optical power output (see Section 4.9.1). These parameters are shown in the diagram of Figure 3.14.

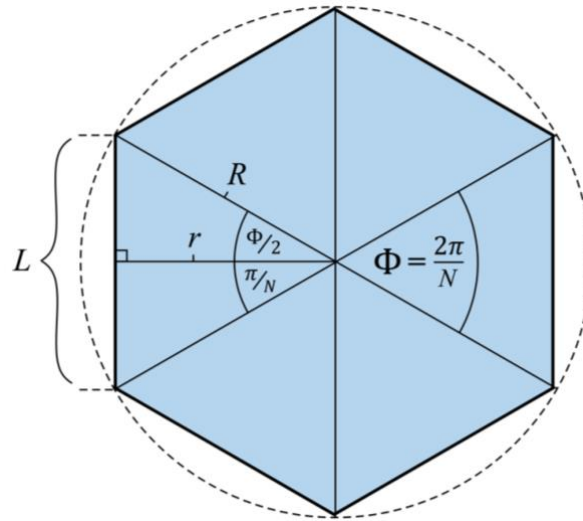


Figure 3.14. Polygon geometry for calculating the width of the facet, L , with respect to the polygon radius, R , and the number of facets, N . The facet-to-facet angle, Φ , is given by $2\pi/N$ and the apothem of the polygon, r , is also shown.

The polygon has a radius, R , apothem, r , and a physical facet width, L . The angle subtended by a single facet or ‘facet-to-facet’ angle, Φ , is inversely proportional to the number of facets, N .

$$\Phi = \frac{2\pi}{N} \quad \text{Eq. 3.11}$$

The physical facet width, L , is calculated geometrically and is a function of the number of facets and the radius (or apothem).

$$L = 2R \sin\left(\frac{\Phi}{2}\right) = 2r \tan\left(\frac{\Phi}{2}\right) \quad \text{Eq. 3.12}$$

The data sheet accompanying the PM in this research (Appendix B) states a radius $R = 31.75 \text{ mm}$, an operational facet width, $L = 2.77 \text{ mm}$ and a facet height of 4.80 mm . This introduces a restriction to the diameter of the beams that can be successfully accommodated by the polygon without overlapping onto an adjacent facet: $W_2 \leq 2.77 \text{ mm}$.

The restriction to the beam width can be improved either by increasing the radius of the polygon or by decreasing the number of facets. However, both of these options are undesirable for several reasons. Firstly, increasing the radius will introduce more mass to the polygon, which will raise its moment of inertia and require more energy to accelerate to, and maintain, the same operating speed. Secondly, if the number of facets is reduced, the maximum tuning frequency per rotation of the polygon will decrease and make the accompanying OCT system slower. A lower facet count will also force the polygon to make a larger departure away from the circular shape that is approached by having a high facet count. This produces more aerodynamic drag when the polygon rotates, which also requires more energy to overcome. However, this limitation can be rectified by placing the polygon inside an enclosed vacuum chamber with a transparent access window. A state of the art polygon scanner such as this would cost considerably more but could achieve up to 70,000 RPM as a result, producing swept spectra at a maximum frequency of ~84 kHz [17] before applying additional techniques to increase the speed further [9] (see Section 4.3.2).

3.7 Discussion

Section 3.3 concluded that wider beam collimators are preferable since their lower beam divergence will allow more rays to return to the optical fibre, producing higher coupling efficiency and increasing power output. They also allow the illumination of more lines/grooves on the diffraction grating, which improves the spectral resolution (Section 3.4.1) and therefore increases the maximum axial scanning range (Section 1.4.3). However, a larger beam diameter at the grating must be reduced accordingly by the telescope's magnification to fit within the dimensions of the polygon facets in order to limit the amount of primary vignetting (Section 2.7.1). If the primary vignetting is not minimised, the advantage gained from maintaining collimation (to improve the coupling efficiency) will most likely be lost.

Ideally, a high line/groove density diffraction grating should be illuminated by a wide beam diameter collimator to maximise the spectral resolution and minimise the instantaneous laser linewidths (Section 3.4.1). Additionally, multiple interactions with the grating (transmissions or reflections) can also be used to reduce the linewidths. Although only two interactions with the grating occur in this research project, it would be beneficial to explore alternative spectral filter designs that incorporate further

interactions, especially if only a small beam diameter collimator or a low line/groove density grating are available.

Using a polygon with a high facet count (72 or above) is beneficial since it helps increase the bandwidth sweeping frequency of the SS output. This improves the data acquisition rate and the quality of real-time images (Section 1.5), but also reduces the size of the facets (assuming a constant radius). Any such facet size reduction would then require either a smaller beam diameter collimator or a more powerful telescope magnification. However, a high facet count also reduces the facet-to-facet sweeping angle (acceptance angle, see Section 4.2). This forces the design to incorporate a narrow convergence angle, which is the opposite of that obtained by the telescope when attempting to decrease the size of the beams (Eq. 3.9 and Eq. 3.10, Section 3.5).

CHAPTER 4

THEORETICAL DEVELOPMENT

4.1 Chapter Introduction

The theoretical work in this chapter was developed through observations made in the simulations and during the experiments. The theoretical aspects address the properties of the components in the filter and how they impact specific parameters, which are crucial to the filter's performance. This work begins by examining the properties of the PM; the acceptance angle, duty cycle, eccentricity, visible facet width and simultaneous tuning, and then examines the width of the beam as it propagates through the filter. A formula is then derived to approximate the TSB that the system is capable of delivering, based on the light source and the properties of the components that are used. Finally, the knowledge acquired in the theoretical studies has been summarised in a hierarchy table. This table considers the complex relationships between the components and lists them in order of importance. The design hierarchy can then be used as a guide to find the most suitable combination of components for a particular OCT application.

4.2 Acceptance Angle

The choice of PM determines the acceptance angle of the spectral filter. This is the magnitude of the angular range through which a single polygon facet can be rotated before an adjacent facet becomes active. Initially, the acceptance angle, φ , is equivalent to the facet-to-facet angle, Φ (Eq. 3.11), since the polygon's centre of rotation is aligned with the optical axis. This configuration is termed 'on-axis' and the acceptance angle will be determined by the number of facets, N , on the polygon, i.e. $\varphi \equiv \Phi = \frac{2\pi}{N}$. The converging spectrum is distributed over a range of incidence angles throughout the convergence angle, ψ , but a single facet will only select those wavelengths which are contained within the range of the acceptance angle, and are capable of meeting the normal incidence condition on the facet as the PM rotates. This can be thought of as equivalent to matching the image space NA of the telescope with what is essentially the NA of a polygon facet. Light that converges onto the PM at an angle that is greater than this acceptance angle will not become part of the TSB. Therefore, the convergence angle should be less than or equal to the acceptance angle, which, for a 72 facet on-axis polygon, will be $\psi \leq \varphi = 0.0873 \text{ rad}$ or 5° .

The TSB will be physically limited to a narrower wavelength range than the source is capable of supplying whenever $\psi > \varphi$ (Figure 4.1 a). This also establishes the condition for simultaneous tuning, which is discussed later in Section 4.6.

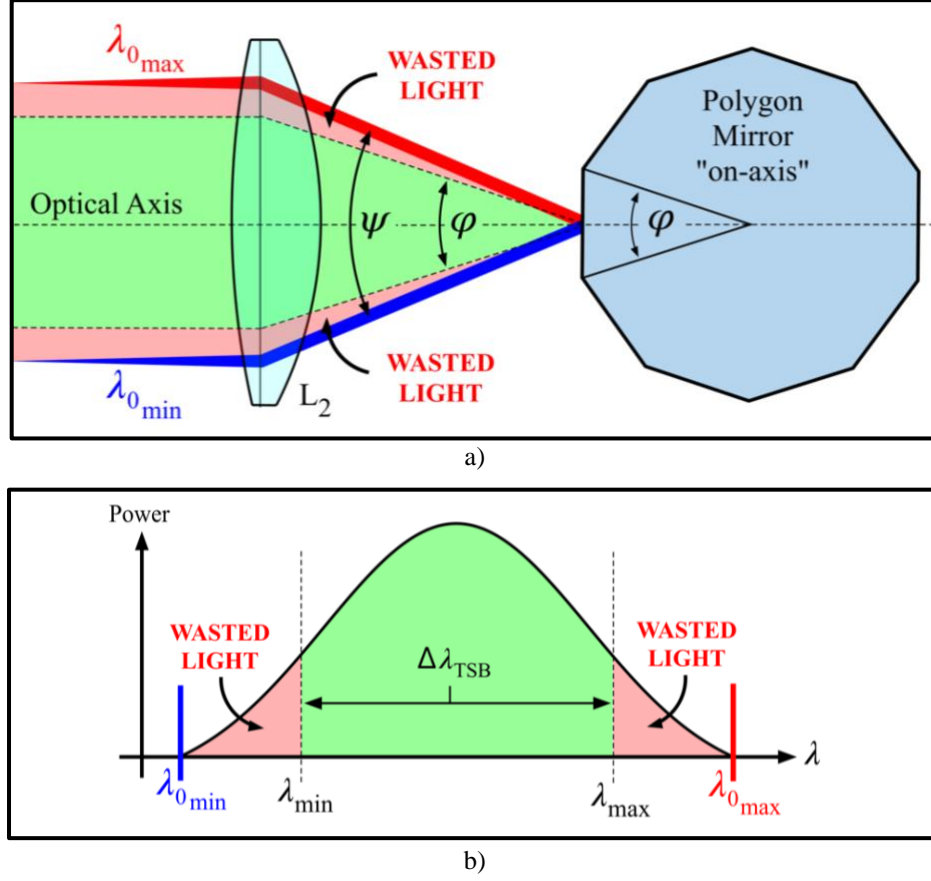


Figure 4.1. Wasted light at the margins of the input spectrum. **a)** Light is shown passing through the second lens, L_2 , and converging onto the on-axis PM, where $\varphi \equiv \Phi = \frac{2\pi}{N}$. Light is lost when the convergence angle, ψ , measured between the marginal rays, $\lambda_{0\min}$ and $\lambda_{0\max}$, is larger than the acceptance angle, φ , of the PM. **b)** The TSB, $\Delta\lambda_{\text{TSB}}$, of the spectral filter, measured between λ_{\min} and λ_{\max} , will be reduced whenever $\psi > \varphi$.

However, the acceptance angle can be made larger if the polygon is translated in a direction perpendicular to the optical axis of the telescope, thereby positioning its centre of rotation 'off-axis', and introducing an additional retroreflector mirror (RM) to act as the final surface in the sequence of components (Section 4.4). Increasing the acceptance angle allows for a larger convergence angle to be accommodated by the polygon, and a larger convergence angle will spread a fixed set of wavelengths over a wider angle, which is detrimental to the wavelength tuning speed. If the acceptance angle is increased and the convergence angle remains unchanged, the wavelength tuning speed will increase but also lower the duty cycle (see Section 4.3 below), since the facet must still rotate through the rest of the sweeping angle, φ , before initiating the next sweep on the subsequent facet.

A larger acceptance angle also means that the components can have a wider variety of parameters and still be suitable for use in the filter, e.g. the line/groove density of the diffraction grating and the focal lengths of the telescope can be experimented upon more freely without the concern of clipping the edges of the converging spectrum as a consequence of having a narrow acceptance angle.

4.3 Duty Cycle

The ratio between the convergence angle and the acceptance angle, ψ/φ , is proportional to the duty cycle of the PM-based spectral filter. If the two angles are equal ($\psi/\varphi = 1$) the duty cycle will be 100 % and the filter will produce continuous sweeps of the spectrum without any time-delay between them. This is one of greatest advantages of spectral sweeping with a PM (under these circumstances). If the convergence angle is larger than the acceptance angle ($\psi/\varphi > 1$) the duty cycle will be > 100 % and adjacent swept spectra will overlap one another, which causes simultaneous tuning (discussed later in Section 4.6). If the convergence angle is less than the acceptance angle ($\psi/\varphi < 1$), an interval of ‘dead time’ will appear between adjacent sweeps of the spectrum. This interval will increase as the convergence angle decreases, which will lower the duty cycle.

In general, a high duty cycle is preferable since it will improve the data acquisition rate whilst scanning the sample – maximising the number of A-scans for a given oscillation amplitude of the galvanometric scanning mirror (Section 1.5). Fortunately, both angles can be changed by varying the parameters of the components and a 100% duty cycle can be achieved under the right conditions, although this will usually involve sacrificing another property of the spectral filter.

4.3.1 Central Wavelength and the Optical Axis

Consideration is given in the following section to the optimal choice of wavelength propagating along the telescope’s optical axis. With an on-axis polygon (Figure 4.1), the acceptance angle (5°) is distributed equally onto either side of the telescope optical axis, in the image space of the second lens. This means that all wavelengths which are converging up to $\pm \frac{\varphi}{2}$ ($\pm 2.5^\circ$) from the optical axis will fulfil the acceptance angle condition and form part of the swept bandwidth, while those outside of this angle will be filtered out. However, as shown in Section 3.4.3, the spectrum is not distributed evenly on either side of the optical axis. Consider when the magnitude of the convergence angle

and the acceptance angle are equal, $\psi = \varphi$, and when the central wavelength is chosen to align with the telescope optical axis. This will force the longest wavelength to fall outside of the $+\frac{\varphi}{2}$ ($+2.5^\circ$) maximum converging angle whilst simultaneously preventing the shortest wavelength from reaching the equivalent angle on the opposite side of the optical axis (falling short of $-\frac{\varphi}{2}$ (-2.5°)). Although the two angles, ψ and φ , are equal, they will not overlap completely to fully occupy the same angular space, which causes the duty cycle to be less than 100 %. Therefore, perfectly capturing the full bandwidth and simultaneously maintaining the maximum duty cycle requires an alternative approach.

Rather than selecting the central wavelength, λ_c , to align with the telescope optical axis, a separate wavelength can be chosen that equally divides the magnitude of the divergence angle, $\Delta\delta$, instead of being assigned to the midpoint of the spectral bandwidth (Figure 3.8). Note that the convergence angle and the acceptance angle are still considered equal in magnitude ($\psi/\varphi = 1$). Using the values from Table 3.1 (Section 3.4.3) in Eq. 3.6 allows the mean diffraction angle to be calculated, $\delta_m = 51.37^\circ$. The grating equation (Eq. 3.2) can then be used to find the wavelength that corresponds to the angle halfway between the maximum and minimum divergence angles. This gives a mean wavelength value of 1337.38 nm , which is 7.38 nm larger than the central wavelength of the spectral bandwidth. Aligning this wavelength to the telescope optical axis allows the convergence angle to be distributed equally on either side of the optical axis and should therefore maximise the duty cycle of the spectral filter (if $\psi = \varphi$). Although, since the final alignment of the filter is typically completed when the operator is satisfied that the output has been maximised, it is possible that this central wavelength shift could be achieved without realising it during the alignment process.

4.3.2 Low Duty Cycles

In some circumstances, it can be desirable to deliberately create a low duty cycle. Wang-Yuhl Oh *et al.* intentionally reduced the duty cycle of their spectral filter in order to place multiple, delayed signals in between the primary sweeps of their output spectrum, which produced a SS capable of operating at $> 400 \text{ kHz}$ [9]. They achieved this using an off-axis polygon with multiple end reflectors to maximise the acceptance angle whilst simultaneously selecting specific component properties (grating and telescope) to deliberately reduce the convergence angle. This action caused their total spectral range to

be distributed over a narrow convergence angle, which dramatically increased the wavelength tuning speed. The delayed signals were also carefully timed to fit within the primary sweeps in order to maximise the final duty cycle. The standard duty cycle of their spectral filter was reduced to just 6.2 % but the output leading into the OCT system was increased to 99.2 % after collecting and stacking together the delayed swept spectra from the SS. Although this technique was briefly studied during this research, it will not be discussed in further detail in this thesis since maximising the wavelength tuning speed was not necessarily the objective for every configuration and/or experiment. However, a high duty cycle is still an important feature of the PM-based spectral filter and must be considered during the design process and maximised whenever possible.

4.4 Polygon Eccentricity

The acceptance angle, φ , can be doubled by translating the PM off-axis (i.e. in a direction perpendicular to the telescope optical axis) and installing a planar mirror to act as a retroreflector (RM). As the polygon sweeps through the spectrum, each wavelength meets the normal incidence condition on the RM, instead of the TF, before returning back through the filter to the optical fibre. The polygon is stated as having gained positive or negative eccentricity when its centre of rotation is translated onto either side of the telescope optical axis. Figure 4.2 shows the two possible translations of the off-axis PM; (a) below-axis (negative) and (b) above-axis (positive). These two positions constitute the PM's orientation, which shall be discussed in more detail and compared experimentally in Section 5.7.

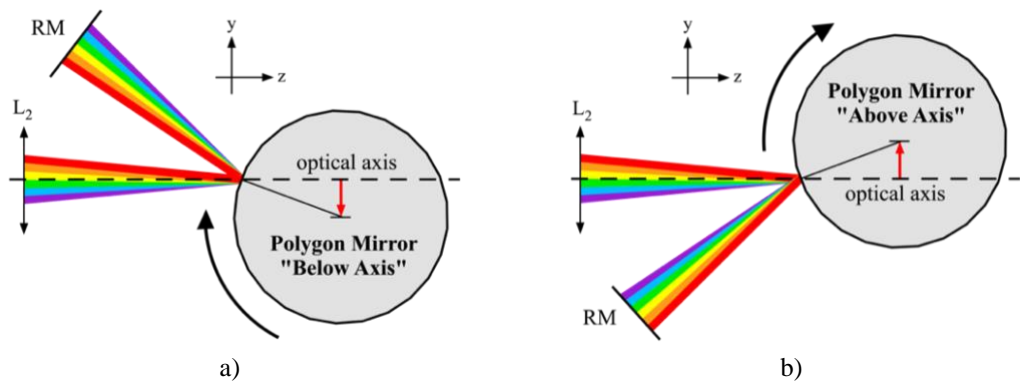


Figure 4.2. Orientation of an off-axis PM (red arrow), using a retroreflector mirror, RM, acting as the final surface in the sequence of components. Only the second lens, L_2 , in the telescope is shown. The two polygon orientations are **a)** 'above-axis' and **b)** 'below-axis' with respect to the optical axis. The polygon rotation direction is clockwise as seen from above, which filters the spectrum from short-to-long wavelengths in both orientations.

The addition of polygon eccentricity doubles the acceptance angle with respect to the value prescribed by the polygon in the on-axis position. This occurs for any amount of eccentricity, above or below the telescope optical axis. The new acceptance angle for the off-axis polygon in this research increases to 0.175 rad or 10° , which is also consequently twice the facet-to-facet angle, $2\Phi = \frac{\pi}{N}$ (see Figure 3.14). Note, the sweeping direction of the polygon does not change when the polygon's orientation is inverted.

The geometry for a below-axis polygon can be seen illustrated in Figure 4.3 below. The eccentricity, E , is measured laterally from the optical axis to the centre of the polygon, which is considered off-axis whenever $E > 0$. When this happens, the TF is no longer perpendicular to the optical axis and the central wavelength, λ_c , no longer strikes the TF at normal incidence. The TF is shown after having rotated clockwise, about the PM's axis of rotation, through the angle θ_E , introduced by adding the eccentricity, and is measured from the horizontal to the apothem, r , of the TF. The addition of eccentricity requires an angle of $2\theta_E$ between the optical axis and the RM's surface normal in order to reflect λ_c at normal incidence. This angle is called the retro-angle, Ω . It is a function of PM eccentricity and will become important later in Section 4.6.1.

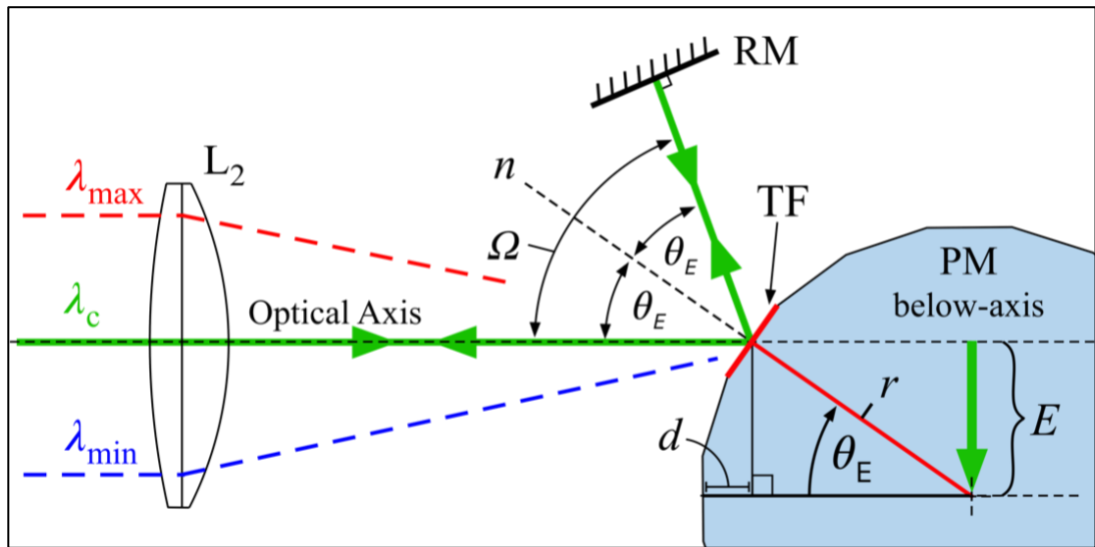


Figure 4.3. Off-axis polygon geometry. L_2 is the second lens in the telescope, r is the apothem of the polygon mirror, PM, and d is the amount that the PM must be shifted forwards to meet the focal plane of the second lens. Eccentricity, E , is introduced by radially translating the centre of the PM, away from the optical axis (green arrow). The central wavelength, λ_c , now strikes the TF with an incidence angle equal to the polygon rotation angle, θ_E . The retroreflector mirror, RM, is positioned at an angle $2\theta_E$ from the optical axis in order to intercept λ_c at normal incidence. This angle is called the retro-angle, Ω , and is a function of E . With this configuration, the acceptance angle of the polygon will double due to the inclusion of the incidence and reflection angles on the TF.

The eccentricity, E , is given by the polygon rotation angle, θ_E , and the apothem, r , of a single facet using

$$E = r \sin \theta_E \quad \text{Eq. 4.1}$$

where the apothem, r , is (introduced in Section 3.6.1)

$$r = R \cos \left(\frac{\Phi}{2} \right) \quad \text{Eq. 4.2}$$

Combining these two equations and inserting the facet-to-facet angle, Φ (Eq. 3.11), yields the eccentricity as a function of the PM parameters and its rotation angle.

$$E = R \cos \left(\frac{\pi}{N} \right) \sin \theta_E \quad \text{Eq. 4.3}$$

Equation 4.3 can then be used to find the retro-angle as a function of the PM parameters and its eccentricity value.

$$\Omega = 2 \sin^{-1} \left[\frac{E}{R} \sec \left(\frac{\pi}{N} \right) \right] \quad \text{Eq. 4.4}$$

The PM will also require an axial shift towards the telescope by an amount $d = r - \sqrt{r^2 - E^2}$ to ensure that the TF remains at the focal plane of the second lens. This shift can also be expressed in terms of polygon radius, R , and the number of facets, N .

$$d = R \cos \left(\frac{\pi}{N} \right) - \sqrt{\left(R \cos \left(\frac{\pi}{N} \right) \right)^2 - E^2} \quad \text{Eq. 4.5}$$

4.5 Visible Facet Width

There are several consequences of introducing eccentricity to the polygon. The first is due to the apparent change in size of the effective TF width with respect to the incident beams. In the ideal case, the TF would always accommodate and reflect all of the light in the converging spectrum but when the polygon is positioned ‘off-axis’ the TF size reduces from the perspective of the incident light. If the beam width and the physical facet size are initially equal, any reduction to the facets apparent size will cause primary vignetting to occur and reduce the total power output of the filter (Section 2.7.1).

An intuitive solution to this problem is to reduce the beam width until primary vignetting has been avoided. However, this is governed by the amount of eccentricity, since the more the polygon is laterally translated away from the optical axis, the smaller the facet will appear to be. The minimum value of eccentricity depends upon several features of the setup that will be explored in the following sections, but the visible facet width can be examined through the geometry of the system with respect to the incident central wavelength beam, as it propagates along the telescope optical axis (Figure 4.4).

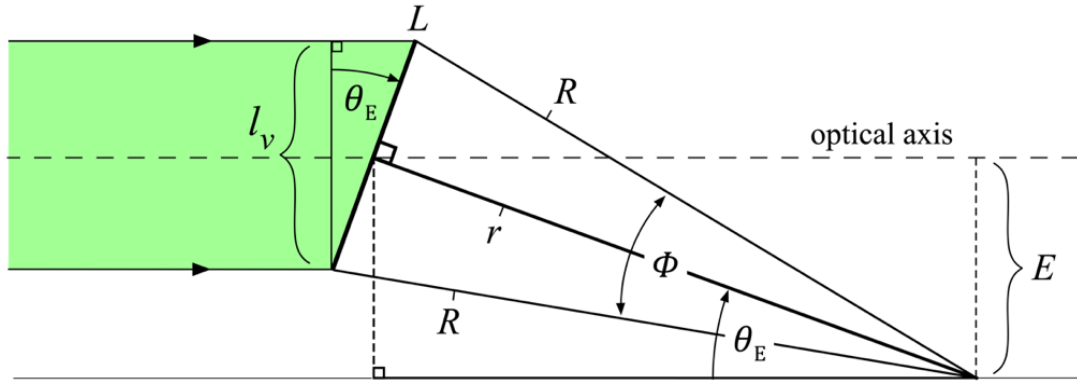


Figure 4.4. The visible facet width, l_v , decreases with increasing eccentricity, E , until $E = r$, the polygon apothem, whereupon the visible facet width will have reduced to zero. L is the physical facet width, R is the radius of the polygon, Φ is the facet-to-facet angle and θ is the angle of the facet with respect to the incoming beam of the central wavelength, which is also the rotational displacement of the polygon measured from the optical axis.

In the first approximation, the TF can be assumed to pivot about its own centre rather than the centre of the PM. In reality, as the polygon rotates, the TF sweeps across the beams rather than rotating underneath them, which is a more complicated process (Section 4.5.1). By making this assumption, an expression for the visible facet width is obtained with respect to polygon eccentricity.

When eccentricity is introduced, the light travelling along the optical axis will observe an effective, or visible facet width, l_v , given by the product of the physical facet width, L , and the cosine of the rotational displacement of the TF from the horizontal.

$$l_v = L \cos \theta_E \quad \text{Eq. 4.6}$$

The physical facet width is given by Eq. 3.12, which introduces the polygon's radius and the number of facets, since $\Phi = \frac{2\pi}{N}$ (Eq. 3.11). The polygon rotation angle of the TF, θ_E , measured clockwise from the optical axis, is related to the eccentricity, E , and the apothem, r , using the rearranged version of Eq. 4.1, $\theta_E = \sin^{-1}\left(\frac{E}{r}\right)$. Eq. 4.2 can then be

used to relate the apothem to the radius, R . Connecting all of the above relationships together gives the first approximation of the visible facet width from the perspective of the central wavelength beam travelling along the optical axis. This formula is independent from the other components in the filter and is a function of the ratio between the polygon's eccentricity and radius, $\frac{E}{R}$.

$$l_{\lambda_c} \left(\frac{E}{R} \right) = 2R \sin \left(\frac{\pi}{N} \right) \cos \theta_E = 2R \sin \left(\frac{\pi}{N} \right) \cos \left(\sin^{-1} \left[\frac{E}{R} \frac{1}{\cos \left(\frac{\pi}{N} \right)} \right] \right) \quad \text{Eq. 4.7}$$

However, the visible facet width is different for each wavelength in the spectrum since each beam converges onto the polygon with a different angle of incidence. The smallest visible facet width will be seen by the beam striking the facet with the largest incidence angle. This is visually apparent from the diagrams in Figure 4.5, which gives an exaggerated illustration of the TF in the three orientations suitable for successfully reflecting each of the three most significant wavelengths; a) λ_{min} , b) λ_c and c) λ_{max} . The incidence angle, i , can be seen slowly decreasing through a) to c) and indicates that in this particular component arrangement, with the PM below-axis, the shortest wavelength, a) λ_{min} (blue ray), will observe the smallest visible facet width. It is therefore more useful to establish the visible facet width for the marginal wavelength that experiences the greatest decrease in facet size.

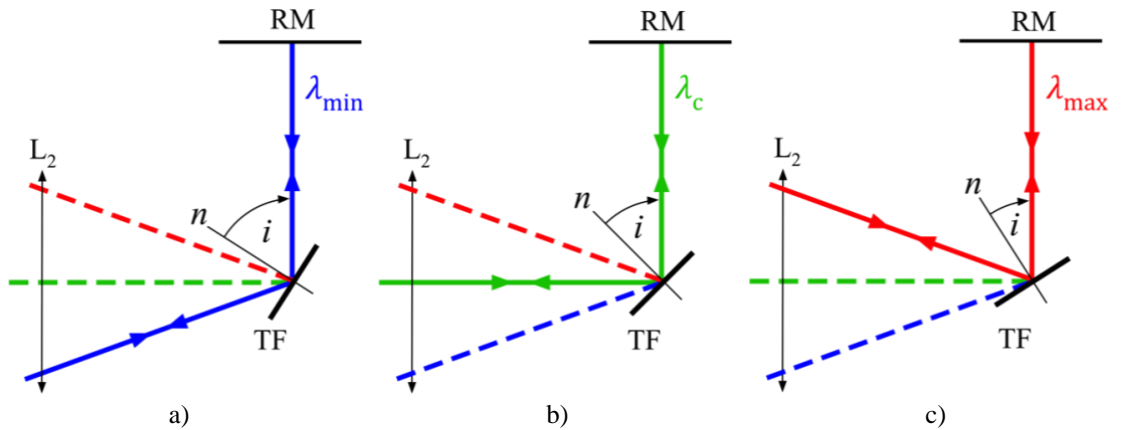


Figure 4.5. Examples of converging light rays from the second lens, L_2 , at three incidence angles on the TF for a below-axis PM, rotating clockwise. a) the smallest visible facet width occurring for the shortest wavelength, λ_{min} , in the spectrum. Image b) and c) show decreasing incidence angles, i , and therefore increasing visible facet widths, for the central, λ_c , and longest, λ_{max} , wavelengths respectively. RM is the retrorreflector mirror and n is the surface normal to the facet.

Eq. 4.7 must be modified to accommodate the incidence angles of the marginal wavelengths, which, in this first approximation, is trivial since the rays will always be restricted by the acceptance angle of the polygon, $\frac{\varphi}{2}$, given by $\pm \frac{2\pi}{N}$ ($\pm 5^\circ$) from the optical axis. This extra amount must be added to the rotational displacement of the TF in order to establish the magnitude of the visible facet for the two marginal wavelengths: $+\frac{2\pi}{N}$ for the longest wavelength and $-\frac{2\pi}{N}$ for the shortest wavelength.

$$l_v = 2R \sin\left(\frac{\pi}{N}\right) \cos\left(\theta_E \pm \frac{2\pi}{N}\right) = 2R \sin\left(\frac{\pi}{N}\right) \cos\left(\sin^{-1}\left[\frac{E}{R} \frac{1}{\cos(\frac{\pi}{N})}\right] \pm \frac{2\pi}{N}\right) \quad \text{Eq. 4.8}$$

The graph in Figure 4.6 shows the plot of Eq. 4.8 using the values for the polygon used in this research ($N = 72$, $R = 31.75 \text{ mm}$). Curves have been plotted for the angle that corresponds to each of the three rays; λ_{max} (red, $-\frac{2\pi}{N}$ or -5°), λ_c (green) and λ_{min} (blue, $+\frac{2\pi}{N}$ or $+5^\circ$).

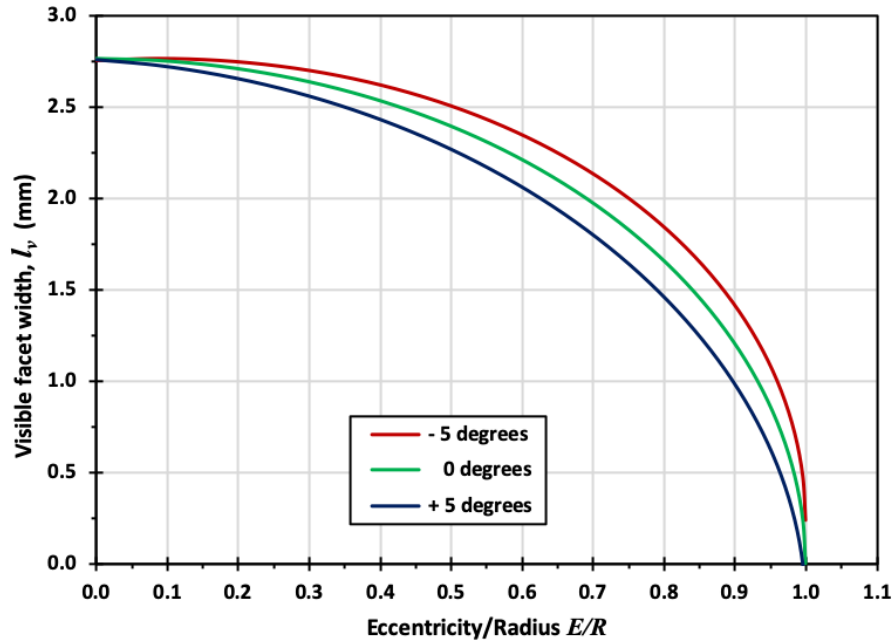


Figure 4.6. Visible facet width, l_v , with respect to the ratio of the eccentricity and polygon radius given by Eq. 4.8. In this example, the polygon is positioned 'below-axis' making the longest wavelength correspond to -5° (red), the central wavelength at 0° (green) and the shortest wavelength at $+5^\circ$ (blue). The curves drop to zero when the eccentricity is equal to the apothem of the polygon. High values of eccentricity should be avoided to maximise the visible facet width and reduce unnecessary vignetting.

The visible facet width decreases with increasing eccentricity for all three wavelengths, as anticipated by the geometry of the arrangement, until the eccentricity is equal to the apothem of the polygon ($E = r$), at which point the TF can no longer be seen by any of

the beams. In this particular example, with the PM's centre of rotation positioned below the optical axis, the shortest wavelength, λ_{min} (blue), experiences the smallest visible facet width. The results confirm the predictions and encourage small eccentricity values to be used in order to maximise the visible facet width and minimise primary vignetting. The facet's rotation is approximated here to that of a scanning galvanometer mirror pivoting around an axis on its own surface. Further analysis is carried out in Section 4.5.1 to establish if this approximation can be applied to a facet executing a rotation around the centre of the PM.

4.5.1 Sweeping Facet Width

The radial displacement of the facets from their axis of rotation produces a sweeping motion across the converging beams, rather than pivoting underneath them like a mirror on a galvanometer scanner. Since the beams in the converging spectrum are all brought to a single, near circular spot incident on the PM, and assuming that the size of this spot and the facet width are approximately the same, the TF will cut across the beams as it moves to select each of the wavelengths in the converging spectrum. This is precisely one of the reasons for primary vignetting and is a complicated process that needs to be understood clearly if it is going to be remedied or removed.

The motion of the sweeping facet can be described by a small change in the polygon's rotational angular displacement, $\delta\theta$, which is measured from zero when the centre of the facet meets the telescope optical axis. The sign of $\delta\theta$ is either positive or negative depending on whether the facet is sweeping above or below the optical axis respectively. The sweeping angle of the PM is determined by the facet-to-facet angle, Φ , which in turn is given by the number of facets, N (Eq. 3.11). Therefore, the PM rotates through an angle with the boundary condition $-\frac{\pi}{N} \leq \delta\theta \leq +\frac{\pi}{N}$, which, in this research, is equivalent to $-2.5^\circ \leq \delta\theta \leq +2.5^\circ$ because $N = 72$ facets. Once the PM has rotated outside of these boundary angles, the TF ceases to be active and an adjacent facet will begin sweeping through the spectrum. Note that the off-axis PM already has some arbitrary fixed value of eccentricity, E , and therefore an associated PM rotation angle value ($\theta_E \neq 0$), providing the reference location of the facet when sweeping the central wavelength at $\delta\theta = 0$.

107

Two formulas must be constructed to describe the sweeping facet width; one for when the facet sweeps the wavelengths above the telescope optical axis, l_{2+} (when $\delta\theta$ is positive), and one for below, l_{2-} (when $\delta\theta$ is negative). They are both necessary for deriving the sweeping facet width since the distance between the telescope optical axis and the central point of the sweeping facet, P , forms the opposite side in a right triangle, given by $r \sin(\theta_E + \delta\theta)$, which is equal to $E + e$ or $E - e$ depending on if the facet is sweeping above or below the telescope optical axis respectively. The sweeping facet width, in either case, is given by

$$l_{2\pm} = l_1 + h \quad \text{Eq. 4.9}$$

Where l_1 is half the initial visible facet width identified earlier ($l_v = 2l_1$), given by $\frac{L}{2} \cos \theta_E$, and $h = H - e$, which are all variables in the diagram and are used exclusively for the derivation.

Introducing these substitutions produces the following expression.

$$l_{2\pm} = \frac{L}{2} \cos \theta_E + H - e \quad \text{Eq. 4.10}$$

Substituting for H and e depends upon whether the facet is sweeping above or below the telescope optical axis. When the facet sweeps above the telescope optical axis (Figure 4.7 a), the substitutions are

$$H = \frac{L}{2} \cos(\theta_E + \delta\theta) \quad \text{Eq. 4.11}$$

and

$$e = r \sin(\theta_E + \delta\theta) - E \quad \text{Eq. 4.12}$$

When the facet sweeps below the telescope optical axis (Figure 4.7 b), the substitutions are

$$H = \frac{L}{2} \cos(\theta_E - \delta\theta) \quad \text{Eq. 4.13}$$

and

$$e = E - r \sin(\theta_E - \delta\theta) \quad \text{Eq. 4.14}$$

However, Eq. 4.13 is equivalent to Eq. 4.11 since the value of $\delta\theta$ is either positive or negative depending on the sweeping direction and therefore the subtraction sign can be replaced by an addition sign. Selecting the second pair of expressions (Eq. 4.13 and Eq. 4.14) for below-axis sweeping gives

$$l_{2-} = \frac{L}{2}(\cos \theta_E + \cos(\theta_E + \delta\theta)) + (r \sin(\theta_E + \delta\theta) - E) \quad \text{Eq. 4.15}$$

whereby the subtraction signs inside the cosine and sine functions have been replaced by addition signs for the same reason outlined above. Further substitutions can be made for L , E and r using equations Eq. 3.12, Eq. 4.1 and Eq. 4.2 respectively as well as several trigonometric identities listed in Table 4.1, which significantly contribute toward simplifying the two formulae.

Table 4.1. Trigonometric identities used in the derivation of the sweeping facet width.

Identity	Used for...
$\cos A + \cos(A + B) = 2 \cos\left(\frac{B}{2}\right) \cos\left(A + \frac{B}{2}\right)$	l_{2+} and l_{2-}
$\sin A - \sin(A + B) = -2 \sin\left(\frac{B}{2}\right) \cos\left(A + \frac{B}{2}\right)$	l_{2+}
$\sin(A + B) - \sin A = 2 \sin\left(\frac{B}{2}\right) \cos\left(A + \frac{B}{2}\right)$	l_{2-}
$\sin A \cos B - \cos A \sin B = \sin(A - B)$	l_{2+}
$\sin A \cos B + \cos A \sin B = \sin(A + B)$	l_{2-}

The final expressions for the sweeping facet width, in both sweeping directions, above and below the telescope optical axis, are given by the two formulae in Eq. 4.16 respectively.

$$\begin{aligned}
 l_{2+} &= 2R \cos\left(\theta_E + \frac{\delta\theta}{2}\right) \sin\left(\frac{\pi}{N} - \frac{\delta\theta}{2}\right) \\
 &\text{or} \\
 l_{2-} &= 2R \cos\left(\theta_E + \frac{\delta\theta}{2}\right) \sin\left(\frac{\pi}{N} + \frac{\delta\theta}{2}\right)
 \end{aligned} \quad \text{Eq. 4.16}$$

The final forms of these two equations are essentially the same as the first approximation to the visible facet width derived previously in Section 4.5 (Eq. 4.8). The only difference is the additional variable giving the change in polygon rotation angle inside the two trigonometric functions, $\frac{\delta\theta}{2}$. An additional term also exists inside the sine function of Eq.

4.8 ($\pm \frac{2\pi}{N}$) but it was deliberately added afterwards to establish the visible facet width for the marginal wavelengths at the edges of the spectrum. In this case, however, the additional incidence angles of the marginal wavelengths have not yet been considered and the two new formulae apply to the beam of the central wavelength only. Since the small change in polygon rotation angle is zero when sweeping this wavelength, the two formulae in Eq. 4.16 become equivalent to Eq. 4.8 and does not change unless the other wavelengths and their facet rotation angles are considered, which is the subject of Section 4.5.2.

4.5.2 Final Visible Sweeping Facet Width

The two formulae in Eq. 4.16 provide the sweeping facet width from the perspective of the incident beam propagating along the telescope optical axis (central wavelength). However, a correction must be made, similar to that used on Eq. 4.7, to accommodate the range of incidence angles for each of the other wavelengths. This time the sweeping facet width is multiplied by the correction factor, instead of being added, and results in the combined sum of two angles. Figure 4.8 demonstrates the extra angle ($\delta\theta$) belonging to one of the longer wavelengths in the spectrum (red ray). The multiple of 2 seen factored into the new incidence angle takes into account the doubled acceptance angle gained from translating the PM off-axis.

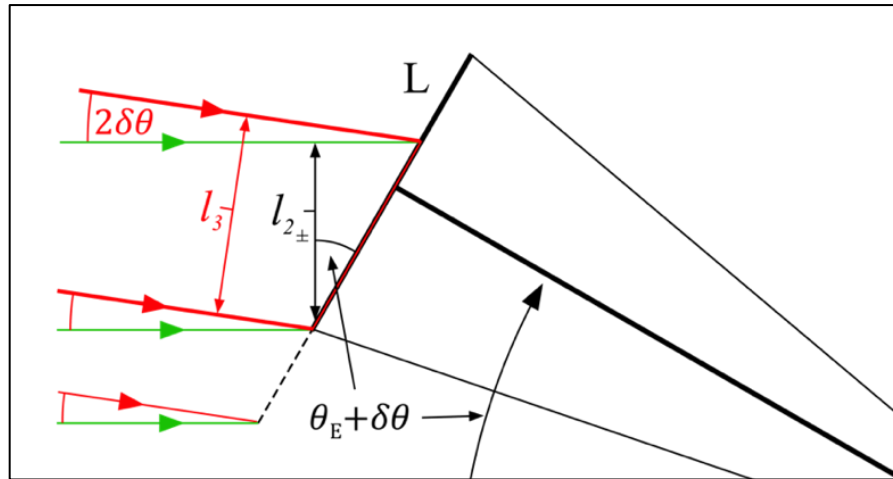


Figure 4.8. The final visible facet width, l_3 , adjusted to consider all aspects of the sweeping facet and the incident beams from each wavelength. The polygon has an initial rotational displacement, θ_E , providing eccentricity. The central wavelength is aligned and experiences a visible facet width, $l_{2\pm}$. A small change, $\delta\theta$, is added to the displacement to sweep through the wavelengths above and below the optical axis. The incident wavelengths approach the facet at twice the small angular change since the polygon is off-axis ($2\delta\theta$).

The final visible sweeping facet width is given by Eq. 4.17. This expression does not need to account for the sweeping position or the sign of its angle since the derivation relies upon the shared hypotenuse of the visible facet and the fact that the cosine function is even.

$$l_3 = l_{2\pm} \frac{\cos(2\delta\theta)}{\cos(\theta_E + \delta\theta)} \quad \text{Eq. 4.17}$$

This final expression delivers the visible facet width for all incident wavelengths, converging from above or below the telescope optical axis and has been used to plot the graph in Figure 4.9. Three different polygon rotation angles are shown; $\theta_E = 5.0^\circ$ (red line), $\theta_E = 22.5^\circ$ (green line) and $\theta_E = 45.0^\circ$ (blue line), corresponding to eccentricities $E = 2.76 \text{ mm}$, 12.14 mm and 22.43 mm respectively (for the central position of the polygon aligned to reflect the central wavelength only).

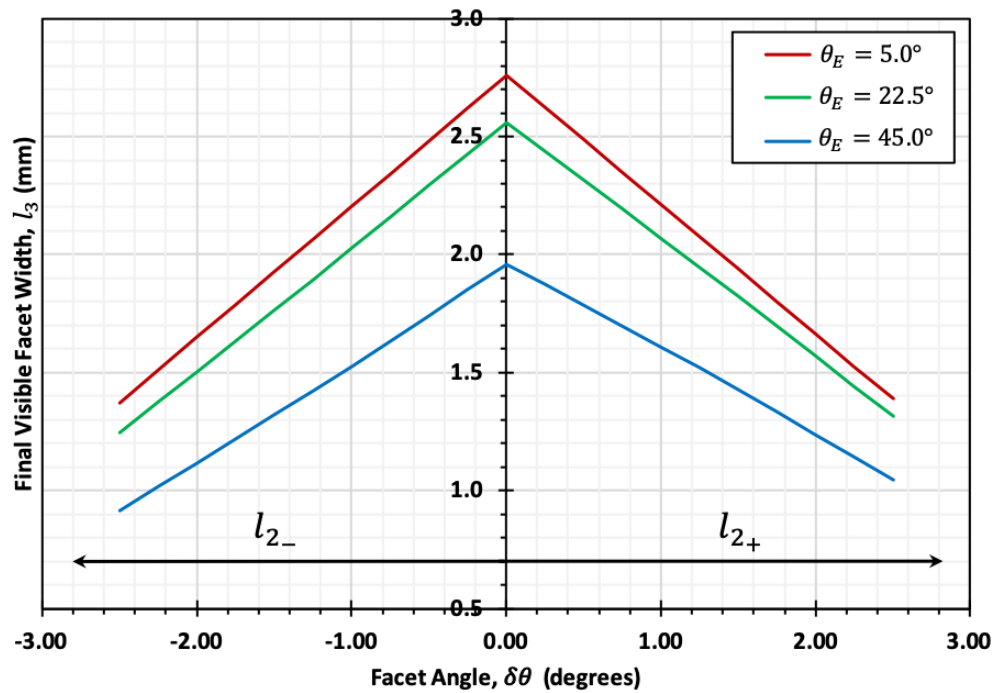


Figure 4.9. The final visible facet width, l_3 , for three initial polygon rotation angles, $\theta_E = 5.0^\circ$, 22.5° and 45.0° (Eq. 4.17). The x-axis depicts the angle of the sweeping TF, $\delta\theta$, above (+ve) and below (–ve) the optical axis (see Section 4.5.1, Figure 4.7). Smaller eccentricities (e.g. 5.0°) produce larger visible facet widths, which decrease in size more rapidly with larger eccentricity values (e.g. 45.0°). There is also a slight bias in favour of producing a wider visible facet width when positive sweeping takes place.

A careful examination of the results in Figure 4.9 shows an asymmetric distribution of the values on either side of the optical axis, indicating that positive sweeping of the facet ($+\delta\theta$), above the optical axis, results in a fractionally larger visible facet width than the

equivalent (mirror) negative sweeping angles, below the optical axis. The formula for the final visible sweeping facet width, l_3 , is in agreement with the first approximation (Eq. 4.8), which suggested that, with the PM orientated below-axis, shorter wavelengths were exposed to a smaller visible facet width and would therefore experience a greater loss from primary vignetting.

A more significant result comes from observing the difference in the visible facet width with respect to the three polygon rotation angles. The change in eccentricity between $\theta_E = 5^\circ$ (red line) and $\theta_E = 22.5^\circ$ (green line) is 9.38 mm , which produced a maximum decrease in the visible facet width of 0.2 mm (when $\delta\theta = 0.00^\circ$), whereas the change in eccentricity between $\theta_E = 22.5^\circ$ (green line) and $\theta_E = 45.0^\circ$ (blue line) is 10.29 mm ($< 1 \text{ mm}$ larger) but produced a maximum decrease in the visible facet width of 0.6 mm (again when $\delta\theta = 0.00^\circ$). The rate of decrease in visible facet width, with respect to eccentricity, is less significant at smaller eccentricity values than larger ones, demonstrated by the 3 times greater loss experienced when changing the eccentricity by approximately the same amount ($< 10 \%$ difference).

This analysis highlights the need to lower the eccentricity as much as possible to achieve the largest visible facet width and reduce the effects of primary vignetting, since small changes to low value eccentricities will have less impact when compared to small changes when using large eccentricity values. However, careful attention must be paid to the orientation of the PM since the wavelength that experiences the largest visible facet width will depend upon whether the polygon is positioned ‘above’ or ‘below’ the telescope optical axis. Identifying the correct orientation of the polygon with respect to the distribution of the spectrum will be important later when considering the impact of eccentricity on the width of the individual beams (Section 4.8) and when studying the polygon orientation in Section 5.7. Firstly though, there are some additional consequences, discussed in Section 4.6, that place a fundamental limit on the minimum value of eccentricity that can be used.

4.6 Simultaneous Tuning

Simultaneous tuning describes the selection of more than one spectral component during the tuning process. It was first mentioned in the literature by S.H. Yun *et al* who observed that two spectral components were returned by their system after translating their stationary PM along the optical axis, towards the telescope [67]. Without discussing this

phenomena in any more detail, the authors used this observation to estimate the experimental free spectral range of their system, equivalent to the total swept bandwidth (TSB) used in this thesis, defined in Section 1.6.2.

Under certain conditions it is possible for two discrete laser linewidths to be returned to the optical fibre at the same instantaneous moment during a single sweep of the spectrum. When this happens, the combined sum of the two signals will be interpreted by the photodetector as a single scanning event with a single time stamp rather than two independent events containing depth information from two separate axial locations in the sample. This creates a false reading that will manifest itself as noise in the OCT images. Simultaneous tuning is also responsible for decreasing the TSB from an otherwise wider spectral range (Figure 4.10), which therefore lowers the resolution of the OCT images (Section 1.5.2). Every effort should be made to avoid simultaneous tuning to maximise the axial resolution and improve image quality.

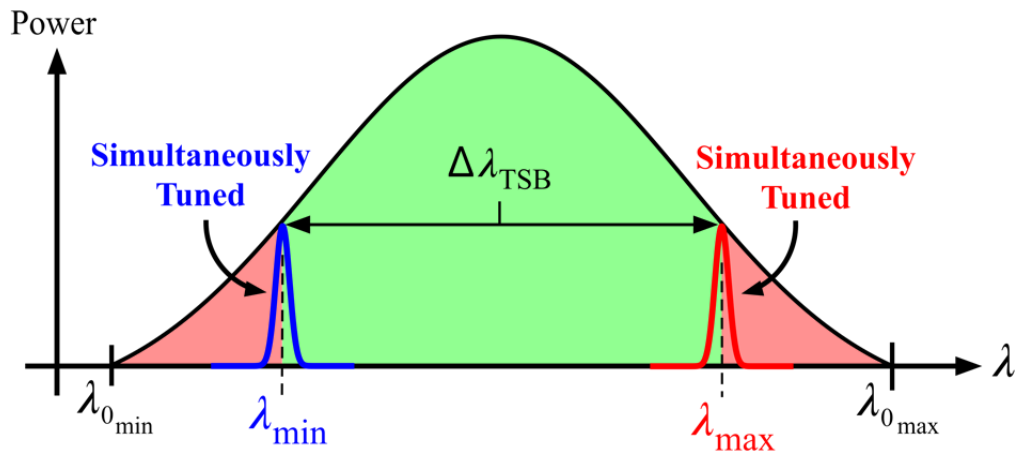


Figure 4.10. Bandwidth reduction due to simultaneous tuning. The total spectral range of the light source, between $\lambda_{0\min}$ and $\lambda_{0\max}$, is reduced to the TSB, $\Delta\lambda_{TSB}$, whenever $\psi > \phi$ (see Section 0). The two marginal wavelengths, λ_{\min} and λ_{\max} , are simultaneously tuned by reflecting off two adjacent facets on an on-axis PM respectively. Another form of simultaneous tuning can also occur when the PM is off-axis, which affects the central region of the TSB as well as the marginal swept wavelengths (discussed shortly in Section 4.6.1).

There are several ways that simultaneous tuning can occur within the spectral filter but the basic principle is that two narrow spectral regions retroreflect off one or more surfaces that simultaneously satisfy the normal incidence condition for two different wavelengths. This can happen on two adjacent facets, using an on-axis or an off-axis PM configuration, or by extension on the RM, using the off-axis configuration only, whereby one of the wavelengths retro-reflects directly off the TF (to follow in Section 4.6.1). This double,

normal incidence condition was explored in the simulations using an on-axis PM to gain a better understanding of the phenomenon.

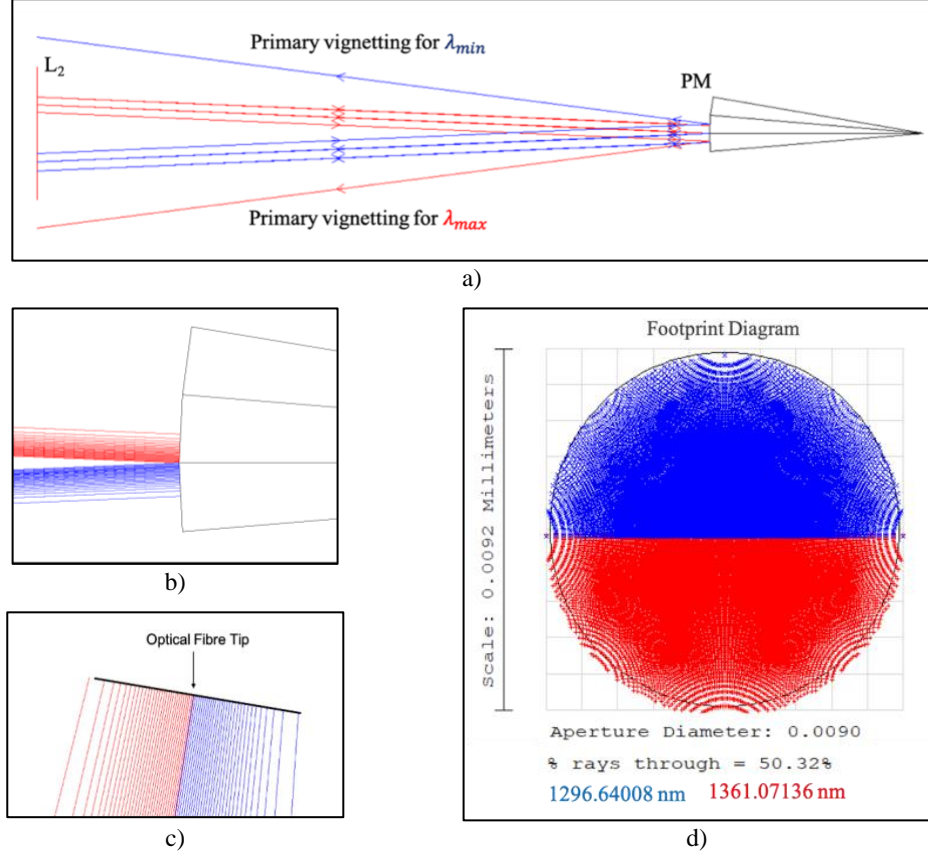


Figure 4.11. **a)** 3D layout view from the simulation demonstrating simultaneous tuning for an on-axis polygon mirror, PM, using paraxial surfaces for lenses. Two beams emerge from the second lens, L_2 , and interact with the PM, which has been rotated by half the facet-to-facet angle ($\delta\theta = +2.5^\circ$). **b)** A close-up view of the three-facet segment of the PM shows the beams interacting with two adjacent facets (the vignetted light is not shown). **c)** shows a side view of the light returning to the optical fibre tip and **d)** shows the aperture of the optical fibre illuminated by the rays from both beams. The two wavelength values selected were $\lambda_{max} = 1361.1 \text{ nm}$ (red) and $\lambda_{min} = 1296.6 \text{ nm}$ (blue), producing a TSB $\Delta\lambda_{TSB} = 64.5 \text{ nm}$.

Figure 4.11 a) shows the simulated, 3D layout of an ideal spectral filter using fletched rays (arrows) and paraxial surfaces for the telescope lenses ($75 \times 100 \text{ mm}$). A transmission grating with a 1145 l/mm line/groove density was also used. Only the second paraxial lens, L_2 , and a three-segment section of an on-axis PM are shown. Two beams (red and blue) can be seen emerging through L_2 and converging to meet the polygon. The three-segment portion of the PM (Figure 4.11 b) has been rotated by an amount $\delta\theta = +2.5^\circ$ to set up the instantaneous moment between two adjacent sweeps of the spectrum. The two converging beams occupy approximately the same location when they arrive at the PM. In this way, both beams illuminate two adjacent facets

simultaneously (and the border between them) and reflect the light at normal (shown) and non-normal incidence (not shown). The light reflecting at non-normal incidence is lost due to primary vignetting, represented by the two single rays (red and blue) terminating in the plane of L_2 in Figure 4.11 a). The remaining light that reflects at normal incidence returns to the optical fibre tip (Figure 4.11 c), where the rays in each wavelength can be seen filling approximately half of the aperture each (Figure 4.11 d).

When the PM is positioned on-axis, the acceptance angle, φ , will be equal to the facet-to-facet angle, Φ (Eq. 3.11). This will be the same as the angle between the two simultaneously tuned wavelengths (assuming $\psi > \varphi$) since the PM must rotate through this angle in order to end one sweep of the spectrum and initiate the start of the next. The geometric boundary condition for simultaneous tuning, either on or off-axis, is $\psi < \varphi$, i.e. the angular displacement of the converging spectrum must be less than the sweeping range of the PM⁷, otherwise simultaneous tuning will occur (see Figure 4.1). All wavelengths within the converging spectrum that are outside of the acceptance angle will be subject to simultaneous tuning and contribute towards worsening the OCT images.

The minimum and maximum wavelengths accommodated by the acceptance angle establish the boundaries of the TSB. In the simulation, the TSB was found by manually adjusting the wavelength values until the chief ray from each beam successfully returned to the centre of the optical fibre tip. Using the same setup described above, the values found were 1361.1 nm (red rays) and 1296.6 nm (blue rays) for the longest and shortest wavelengths respectively⁸. This produced a TSB of 64.5 nm, which is less than half of the available bandwidth produced by the light source (40.3 % of 160 nm). Therefore, any spectrum wider than 64.5 nm used in this particular, on-axis PM setup will experience simultaneous tuning.

4.6.1 Secondary Simultaneous Tuning

The description of simultaneous tuning, presented above, also applies to an off-axis PM, although in this case the acceptance angle, φ , will have doubled from adding the

⁷ Although it can be closely approached.

⁸ The wavelength values stated here are only an approximation of the actual values used in the simulation since the precision needed to return the rays sufficiently required 5 decimal places. The actual values were 1361.07136 nm and 1296.64008 nm for the longest and the shortest wavelengths respectively.

eccentricity and installing the RM. Again, simultaneous tuning will occur if $\psi > \varphi$ but there is another possibility for simultaneous tuning to occur in the off-axis PM configuration. Specifically, when attempting to maximise the visible facet width by minimising the eccentricity (Section 4.4). This happens whenever the eccentricity is less than a certain critical value, and has been defined here as Secondary Simultaneous Tuning (SST).

The following analysis assumes that the convergence angle is equal to the acceptance angle ($\psi = \varphi$), which simplifies the situation by allowing the minimum value of eccentricity to be calculated from the perspective of the PM (and its fixed acceptance angle) rather than considering the asymmetric distribution of the spectrum in the convergence angle (Section 3.4.3). The diagram in Figure 4.12 describes the condition when the chosen eccentricity value produces a polygon rotation angle that is equal to half the acceptance angle, $\theta_E = \frac{\varphi}{2}$. In this configuration, the retro-angle, Ω , will also be equal to the acceptance angle ($\Omega = \varphi$) since the RM must be aligned to reflect the central wavelength, λ_c , at normal incidence (see Figure 4.3, Section 4.4).

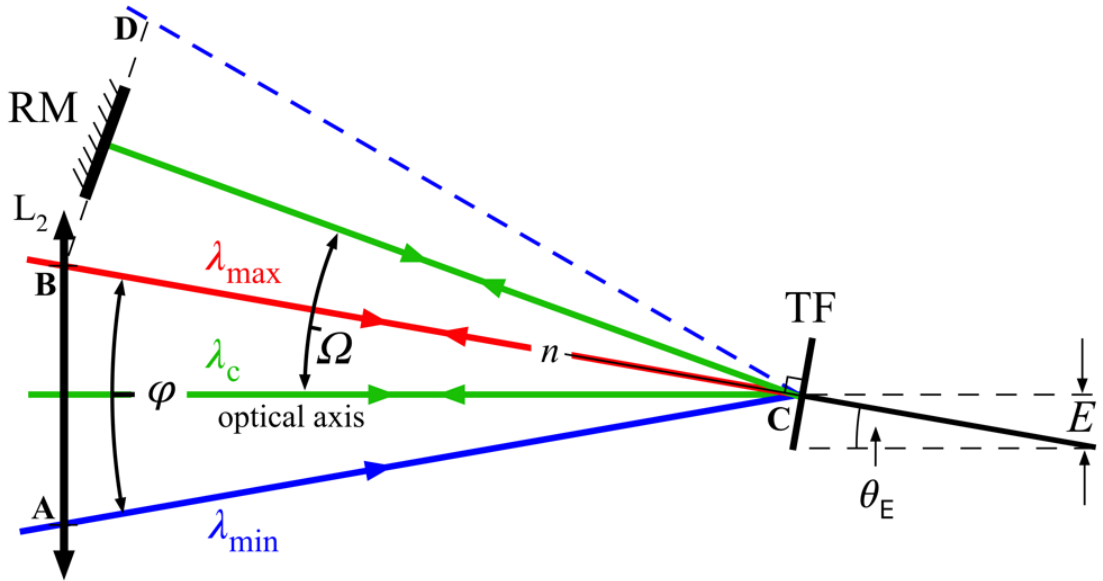


Figure 4.12. Demonstration of SST for an off-axis PM. L_2 is the second telescope lens and Ω is the retro-angle measured between the optical axis and the surface normal of the retroreflector mirror, RM. The central wavelength, λ_c (green), retro-reflects at normal incidence off the RM, but the longest wavelength, λ_{max} (red) simultaneously retro-reflects at normal incidence off the TF. The eccentricity, E , provides the polygon rotation angle, θ_E , which must be greater than half the acceptance angle, $\theta_E > \frac{\varphi}{2}$, to prevent λ_{max} from retroreflecting off the TF. The dotted line in the plane of the RM intersects the lens L_2 at point B, which is at the same location as the intercept of λ_{max} .

In this particular configuration (with the PM below-axis), the light reflecting off the TF towards the RM, represented by the triangle BCD, will lay directly adjacent to the converging spectrum, represented by the triangle ABC. This allows the TF to reflect the longest wavelength (λ_{max} , red) at normal incidence along BC whilst simultaneously reflecting λ_c off the RM. Both of these rays (λ_c and λ_{max}) will return along their inbound paths and be recoupled back into the receiving fibre, which in this case will produce unambiguous sweeping from λ_{min} up to just before λ_c , and then again after λ_c up to λ_{max} . This will effectively halve the usable TSB of the spectral filter. The same situation will occur if the PM is oriented above-axis, although in this case λ_{min} will reflect at normal incidence off the TF instead of λ_{max} . The arrangement described by Figure 4.12 demonstrates the limit for the minimum amount of eccentricity that should be used. The polygon rotation angle must be greater than half the value of the acceptance angle, $\theta_E > \frac{\varphi}{2}$, in order to avoid SST (assuming $\psi = \varphi$). When $\theta_E < \frac{\varphi}{2}$, the retro-angle will necessarily decrease to maintain the alignment of λ_c but the reflected light (represented by the triangle BCD) will consequently overlap with the converging spectrum, which will introduce multiple pairs of simultaneously tuned wavelengths instead of just one (λ_c and λ_{max}).

The minimum value of eccentricity, E_{min} , required to avoid SST can be quickly assessed by using $\theta_E > \frac{\varphi}{2}$ in Eq. 4.3 to arrive at Eq. 4.18. This calculation is constructed from the perspective of an off-axis PM since it considers the magnitude of the acceptance angle, rather than the converging spectrum, and therefore also assumes that $\psi = \varphi = 2\Phi = \frac{4\pi}{N}$, making it a function of the PM parameters only.

$$E_{min}(R, N) = R \cos\left(\frac{\pi}{N}\right) \sin\left(\frac{2\pi}{N}\right) \quad \text{Eq. 4.18}$$

Using $R = 31.75 \text{ mm}$ and $N = 72$ (Section 3.6.1), and assuming an ideal setup where $\psi = \varphi$, the minimum value of eccentricity needed to prevent SST is $E_{min} = 2.765 \text{ mm}$, which is 8.7 % of the PM radius. With this information, the visible facet width can also be calculated (Eq. 4.8) as well as the PM's axial translation (Eq. 4.5), which in this case are $l_v = 2.767 \text{ mm}$ (for the central wavelength) and $d = 0.12 \text{ mm}$ respectively. Using this value of eccentricity reduces the visible facet width by 0.11 % of its true value and the axial translation required here is comparable to the error margin of the adjustment on the translation stage ($\pm 0.01 \text{ mm}$). Under ideal conditions, an eccentricity value $E >$

2.765 mm will prevent SST and ensure that the visible facet width has been maximised (for λ_c). The next step is to perform the same analysis from the perspective of the converging spectrum to achieve a more accurate representation of the situation.

4.6.2 Optimising Eccentricity

The minimum value of eccentricity was calculated in Eq. 4.18 using just the parameters of the PM. Although this was only an approximation, it did provide a good indication of the appropriate alignment required, and the properties that the other components must have, in order to prevent SST and optimise the system. However, the analysis assumed that $\psi = \varphi$, and was carried out from the perspective of the acceptance angle, rather than using the true angles attributed to the marginal wavelengths in the converging spectrum. In reality, the distribution of the spectrum is known to be non-linear (Section 3.4.2), and asymmetric about the telescope optical axis, and a new approach is therefore needed to take this property into consideration.

The longest wavelength in the spectrum, $\lambda_{0_{max}} = 1410 \text{ nm}$, was established in Section 3.4.3 (Table 3.1) as having the largest angular displacement at the diffraction grating ($\delta_+ = 9.21^\circ$), measured from the telescope optical axis. Figure 4.13 shows this marginal ray as it traverses through the telescope and falls incident on the PM. The angle between the ray and the telescope optical axis has been given the symbol ψ_+ since it is measured as being above the optical axis from this particular point of view.

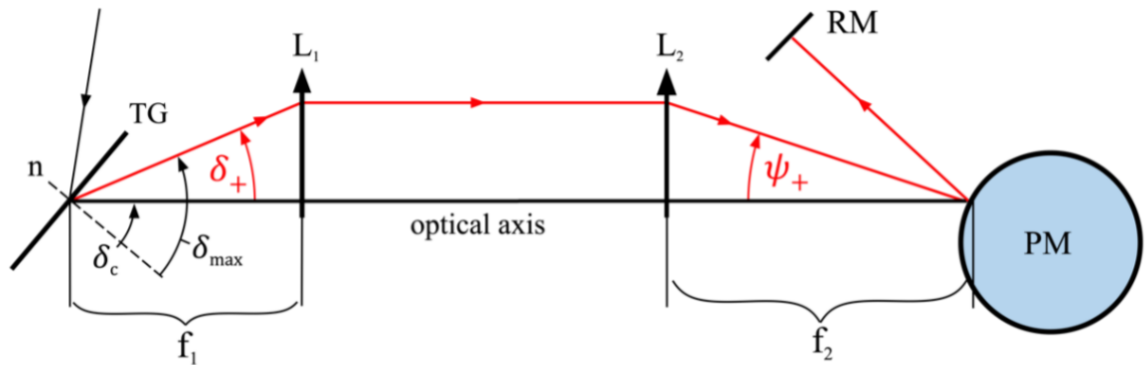


Figure 4.13. Simple diagram of the spectral filter indicating the geometry and the parameters needed to establish the angle, ψ_+ , of the marginal wavelength (red chief ray) as it converges onto the polygon mirror, PM. The properties of the transmission grating, TG, give the angle of the ray from the optical axis, δ_+ (see Table 3.1), before entering the lenses of the telescope, L_1 and L_2 . RM is the retroreflector mirror.

In the previous analysis from Section 4.6.1, the minimum eccentricity value needed to prevent SST was found by matching the PM rotation angle to half the value of the acceptance angle, $\theta_E = \frac{\varphi}{2}$. In this more detailed analysis, the PM rotation angle must be equal to the larger of the two marginal angles, which in this case occurs for the longest wavelength in the converging spectrum, $\theta_E = \psi_+$. Incidentally, the marginal angle for the shortest wavelength can be given the symbol ψ_- , and is measured below the telescope optical axis but has a smaller value than ψ_+ and is therefore not shown in the diagram.

Examining the path of the chief ray as it propagates through the filter and applying some basic trigonometry allows this new angle to be calculated as a function of the longest wavelength, $\psi_+(\lambda_{0_{max}})$. The chief ray of $\lambda_{0_{max}}$ (red) is seen emerging from the diffraction grating and making an angle with the optical axis, δ_+ . This angle is given by the difference between the diffraction angles of the longest wavelength and the central wavelength, $\delta_+ = \delta_{max} - \delta_c$ (see Table 3.1, Section 3.4.3). Both of these angles are a function of their respective wavelength and are given by rearranging the grating equation (Eq. 3.2). The desired angle, ψ_+ , is then calculated using the two right triangles formed in the telescope and by assuming that the radial distance of the chief ray from the optical axis is equal on both lenses.

The final expression for calculating the peripheral angle to the longest wavelength, $\psi_+(\lambda_{0_{max}})$, is given by Eq. 4.19 below. This formula depends upon the properties of the light source ($\lambda_{0_{max}}$ and λ_c), the diffraction grating (γ , m and G) and the telescope magnification (f_1 and f_2), which therefore can only be used after these components have already been selected.

$$\psi_+(\lambda_{0_{max}}) = \tan^{-1} \left(\frac{f_1}{f_2} \tan[\sin^{-1}(Gm\lambda_{0_{max}} - \sin \gamma) - \sin^{-1}(Gm\lambda_c - \sin \gamma)] \right) \quad \text{Eq. 4.19}$$

Once these parameters are known⁹, they can be inserted into Eq. 4.19, and the angle it provides can be used in Eq. 4.18 to calculate the new minimum value of eccentricity. The result gives $\psi_+(\lambda_{0_{max}}) = 6.9^\circ$, which is 1.9° larger than $\frac{\varphi}{2}$ due to the off-axis PM (where

⁹ The parameters of the light source are the same as those presented in Table 3.1 (Section 3.4.3). The diffraction grating has an incidence angle $\gamma = 48.6^\circ$ and a line density $G = 1145 \text{ l/mm}$. The telescope lenses have focal lengths $f_1 = 75 \text{ mm}$ and $f_2 = 100 \text{ mm}$.

$\varphi = 2\Phi = \frac{4\pi}{N}$ or 10°). The new minimum eccentricity value required to prevent SST is $E_{min} = 3.83 \text{ mm}$, which is 12 % of the PM radius (compared with 8.7 % from before). The associated retro-angle can also be calculated using Eq. 4.4, which gives a value of $\Omega(E_{min}) = 13.87^\circ$. The calculated value of eccentricity creates a visible facet width $l_v = 2.764 \text{ mm}$ (for the central wavelength), which is a reduction of 0.23 %, or more than double the value found earlier using only the properties of the PM (acceptance angle).

The analysis above shows that SST can be prevented if the eccentricity is set above a certain critical threshold value. This value is determined by the marginal angle of the longest wavelength, ψ_+ , which depends upon the parameters of the light source, diffraction grating and the telescope. Although the magnitude of ψ_+ is relatively small in this analysis, the spectral filter could easily be designed to incorporate a much larger angle, which would necessarily increase the minimum eccentricity value. This could be thought of as increasing the apex angles of the two triangles ABC and BCD in Figure 4.12. However, primary vignetting at the TF lowers the optical power output of the system, which creates an incentive to minimise the amount of eccentricity in order to maximise the visible facet width (Section 4.5). If the spectral filter is assembled without knowledge of the minimum eccentricity value, the RM could be unknowingly aligned in the wrong position and SST could occur as a consequence. Although this analysis provides the mathematical tools to help prevent this from happening, in reality the success of the spectral filter's alignment still depends upon the precision of the instruments being used.

4.7 Instantaneous Wavelength With Respect To PM Rotation Angle

Eq. 4.19 gives the peripheral angle to the longest wavelength in the spectrum converging onto the PM, $\psi_+(\lambda_{0max})$. However, this equation can also give the angle for any arbitrary wavelength in the converging spectrum, $\psi_\pm(\lambda_n)$, and uses a positive or negative notation to indicate whether the selected wavelength is converging from above or below the telescope optical axis respectively. In this way, when the central wavelength is selected, λ_c , the angle returned will be zero since it is aligned with the telescope optical axis. The significance of Eq. 4.19 is that ψ_\pm is equivalent to the instantaneous rotational angle, θ , of the PM as it performs a single sweep through the spectrum and therefore provides a way to establish the timing signal of each instantaneously swept wavelength.

Eq. 4.19 can be rearranged to give the wavelength as a function of the PM rotational angle, $\lambda(\theta)$, provided that the properties of the light source (λ_c), diffraction grating (G, m, γ, δ_c) and telescope (f_1, f_2) are already known. The result of the rearrangement is given by Eq. 4.20 below.

$$\lambda(\theta) = \frac{1}{Gm} \left[\sin \left(\tan^{-1} \left(\frac{f_2}{f_1} \tan \theta \right) + \delta_c \right) + \sin \gamma \right] \quad \text{Eq. 4.20}$$

Plotting this function shows the non-linear wavelength distribution with respect to the rotational angle of the PM (Figure 4.14). The 72 facet PM rotates through 5° for each sweep of the spectrum, $-2.5^\circ \leq \theta \leq +2.5^\circ$, even though the acceptance angle may have been doubled by placing the PM off-axis, which is accounted for by taking the tangent of 2θ instead of only $\tan \theta$ in Eq. 4.20. The derivative of this function can be used to compare the difference in the rate of change of wavelength with rotational angle of the PM, $\frac{d\lambda}{d\theta}$, between the two extreme sweeping angles, which can either be carried out on Eq. 4.20 or on the trend line equation from Figure 4.14. The difference between these two values, with respect to the midpoint at $\lambda(0)$, yields a 14% decrease from the shortest wavelength to the longest wavelength.

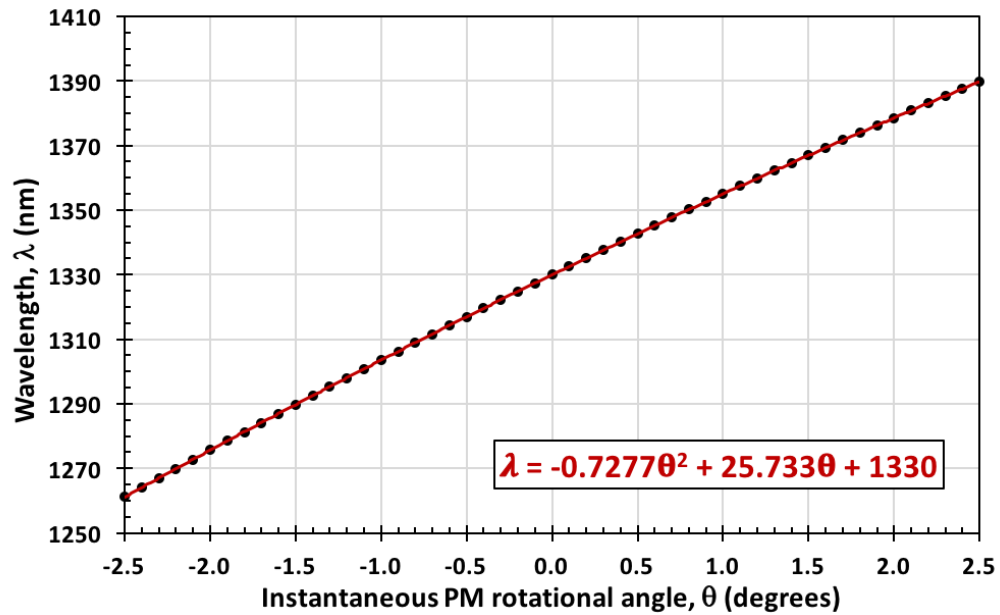


Figure 4.14. Instantaneously swept wavelength as a function of PM rotation angle, measured from zero for the location of the central wavelength.

4.8 Beam Width Analysis

The spectrum entering the filter can be modelled as the superposition of an arbitrary number of discrete, adjacent, narrowband laser linewidths. Each linewidth can be conceptualised as travelling through the filter in a collimated beam (Figure 4.15). The cross-sectional profile of each beam changes due to the interaction with the filter components and does not remain constant as it propagates through the filter. Therefore, the final footprint of each beam can change dramatically from its original shape by the time it is being recoupled back into the optical fibre.

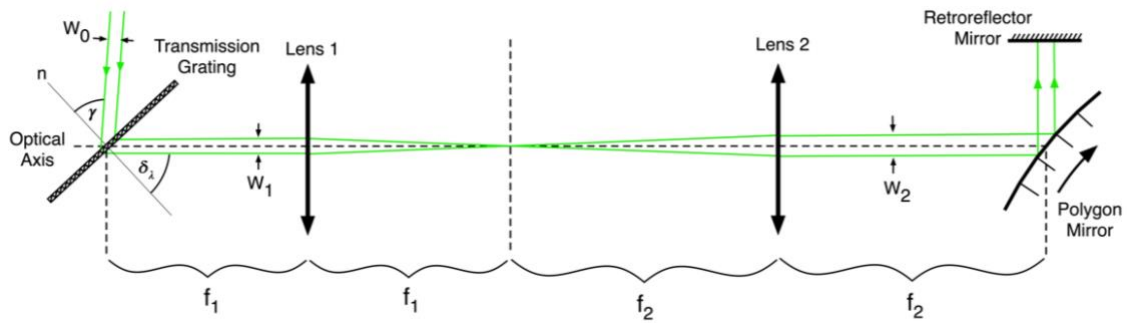


Figure 4.15. Spectral filter beam propagation. The initial beam width W_0 increases to W_1 by travelling through the grating. It then changes again depending on the magnification of the telescope, either increasing or decreasing in size. By carefully selecting the focal lengths, the final width of the beam can be made to approximately match the width of the facets on the polygon and therefore limit the amount of primary vignetting.

For example, the collimator will introduce beam divergence, which slowly increases the diameter of the beams over distance, the degree of which depends on the collimator being used (Section 3.3). Also, the grating and the two-lens telescope will introduce varying amounts of diffraction, refraction and aberration depending on wavelength and incidence angle, all of which contribute towards redirecting the rays and deforming the final shape of the beams as they attempt to exit the filter. Allowing the beams to deviate from their quasi-circular cross sectional shape is not particularly problematic as long as the constituent rays all manage to exit the filter through the aperture of the optical fibre tip. Secondary vignetting is concerned with the proportion of the beam that falls outside of the aperture of the optical fibre tip and the loss in optical power caused as a result (Section 2.7.2). The choice of collimator alone could cause significant secondary vignetting if the beam produced is too narrow and/or if the free-space path length is too long (Section 3.3).

Another problem is the size of the beams arriving at the PM, which should ideally fit within the area of a single facet to ensure that all of the rays are reflected in the correct

direction. If the facet is over illuminated, the overlapping rays will reflect off the adjacent facets at the wrong angle and light will be lost due to primary vignetting (Section 2.7.1). Therefore, the collimator should not produce a beam that is too wide either.

Beam deformations can be explored in the simulations by examining their shape as they traverse through the filter and measuring their degree of deviation from circularity (ellipticity). The shape of a beam on the surface of each component can be quantified by measuring the maximum and minimum x and y values of the beam's spot profile. The ellipticity of the beam is then given by the x/y ratio. The graph in Figure 4.16 highlights the irregularities in the shape of an arbitrary beam as it propagates back and forth through a simulated, ideal spectral filter, using paraxial surfaces on the lenses and the diffraction grating. The surface numbers along the x-axis correspond with the different components in the spectral filter. The beams are seen to deviate from circular by as much as 35 %, for example, on surface 21, which is the second pass through the mid-focal plane between the two paraxial telescope lenses, or on surface 24, which is the second pass through the diffraction grating. This particular pair of spot profiles have changed dramatically since their initial encounters with surface 7 and 4 respectively. Beams that have been changed by such amounts and then proceed to interact with refractive components will suffer more significantly from secondary vignetting.

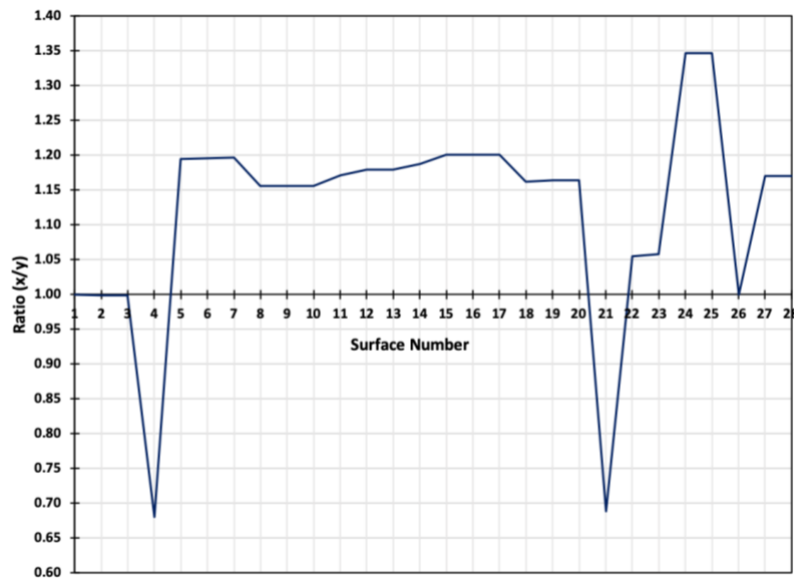


Figure 4.16. Ellipticity of an arbitrary beam propagating back and forth through the simulated spectral filter. The ellipticity is zero when the x and y values are equal, which only occurs for the first two surfaces in the filter. Every other surface experiences an elliptical spot, which never returns to circular throughout the rest of the filter. The surfaces are; optical fibre entrance/exit aperture (1 & 28), collimator lens (2 & 26), diffraction grating (4 & 24), telescope lenses (6 & 8 and 20 & 22), PM (11 & 17) and the retroreflector mirror (surface 14).

The parameters that influence the shape and size of the beams preclude the possibility of simply matching the collimator's beam width to the size of the polygon facets, especially when eccentricity is introduced (Section 4.4). Furthermore, the goal of improving the spectral resolution encourages the use of larger-beam diameter collimators to illuminate more lines on the diffracting grating (Section 3.4) but this would require a reduction in the width of the beams afterwards, carried out through the magnification of the telescope, which also affects the convergence angle (Figure 3.11, Section 3.5). Therefore, it is necessary to carry out a quantitative analysis to understand precisely how the beam changes as it propagates through the filter. This is essential for finding a satisfactory solution to the problems discussed above and to help guide the choice of components used in the construction of an optimised spectral filter. The analysis begins by examining the interaction of the light rays with the diffraction grating.

The single, multi-chromatic beam from the collimator is distributed by wavelength across a small angular displacement after interacting with the transmission grating. The geometrical arrangement and orientation of the collimator and grating causes the beam at each wavelength to acquire a different width as it emerges from the grating into the object space of the first lens in the telescope. The beam widths decrease in size as the diffraction angle from the surface normal increases, which can be seen by examining the 3D layout images from the simulations in Figure 4.17 a) & b).

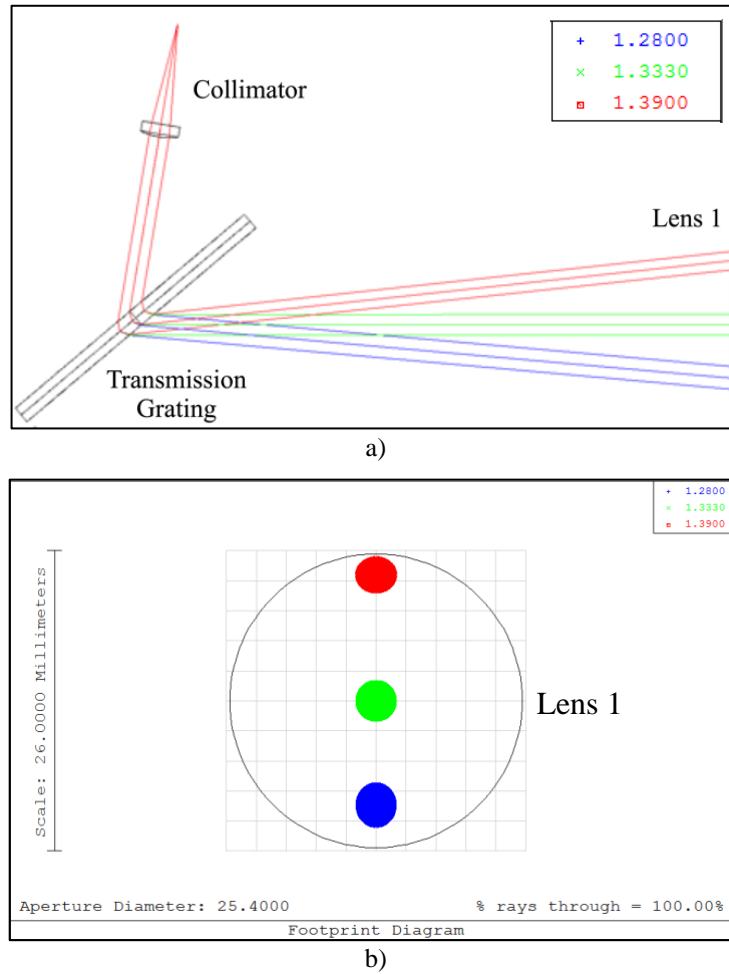


Figure 4.17. Aspect ratios of beam cross sections at different wavelengths at the surface of Lens 1. **a)** 3D viewer showing the first three components; collimator lens, diffraction grating and the image plane of lens 1. The beams associated with the longest wavelength (red, 1390 nm), central wavelength (green, 1333 nm) and the shortest wavelength (blue, 1280 nm) are depicted by 3 rays each. Only a very subtle change to their beam width is observed. **b)** Footprint diagram of the three beams striking the first lens. The elliptical nature of the beams is caused by the non-normal incidence angle of a circular beam on the flat image plane.

Three different wavelengths are shown emerging from the transmission grating in Figure 4.17 a) and propagating from left to right. Each wavelength is modelled by three rays (chief ray, lower marginal and upper marginal), which represent the central axis and total width of each beam. The three beams are associated with the longest (red – 1390 nm), central (green – 1333 nm) and the shortest (blue – 1280 nm) wavelengths in the simulated spectrum. The bandwidth used is deliberately narrow (110 nm) since the more realistic spectral width of the SOA (160 nm) would over fill the 1-inch diameter lenses used in this simulation.

The difference in width between the three beams is subtle but still noticeable. Figure 4.17 b) shows the footprint diagram for the three beams striking the first surface of the lens

after the diffraction grating. The elliptical shape of the two extreme beams (red – 1390 nm and blue – 1280 nm) is caused by the rays striking the surface of the first lens at non-normal incidence. In this example, the image plane is flat but in reality, the front surface of the lens is curved away from the incident beams, which increases their incidence angle further, making their spot profiles even more elliptical.

4.8.1 Beam Width Calculations

An expression for the final beam width, W_2 , incident on the PM, can be constructed by examining the interaction of the beams with the transmission grating and the two-lens telescope. The width of the beam exiting the grating, W_1 , shares the same hypotenuse on the transmission grating as the initial beam width, W_0 , exiting the collimator (Figure 4.18), which is given by Eq. 4.21 after specifying the parameters of the diffraction grating, i.e. the incidence angle, γ , and the diffraction angle, $\delta(\lambda_n)$.

$$W_1 = W_0 \frac{\cos \gamma}{\cos \delta} \quad \text{Eq. 4.21}$$

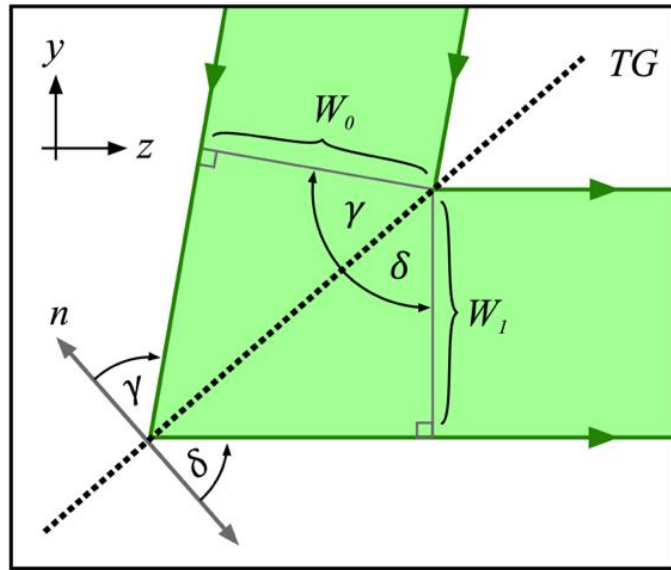


Figure 4.18. Close up image of the beam interaction on the transmission grating, TG. The incident beam from the collimator, W_0 , illuminates the grating at an incidence angle, γ , from the surface normal. An arbitrary diffraction angle, δ , is shown for the beam exiting the grating, with a different width, W_1 .

The function for the final beam width, W_2 , is then found by substituting Eq. 4.21 into the formula for the telescope magnification (Eq. 3.9). The combination of these relationships provides an approximation to the size of the beam striking the facets of the PM with respect to wavelength.

$$W_2(\lambda_n) = W_0 \frac{f_2}{f_1} \frac{\cos \gamma}{\cos \delta(\lambda_n)} \quad \text{Eq. 4.22}$$

Figure 4.19 shows the graph of Eq. 4.22 using four different initial beam widths, $W_0 = 1, 2, 3$ and 4 mm , over a wavelength range between $1250 \text{ nm} - 1410 \text{ nm}$ to represent the bandwidth of the light source (160 nm). The magnification of the two-lens telescope was zero ($\frac{f_2}{f_1} = 1$) and the grating parameters were the same as those used in the experiments and the simulations ($G = 1145 \text{ l/mm}$ and $\gamma = 48.6^\circ$).

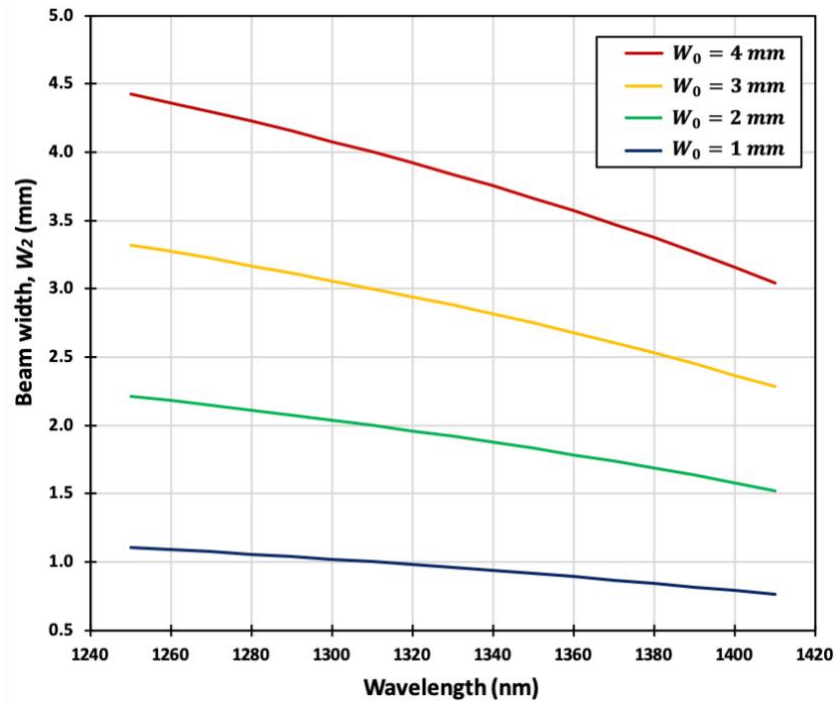


Figure 4.19. Beam width, W_2 , as a function of wavelength over 4 initial beam widths, W_0 . Blue = 1 mm , Green = 2 mm , Yellow = 3 mm and Red = 4 mm . $G = 1145 \text{ l/mm}$, $\gamma = 48.6^\circ$ and $\Delta\lambda_T = 160 \text{ nm}$ ($1250 \text{ nm} - 1410 \text{ nm}$). Shorter wavelengths have wider beam widths than longer wavelengths and the fractional change is constant at $\sim 35\%$. However, the narrower initial beams produce a smaller change in their size than larger beams. The smallest beam (Blue, 1 mm) changed size by 0.35 mm , while the largest beam (Red, 4 mm) changed by 1.40 mm , which would require a larger telescope magnification to match the widest beam to the TF on the PM.

The four curves all show that the longest wavelength in the spectrum has the narrowest beam whilst the shortest wavelength has the widest beam, in agreement with the simulation observations, and that the fractional change in beam width between the two marginal wavelengths is constant at $\sim 35\%$ for all W_0 values used. However, the largest beam ($W_0 = 4 \text{ mm}$, red) changes size by the greatest amount over the total spectral bandwidth (1.40 mm) compared with the smallest beam diameter (1 mm , blue) over the same wavelength range (0.35 mm).

The demagnification of the telescope would therefore need to be more significant for larger-beam collimators in order to sufficiently reduce their size down to the width of the facets – the scaling is not simply proportional to the initial beam width due to the diffraction grating. The results also suggest that the shortest wavelength in the spectrum should be considered when choosing the magnification since it has the largest beam diameter when entering the telescope and therefore a greater risk of over filling the TF and causing primary vignetting. However, the magnification of the telescope provides an inverse relationship between the final beam width and the convergence angle – reducing the beam width will increase the convergence angle, which will limit the swept bandwidth if it becomes greater than the acceptance angle (Section 4.2). Larger beam widths are more desirable and offer better performance but they also demand a higher magnification from the telescope, which puts the TSB at risk of being reduced.

4.9 Total Swept Bandwidth Equation (TSB)

The resolution of SS-OCT relies upon having a wide spectral bandwidth. Ultimately, this depends upon the spectral width of the light source but it also depends upon how well that width is maintained as it travels through the filter. The properties of the components in the filter can affect the bandwidth that is successfully transmitted to the OCT system, which has been demonstrated throughout the previous theoretical developments. The next task is to use this knowledge to formulate a theory that delivers an estimate for the bandwidth of light that is successfully swept and delivered by the filter. The derivation that follows is a multi-parameter study to establish an approximate value for the TSB and is applicable to a PM-based spectral filter using a diffraction grating and a two-lens telescope in either the on-axis or off-axis configuration. It is only concerned with the range of wavelengths that are tuned rather than giving the values of the wavelengths themselves, although they can be approximated from its results. It is independent of the incident beam width exiting the collimator and does not concern itself with any form of vignetting or power throughput. It simply states the approximate, maximum swept spectral range based on the properties of the components used in the filter.

The parameters used in the derivation are associated with the light source, diffraction grating, telescope lenses, and the PM. The light source provides the central wavelength, λ_c , incident on the diffraction grating, which has an incidence angle, γ , groove density, G , diffraction order, m , and a diffraction angle, δ_n , for any arbitrary wavelength value,

λ_n . The two-lens telescope has focal lengths f_1 and f_2 and the PM has a number of facets, N . The PM can be placed on or off axis, and this is described by the constant, κ , which can have the value of 1 (on-axis) or 2 (off-axis). This allows the acceptance angle of the PM to double when placed off-axis, which has the advantage of allowing the filter to potentially tune through a bandwidth that is twice as large compared with when it is placed on-axis. The TSB is also independent of the amount of eccentricity the PM has when placed off-axis (assuming simultaneous tuning has already been prevented).

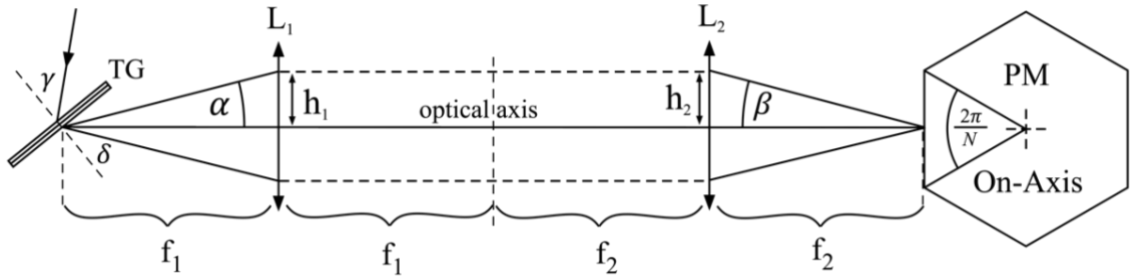


Figure 4.20. On-Axis, spectral filter depicting the variables used in the derivation for the TSB equation. Transmission grating, TG, incidence angle, γ , diffraction angle, δ , telescope lenses, L_1 and L_2 , the height of an arbitrary beam on the face of the lenses, h_1 and h_2 , the focal lengths of the two lenses, f_1 and f_2 , the polygon mirror, PM, and the two half-angles, projected into the telescope by the polygon, depicting the maximum swept divergence and convergence angle, α and β respectively.

Figure 4.20 shows the geometric arrangement of the components and the parameters that are used in the derivation. The half angles α and β are measured from the optical axis of the telescope, which is aligned with the central wavelength λ_c , and depicts the largest divergence of the maximum and minimum wavelengths that can be tuned. Each half angle is equal on either side of the optical axis and independent of the wavelength. They are not a measure of the numerical aperture of the lens but rather the direct projection of the acceptance angle of the PM into the working space of the second lens, i.e. $2\beta = \frac{2\pi}{N}$. Therefore, the value of β is given by $\frac{\kappa\pi}{N}$, which is half the facet-to-facet angle when the PM is situated on-axis ($\kappa = 1$) and doubles when the PM is positioned off-axis ($\kappa = 2$).

The TSB is the difference between the maximum swept wavelength minus the minimum swept wavelength, $\Delta\lambda = \lambda_{max} - \lambda_{min}$, which is depicted by the acceptance angle of the PM. These marginal wavelengths are given by the grating equation, (Eq. 3.2), which is a function of the incidence angle, γ , and the diffraction angle, δ_n . Therefore, the TSB is simply given by the difference, using the variables for the maximum and minimum wavelengths.

$$\Delta\lambda = \frac{1}{Gm} [(\sin \delta_{max} + \sin \gamma) - (\sin \delta_{min} + \sin \gamma)] = \frac{1}{Gm} [\sin \delta_{max} - \sin \delta_{min}] \quad \text{Eq. 4.23}$$

The maximum and minimum diffraction angles are given by the central wavelength's diffraction angle plus or minus the diffraction angle permitted by the telescope and the PM; $\delta_{max} = \delta_c + \alpha$ and $\delta_{min} = \delta_c - \alpha$. Substituting these into Eq. 4.23 gives

$$\Delta\lambda = \frac{1}{Gm} [\sin(\delta_c + \alpha) - \sin(\delta_c - \alpha)] = \frac{1}{Gm} [2 \cos \delta_c \sin \alpha] \quad \text{Eq. 4.24}$$

The diffraction angle for the central wavelength, δ_c , and the maximum permitted angle from the optical axis, α , are given by the grating equation (Eq. 3.2) and by the geometry of the telescope respectively.

$$\alpha = \tan^{-1} \left(\frac{f_2}{f_1} \tan \beta \right) \quad \text{Eq. 4.25}$$

The expression for α assumes that the lateral displacement of the chief rays, measured radially from the optical axis, for either the maximum or minimum wavelength, are equal on both lenses within the telescope, i.e. $\pm h_1 = \pm h_2$. This is only approximately true since the filter must contend with the unavoidable consequence of aberrations. Substituting these two equations into the formula gives the full expression for the TSB as a function of the parameters of the light source, diffraction grating, two-lens telescope and PM.

$$\Delta\lambda = \frac{2}{Gm} \times \cos[\sin^{-1}(Gm\lambda_c - \sin \gamma)] \times \sin \left[\tan^{-1} \left(\frac{f_2}{f_1} \tan \left[\frac{\kappa\pi}{N} \right] \right) \right] \quad \text{Eq. 4.26}$$

This derivation assumes that the acceptance angle of the PM is equal to or smaller than the convergence angle of the incident rays, $\varphi \leq \psi$. This is typically the case when using a PM with a high number of facets, but when the acceptance angle is larger than the convergence angle, $\varphi > \psi$, the PM has the potential to accommodate a wider spectrum, which would suggest that additional wavelengths could be tuned if a larger bandwidth is used. The TSB equation (Eq. 4.26) is also derived by using the PM as a starting point, which only considers the light that is accommodated by its acceptance angle. The acceptance angle could conceivably end up being projected over a wider angle than the parameters of the second lens will allow, i.e. the lens diameter could be too small or the focal length too long, so that the rays pass around the lens instead of through it.

Another assumption is that the diffraction grating can accommodate a very wide spectral range, i.e. that the grating is capable of producing a divergence angle large enough to accept the angular displacement provided by the parameters of the PM (the diagram in Figure 4.20 shows a good example of this since the PM has been drawn with only 6 facets). This limitation of the TSB equation is only a concern when the PM has a low number of facets, producing a very wide acceptance angle. This is less problematic though since the requirement for obtaining higher speeds in OCT is to maximise the sweeping speed and therefore maximise the number of facets, which produces a very narrow acceptance angle.

Despite the approximations and assumptions used in the derivation of the TSB equation, the values it predicts agree with the measured outputs recorded by similar spectral filter designs given in the literature [68], [7], [21], [16]. This validates the TSB Equation and therefore enables the maximum potential wavelength range to be found for a spectral filter using a specific set of components. This is particularly useful in a laboratory setting for testing the efficiency of a particular spectral filter setup or when the operator may have a variety of components available but no knowledge of the correct combination to select to maximise the TSB.

4.9.1 Design Hierarchy

The parameters of the PM physically constrain the choice of applicable components that can be used in the spectral filter. This establishes an initial hierarchy to the design process of the system. The PM's radius and the number of facets determine the limit of the incident beam width, which place constraints on the choice and combination of collimator and telescope. These parameters also determine the acceptance angle (or sweeping angle), which governs the maximum convergence angle and therefore the choice of diffraction grating and telescope combination. Overstepping these limits will cause primary vignetting to occur for beams that are too wide, lowering the maximum optical power transmission, and also decrease the TSB as a result of simultaneous tuning, worsening the axial resolution and causing unwanted noise in the images (Section 4.6). Although the theoretical work suggests how some components can be selected to maximise their own performance, there are additional consequences to these decisions that must be taken into consideration during the design process.

The design of the spectral filter can be aided by the hierarchy list provided in Table 4.2 to establish the relationships and the dependence of the components with respect to each other. This table lists the five main components of the filter and places them in order of importance. The light source (step 1) and the PM (step 2) are at the top of the hierarchy list since they can be selected independently from any other component (and each other). Every other component that follows depends upon at least one of these two components and their properties.

Table 4.2. Design Hierarchy. A list of the main components in the spectral filter, listed in their order of importance with respect to each other. The variables that each component introduces are given in the Notes column and the impact on the OCT system is discussed in terms of resolution, sample penetration depth and speed.

Step	Component	Notes	Impact on OCT System	Depends On
1	Light Source	Provides the total spectral bandwidth, $\Delta\lambda_T$, and the three most significant wavelengths, λ_{min} , λ_c & λ_{max}	Axial Resolution	None
2	Polygon Mirror	Provides the frequency of swept spectra, given by N , which also provides the facet-to-facet angle, Φ , the acceptance angle, φ , and the facet width, L	Bandwidth Sweeping Frequency & Wavelength Sweeping Speed	None
3	Diffraction Grating	Provides the divergence angle as a function of wavelength, $\Delta\delta(\lambda_n)$, given by the incidence angle, γ , line density, G , and order, m .	Spectral Resolution/Laser Linewidths – Axial Scanning Range	1 ¹⁰
4	Collimator	Provides the initial beam width, W_0	Spectral Resolution/Laser Linewidths – Axial Scanning Range	1 & 2 ¹¹
5	Telescope	Provides the magnification, given by the two focal lengths, f_1 & f_2	Axial Resolution & Wavelength Sweeping Speed	1, 2, 3 & 4

The last three components, the diffraction grating (step 3), the collimator (step 4) and the telescope (step 5), share various links with each other but can be placed in order of importance by considering their impact on the OCT system and how many other components they depend upon, e.g. the collimator (step 4) depends on the wavelength of

¹⁰ Although the choice of grating depends on step 1, it should also ideally have as many lines/grooves per mm as possible to narrow the linewidths and maximise the axial scanning range.

¹¹ The collimator is not directly influenced by the PM but it does inform the decision to choose one since the beam it produces must eventually fit within the area of a single facet if primary vignetting is to be avoided.

light being used (step 1) and the size of the facets on the polygon (step 2), whilst the telescope (step 5) depends upon the properties of all the other components.

The choices become slightly more complicated towards the end of the table because certain combinations of components will create additional consequences that have an effect on the filter's performance. For example,

- The final beam width, W_2 , is determined by the combination of the choices made in steps 3, 4 & 5 but is limited by the choice made in step 2 (facet width). Together, they determine the amount of optical power transmission through the filter due to primary and secondary vignetting.
- The convergence angle, ψ , is determined by the combination of the choices made in steps 3 & 5, which is also restricted by the choice made in step 2 (acceptance angle), but determines the TSB and the wavelength tuning speed of the filter.

Table 4.2 will therefore only guide the user so far. After a certain point the user must decide for themselves what parameters to priorities in their spectral filter. For example, the axial scanning range could be prioritised by selecting a high-resolution grating with a wide beam diameter collimator but the TSB will decrease as a result of using the telescope magnification to prevent primary vignetting. Alternatively, the optical power output could be sacrificed in favour of achieving a high axial resolution (maximising the TSB), which can be achieved by selecting a telescope magnification to priorities the convergence angle rather than reducing the beam width to fit onto the facets. Therefore, the components and their parameters should be selected as a function of the intended OCT imaging application and prioritised accordingly.

4.10 Discussion

Despite multiple reports of functional PM-based spectral filters for SS-OCT, a fully comprehensive, multi-parameter, theoretical study of their operation is not widely discussed in the literature. The rigorous analysis presented in this chapter has shown that the choice of components and their combination strongly influence the operation of the filter. Optimising the SS depends upon successfully identifying the parameters that have the biggest impact, which requires careful consideration of the components, individually and collectively, in order to understand how to maximise the system's performance.

Failing to consider and respect these parameters may severely limit the output, which won't be possible to remedy through the alignment process alone.

The acceptance angle, defined in Section 4.2, was shown to be one of the key parameters of the spectral filter. It is determined by the PM and it places a limit on the maximum angular displacement of the converging spectrum. It also partly governs the duty cycle of the SS (Section 4.3), since it depends on how efficiently the facet sweeping period is used. If the spectrum is continuously swept throughout the entire period of an active facet, the duty cycle will be 100 %. This is achieved whenever the convergence angle is equal to or larger than the acceptance angle ($\psi \geq \varphi$), although having a convergence angle larger than the acceptance angle will lower the potentially available TSB. The acceptance angle can also be doubled by introducing eccentricity to the PM and installing a RM (Section 4.4). This increases the angular sweeping range and therefore widens the limit on the convergence angle. If the convergence angle remains unchanged during this modification, the wavelength tuning speed will increase, but at the cost of lowering the duty cycle.

The non-linear distribution of the wavelengths in the diverging spectrum, caused by the diffraction grating (Section 3.4.2), translates through the telescope to the converging spectrum. It was shown in Section 4.3.1 that the central wavelength would need to be offset by $> 7 \text{ nm}$ to distribute the total angular displacement of the converging spectrum equally on either side of the telescope optical axis. Therefore, even if the convergence angle is perfectly matched to the acceptance angle, the TSB and the duty cycle may still suffer if this shift is not taken into consideration during the alignment process.

The study in Section 4.5 showed how the visible facet width changes from the perspective of the incident beams depending on the wavelength and the amount of PM eccentricity. The equation derived for the final visible sweeping facet width (Section 4.5.2) closely matched the first approximation given by Eq. 4.8, and became equivalent when using the central wavelength. In the first approximation, the facet was considered to rotate underneath the converging spectrum, rather than sweeping through it, but both equations gave the expected result that larger eccentricity values would progressively worsen the visible facet width. This study also established the wavelengths that are the most affected by eccentricity, but this depends upon the orientation of the PM – above or below the telescope optical axis (Section 4.4). The inclusion of PM eccentricity and the nature of the sweeping facet both contribute towards increasing the amount of primary vignetting,

which can significantly reduce the amount of successfully transmitted light. Maximising the visible facet width requires minimising the PM eccentricity but this is limited by the potential to introduce simultaneous tuning (Section 4.6).

Section 4.6 described the system's ability to produce two spectral components during a single sweep of the spectrum (simultaneous tuning). This occurs on two adjacent facets of the PM, whereby the two simultaneously returned wavelengths are typically at opposite ends of the spectrum. This property of the filter is responsible for reducing the TSB of the SS and introducing unwanted noise in the signal output. Simultaneous tuning occurs whenever the convergence angle is equal to or larger than the acceptance angle, $\psi \geq \varphi$, which applies to both on-axis and off-axis PMs, but can be prevented by selecting components with certain parameters to ensure that $\psi < \varphi$.

Secondary simultaneous tuning (SST) occurs on a single facet rather than two and arises whenever the eccentricity of an off-axis PM is reduced below a certain critical threshold value, E_{min} (Section 4.6.1). This value depends on the properties of the converging spectrum, which is determined by the parameters of the components used in the filter. It was shown that the PM rotation angle must be larger than the marginal angle of the longest wavelength, $\theta_E > \psi_+$, in order to prevent SST. Eq. 4.18 and Eq. 4.19 were developed and used to establish the value $E_{min}(\psi_+)$, as well as giving the correct retro-angle, $\Omega(E_{min})$, for the RM.

The desire to minimise the eccentricity is borne out by the objective to reduce primary vignetting, since smaller eccentricity values will maximise the visible facet width. However, certain spectral filter designs allow the possibility of unintentionally lowering the eccentricity below the critical value. Eq. 4.18 and Eq. 4.19 should be consulted whenever an off-axis PM is used in order to ensure that the visible facet width has been maximised without reducing the eccentricity so much that it introduces SST.

Section 4.8 examined the individual beams as they propagate through the spectral filter. The analysis showed that the beam diameter gradually decreases in size towards the longer wavelengths in the spectrum due to the interaction with the diffraction grating (Figure 4.17). This makes the shorter wavelength beams more susceptible to primary vignetting since their larger spot size could over illuminate the PM facets if the initial beam width is relatively wide. The addition of PM eccentricity will also magnify this

effect. Figure 4.19 demonstrated that wider beam collimators require even higher telescope magnifications than smaller beam collimators in order to reduce their width to fit onto the facets of the PM. Since the final beam width and the convergence angle are inversely affected by the telescope magnification, the more the beam diameter needs to be reduced, the greater the potential to cut off the TSB at the margins.

In conclusion, optimising the spectral filter depends upon finding a satisfactory balance between all of these parameters, since the chain of connections between them does not allow for a single, simple solution. Understanding which parameters have the greatest impact on the system is essential for maximising the swept bandwidth and achieving the highest spectral resolution whilst minimising the amount of primary and secondary vignetting to maximise the total power output. At this stage, the recommended route to optimise the spectral filter is to follow the design hierarchy list in Table 4.2 whilst also giving careful consideration to the final beam width and the convergence angle as well as ensuring that no simultaneous tuning occurs (especially SST). This approach shall be revisited again in Chapter 7, after the results of the subsequent experimental chapters have been collected and considered.

CHAPTER 5

SPECTRAL FILTER DESIGN

5.1 Chapter Introduction

This chapter contains a presentation and discussion of experimental results from the work carried out on the PM-based spectral filter. The goal was to identify the parameters that had the most significant impact on the filters performance and demonstrate them experimentally in the laboratory, with supporting evidence from Zemax™ ray tracing software, as well as validating the theoretical work from Chapter 4. However, the experimental work was not always carried out in parallel with the theoretical development and therefore each study does not necessarily demonstrate the optimum setup for the filter. Instead, this experimental selection reveals insight about the operation of the spectral filter, such as the limitations and difficulties that were encountered and the solutions found to circumvent them.

5.2 Experimental Work

The experimental work that follows offers a detailed examination of the components in the spectral filter, making a direct comparison between similar components with slightly different properties or alignments, and then suggests the best methods to use to optimise the system. A variety of experiments were carried out on the telescope design, which concluded that larger diameter lenses with medium focal lengths ($< 100\text{ mm}$) produced the widest swept bandwidth and the highest power output. The advantages and disadvantages of changing the location of the PM with respect to the optical axis was also explored and the results show how primary vignetting can be eliminated under certain conditions. This work concludes by identifying aberrations (introduced by using refractive optics, e.g. lenses) as one of the biggest contributors to poor performance in the spectral filter and then suggests a novel solution to the problem, which is given much greater attention in the following chapter.

An examination of the factors that lead to higher power transmission and more uniform, spectral power distribution by reducing the effects of chromatic aberration will be presented. An analysis of the spectral power distribution, carried out on 1-inch and 2-inch diameter telescope designs, shows that wider diameter lenses provide greater performance across the selected wavelength range. Experimental measurements were

compared with simulation results carried out using ZemaxTM Optics Studio ray tracing software showing the potentially achievable power distribution from low aberration optimized telescope designs. Observations of these features were made throughout the experimental and simulation work and have been presented here with supporting evidence wherever possible.

5.3 Collimator Comparison

The following work is an adaptation from a conference paper submitted to the ‘2nd Canterbury Conference in Optical Coherence Tomography with an emphasis on Swept Sources’ [69]. The performance of the SS spectral filter was compared for two different fibre collimators. Although the beam width on the grating is different for each of the two collimators, the spot size at the PM facet can be made approximately equal by selecting an appropriate magnification in the telescope for each arrangement. An improvement in the signal drop-off (Section 1.4.4) at the interferometer output of $\sim 1.0 \text{ dB/mm}$ was obtained when using a wider 3.4 mm collimator compared to a 1.5 mm collimator. This result is attributed to the combination of illuminating the diffraction grating with a wider beam and the optical properties of the lenses used in the telescope.

5.3.1 Collimator Analysis

Using the symbols and terminology in Figure 4.18, Section 4.8.1, the initial beam width, W_0 , measured at the collimator output, changes as a result of interacting with the diffraction grating to produce W_1 . The beam width changes again if the focal lengths in the telescope, f_1 and f_2 , are different (Figure 3.11, Section 3.5). Multiple telescope designs, using different collimators and lenses, were considered for experimental comparison but the resulting theoretical values for W_2 varied between the different arrangements. However, some designs resulted in W_2 values that were very close to one another (within $\pm 20 \text{ }\mu\text{m}$). This made it possible to compare two different collimators, with different W_0 values, whilst maintaining the same spot size on the facets of the PM. This essentially provides the same conditions for both beams as they interact with the PM facets, which minimised the impact of primary vignetting during the experimental comparison. Illuminating the grating with a wider beam improves the spectral resolution, according to Eq. 3.3 from Section 3.4, but the telescope magnification will also affect other properties of the spectral filter. Different lens combinations will change the length of the telescope,



and therefore the free-space path length. Shorter path lengths are more desirable since they minimise the amount of beam divergence (Section 3.3) and reduce the overall size of the experimental setup.

Several properties of the filter must be considered when selecting telescope lens combinations to suit each collimator. The top-level constraint is set by the size of a PM facet which will restrict the maximum value of the beam width that can be effectively used on it. Any beam width larger than the size of a single facet, after propagating through the telescope, would instantly lead to primary vignetting. The PM physical facet width is $L = 2.77 \text{ mm}$ (Eq. 3.12). However, the additional eccentricity, E , taking the PM off-axis, reduces the visible facet width from the point of view of the beam incident on it. Also, the shortest wavelength ($\lambda_{0min} = 1250 \text{ nm}$) produces the widest beam originating from the grating, as described earlier in Section 4.8.1. However, in this instance, only the visible facet width for the central wavelength, l_{λ_c} , was considered. The PM in the experimental comparison had an eccentricity of approximately 10 mm , giving a PM rotation angle $\theta_E = 18.38^\circ$ and a visible facet width $l_{\lambda_c} = 2.63 \text{ mm}$ (Eq. 4.7). Therefore, any telescope lens combination that produced a final beam width, W_2 , that was larger than this value was discarded.

The two collimators selected for comparison were F240APC-C ($\emptyset = 1.5 \text{ mm}$) and F280APC-C ($\emptyset = 3.4 \text{ mm}$) (Thorlabs, USA). W_2 was calculated (Eq. 4.22) for both collimators using a variety of different telescope magnifications. All possible combinations were explored for 6 different focal lengths; 35 mm , 40 mm , 60 mm , 75 mm , 100 mm and 150 mm . Out of 72 possible lens combinations (36 for each collimator) only 37 complied with the condition that $W_2 < L$; specifically, 24 combinations for the first collimator (1.5 mm) and 13 for the second collimator (3.4 mm). However, out of those 37, only 7 had beam widths for both collimators that were approximately equal in size. The pairing selection process allowed up to a $\pm 20 \mu\text{m}$ difference between the two final beam widths. Since the total cavity length, and therefore the overall size of the experimental setup, is a concern, lens pairs that exceeded a particular telescope length were excluded. For example, two 150 mm focal length lenses would result in a total, back and forth, telescope path length of 600 mm . Adding this to the approximate dimensions and path lengths of the other components (collimator, grating and PM plus their mounting stages) would extend the length of the experimental setup to

at least 800 mm, which allows the beam divergence to have a greater impact and is generally less desirable when considering, for instance, storage or transportation. The telescope length was therefore restricted to a maximum of 350 mm, which reduced the 7 pairs down to just 3. Table 5.1 shows the three possible lens combinations for the two collimators and the final beam widths they produce.

Table 5.1. The final three lens combinations for each of the two collimators. All possible combinations were considered but filtered down to just three after the criteria was met to ensure that the final beam width W_2 is smaller than the facet width. The Telescope Length is equal to $2(f_1 + f_2)$. Matching pairs of beam widths were allowed up to a $\pm 20 \mu\text{m}$ difference between their values when selecting for comparison.

F240APC-C $W_0 = 1.5 \text{ mm}$			F280APC-C $W_0 = 3.4 \text{ mm}$		
					
Lens Combination ($f_1 \times f_2$)	Telescope Length (mm)	Final Beam Diameter W_2 (mm)	Lens Combination ($f_1 \times f_2$)	Telescope Length (mm)	Final Beam Diameter W_2 (mm)
75 × 100	350	1.92	60 × 35	190	1.90
40 × 60	200	2.16	60 × 40	200	2.18
75 × 60	270	1.15	100 × 35	270	1.14

The first pair of telescopes in this table (top row, green boxes) were selected for experimental comparison (75 × 100 mm and 60 × 35 mm) and produced final beam diameters of 1.92 mm and 1.90 mm for the 1.5 mm and 3.4 mm collimators respectively. This conscientious selection process demonstrates that, despite many possible combinations existing for just six different focal lengths, only a few will satisfy the constraints imposed by the properties of the PM, which supports the spectral filter design hierarchy established in Section 4.9.1. Therefore, care must be taken when choosing the focal lengths in order to avoid unwanted power loss from primary vignetting.

5.3.2 Experimental Comparison

The two collimator and telescope arrangements identified in the top row of Table 5.1 (green boxes) were sequentially built into the spectral filter and experimentally tested and compared. The first arrangement used the 1.5 mm collimator with the 75 × 100 mm telescope and the second arrangement used the 3.4 mm collimator with the 60 × 35 mm telescope. Two separate cage assemblies were employed to accommodate each telescope lens combination, which were pre-aligned at the correct focal distances to minimise the

necessity for any further adjustment once positioned inside the spectral filter. The collimators were also swapped with relative ease by way of a single grub screw, thereby minimising additional alignment. In both cases, the spectral filter was carefully adjusted to provide optimum performance. This was achieved by observing the output in real-time on the OSA and making fine adjustments until the power output and bandwidth had been maximised. Figure 5.1 shows the results displayed on the spectrum analyser in peak hold mode. The first arrangement (blue trace) produced a TSB of 101 nm whilst the TSB of the second arrangement (red trace) was almost half this value at 52 nm. However, the second arrangement had a noticeably greater power output ($\sim 27\%$ increase).

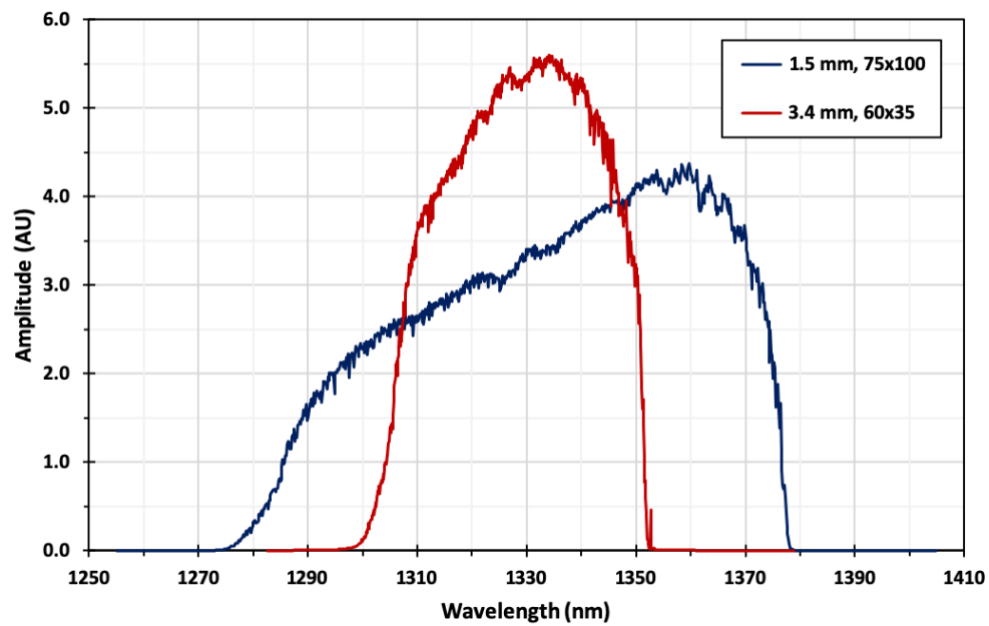


Figure 5.1. Comparison between two collimators with different beam diameters. The blue trace used a 1.5 mm beam diameter with a 75×100 mm telescope producing a FWHM of 77 nm and a TSB of 101 nm. The red trace used the 3.4 mm beam diameter with a 60×35 mm telescope and produced a FWHM of 43 nm with a TSB of 52 nm. The two different telescope magnifications were chosen to match the two final beam widths ($W_2 \sim 2.0$ mm) and ensure they fit onto the visible facet width of the polygon.

After each arrangement had been optimised, the spectral filter was connected to the optical fibre-based interferometer array and a planar mirror was installed in the object arm to obtain an ideal interference signal. An oscilloscope measured the intensity of the interference signal as the optical path difference (OPD) was changed by $50 \mu\text{m}$ increments, 3 mm either side of zero OPD, over a total range of 6 mm. A fast Fourier transform of the signal was then taken on the oscilloscope to measure the interference signal intensity and the frequency of the fringe spacing (Figure 5.2). These graphs essentially show the decrease in signal strength (or signal drop-off) with increasing

imaging depth (or OPD), as the two interfering wave trains (from the reference and object arms) gradually decorrelate from one another, and therefore provide an experimental method for measuring the sensitivity of the SS system (Section 1.4.4). The longer the signal strength is maintained, the greater the axial scanning range and the more detail can be extracted from greater depths. As discussed in Section 3.4.1, this largely depends on the width of the laser linewidths, $\delta\lambda$, which should be as narrow as possible.

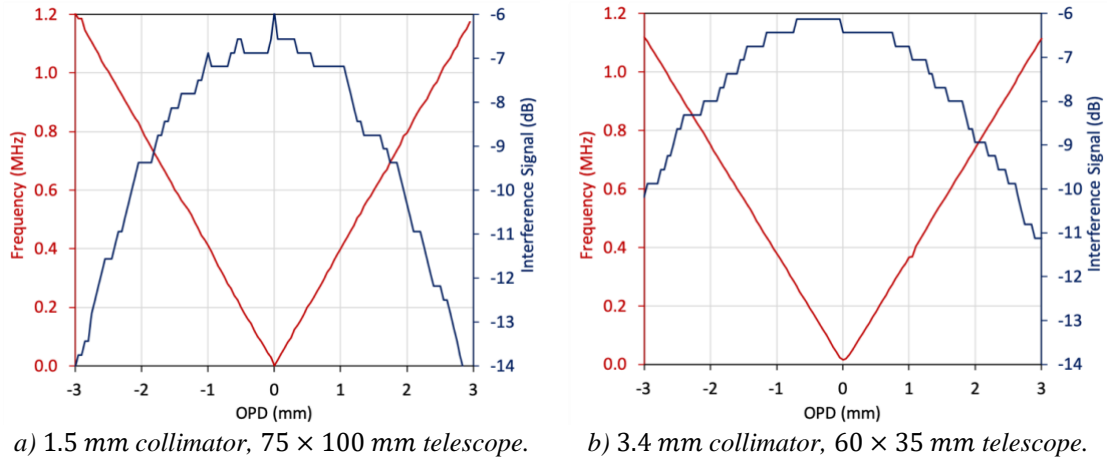


Figure 5.2. Sensitivity measurements (signal drop-off) comparison for both collimator and telescope configurations. The average signal drop-off is 2.67 dB/mm for the small beam diameter collimator (a) and 1.67 dB/mm for the larger beam collimator (b). Maintaining the signal strength over larger OPDs increases the axial scanning range of the SS-OCT system.

The results indicate that a stronger signal is maintained over a larger OPD for the second arrangement using the 3.4 mm collimator, whereby less of the signal is lost over a 3 mm displacement. There was an average intensity decrease of approximately 2.67 dB/mm for the 1.5 mm collimator (75 × 100 mm telescope) (Figure 5.2 a) and 1.67 dB/mm for the 3.4 mm collimator (60 × 35 mm telescope) (Figure 5.2 b). The larger beam width and shorter focal lengths in the second arrangement have resulted in an average power improvement of 32.5 %. However, it was the first arrangement (1.5 mm, 75 × 100 mm) that produced the widest spectral bandwidth. The stronger signal output of the second arrangement (3.4 mm, 60 × 35 mm telescope) is suspected to be caused by the larger beam diameter collimator illuminating more lines on the grating (producing higher spectral resolution and minimising the instantaneous laser linewidths, $\delta\lambda$) but the wider bandwidth produced by the first arrangement (75 × 100 mm telescope) is suspected to be the result of more closely matching the convergence angle of the telescope to the acceptance angle of the PM.

Understanding the reason for the two different bandwidths can be explained by considering the divergence angle of the diffraction grating and the telescope magnification. If the divergence angle is known ($\Delta\delta = 16.88^\circ$, Eq. 3.4, Section 3.4.2), the theoretical convergence angle of each arrangement can be calculated using the ratio of the telescope focal lengths (Eq. 3.10). The $75 \times 100 \text{ mm}$ telescope creates a convergence angle of 12.66° , whilst the $60 \times 35 \text{ mm}$ telescope creates a convergence angle of 28.23° . Both of these convergence angles are larger than the acceptance angle of the off-axis PM (10°), meaning that it is not possible to sweep through the total spectral range of the light source (160 nm). The convergence angle of the second arrangement, however, is almost three times the acceptance angle of the PM, which is why the swept region has decreased by such a large amount (see Figure 4.1, Section 0). The wider angular distribution of the spectrum, converging onto the PM from the 35 mm lens, will force a much narrower swept portion of the total available bandwidth, which, incidentally, also lowers the wavelength tuning speed of the spectral filter.

Taking the ratio of the calculated convergence angle and the known acceptance angle for each arrangement yields an approximation of the percentage of total available bandwidth that should be swept by each arrangement. This result can then be used (assuming ideal conditions) to estimate the success of each filters' alignment. The predicted percentage of the total bandwidth (160 nm) swept by the first arrangement is 79%, giving a TSB of 126 nm , which is 25 nm wider than what was achieved and suggests that this filter alignment was less than ideal. The predicted percentage of swept bandwidth for the second arrangement was 35%, which should give a TSB of 57 nm . This is only 5 nm larger than what was found and suggests a better filter alignment was achieved. The calculated TSB (using Eq. 4.26) also agrees with the predictions, which gives values of 128.46 nm and 56.51 nm respectively. Regardless of the filter alignment, these results demonstrate the importance of selecting the correct combination of components if power output and spectral bandwidth are intended to be optimised simultaneously.

5.4 Telescope Design Considerations

In the previous study, the telescope magnification was used to manipulate the beam width so that both arrangements had the same spot size when they arrived at the PM facets. In the study that follows, a more rigorous examination of the telescope design and its effects

on the spectral filter's performance is explored. The goal at this stage is to understand how the properties of the telescope (e.g. focal length and lens diameter) affect the spectral filter's function and influence the design based on the requirements of the system and the fundamental limitations established by the parameters of the other components. This body of work therefore assumes that steps 1, 2 & 3 in the spectral filter design hierarchy have already been carried out, i.e. the light source, PM and diffraction grating have already been correctly selected (Table 4.2, Section 4.9.1) and shall act as the starting point for many of the investigations that follow.

5.4.1 Telescope and Lens Parameters

The telescope is necessary for inverting the diverging spectrum, emerging from the diffraction grating, into a converging spectrum onto the PM. The required two lenses can either be identical, providing no magnification, or dissimilar, providing magnification or demagnification. In the simplest case, the two lenses would be the same and have very short focal lengths for the purpose of reducing the path length to minimise beam divergence. Alternatively, when different focal lengths are used, many possible combinations can be employed and the function of the spectral filter will not change. However, if an unsuitable combination of lenses are chosen, the performance of the spectral filter can be drastically altered (as demonstrated above, Section 5.3).

Even if both lenses are equal, making the correct choice involves understanding where the light will be and how it is affected by the telescope. The properties of the first lens should be chosen to capture all of the light emerging from the diffraction grating, which depends upon the incidence angle ($\gamma = 48.6^\circ$) and the grating's groove density ($G = 1145 \text{ l/mm}$). Choosing the second lens depends upon the choice of the first lens and the parameters of the PM (acceptance angle, $\varphi = 10^\circ$, when off-axis). The process starts by considering the divergence angle of the diffraction grating ($\Delta\delta = 16.88^\circ$, Eq. 3.4), which depends upon the properties of the light source (bandwidth, shortest, longest and central wavelengths provided in Table 3.1 from Section 3.4.3). Knowledge of the divergence angle allows the operator to instantly recognise whether or not the telescope requires any magnification to match the convergence angle to the acceptance angle of the PM. Whenever $\Delta\delta > \varphi$, the telescope requires two different focal lengths to change the convergence angle in order to successfully filter all of the available wavelengths in the

output spectrum of the SOA. Since the inequality in this analysis is true for this selection of components, telescope magnification is required¹².

However, selecting the first lens is less than trivial, since the spectral distribution is non-linear and the two opposite, marginal wavelengths ($\lambda_{0_{max}}$ and $\lambda_{0_{min}}$) do not sit equidistant on either side of the central wavelength (Figure 3.9, Section 3.4.3), which is aligned to the telescope optical axis. This asymmetry situates the longest wavelength at $+9.21^\circ$ ($\delta_+ = \delta_{max} - \delta_c$) above the telescope optical axis and the shortest wavelength at -7.67° ($\delta_- = \delta_c - \delta_{min}$) below the telescope optical axis. The first lens in the telescope should accommodate all of the spectrum and therefore the longest wavelength, $\lambda_{0_{max}}$, with the widest diffraction angle from the horizontal, δ_+ , should be considered.

The minimum numerical aperture (NA) of the first lens, L_1 , required to accommodate $\lambda_{0_{max}}$ is calculated to be 0.16 (Eq. 3.8). As depicted in Figure 5.3, any lens (Lens A or Lens B) with an appropriate ratio between its focal length, f , and lens diameter, D , which meet this particular NA value will be sufficient to accommodate the entire spectrum diverging from the diffraction grating.

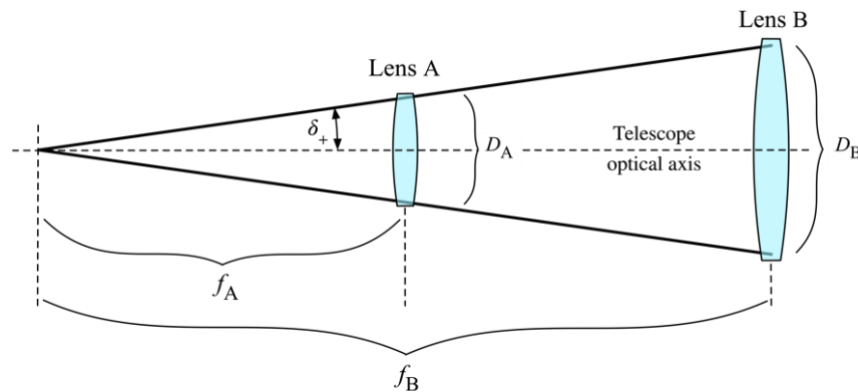


Figure 5.3. Comparison between two lenses, A and B, with different focal lengths, f_A and f_B , and lens diameters, D_A and D_B , respectively. Both lenses represent L_1 in the telescope and meet the NA of the diverging spectrum originating from the diffraction grating (not shown) determined by the angle between the telescope optical axis and the chief ray of the longest wavelength, δ_+ . These marginal rays will experience the greatest amount of aberration, which increases disproportionately towards the edges of the lens.

However, this assumes that the diverging spectrum will fill the entire lens to its edge, which is not necessarily desirable or practical since refractive errors, caused by

¹² Although the convergence angle in this case needs to be decreased, the telescope must still provide magnification as opposed to demagnification. The consequence of this, however, is that the beam width will increase in size which may lead to primary vignetting.

aberrations, will increase disproportionately towards the edges of the lens. It is therefore reasonable to assume that illuminating a smaller (near paraxial) area around the centre of the lens, closer to the telescope optical axis, will reduce the effects of aberration for the marginal wavelengths and encourage more rays to successfully return to the optical fibre. This can be achieved by selecting a diffraction grating with a small line/groove density, providing a smaller divergence angle and therefore a smaller area of illumination on the lens. This is undesirable though since it will worsen the grating's spectral resolution (Eq. 3.3) and therefore limit the maximum theoretical axial scanning range of the accompanying OCT system (Section 1.4.3). Another way to achieve this is by selecting a lens with a higher NA than the value calculated above. This will force the diverging spectrum to illuminate a smaller, central region of the lens, closer to paraxial propagation, and therefore should reduce the amount of refraction and aberration for the marginal wavelengths in the spectrum. However, the percentage of radial illumination on L_1 depends upon its focal length and lens diameter.

Figure 5.4 lists a selection of the shortest focal length lenses available from Thorlabs, USA, together with their associated percentage of radial illumination across 1-inch (AC254-C) and 2-inch (AC508-C) diameters (with respect to the largest diffraction angle, $\delta_+ = +9.21^\circ$, for the longest wavelength, $\lambda_{0_{max}}$). Theoretically, the radial distance from the optical axis, y , for the chief ray of the longest wavelength, in the principal plane of L_1 , can be approximated using $y = f_1 \tan(\delta_+)$ and assuming that the rays originate from a point source on the diffraction grating. The percentage of radial illumination is then given by the ratio of this y -coordinate and the radius of each lens.

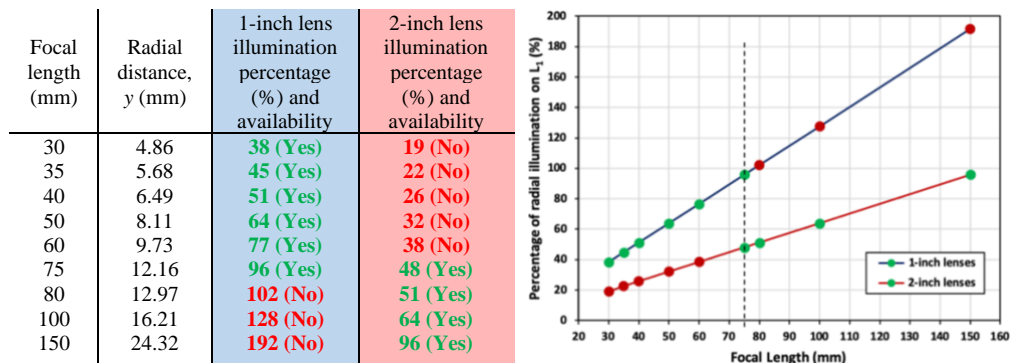


Figure 5.4. Percentage of radial illumination on lens L_1 for 1 inch (blue) and 2-inch (red) diameter lenses over a range of different focal lengths. The sequence of 1-inch lenses will fill twice as fast as the 2-inch lenses. 1-inch diameter lenses with a focal length greater than 75 mm lead to over illumination (red values) while 2-inch lenses less than 75 mm are less easily sourced, requiring bespoke manufacturing (red values). The only directly comparable pair is when $f = 75$ mm, indicated by the vertical dotted line in the graph.

1-inch diameter lenses are available with focal lengths as short as 30 *mm*, whilst the shortest focal length available with a 2-inch diameter lens is 75 *mm*. The percentage values for the radial illumination on the 2-inch diameter lenses are therefore coloured red for all focal lengths that are less than this value. Lenses with a percentage value of radial illumination that are greater than 100% are not able to capture all of the incident spectrum and are therefore also coloured in red. All other acceptable percentage values of radial illumination are coloured green.

This analysis shows that 1-inch diameter lenses with a focal length larger than 75 *mm* will be unsuitable for use in the telescope since the marginal wavelengths will arrive at the principal plane of L_1 with a greater lateral y -value than its radius. The smallest percentage of radial illumination, out of the readily available options, is seen to occur on a 1-inch diameter lens with a 30 *mm* focal length (38%). This analysis also identifies that only one pair of lenses exist (in this selection) that share the same focal length (75 *mm*). The percentage of radial illumination on the 1-inch and 2-inch diameter lenses with a 75 *mm* focal length are 96% and 48% respectively, as indicated by the vertical dashed line on the graph in Figure 5.4. This pair of lenses will be revisited in Section 5.5, which compares two telescope designs with identical magnification but different lens diameters. The following section however, investigates the suitability of using the smallest available lens with the lowest percentage of radial illumination.

5.4.2 Short Focal Length Simulation

A simulation was constructed to explore the effect of minimising the percentage of radial illumination across the surface of the first lens, L_1 , in the telescope. This was carried out after considering the results of the analysis conducted in Section 5.4.1, which showed that, out of all the viable options, the smallest percentage of radial illumination occurred on 1-inch diameter lenses with 30 *mm* focal lengths (Figure 5.4). Using this lens (AC254-030-C, Thorlabs, USA), the y -coordinate of the chief ray for λ_{0max} , in the principal plane of L_1 , was calculated to be 4.86 *mm*, which means that $< 38\%$ of the lens diameter will be illuminated by the incident spectrum, forcing the light to propagate closer to the centre of the lens, near paraxial. This was expected to improve the performance of the spectral filter by decreasing the amount of aberration and increasing the power output by allowing more light rays to return to the optical fibre tip.

With the first lens already determined, the focal length of the second lens needed to be selected to achieve the desired telescope magnification, i.e. to match the convergence angle to the acceptance angle of the polygon. The diffraction angle of the longest wavelength ($+9.21^\circ$ from the horizontal) should again be considered since it is larger than the equivalent angle for the shortest wavelength. The half acceptance angle of the off-axis PM is $+5^\circ$ from the horizontal. Therefore, the divergence angle must be approximately halved by the telescope magnification, which means that the second focal length should be roughly twice as long as the first ($\sim 60\text{ mm}$) to ensure that the whole spectrum is swept by the filter (Figure 5.5).

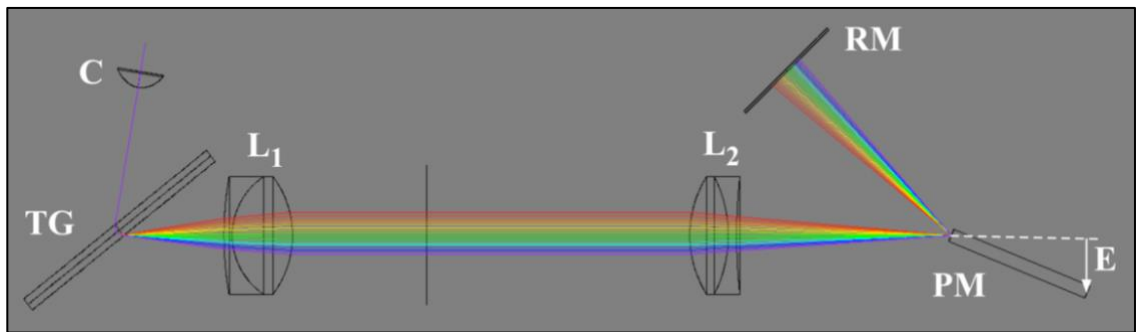


Figure 5.5. Simulation layout using 1-inch diameter (25.4 mm) lenses. The chief ray of each wavelength in the simulation is shown propagating through each component, starting with the collimator, C, transmission grating, TG, two-lens telescope ($30 \times 60\text{ mm}$), L_1 and L_2 , polygon mirror, PM, and retroreflector mirror, RM. Wavelengths are coloured in order of the visible spectrum for clarity. Red indicates the longest wavelength while purple indicates the shortest wavelength. The active facet of the PM is modelled as a single surface at the proximal end of a rectangular block with a thickness / length set equal to the polygon radius (31.75 mm). Facet rotation is achieved by rotating the block about the centre of its distal end. PM eccentricity, $E = 12.14\text{ mm}$.

The beam diameter from the collimator will consequently increase from using a $30 \times 60\text{ mm}$ telescope. Therefore, the initial beam width should be small to ensure that it does not over illuminate the active polygon facet and cause any unnecessary primary vignetting. A collimator with a beam diameter of 1.5 mm was selected (F240-APC-C, Thorlabs, USA), which produced a 2.88 mm beam for the central wavelength after traversing through the telescope (Eq. 3.10). This value is a tenth of a millimetre larger than the facet width and therefore some primary vignetting can be expected to occur.

The results of the simulation can be seen in the graph of Figure 5.6 a), which gives the amount of primary and secondary vignetting. Primary vignetting accounts for about 50% of the rays lost at the margins, however secondary vignetting is responsible for a far greater loss – less than 25% of rays are recaptured for only a few of the wavelengths at

the margins of the spectrum and significantly less over the central region. This high loss is caused by the enlarged spot profiles on the optical fibre tip (small black circle) seen in Figure 5.6 b). Light from each wavelength has been distributed over a far larger area than the optical fibre tip can accommodate. The shape of the spots are also dramatically misshapen, which is indicative of large amounts of aberration.

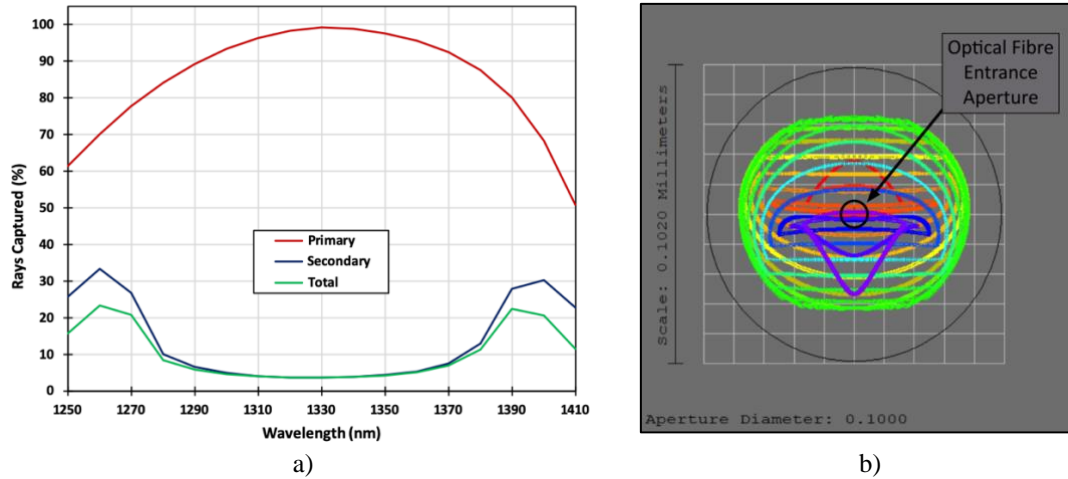


Figure 5.6. *a) Primary and secondary vignetting for the simulated setup using a 30×60 mm telescope. The number of rays successfully captured by the polygon facet (primary vignetting) is as anticipated but the severe loss seen at the optical fibre (secondary vignetting) is greatly unexpected. b) Large amounts of secondary vignetting occur on the optical fibre tip (smaller black circle), which is suspected to be caused by aberration due to the drastically altered shape of the illuminating spots.*

The shorter focal length telescope was suspected to improve the effects of aberration by illuminating a smaller area on the surface of the first lens but the simulation results show that much less light is recaptured overall. Despite illuminating $< 40\%$ of the first lens, and significantly reducing the telescope length to just 180 mm (one way), the final output of the filter was so low that it would be inadequate for use in the accompanying OCT system. This analysis demonstrates the importance of selecting the correct components for the spectral filter and highlights the necessity to reduce the effects of aberration, which is strongly recommended in this type of system in order to guarantee sufficient power transmission is achieved. The results of this study open the discussion to whether or not there could be any advantage from using larger diameter lenses to reduce the effects of aberration and achieve a higher power output (Section 5.5).

5.5 1-inch Verses 2-inch Diameter Lens Experiment

The following work is an adaptation from a conference paper submitted to ‘*SPIE – Optical Systems Design*’, Frankfurt, Germany [70]. This study is a comparison of overall system performance between using telescope designs with different lens numerical apertures and diameters. The evidence presented earlier in this chapter has led to the indication that using larger diameter, achromatic lenses could improve the systems performance by counterintuitively reducing the effects of aberration created when light rays at the spectral extremes ($\lambda_{0_{min}}$ & $\lambda_{0_{max}}$) propagate and refract through the lenses of the telescope. The simulation results from Section 5.4.2 show that the effects of aberration were greater when using a high NA, short focal length (30 mm), 1-inch diameter (25.4 mm) lens, which was selected to minimise the percentage of illuminated surface area. The negative effects from using this lens were so great that the optical power output was no longer suitable for use in the accompanying OCT system (Figure 5.6). This led to the exploration of using different lens diameters to establish their impact on the system. It was hypothesised that larger diameter lenses might increase the maximum power transmission through the filter, provided that the focal lengths were kept short, since using long focal lengths would go against the already established motivation to minimise the cavity length [58] due to beam divergence (Section 3.3). The shortest (and most applicable) focal length available for experimental comparison, in both 1-inch and 2-inch diameters, was found to be 75 mm (Section 5.4.1, Figure 5.4).

5.5.1 Lens Aberration Analysis

Before the experimental comparison was conducted, an aberration analysis was carried out in the simulations to study the amount of ray deflection produced by different lens diameters. The spherical aberration of a 1-inch diameter lens (AC254-075-C) was compared with that of a 2-inch diameter lens (AC508-075-C), both using the same 75 mm focal length to match the first lens in the telescope. Each simulation contained only the surfaces needed to construct the lenses and analyse the results. The standard method was employed whereby a point light source, operating at 1330 nm, was placed at infinity to illuminate each lens with collimated light rays. The graph in Figure 5.7 is a ray fan diagram showing the amount of ray deflection (μm) as a function of lens radius (mm). Only one radial axis (x -axis) is needed to explore the ray deflection since the surface of the lens, $z(x, y)$, is radially symmetrical.

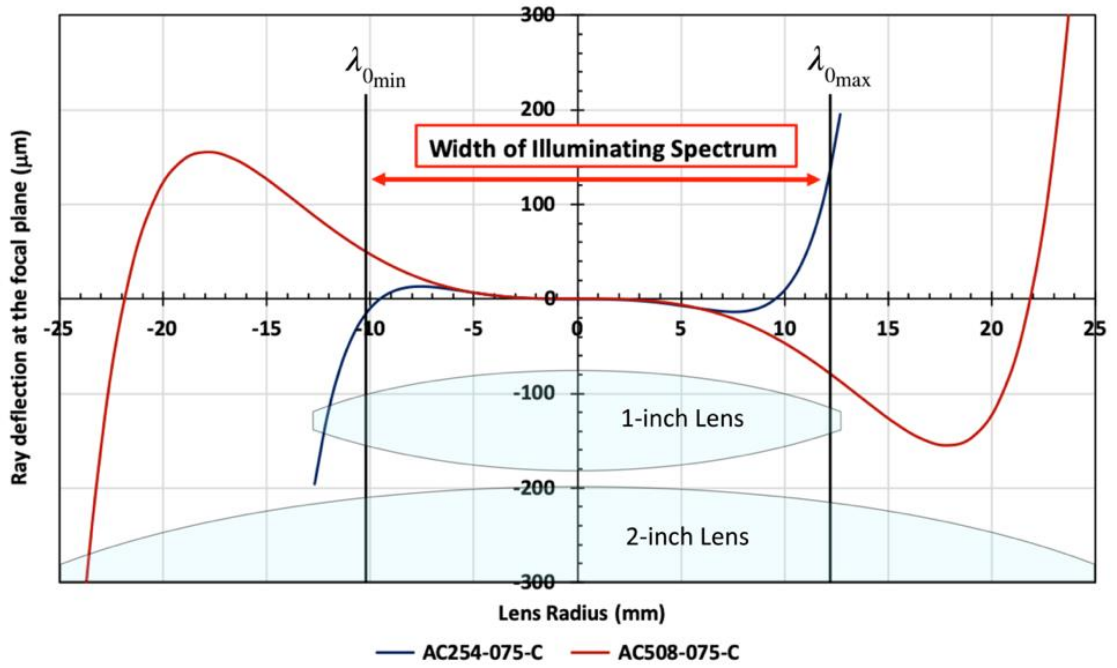


Figure 5.7. Simulation Ray Fan diagram example comparing the ray deflection at the focal plane of two lenses with respect to lens radius. The ray deflection is due to aberration errors and is measured from the optical axis. A point light source located at infinity illuminates the entire aperture of each lens with collimated light rays (at 1330 nm). The blue curve corresponds to a 1-inch diameter lens (AC254-075-C) and the red curve corresponds to a 2-inch diameter lens (AC508-075-C). Both lenses have a 75 mm focal length. The vertical black line markers indicate the width of the illuminating spectrum from the diffraction grating and the approximate amount of deflection for the marginal chief rays on each lens, $\lambda_{0min} = 1250 \text{ nm}$ (negative x -values) and $\lambda_{0max} = 1410 \text{ nm}$ (positive x -values).

The amount of ray deflection in the focal plane for both the smaller, 1-inch diameter lens (blue curve) and the larger, 2-inch diameter lens (red curve) is approximately equal up until a radial distance of about $\pm 6.5 \text{ mm}$. Outside of this value, the ray deflection increases sharply for the 1-inch diameter lens ($> 20 \text{ } \mu\text{m}$ after $\pm 10 \text{ mm}$) but rises more steadily for the 2-inch diameter lens ($> 20 \text{ } \mu\text{m}$ after $\pm 7 \text{ mm}$). The overlaid graphics illustrate the location of the chief ray of the two extreme marginal wavelengths, $\lambda_{0min} = 1250 \text{ nm}$ (negative x -value) and $\lambda_{0max} = 1410 \text{ nm}$ (positive x -value), on the surface of each lens, indicated by the two black vertical lines. The location along the x -axis of each vertical line is found using the same method described in Section 5.4.1 and the values from Table 3.1 in Section 3.4.3. These lines mark the extent to which the aperture of the first lens is filled by the diverging spectrum (see Figure 5.8). The span between the two lines (from -10.10 mm to $+12.16 \text{ mm}$) represents the width of the spectrum emerging from the diffraction grating and provides a better visual examination of the percentage of illuminated area on the surface of each lens.

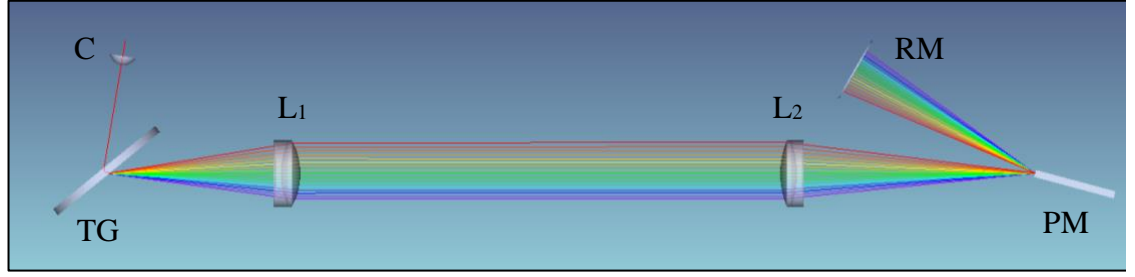
The overlay suggests that light from the longer wavelength region of the spectrum will experience more ray deflection as a result of the wider diffraction angle from the optical axis ($\delta_+ = 9.21^\circ$), compared to light from the shorter wavelength region with the smaller diffraction angle ($\delta_- = 7.67^\circ$) and therefore a smaller radial coverage. This appears to be more favourable for the 2-inch diameter lens, which has an overall shallower increase in ray deflection compared with the sharper increase, after roughly $+8.5 \text{ mm}$, for the 1-inch diameter lens. The asymmetry of the illuminating spectrum favours the shorter wavelengths and suggests that more of the rays from this region might return successfully to the optical fibre than those from the longer wavelength region, which could be noticeable as an increase in optical power at the shorter wavelength region of the spectrum. This observation is borne out by the visual inspection of the area under each curve.

This short analysis of spherical aberration has been carried out at the central wavelength, λ_c , however at all other wavelength values ($\lambda_{0_{min}} < \lambda_c < \lambda_{0_{max}}$) the aberration curves look very similar (less than a few microns of ray deflection). In reality, at each wavelength, the beam (represented by its chief ray) strikes the lens, L_1 , at different locations and incidence angles. It should be noted that while the lenses are comparable for their spherical aberration performance, the coma, defocus and lateral colour will play a role in the overall refractive error analysis that could be carried out.

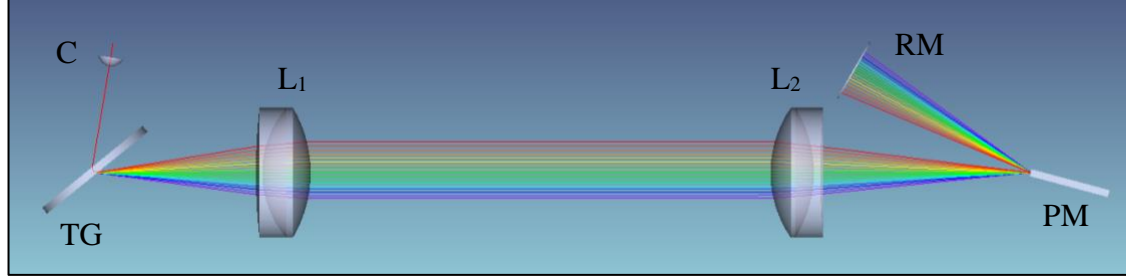
5.5.2 Telescope Comparison Setup

A comparison was carried out on two telescope designs (Figure 5.8). The first design consisted of 1-inch (25.4 mm) achromatic lenses (AC254-C, Thorlabs, USA) and the second consisted of 2-inch (50.8 mm) achromatic lenses (AC508-C, Thorlabs, USA). Both telescopes utilised $75 \times 100 \text{ mm}$ focal lengths on f_1 and f_2 respectively, which were chosen for their greater success at providing a wider swept bandwidth (seen earlier in the simulations from Section 5.3) as well as their availability in both sizes¹³.

¹³ Shorter focal length lenses ($< 75 \text{ mm}$) with a large 2-inch diameter (50.8 mm) are less common and significantly more expensive.



a) 1-inch diameter telescope lenses



b) 2-inch diameter telescope lenses

Figure 5.8. Simulation 3D layout images comparing (a) 1-inch lenses with (b) 2-inch lenses. All other components and their parameters are identical. Collimator, C, Transmission Grating, TG, Two-lens Telescope, L_1 & L_2 , Polygon Mirror, PM, and Retroreflector Mirror, RM.

The selected magnification will also increase the width of the beam, which must be taken into consideration in order to minimise the amount of primary vignetting (Section 2.7.1). It is for this reason that the smaller beam diameter collimator (F240-APC-C, $\varnothing = 1.5 \text{ mm}$, Thorlabs) was chosen to inject the light into the spectral filter, which in this case means that minimising the amount of primary vignetting was prioritised over maximising the spectral resolution of the diffraction grating (Eq. 3.3, Section 3.4) and minimising the beam divergence (Figure 3.3, Section 3.3).

The telescopes were pre-aligned within their own cage assemblies to reduce the amount of realignment when switching between the two configurations. In this way, only the distance along the telescope optical axis required adjusting (between the grating and the PM). The PM was placed below the telescope optical axis with an eccentricity value of $E = 8.22 \text{ mm}$ ($\theta_E = 15.02^\circ$), which produced a visible facet width for the central wavelength of 2.68 mm (Eq. 4.17). The collimator had a 1.5 mm beam diameter, which increased to 2.08 mm for the central wavelength, after propagating through the telescope (Eq. 4.22). Therefore, primary vignetting was not expected to occur across the central region of the spectrum and could only be impactful at the margins.

5.5.3 Simulation and Experimental Results

The two configurations were fully constructed in the simulation for comparison. The 3D layout view shows that rays travelling in the margins of the spectrum are more strongly influenced by the effects of aberration within the telescope (Figure 5.9). The ‘defocus’ of each wavelength beam is not the same as the classical interpretation of defocus described in the literature on aberrations and instead demonstrates a combined effect of chromatic and field curvature aberration. This is ultimately responsible for enlarging the spot size of the marginal wavelengths, which therefore experience a greater loss from secondary vignetting as a result. By contrast, the paraxial rays from within the central region of the spectrum, propagating close to the telescope optical axis, are less affected by field curvature. This has a greater impact when the smaller, 1-inch diameter lenses are used, as shown in Figure 5.9 a), compared to when the larger, 2-inch diameter lenses are used, seen in Figure 5.9 b).

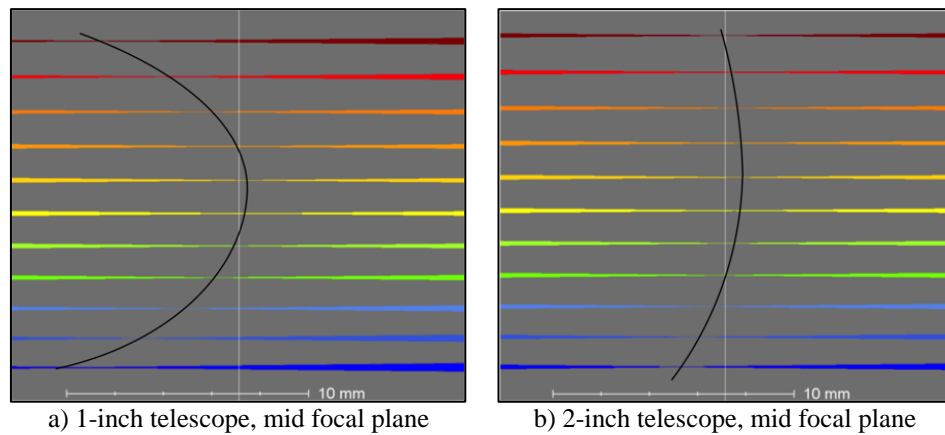


Figure 5.9. The effect of ‘defocus’ due to chromatic and field curvature aberrations in the two telescope arrangements. A selection of wavelengths converging at the mid focal point inside the 1-inch diameter lens telescope (a) and the 2-inch diameter lens telescope (b). The black overlaying curve represents the approximate location of the tightest beam focus for each wavelength.

The graph in Figure 5.10 maps the axial location of the minimum waist point for each wavelengths’ ray bundle, using the 1-inch and 2-inch diameter lenses. The values were obtained using the RMS versus Focus analysis tool. Both curves produced are asymmetric and experience a peak shift that has translated towards the longer wavelengths. However, the change in minimum waist location over the total spectrum for the 2-inch diameter lenses (red curve) is significantly less than the change for the 1-inch diameter lenses (blue curve). Hence the proportion of light coupled into the fibre is expected to decrease in a way that is closely correlated with the trend of the minimum waist values across the spectrum, as seen in Figure 5.10.

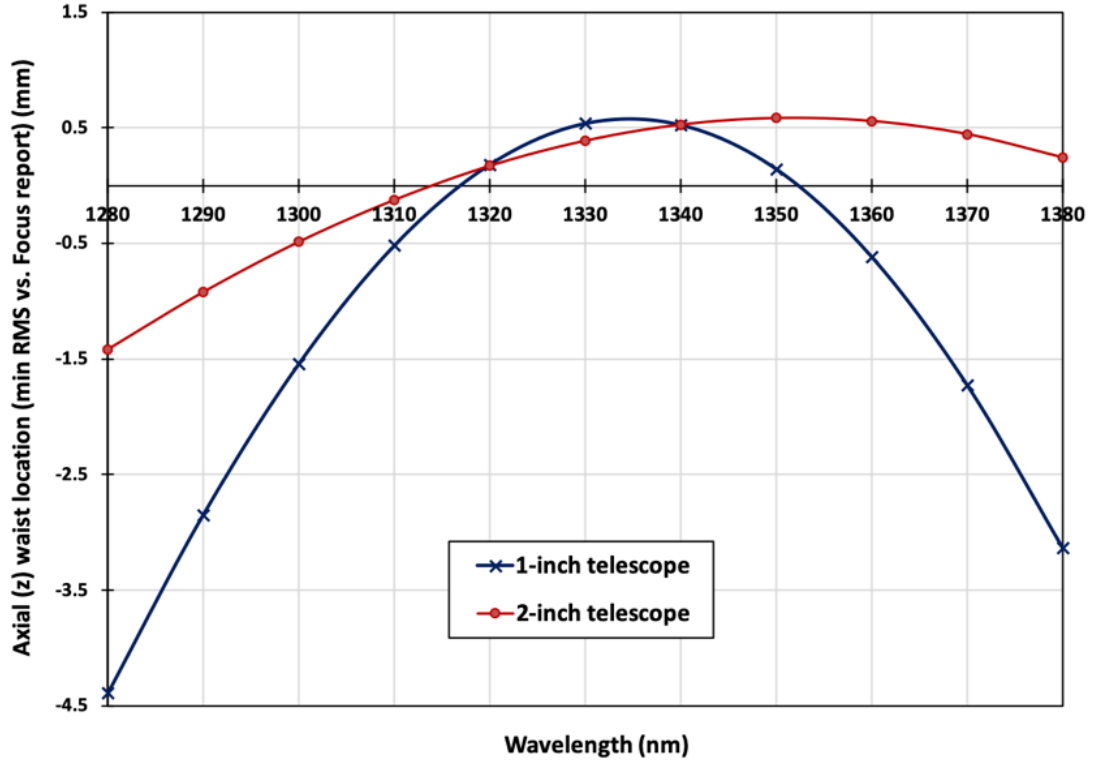


Figure 5.10. Simulation results for the minimum values of axial (z) waist location for the 1-inch diameter lens (blue) and the 2-inch diameter lens (red) telescopes, obtained from the RMS vs. Focus analysis tool.

The diagrams shown in Figure 5.11 were obtained at the receiving fibre and show the spot outlines corresponding to each of the wavelengths in the simulation. The significant variations recorded for the shape of the spot profile at the fibre tip support the assertion that secondary vignetting of light by the fibre's mode field diameter is linked to the loss of light at the edge of the spectrum, with the most marginal wavelengths in this model ($\lambda_{\min} = 1280$ nm and $\lambda_{\max} = 1380$ nm) affected by the largest axial displacements (> 4 mm) and resulting in the largest spot sizes. The optical fibre entrance aperture, whose diameter is equal to the mode field diameter ($9\text{ }\mu\text{m}$), is shown by a black circular outline in Figure 5.11 a) and b).

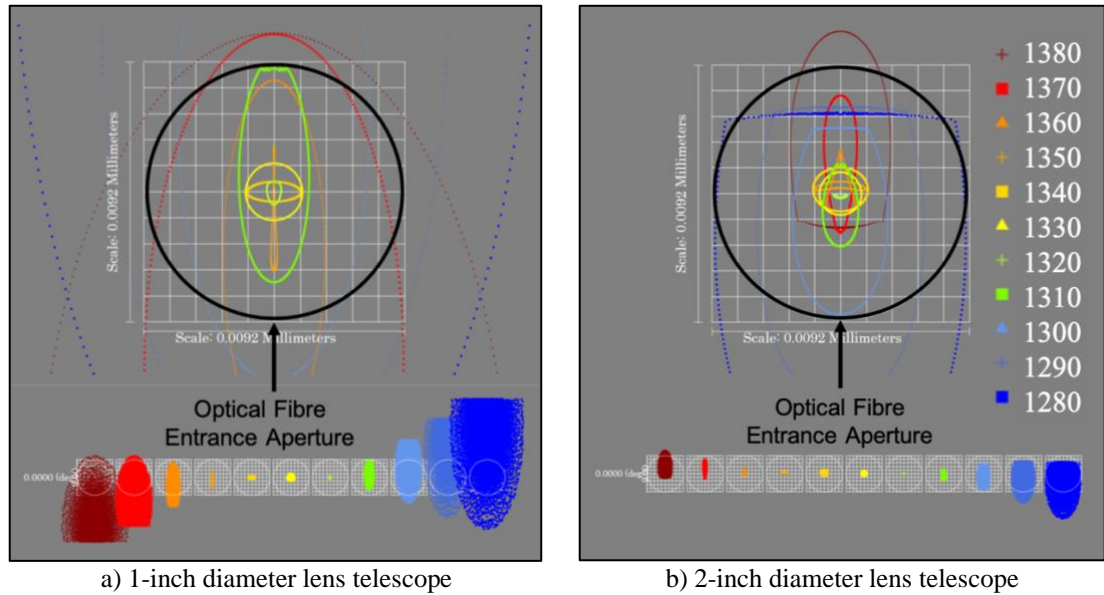


Figure 5.11. a) 1-inch telescope; b) 2-inch telescope Spot diagram beam profiles for each wavelength terminating on the 9 μm diameter single mode optical fibre. Beam profiles for the central wavelengths are approximately circular but become progressively more elongated towards the edges of the spectrum. Wavelength values in nanometers.

Apart from field curvature, other aberrations including astigmatism and off-axis coma are a contributing factor to the variation in the shape of the beams footprint at the receiving fibre. In some cases, the footprint is not elliptical. It is noticeable that, regardless of the apparent vignetting, marginal beams (i.e. those light beams from the edges of the spectrum, propagating furthest away from the telescope optical axis) demonstrate well-defined yet oversized elliptical footprints while those from the centre of the spectrum experience significant beam distortion due to the telescope aberrations but still remain contained within the aperture of the optical fibre tip. The shape of the footprints are mostly elliptical (or at least elliptical sections) but there is a clear difference between the spot sizes in the 1-inch and 2-inch telescope configurations, which is a direct consequence of the defocus introduced by the telescope. However, at certain wavelengths in both configurations, the shape of the footprint clearly indicates prior, primary vignetting had taken place at the PM facet.

The amount of primary and secondary vignetting, on the PM facets and the optical fibre respectively, was recorder for each wavelength in the setup. This was done by measuring the percentage of rays successfully striking each of the two surfaces out of the total number of rays passing through the filter (Figure 5.12 a). The final amount of light coupled back into the receiving fibre was also measured as a proportion of the total number of rays from the input of the system (Figure 5.12 b).

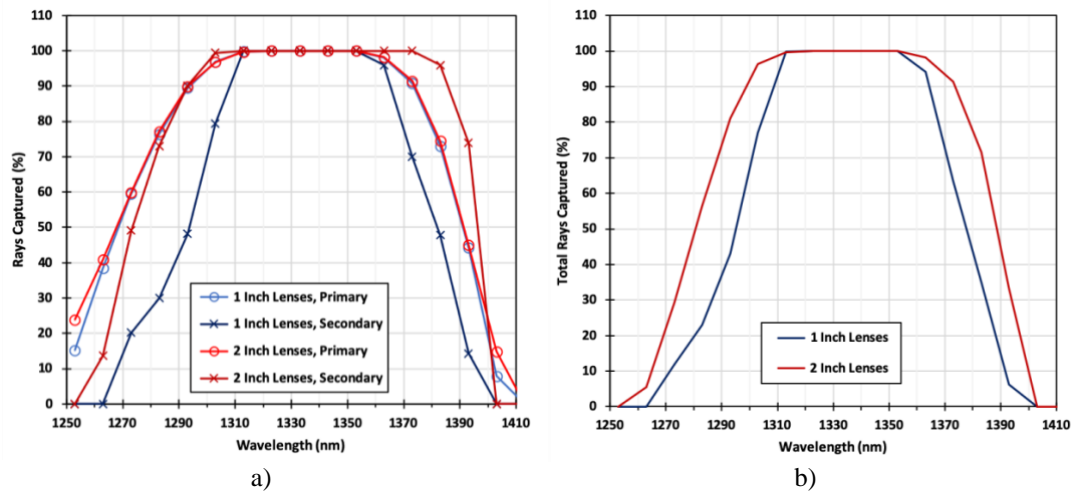


Figure 5.12. Comparison between the percentage of rays captured using 1-inch (blue lines) and 2-inch lenses (red lines). **a)** The percentage of rays captured due to the losses caused by primary (circles) and secondary (crosses) vignetting. **b)** Comparison between the percentage of the total number of light rays terminated to the 9 μm diameter, optical fibre for 1-inch versus 2-inch lenses. Primary vignetting on both setups share approximately equal values while secondary vignetting is reduced for the larger, 2-inch diameter lenses.

The amount of primary vignetting for both diameter lenses is approximately equal but the amount of secondary vignetting has reduced for the larger 2-inch diameter lenses. The results also show a significantly higher percentage of recaptured light at the edges of the spectrum when the 2-inch telescope is used, increasing the overall swept bandwidth of the filter by approximately 20 nm (Figure 5.12 b). A slight bias can be seen towards the longer wavelength values in both configurations, as predicted after viewing the results from the minimum waste location analysis caused by the field curvature aberrations (Figure 5.10). The experimental results show a similar trend occurring when the two configurations are compared (Figure 5.13).

The experimental, 2-inch diameter lens telescope configuration produced a 96 nm wide TSB compared with 75 nm for the 1-inch diameter lenses, which matched the expected increase from the simulated data. A higher proportion of the input spectrum has been recaptured by filling less of the aperture of each lens, and therefore making light propagate closer to paraxial and experiencing less aberration. Although this drop-off effect is experienced by both short and long wavelengths, there is a more marked reduction in the proportion of light recaptured at the short end of the spectrum, as indicated by the skewed graphs in Figure 5.13. This type of analysis opens the possibility of achieving a rebalancing of the spectrum to make it more symmetrical on either side of the central wavelength, minimising the effects of vignetting and aberration.

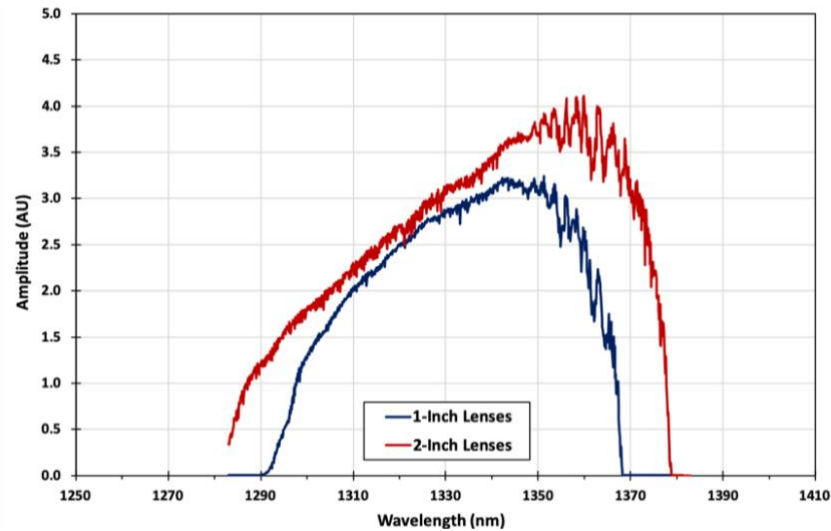


Figure 5.13. TSB for each of the two configurations. The 2-inch lenses (red trace) show a higher optical power amplitude and a wider TSB range (96 nm) compared with the 1-inch lenses (75 nm).

Figure 5.14 is an example B-scan image (see Section 1.5.3) of a thumb. It was obtained using the 1.5 mm collimator, 1145 l/mm TG, 75 × 100 mm telescope with 2-inch diameter lenses and an off-axis (below-axis) PM. It was produced by stacking 32 images together and applying various smoothing and contrast techniques in post processing. The thumbprint ridges on the surface, and the tissue layers beneath it, are clearly identifiable as well as the helical structure of several sweat ducts in the first tissue layer (epidermis). The high reflectivity on the surface layer suggests that the system had a poor sensitivity, which is most likely due to the small beam diameter incident on the grating leading to a poor spectral resolution (Section 3.4).

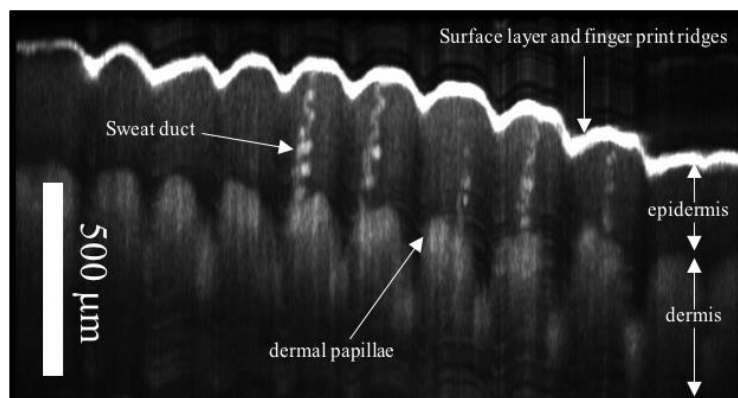


Figure 5.14. OCT image obtained using the PM-based SS system used in this section with the wider 2-inch diameter lenses. The image shows a B-scan of a thumb (see Section 1.5.3). The bright ridges at the top of the image are the finger print in the surface layer. Well defined tissue layering is clearly visible, including the helical structure of several sweat ducts in the epidermis and the dermal papillae at the start of the dermis. The high reflectivity of the surface layer suggest a poor sensitivity, most likely caused by the poor spectral resolution from the small beam diameter collimator (1.5 mm) incident on the grating.

5.6 On-Axis Verses Off-Axis Polygon Mirror Experiment

When the PM is positioned ‘on-axis’ its centre of rotation is aligned with the telescope optical axis and the rays retroreflect off the facets at normal incidence. When the PM is shifted ‘off-axis’ the rays must strike an additional planar mirror at normal incidence before retroreflecting back through the filter. The significance of moving the PM off-axis is that it has the effect of doubling the acceptance angle (Section 4.4), which allows for a wider convergence angle to be accommodated by the PM and therefore a larger spectral range can be filtered. However, this assumes that a much wider convergence angle is already being produced by the combined effect of the diffraction grating and the telescope magnification.

The spectral filter will only accommodate a convergent spectrum with an angular displacement that is equal to or less than the acceptance angle ($\psi/\varphi \leq 1$). Therefore, doubling the acceptance angle does not necessarily double the spectral range unless the convergence angle is already at least twice the on-axis acceptance angle of the PM ($\psi/\varphi \geq 2$). W.Y. Oh et al used this technique to double the swept spectral range of their filter [18], which was necessary because the focal lengths of their telescope (chosen to reduce the beam width to match that of the facets) introduced a very large convergence angle and consequently only gave an edge-to-edge tuning range of 21 nm. Positioning their PM off-axis doubled their spectral tuning range to 42 nm.

A direct comparison between on-axis versus off-axis was tested experimentally in the laboratory. This was initially carried out to confirm the result reported above and to test the reliability of the TSB equation, but also to explore the two configurations in an attempt to understand and identify any potential areas that could be improved. The setup used a 1145 l/mm transmission grating (Wasatch) and a 200 mm × 75 mm telescope (AC508-200-C & AC508-075-C, Thorlabs, USA). This pair of lenses were deliberately selected to create a very wide convergence angle ($> 46^\circ$), much larger than the acceptance angle of the on-axis PM (5°), which would allow the swept spectral range to be doubled. During each facet sweep, only a small range of the convergence angle can therefore be sampled. Translation of the PM into the off-axis position and installation of the RM were the only modifications to be carried out between measurements, no other components or settings needed to be changed.

Before the comparison was carried out, measurements of the total available spectral range were recorded for the on-axis configuration (Figure 5.15). Different regions of the swept spectrum were explored by translating the PM laterally, either side of the optical axis (y-direction). This essentially takes the PM off-axis by adding eccentricity but the magnitude of the translation was so small that the normal incidence condition could be met for a range of wavelengths up to a certain lateral distance.

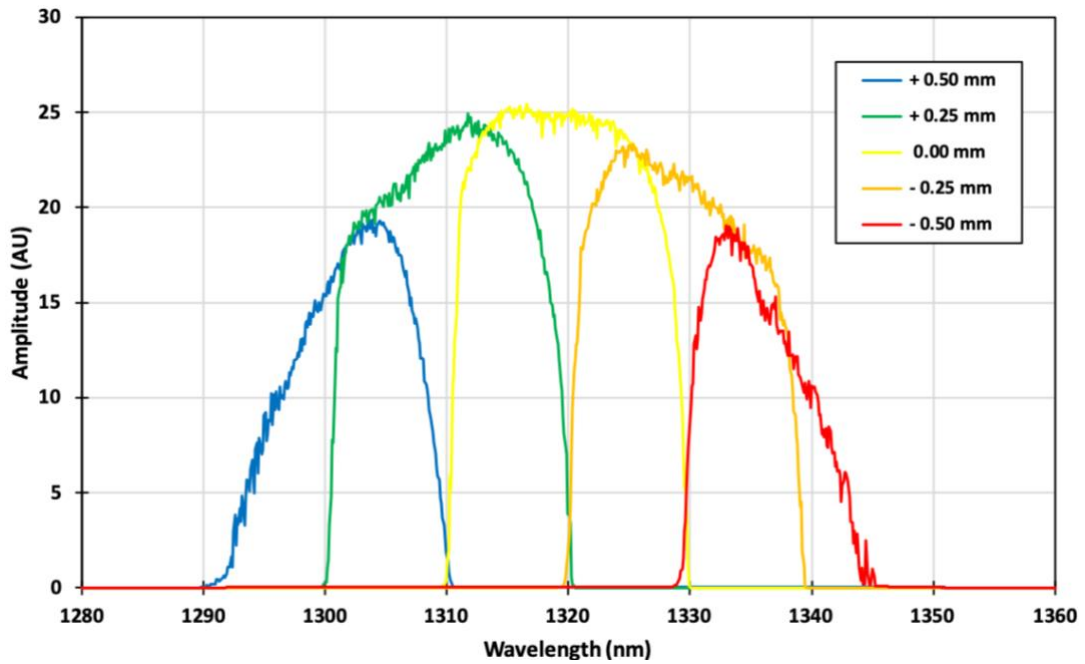


Figure 5.15. Total available spectral range of the filter. Coloured regions were selected by translating the polygon either side of the optical axis. Each spectral region corresponds to a change in laterally displacement of 0.25 mm and has a bandwidth between 15 – 20 nm for a combined edge-to-edge spectral width of 55 nm.

The TSB was measured for five different PM positions. Each of the five positions corresponds to an equidistant change in lateral translation (eccentricity) of 0.25 mm, spanning a total displacement of 1.0 mm (0.5 mm either side of the telescope optical axis). The TSB of each region was approximately 20 nm for the three central envelopes (green, yellow and orange traces) but shortened slightly for the two marginal regions on either side (blue and red traces). The total spectral range across all five measurements was approximately 55 nm, edge-to-edge, which made the configuration suitable for exploring the outcome of moving the PM off-axis, i.e. the TSB could be successfully doubled using this particular set of components and configuration.

The PM was then moved off-axis, the RM was installed and the output was compared against the first result with no lateral translation (Figure 5.15, 0.00 mm, yellow trace). The blue trace in Figure 5.16 was produced with the PM on-axis and the wider, red trace was produced when the PM was positioned off-axis.

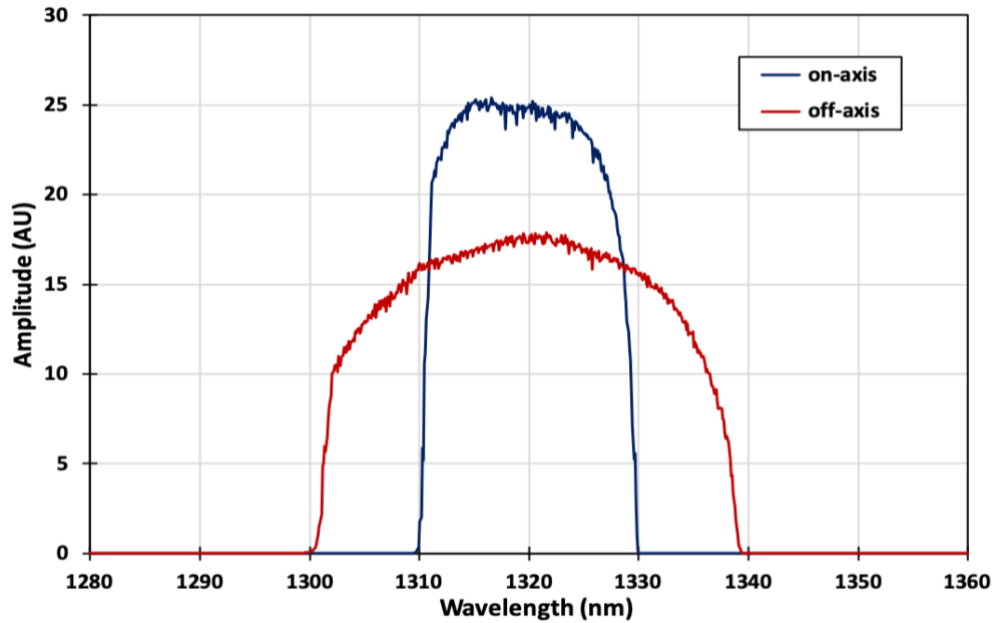


Figure 5.16. Comparison between an on-axis vs. off-axis PM. The experimental setup was identical for both measurements and used a 200 mm \times 75 mm telescope. Translating the polygon off-axis, and installing a retroreflector mirror, increased the TSB from 19.69 nm to 38.56 nm.

It can be clearly seen that the TSB of the off-axis PM is approximately twice the amount of the on-axis PM. The measured values from the experimental data were 19.69 nm and 38.56 nm, which are slightly larger than the calculated TSB values of 18.15 nm and 36.35 nm respectively. The values used in this calculation are given in Table 5.2.

Table 5.2. Parameter values used in the TSB calculation for both the on-axis and the off-axis arrangements.

Parameter	Symbol	Value
Diffraction grating line density	G	1145 l/mm
Diffraction order	m	1
Central Wavelength	λ_c	1330 nm
Diffraction grating incidence angle	γ	48.6° or 0.848 rad
Focal length on Lens 1	F_1	200 mm
Focal length on Lens 2	F_2	75 mm
On/Off Axis	a	1 (on-axis), 2 (off-axis, $E = 8.22$ mm)
Number of facets	N	72 facets

Another observation from the results is that the total power of the off-axis setup has reduced by $\sim 30\%$, and that the envelope of the spectrum appears to adopt a more pronounced curve rather than the approximately flat top seen for the on-axis setup. The flat top is more favourable for use in OCT but this observation could simply be the result of sweeping through a much narrower region of the total spectrum.

Since the convergence angle was still larger than the new acceptance angle of the off-axis PM, there were additional unfiltered regions of the total available bandwidth on either side of the filtered spectrum. This under-sampling meant that the duty cycle of the spectral filter should be 100%. Confirmation of this comes from the fringe pattern (blue) on the oscilloscope trace shown in Figure 5.17. At 12 kHz , the period between sweeps is $83.33\text{ }\mu\text{s}$ and the fringes are seen abruptly stopping at these intervals and beginning again for the next sweep of an adjacent facet.

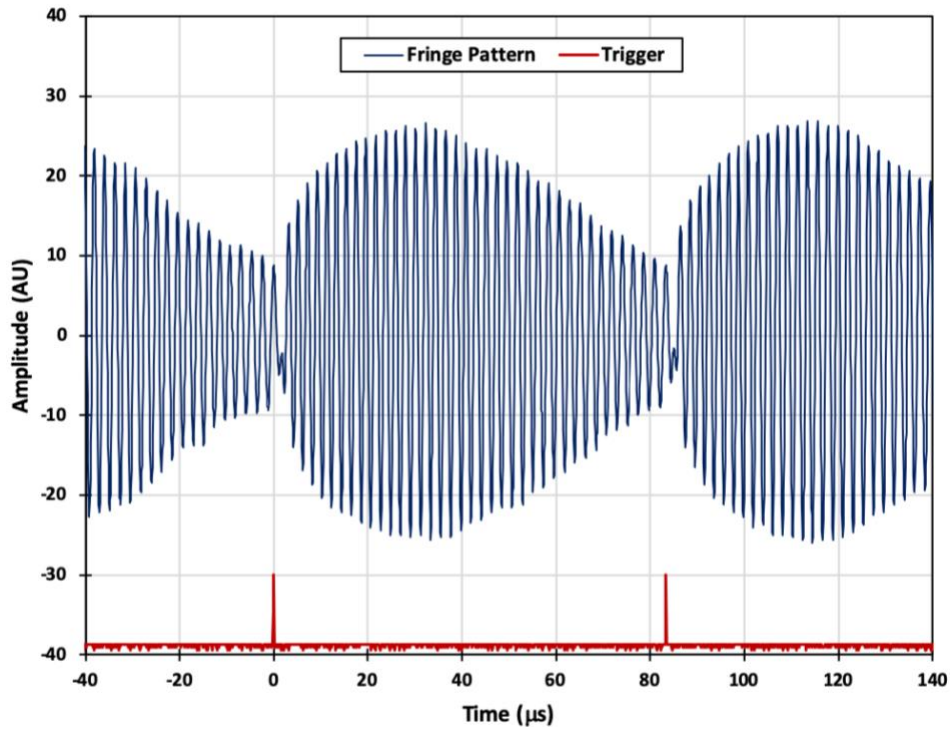


Figure 5.17. Oscilloscope trace for the off-axis polygon using the $200\text{ mm} \times 75\text{ mm}$ telescope. The convergence angle of the spectrum is larger than the acceptance angle of the polygon, which produces a 100% duty cycle with a period of $83.33\text{ }\mu\text{s}$ when the polygon operates at 12 kHz .

It has been shown that the swept bandwidth can be doubled by placing the PM off-axis and installing a RM. Using this particular setup also produced a 100% duty cycle. Both of these features are desirable qualities that benefit the accompanying OCT system, but they were only possible because the convergence angle was already larger than twice the

initial acceptance angle of the PM. If the convergence angle is equal to or smaller than the initial acceptance angle, there will be no additional spectral range available to be filtered. However, when the convergence angle is larger than the initial acceptance angle, the filter also becomes susceptible to simultaneous tuning, which is undesirable and detrimental to the OCT system (Section 4.6).

5.7 Above-Axis Verses Below-Axis Polygon Mirror Experiment

This section investigates whether the performance of the spectral filter is affected by changing the orientation of the PM. The orientation refers to the PM's centre of rotation being placed either above or below the telescope optical axis, after introducing a positive or negative eccentricity respectively, and installing an additional RM (Figure 4.2 a & b, Section 4.4). Initially, and in all of the previous investigations, the PM orientation was below the telescope optical axis, and it was assumed that the opposite configuration would be symmetrical and therefore have no effect on the filter. However, this assumption cannot be correct since the spectrum is distributed asymmetrically in the telescope, whereby the shortest wavelength propagates through the filter below the telescope optical axis and vice versa. The PM's orientation was considered after observing the relative alignment between the PM facet and the image plane of the converging spectrum.

This observation is shown in Figure 5.18, which highlights the area of interest in the simulation. The spectral filter setup used to explore the two different PM orientations had a 1.5 mm beam diameter collimator (F240), 1145 l/mm transmission grating and a 75 × 100 mm telescope with 2-inch (50.8 mm) diameter lenses. The eccentricity and the initial PM rotation angle were 12.14 mm and 22.5° respectively. The asymmetric nature of the spectrum, due to the combined effect of the diffraction grating and the telescope optics, creates a sloped image plane, in excess of 45°, at the point where the converging beams arrive on the TF.

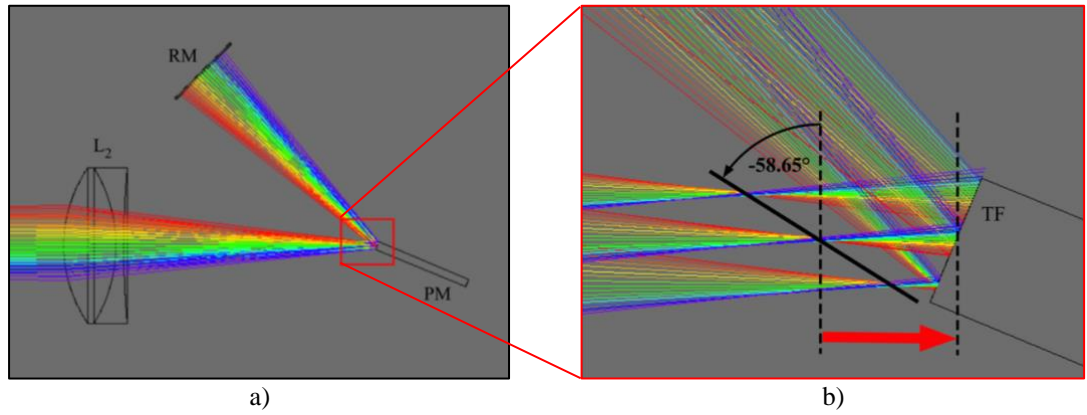


Figure 5.18. Observations from the simulation 3D layout. **a)** shows the spectrum converging from the second lens, L_2 , onto the below-axis polygon mirror, PM, and striking the retroreflector mirror, RM. The red square indicates the enlarged area seen in **b)**. The slope of the image plane and the face of the TF are angled 81.15° from each other, which might decrease the filter's performance. The polygon has been deliberately displaced to the right to clearly show the location of the image plane (red arrow).

With the PM positioned below-axis, the mirrored surface of the TF always slopes in the opposite direction to the image plane of the converging beams (bottom left to top right), which creates a larger misalignment between the two. This is shown clearly in Figure 5.18 b), which is an expanded view of the area highlighted in Figure 5.18 a) (red square) captured from the 3D layout view in the simulation. Three sets of converging rays can be seen striking the TF, representing the chief ray and two marginal rays forming the centre and total width of a single beam respectively, for each of the 17 wavelengths in the simulated spectrum. The location of the PM in Figure 5.18 has been deliberately displaced to the right, further away from the second lens, L_2 , than it would ordinarily be positioned (red arrow), only in order to clearly demonstrate the full slope of the image plane - normally the PM is positioned so that the TF meets the minimum waist point of the converging chief rays for every wavelength.

The slope of the image plane was measured to be approximately -58.65° anticlockwise from the horizontal whilst the TF is rotated in the opposite direction by $+22.5^\circ$. This provides a realistic retro-angle, achievable during the alignment, and gives a total angle between the two planes of 81.15° . It is therefore reasonable to ask if it could be beneficial to the filter's performance to have these two planes aligned. Achieving such an alignment would allow the majority of the rays for each wavelength to strike in approximately the same location, rather than spread them out across the face of the TF, which is demonstrated in Figure 5.19 (with the PM in its normal axial location).

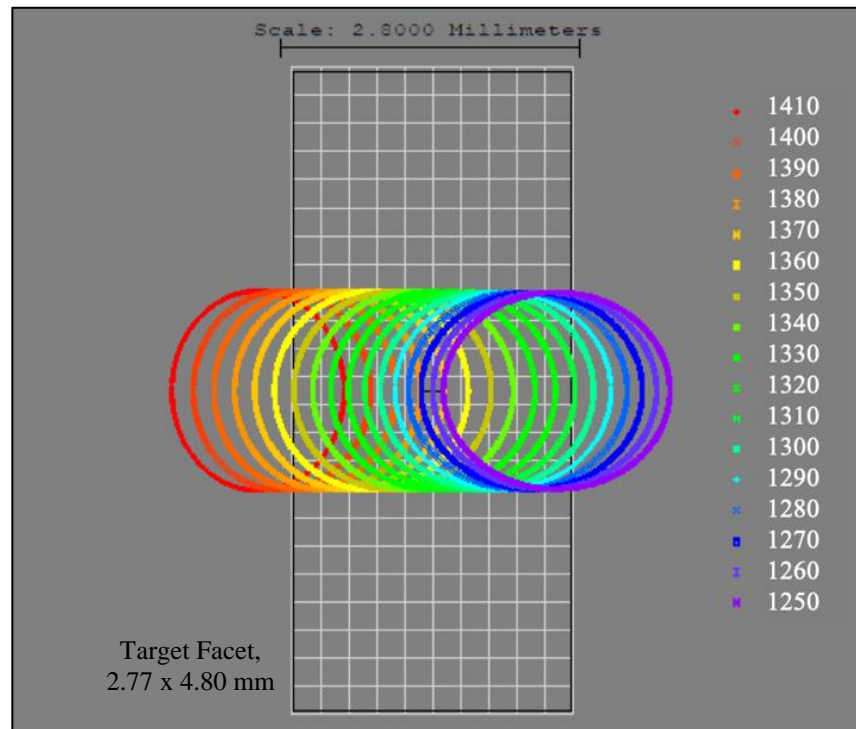


Figure 5.19. TF of the PM showing the circular perimeter of each wavelength in the spectrum. The facet is oriented to successfully reflect the central wavelength only. The beams are seen distributed across the face of the facet, which is caused by the sloping image plane shown in Figure 5.18 b).

The outline of a single facet is seen from the normal (perpendicular) perspective, oriented within the simulation such that it successfully reflects the central wavelength only, but showing the circular profiles of each beam in the spectrum. There is an obvious displacement between the centre of the facet and the beam outlines corresponding to the spectral extremes to such an extent that some of the marginal wavelengths do not fit entirely within the facet's perimeter. This is a perfect example of primary vignetting, previously discussed in Section 2.7.1. Also, visible in the diagram are the elliptical profiles of the individual beams, which gradually stretch out further in the horizontal direction towards the shorter wavelengths.

The alignment between the image plane of the converging spectrum and the TF can be facilitated by shifting the PM's centre of rotation from below to above the optical axis and relocating the RM onto the opposite side of the telescope. The alignment then simply requires adding an appropriate amount of eccentricity to allow the face of the facet to meet the slope of the image plane (Figure 5.20 a) & b).

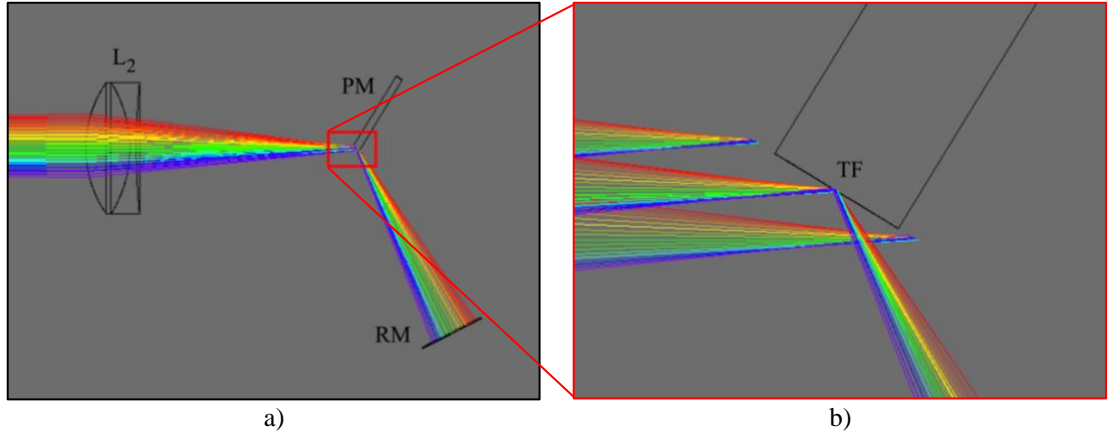


Figure 5.20. 3D layout simulation images. **a)** PM positioned above-axis in the attempt to align the face of the facet to the slope of the image plane. **b)** The TF aligns approximately to the slope of the image plane but introduces a large amount of primary vignetting, shown by the marginal rays terminating on either side of the facet when positioned to accommodate the central wavelength.

The angle of the image plane, resulting from the particular telescope configuration used, is so extreme that a large amount of eccentricity is required to match it to the facet correctly ($E = 27.09 \text{ mm}$, using Eq. 4.18), producing a very large retro-angle (a). This has a negative impact on the visible facet width (b), which is significantly reduced ($l_{\lambda_c} = 1.44 \text{ mm}$ using Eq. 4.7). The beams therefore experience large amounts of primary vignetting, even for the central wavelengths, which is immediately recognised as being too detrimental to the systems performance to be of any practical use and is therefore not a valid solution for aligning the two planes on this occasion.

Although the extreme angle of this particular image plane cannot be matched without creating further complications that reduce the filters performance, a comparison can still be made between two symmetrical configurations to explore any differences between positioning the PM above or below the telescope optical axis. Theoretically, the visible facet width should increase slightly for the longest wavelengths (Section 4.5.1 Eq. 4.8), potentially lowering the amount of primary vignetting they experience and increasing their optical power throughput, but it should also bring the two planes into closer alignment, which could help to answer the initial question with regard to the relative location of the PM – above or below the telescope optical axis.

The angle of the TF with respect to the horizontal (y-plane), in the below-axis configuration, was $+22.5^\circ$ and the opposite value is required for the above-axis configuration, -22.5° , to provide the symmetry for the comparison. The eccentricity of the PM in the simulation is automatically changed to accommodate the chosen facet

angle, which was calculated to be $E = 12.14 \text{ mm}$ (Eq. 4.18). The visible facet width for either configuration is 2.56 mm , which is 0.21 mm shorter than the true value but still larger than the widest calculated beam width, $W_2(\lambda_{min}) = 2.2 \text{ mm}$ (Eq. 4.22, shortest wavelength, $\lambda_{0_{min}} = 1250 \text{ nm}$). Data was collected from both configurations (above vs. below the telescope optical axis) and a comparison between the amounts of primary and secondary vignetting was examined. The results are shown in the graphs of Figure 5.21 below.

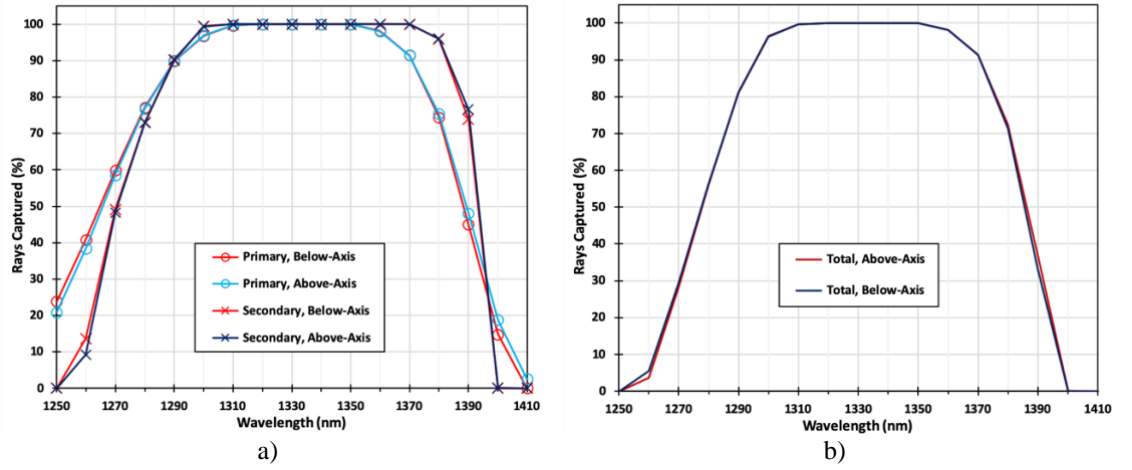


Figure 5.21. **a)** Simulation results of primary (circles) and secondary (crosses) vignetting, on the TF and optical fibre respectively, comparing above-axis (red lines) versus below-axis (blue lines). **b)** Percentage of the total number of rays successfully returned to the optical fibre comparing above-axis (red) versus below-axis (blue). A fractional increase to the number of rays successfully reflected off the TF is detected for the shorter wavelengths when the polygon is below-axis and vice versa for above-axis, as predicted by the theoretical model. The same fractional bias towards the shorter wavelengths is seen for the secondary vignetting although overall fewer rays manage to return to the optical fibre due to the effects of aberration in the lenses.

The difference between the two simulated configurations, for both primary and secondary vignetting, is very subtle and only just distinguishable at the margins of the spectrum. The narrower spectral range returned after the secondary vignetting is indicative of the extra losses caused by the aberrations when the rays travel back to the optical fibre entrance aperture, although the comparative magnitude of this loss is different on either side of the spectrum. The shorter wavelengths appear to experience less primary vignetting on the PM, which is then reduced by the secondary vignetting until both sides of the spectrum are approximately symmetrical. In fact, more rays are successfully captured overall for the longer wavelengths than the shorter wavelengths, despite a higher initial return after primary vignetting. The above-axis PM also appears to slightly favour the longer wavelengths, which would encourage the use of a below-axis PM in an attempt

to recapture some of the lost rays from the shorter wavelength region of the spectrum. However, as already stated, the difference is subtle and does not demonstrate that any significant improvement can be achieved by selecting one PM orientation over the other. The filter's ability to produce larger visible facet widths for the shorter wavelengths, regardless of using an above or below-axis PM, can also be seen in Figure 5.22, which uses Eq. 4.17 to plot the visible facet widths for each of the 17 wavelengths in the simulation (red line). The corresponding facet rotation angles were selected by their ability to successfully return the chief ray of each wavelength to the optical fibre in the simulation (blue line).

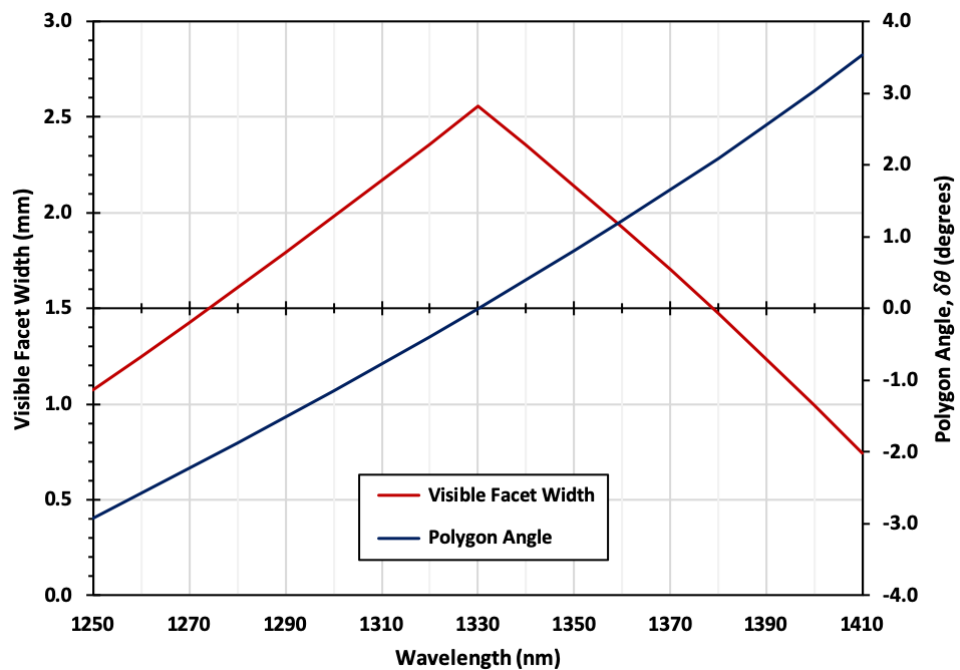


Figure 5.22. Visible facet width as a function of wavelength generated by Eq. 4.17. The increased visible facet width over the shorter wavelength region is due to the non-linear distribution of the spectrum emerging through the diffraction grating, creating a smaller convergence angle in comparison with an equidistant wavelength from the opposite end of the spectrum.

The asymmetry is created by the fact that the shorter wavelengths require a smaller facet rotation angle to successfully return the chief ray to the optical fibre. This is explained by the non-linear distribution of the spectrum as it emerges from the diffraction grating (Section 3.4.3, Figure 3.9) – the shorter wavelengths end up converging onto the PM at a shallower angle than their equivalent, equidistant wavelengths on the opposite side of the spectrum, giving them the advantage of observing a larger visible facet width but not necessarily resulting in more recaptured light, as shown by the previous results. The final

step in this study was to experimentally test the theoretical and simulation results and see if any significant differences could be observed between the two orientations.

The comparison between above-axis and below-axis was simple to replicate experimentally since it only required translating the PM and relocating the RM. All other components could remain aligned and untouched, providing a more accurate comparison. When the experimental results were compared, only a subtle difference was observed (Figure 5.23). The FWHM of the spectrum remained virtually unchanged at approximately 65 nm but a 13 % increase in the peak power output was seen over a 40 nm span around the central region of the spectrum. This could be attributed to the closer alignment between the image plane and the slope of the TF but it cannot be argued conclusively. The maximum swept wavelength also decreases slightly for the above-axis configuration, reducing by 1.7 nm from 1380.5 nm to 1378.8 nm , which is the opposite of that predicted by the theoretical and simulated results.

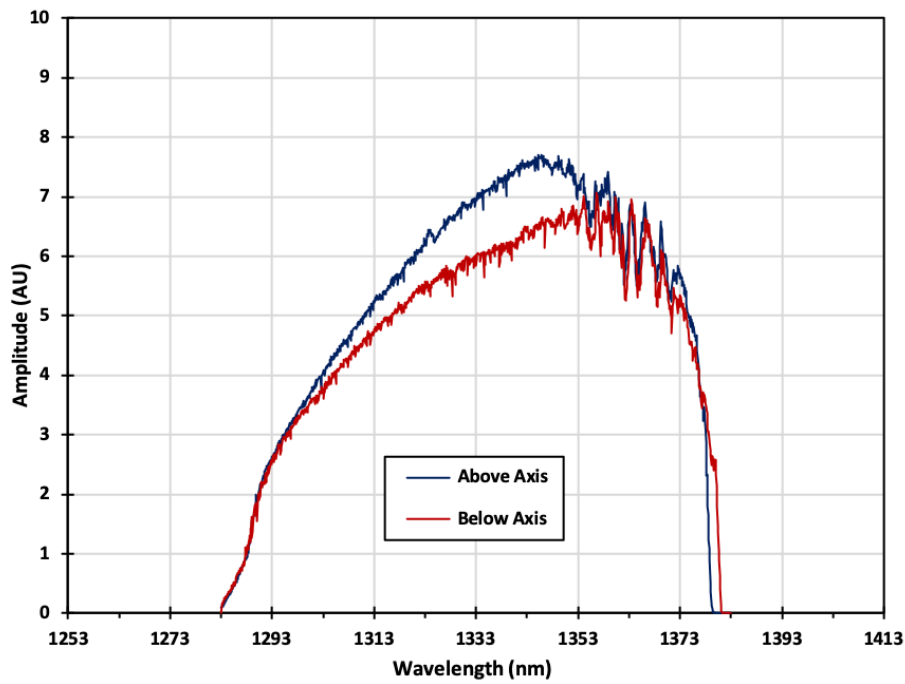


Figure 5.23. SS output for both above-axis and below-axis configurations. The measured FWHM for each is 76 nm and 78 nm respectively. A 13% power increase occurs for the above-axis configuration, which could be attributed to the closer alignment of the image plane and the slope of the facet.

The TSB is 94 nm for above-axis and 96 nm for below-axis, which is $\sim 65\text{ nm}$ shorter than the total available bandwidth provided by the SOA (Figure 2.6, Section 2.3.2.1). However, the predicted TSB is 128.5 nm , which is the consequence of having a larger

convergence angle than the acceptance angle ($\psi > \varphi$), meaning that only 31.5 nm is predicted to be missing. The loss is most likely caused by a less than ideal alignment of the filter, possibly from a misalignment between the path of the central wavelength ray and the telescope optical axis. This highlights the difficulty of maximising the system's performance through the alignment alone, regardless of the challenge to identify the correct components and their positions/orientations. For the same reason, it is unrealistic to expect to measure a noticeable difference in the experimental output due to the change in visible facet width.

Aligning the setup to cause all of the rays to strike the TF at the same location, creating a smaller, more confined spot on the facet, does not necessarily equate to higher performance. This non-intuitive inference is better understood when considering the movement of the TF, which does not pivot around the centre of its own face but rather moves by extension from the centre of the PM itself (Section 4.5.1). The facet therefore sweeps across the converging beams, possessing a different angle and position for each swept wavelength. If the chief rays at each wavelength all converge to the same position, the sweeping facet will undoubtedly produce primary vignetting as a consequence of its movement, regardless of how well the facet size and the beam widths match up, but if the alignment of the filter could be controlled with such precision that the facet aligns with the beam at each wavelength as it sweeps across them, then the primary vignetting could be eliminated altogether, even with a certain amount of aberration present. The following section presents an investigation of this possibility.

5.8 Polygon Mirror Translation Experiment

In Section 5.7, the spectral filter was expected to benefit from aligning the TF on the PM to the image plane of the converging spectrum. The objective was to force the beams to strike the centre of the facet instead of allowing them to spread out laterally across its surface (Figure 5.19). However, aligning these two planes did not demonstrate any significant improvement. The system still suffers from primary vignetting since the TF sweeps across the face of the incident beams rather than simply pivoting beneath them (Section 4.5.1). The following study investigates how this misalignment might be taken advantage of in a different way.

Instead of forcing the converging beams to overlap at a given location, it might be possible to arrange for each beam to be in the correct location of the facet at the right moment of sweeping each individual wavelength. The simulations predicted that primary vignetting could be reduced by displacing the PM axially towards the second lens, in front of its image plane. Figure 5.24 shows an on-axis PM which has undergone a small axial translation. As the PM rotates, the centre of the active facet describes an arc. Due to the axial translation, this arc is now also the locus of chief ray / facet intercepts which used to occur in the focal plane prior to translation. The net result is that the overlap of any one individual beam with the facet is improved, as it now occurs in a location where it could be met more effectively by the sweeping facet.

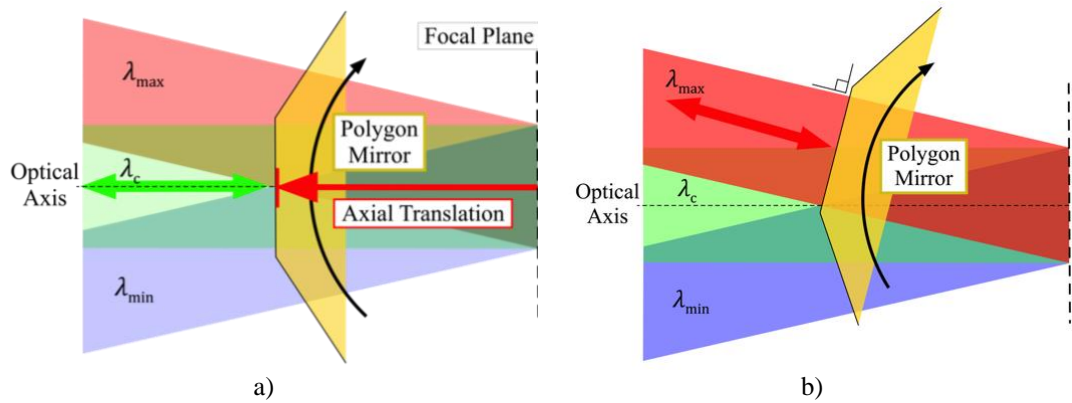
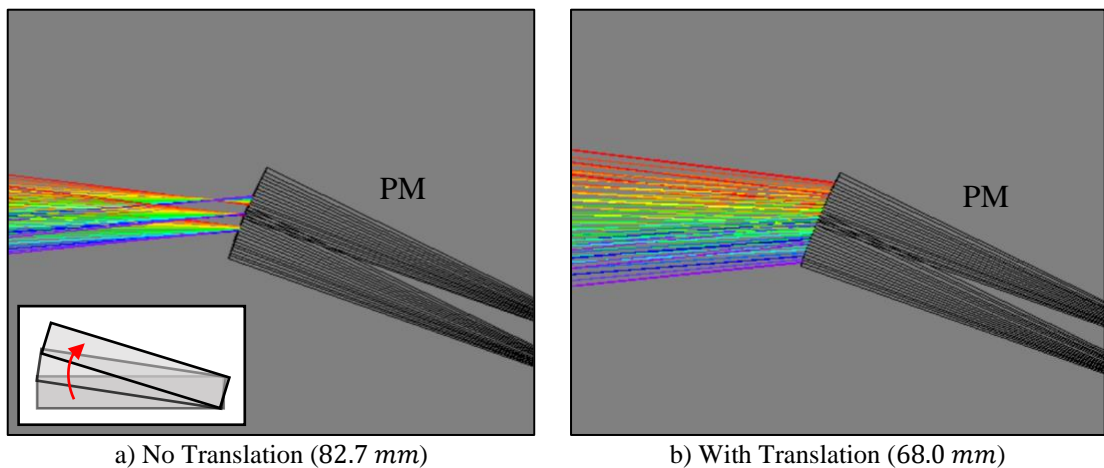


Figure 5.24. On-axis polygon translation. **a)** A slice of the polygon is seen with its TF translated to the left towards the second lens and successfully reflecting the central wavelength only. **b)** As the polygon rotates the TF aligns (at normal incidence) with each converging wavelength, in this case the longest wavelength is swept and the beam is seen completely captured by the TF.

This hypothesis was tested in the simulation to explore its potential. The spectral filter design used a 1.5 mm diameter collimator (F240), 1145 l/mm transmission grating, 75 × 100 mm telescope with 2-inch diameter lenses and the 72-facet PM. Initially, the axial distance of the PM from the final surface of the second lens was selected to align the centre of the TF to the minimum waist point of all the converging chief rays. The simulation used a ‘thickness’ of 82.7 mm. This distance applies to a facet with zero rotation in order to reflect the central wavelength only, although the off-axis PM had an angular displacement of $\theta_E = 22.5^\circ$ provided by the eccentricity, $E = 12.14$ mm. The PM was then rotated by an amount that would successfully reflect the longest wavelength back to the optical fibre and then translated axially towards the second lens until the entire beam of the longest wavelength was observed fitting onto the facet. The longest wavelength was selected, not for its beam width, but for its converging angle (measured

from the telescope optical axis), which is already known to be larger than the equivalent converging angle of the shortest wavelength (on the opposite side of the telescope optical axis) due to the asymmetric distribution of the spectrum emerging from the diffraction grating (Section 3.4.3). The larger, converging angle of the longest wavelength therefore requires a larger axial translation than the shortest wavelength in order to match the PM facet to the incident beam.

The new simulation ‘thickness’ was 68.0 mm from the final surface of the second lens, which is a translation of -14.7 mm towards the telescope (shortening the optical track). In this new location, the TF was able to sweep across the converging beams and match the correct position to capture each wavelength’s beam in its entirety. A comparison between both axial positions is shown in Figure 5.25. Images captured directly from the 3D layout show the PM in its initial position at the focal plane of the second lens in a) and at the new position in b).



*Figure 5.25. Interaction between the incident beams in the spectrum and a single facet of the off-axis PM, undergoing rotation, demonstrated by multiple, overlaid configurations (17 configurations - one for each wavelength in this simulation). **a)** The TF is positioned at the minimum waist point of the converging chief rays (82.7 mm). **b)** The polygon has been translated axially towards the second lens by approx. 14.7 mm , allowing each beam to strike the TF in totality. The insert in **a)** explains the multiple overlaid polygon configurations seen in the main images.*

Both of these images show the position of the TF for every configuration simultaneously. In a) the multiple configurations clearly demonstrate how the facet sweeps across the minimum waist point of all the converging beams. In b) the total sweeping area of the facet is approximately matched by the waist size of the converging beams. After the translation, an examination of the optical fibre surface was carried out for each wavelength to ensure that all of the chief rays were being returned correctly. Any

outbound rays that were not sufficiently aligned to the inbound rays were corrected by changing the facet angle for each wavelength configuration (4 decimal places required).

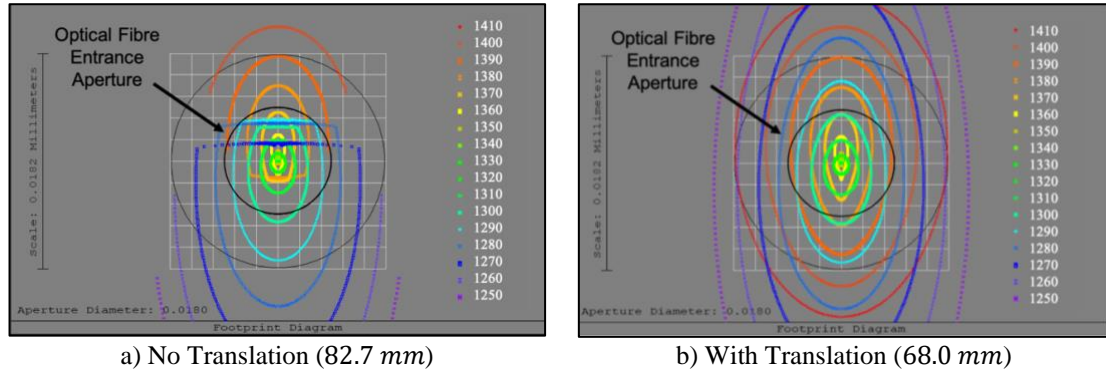


Figure 5.26. **a)** Footprint diagram on the optical fibre tip. Primary vignetting is clearly visible and evident by the abrupt cuts across the perimeter of the incident beams. Secondary vignetting is also seen occurring for some of the shorter, marginal wavelengths. **b)** The footprint diagram for the translated polygon shows no immediate signs of primary vignetting occurring but does present a very similar result for secondary vignetting.

Footprint diagrams of the optical fibre tip are shown in Figure 5.26 a) and b) for both polygon positions respectively. These images simultaneously provide visual confirmation of any primary or secondary vignetting that might be occurring. The cuts across some elliptical beams indicate that primary vignetting has occurred for that particular wavelength whilst any beam perimeter that lies outside the $9\ \mu\text{m}$ diameter of the optical fibre tip (black circles) signifies the occurrence of secondary vignetting, which can be seen predominantly affecting the marginal wavelengths.

The graph in Figure 5.27 a) shows the percentage of rays successfully captured after primary (red lines) and secondary (blue lines) vignetting for the two different configurations. Translating the PM closer to the second lens has completely removed the primary vignetting from occurring, evidenced by the 100 % return of every ray in the simulated spectrum (red crosses). Secondary vignetting has also improved (blue crosses), although a slightly higher percentage of recaptured rays can be seen for some of the shorter wavelengths without translation (blue circles). The asymmetric nature of the graph, about the central wavelength (1330 nm), is caused by the larger spot profiles on the optical fibre tip for the shorter wavelengths. This in turn is suspected to be caused by the wider beam diameters produced by the diffraction grating, combined with the aberrations experienced from travelling through the lenses of the telescope and the collimator.

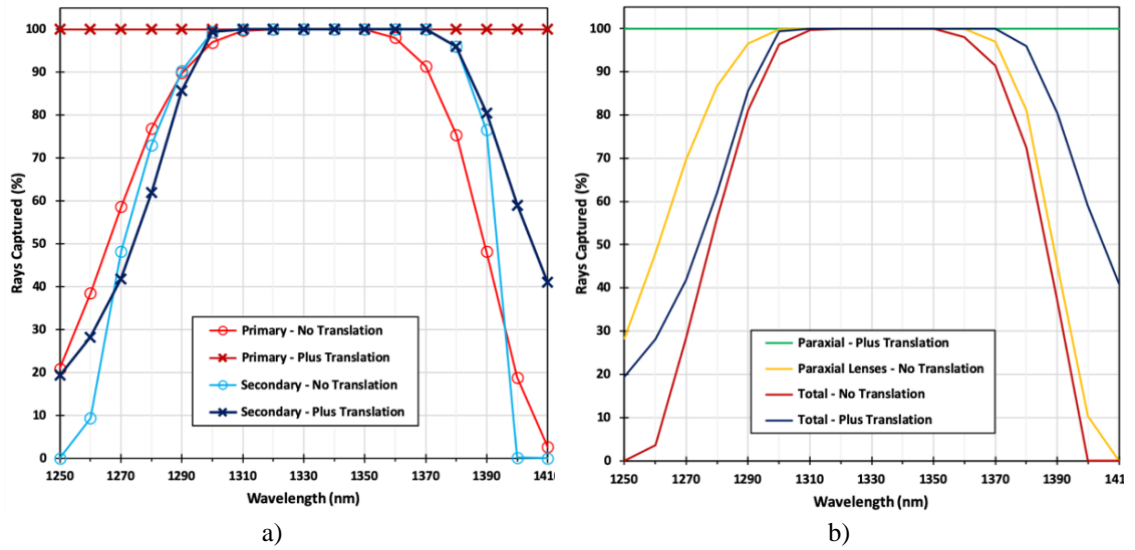


Figure 5.27. The simulation result of translating the PM axially by 14.7 mm towards the second lens. **a)** The effect of primary vignetting has been completely removed (red crosses) and secondary vignetting has also reduced (blue crosses). **b)** Total percentage of recaptured rays, with (blue) and without translation (red). Paraxial lenses were also examined, with (green) and without (yellow) polygon translation, to compare the result of using an ideal setup without the effects of aberration.

In Figure 5.27 b) the total number of rays successfully returned to the optical fibre have been examined, with translation (blue line) and without translation (red line), including a setup using paraxial lenses to compare the performance of the filter without the effects of aberration. Paraxial lenses with translation eliminates both types of vignetting (green line) whilst no translation (yellow line) actually recaptures fewer rays than the realistic result with translation (blue line). However, this is the consequence of primary vignetting occurring on the PM facets, which cannot be escaped by eliminating aberration alone. Interestingly, only a 10 mm translation towards the second lens was needed to remove the primary and secondary vignetting when using the paraxial lenses.

The advantage of performing simulations is that they provide the ability to precisely adjust the distances between each component and then directly observe the consequences. However, knowledge of the exact distances between the components in the experimental setup is limited, making it impossible to replicate the simulations precisely. Even if the optimum distance between the second lens and the PM has been established, in reality the task of fitting them to these exact distances is not realistically achievable. The precise location of the PM can only be estimated because of the inability to accurately measure the exact distances between the components, which block any form of measuring device, and therefore only an approximation can be made. Typically, when aligning the setup, the final location between components depends upon the judgement of the operator,

whereby the task is considered to be complete when the spectral range and optical power output have been optimised. Since the amount of translation needed to remove primary vignetting is small ($\sim 10\text{ mm}$) and that the alignment process is observation based (driven by the goal of maximising the bandwidth), it is even possible that previous alignments were already taking advantage of this translation without realising it. Regardless, it is wise to consider primary vignetting and the axial location of the PM in any future spectral filter builds.

5.8.1 Consequences of Polygon Translation

There is an undesirable consequence that can occur from translating the PM towards the second lens in the telescope. The converging beams may illuminate more than one facet at any given moment during the filtering process and it is possible that the geometry of the arrangement and the specific sizes of the beams and the facet width combine to allow two wavelengths to be filtered simultaneously, which would result in a reduction of the TSB. Section 4.6 introduced this concept and highlighted the specific circumstances that allow this to happen. Simultaneous tuning will occur if the convergence angle is equal to or larger than the acceptance angle, $\psi \geq \varphi$, or if the eccentricity of the PM provides a rotational angle that is equal to or less than half the convergence angle, $\theta_E \leq \frac{\psi}{2}$ (causing SST, Section 4.6.1).

In this particular simulation, the eccentricity was large enough to avoid the latter but the translation of the PM, causing the over-illuminated facets, did allow the former to occur. This is highlighted below in Figure 5.28 a) which shows the spectral filter sweeping two wavelengths simultaneously. In order to demonstrate this effect, two adjacent facets are required. The first facet was positioned at $\delta\theta = -2.5^\circ$ and placed next to a second facet positioned at $\delta\theta = +2.5^\circ$. The first facet sweeps the shortest wavelength (purple rays) while the second sweeps the longest wavelength (red rays) respectively (Figure 5.28 b). The wavelength values for each configuration were manually adjusted until their outbound chief rays returned to the optical fibre. The values of the two wavelengths required 3 decimal place precision in order to align the inbound chief ray to within 50 nm of its outbound self at the entrance aperture of the optical fibre.

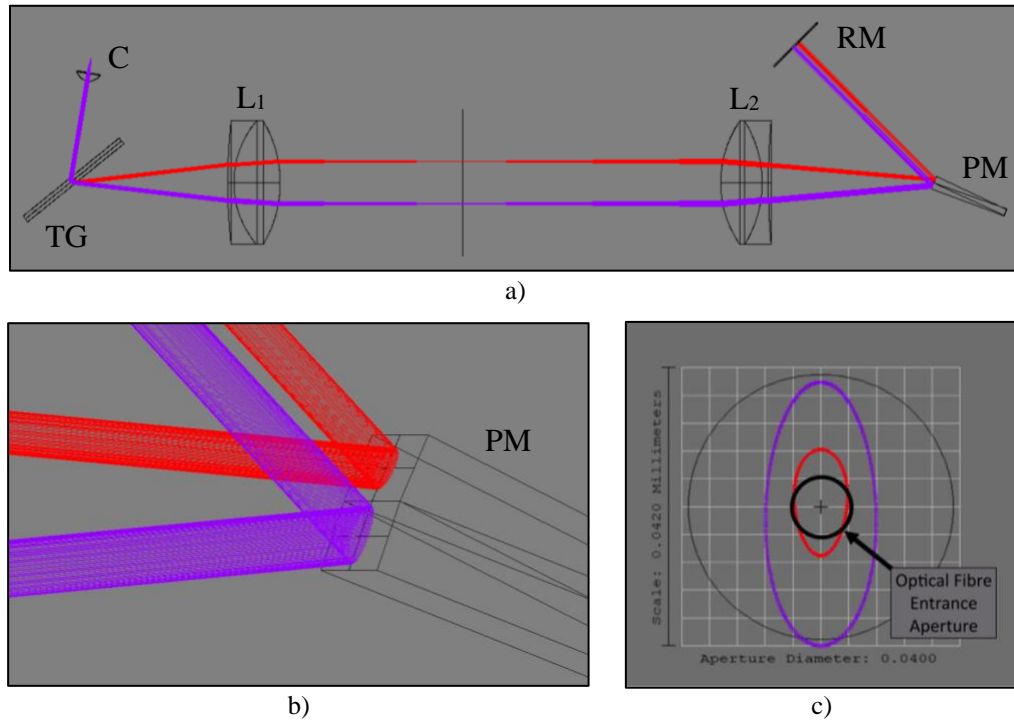


Figure 5.28. 3D layout simulation images of simultaneous tuning. *a)* full setup displaying two wavelengths from opposite margins of the spectrum. Collimator, C, Transmission Grating, TG, Two-lens Telescope, L_1 & L_2 , Polygon Mirror, PM, and Retroreflector Mirror, RM. *b)* close up of two adjacent facets, $\delta\theta = -2.5^\circ$ and $+2.5^\circ$, reflecting both wavelengths simultaneously. The maximum and minimum wavelengths capable of being swept by the filter were 1391.740 nm (red rays) and 1265.245 nm (purple rays) respectively, giving a total spectral width of 126.495 nm. *c)* Footprint diagram of the optical fibre tip (small black circle) displaying no signs of primary vignetting but clearly showing evidence of secondary vignetting due to the overlapping perimeters of each beam – the wider beam of the shorter wavelength suffers the most.

The difference between the two wavelength values gives the TSB of the spectral filter. The longest wavelength was measured to be 1391.740 nm whilst the shortest wavelength was measured to be 1265.245 nm, giving a TSB of 126.495 nm. This value is only 2.0 nm (1.6 %) shorter than the theoretical value predicted by the TSB equation (128.5 nm, Eq. 4.26) and the difference could be explained by the aberrations introduced by the lenses in the telescope and the collimator. Figure 5.28 c) shows the spot profile of both beams as they return to the optical fibre entrance aperture (small black circle). No evidence of primary vignetting can be seen but a significant portion of both beams is lost through secondary vignetting, which is suspected to be caused by aberration.

The agreement between the calculated TSB and the simulation results support the theoretical construction in Chapter 4, and assists with establishing the maximum potential of this type of spectral filter, using known components in a particular arrangement. It has been shown that the extra gain from translating the PM closer to the second lens

significantly improves the output (up to 40 % more recaptured rays for the longest wavelengths) by reducing the amount of primary vignetting and has less impact from simultaneous tuning than expected since the spectral bandwidth is not predicted to be any larger than the value that was found (within 2 %).

5.9 Discussion

The PM-based spectral filter design, using a two-lens telescope, has been systematically explored in an attempt to understand the parameters that govern its operation and how they might be controlled to optimise the filter's performance. The simulations and the experimental work presented in this chapter represent a collection of results that reveal the most about the system's operation. It was shown that certain combinations of component properties can lead to vignetting, which negatively impacts the system by lowering optical power transmission. Primary vignetting at the PM facets and secondary vignetting at the fibre tip are responsible for the majority of optical power loss in the spectral filter. The TSB can also be affected by the choice of components but is fundamentally limited by the parameters of the PM. Nonetheless, the information that was gathered from these experiments has been used to identify the most important parameters and draw useful conclusions about the best approach for optimising the spectral filter.

5.9.1 Collimator Analysis

The collimator comparison presented in Section 5.3 highlighted the importance of selecting the correct combination of collimator beam width and telescope magnification. Specifically, it was shown that whilst a wide range of combinations can be employed, most of them are detrimental to the systems performance because of the final beam widths they produce. If the final beam width is larger than the PM facets, primary vignetting will occur and reduce the maximum power output. However, large beam diameter collimators are preferable for their lower beam divergence and for illuminating more lines/grooves on the diffraction grating – increasing spectral resolution and improving the axial scanning range of the OCT system.

The experimental collimator comparison used two different telescope magnifications to achieve final beam widths that were approximately equal and smaller than the width of the PM facets. The second experimental setup (3.4 mm, 60 × 35 mm) was more

successful at improving the output signal strength (Figure 5.2) but came at the cost of narrowing the returned spectrum (Figure 5.1). The bandwidth reduction experienced by this combination was caused by an uneven pairing between the convergence angle of the telescope and the acceptance angle of the PM ($\psi/\varphi > 1$). This difference reduced the bandwidth of the spectral filter by $\sim 50\%$. The wider bandwidth produced by the first experimental setup (1.5 mm , $75 \times 100\text{ mm}$) is considered to be more beneficial to the accompanying OCT system since it will improve the axial resolution, but the weaker power output will lower the overall image quality (peak loss of $\sim 20\%$). Boosting the swept signal with an additional amplifier, after the ring laser cavity, has been reported in the literature as a solution to this particular problem [20] but a more suitable combination of collimator and telescope magnification, potentially using custom optics, might help mitigate this loss.

The total cavity length and the overall footprint of the experimental setup were also considered in this study, which encouraged the use of short focal length lenses. Telescopes with a short track will reduce the effects of beam divergence and therefore allow the beam to maintain a more consistent and reliable spot size throughout the spectral filter (Section 3.3). Longer track lengths will allow more beam divergence, which increases the risk of primary and secondary vignetting. Although the track length of each telescope in this study was relatively short, the effects of beam divergence cannot be considered negligible when considering the precision required to match the fibres $9\text{ }\mu\text{m}$ MFD.

The properties of the first experimental arrangement, using the smaller beam diameter collimator (F240) and the longer telescope track (350 mm), will lead to an increased beam divergence, compared to the second arrangement (F280 and 190 mm), which is (at least partly) responsible for the lower coupling efficiency and ultimately the reduced power output seen on the OSA (Figure 5.1). This result encourages the use of wide beam diameter collimators and short telescope tracks to minimise beam divergence and the potential losses created by primary and secondary vignetting.

5.9.2 Telescope Design

Section 5.4.1 explored the design of the telescope and made an attempt to determine the parameters that best suited the spectral filter based upon the properties of the other components already established in the first steps of the design hierarchy. Using basic optical geometry, it was found that 1-inch diameter lenses with a focal length up to 75 mm could be successfully employed to capture all of the diverging spectrum emerging from the diffraction grating. All available lenses with focal lengths greater than this value would be over illuminated and therefore reduce the TSB. This emphasised the importance of taking into account the parameters of the light source and the diffraction grating before choosing the properties of the first lens.

The percentage of radial illumination across the surface of the first lens, L_1 , in the telescope was compared for lenses with different focal lengths and diameters. Having a short focal length on L_1 was suspected to reduce the amount of ray deflection for the marginal wavelengths by forcing the beams to propagate closer to the centre of the lenses (paraxial propagation), illuminating a smaller percentage of its total surface area. The marginal rays should then have a higher chance of being successfully recaptured at the entrance aperture of the optical fibre, increasing the system's optical power.

The smallest percentage of radial illumination was shown to occur on a 1-inch diameter lens with a 30 mm focal length (Section 5.4.2) but when it was tested in the simulation it was found that only a small fraction of the rays successfully returned through the aperture of the optical fibre. Many of the rays still made it back to the surface of the fibre tip but were unable to pass through the aperture due to the dramatic changes in the shape and size of their spot profiles. Beam divergence is unlikely to be the cause since the overall path length though the filter was minimised by the shorter track of the telescope (180 mm), even though some losses, caused by primary vignetting, were expected due to the final beam width being slightly larger than the width of the PM facets. Other forms of aberration (e.g. coma, field curvature and astigmatism) were expected to be the cause of the distorted spot profiles. An optimised system must therefore find a way to reduce all forms of aberration if maximum power transmission is going to be achieved.

5.9.3 1-inch Versus 2-inch Diameter Lenses

Section 5.5 explored the effect of using telescope designs with different lens diameters. The results from the simulation and the experimental work both found that the larger, 2-inch diameter lenses were more successful at returning a greater number of rays back to the $9\ \mu\text{m}$ optical fibre tip. In the experimental study, the overall optical power increased and the TSB also widened by $21\ \text{nm}$ compared to the output of the 1-inch diameter lenses (Figure 5.13). This is suspected to be a consequence of minimising the effects of aberration.

The aberration analysis carried out in Section 5.5.1 showed that light rays from the shorter wavelength region of the incident spectrum suffered less from the effects of ray deflection due to propagating closer to paraxial when compared to the light rays from the longer wavelength region (Figure 5.7). This was caused by the asymmetric distribution of the diverging spectrum and suggested that a higher output power might be obtained from the shorter wavelength region. Instead, both lens diameters produced a significantly lower output power at the shorter wavelength region of the spectrum (Figure 5.13), which could be a consequence of the asymmetric distribution of the minimum waist values for each wavelength at the mid focal plane (Figure 5.10). The analysis did not consider the nature of the diverging spectrum or the unique incidence angle of each wavelength on the surface of the lens, which would both introduce additional aberrations (e.g. coma, defocus and astigmatism) that could impact ray propagation.

It was shown how a combination of various aberrations were responsible for secondary vignetting on the $9\ \mu\text{m}$ diameter of the optical fibre tip (Figure 5.11). The spot shape and size at each wavelength on the fibre tip varies across the spectrum according to these aberrations, whereby a unique form of chromatic, field curvature defocus occurs and distorts the focal plane, between the two lenses, consisting of the minimum waist point at each wavelength (Figure 5.9). This surface became less curved as a result of using the larger diameter lenses and peaked at a longer wavelength value than the central wavelength. It is suspected that the filter's performance would improve further if this surface could be made perfectly straight and aligned vertically with the mid-focal plane of the telescope.

5.9.4 On-Axis Versus Off-Axis

Section 5.6 studied the effects of positioning the PM off-axis. It was reported in the literature that this action could increase the TSB of the spectral filter [18]. Positioning the PM off-axis was carried out by applying positive (or negative) eccentricity, translating its centre of rotation laterally above (or below) the telescope optical axis and installing an additional planar mirror to act as a retroreflector. Before the RM was installed, it was shown that small amounts of eccentricity could be applied to an on-axis PM and the spectral filter would continue to operate successfully. However, adjusting the eccentricity of the PM over small displacements, either side of the telescope optical axis, allowed different swept regions of the spectrum to be selected (Figure 5.15). This can only be achieved if the convergence angle is much larger than the acceptance angle of the PM. The spectral filter setup in this study was deliberately designed to produce a very large convergence angle ($\psi > 8\phi$), which caused very narrow swept regions to be returned (15 – 20 nm). If the spectral filter was designed to accommodate a much wider light source (i.e. several hundred nanometers of bandwidth) and the selectable swept region were increased (e.g. 100 – 150 nm), then this technique could be used to perform OCT at different wavelengths simply by adjusting the PM eccentricity. However, various technical challenges would have to be met first in order to achieve this.

Positioning the PM off-axis and installing the RM was shown to successfully double the swept region of the spectrum. Again, this is only due to having a wider convergence angle than the acceptance angle of the PM, which must be at least twice as large if the swept region is to successfully double. Ideally, the convergence angle would be equal to the acceptance angle, after positioning the PM off-axis ($\psi = \phi = 10^\circ$), but this relies on precisely matching the properties of the light source, diffraction grating and telescope, which can be achieved but only at the cost of sacrificing other parameters. This will be picked up again and discussed in more detail in Chapter 7. The experimentally recorded TSB values for the on-axis and off-axis arrangements were both larger than the predicted values given by the TSB equation (Eq. 4.26), which indicates the existence of some residual errors in the filter alignment compared to the parameters used in the TSB calculation. For example, the incidence angle on the grating could not be measured accurately and therefore is unlikely to be exactly the same as the 48.6° value used in the calculations.

5.9.5 Above-Axis Versus Below-Axis

Section 5.7 revealed that switching the PM's orientation from below-axis to above-axis produced no significant improvement to the SS output based on the change in the visible facet width alone (varying the amount of eccentricity will have a much larger impact by itself). However, the final output was shown in the simulations to favour the longer wavelengths when the PM is above-axis and the shorter wavelengths when the PM is below-axis, which agrees with the theoretical work presented in Section 4.5.2 (Figure 4.9). Matching the slope of the TF to the slope of the image plane was shown to be impractical for this particular setup and only succeeded to introduce a larger amount of primary vignetting, which limits the number of recaptured rays and therefore reduces the systems total optical power. However, the peak output power did increase by 13 % in the experimental study, which could be the consequence of bringing the two planes into closer alignment. If the closer image plane/facet alignment is responsible for the increased power, it might not necessarily be desirable since it favoured the central wavelengths at the expense of the marginal wavelengths.

5.9.6 Polygon Mirror Translation

Section 5.8 showed that translating the PM along the optical axis, closer towards the second lens in the telescope, can be an acceptable solution to minimise the effects of primary vignetting (or removing it entirely), provided that the size of the beams are equal to or less than the width of the PM facets. It was only necessary to fulfil this condition for the shortest wavelength since it has the largest beam diameter. However, the longest wavelength has the largest converging angle, incident on the PM (measured from the telescope optical axis), which depicts how far the PM must be translated towards the second lens in the telescope. Assuming that eccentricity has been taken into account at the outset, this distance will change depending on the choice of components but ultimately is decided by the operator, who will adjust the axial position of the PM until the maximum output is achieved. However, the required magnitude of the PM translation, necessary to eliminate the primary vignetting, might not be considered obvious to anyone without this prior knowledge. Rather, a simple use of geometric optical principles would encourage them to align the PM facet to meet approximately at the focal plane of the second lens, which might be significantly further away from the optimum location and therefore could remain undiscovered.

5.9.7 Final Conclusion

The spectral filter should ideally sweep through the entire bandwidth of its input light source and produce narrowband, laser linewidths from every instantaneous point throughout the spectrum. The optical power of each linewidth should also be of sufficient amplitude and ideally equal in magnitude across the whole spectral range. However, various factors make this difficult to achieve in reality. The optical power output and the TSB are both determined by the intrinsic parameters of the individual components and their suitability when used alongside other components. Maximising the optical power across the entire spectral range depends on minimising the amount of primary and secondary vignetting, whilst maximising the TSB mostly depends on meeting the limited extent of the PM facet, whereby the convergence angle must be less than or equal to the acceptance angle. The challenge is to find a balance between these two competing demands, which can be problematic due to the inverse nature of the telescope, acting on the final beam width and the convergence angle, as well as the inherent aberrations caused by the lenses. If the aberrations were removed by replacing the refractive optics with an alternative method, the design of the filter could then focus exclusively on minimising the primary and secondary vignetting. After arriving at this conclusion, it was speculated that two parabolic mirrors might be used, instead of a two-lens telescope design, to invert the diverging spectrum from the grating into a converging spectrum at the PM. Parabolic mirrors would instantly remove the majority of aberrations and therefore should encourage more rays to return to the optical fibre tip. This proposal will be thoroughly introduced in the next chapter where it has been extensively explored both experimentally and in the simulations.

CHAPTER 6

90 DEGREE, OFF-AXIS PARABOLIC MIRRORS

6.1 Chapter Introduction

The following work introduces the concept of using a pair of 90 degree, off-axis parabolic mirrors instead of a two-lens telescope design. This novel approach came from understanding the effects of aberration on the system and the potential benefits that may arise from removing the refractive optics. Replacing the telescope lenses with mirrors minimises the amount of aberration and allows the light rays to more closely follow their intended paths through the spectral filter.

6.2 Parabolic Mirrors

A parabolic mirror can reflect a collimated beam of light at 90 degrees and converge the rays into a single focal point. The distance to this focal point is called the Reflected Focal Length (RFL) and is measured from the axis of collimated beam propagation (Figure 6.1). The rays can then be collimated by a second, inverted parabolic mirror. Therefore, a pair of parabolic mirrors can be used to achieve the same goal as the two-lens telescope – by inverting the diverging spectrum from the grating into a converging spectrum onto the PM.

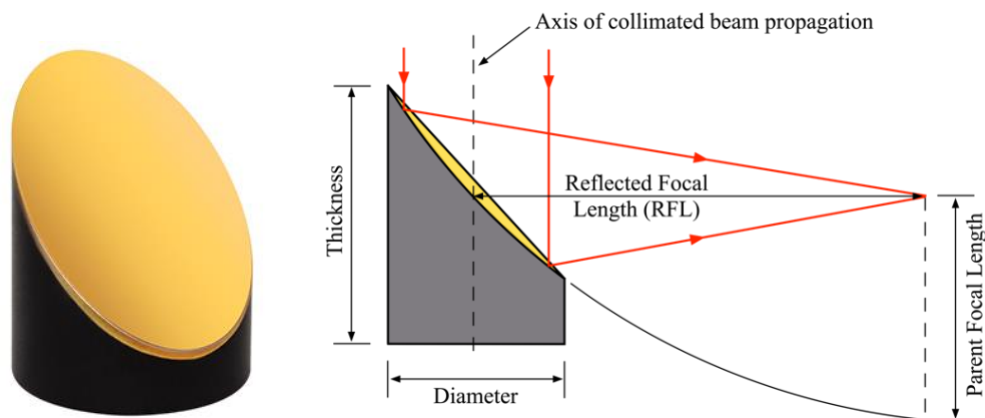


Figure 6.1. 90 degree, off-axis parabolic mirror (MPD129-M01, Thorlabs, USA). Incident beams of light (red rays) strike the parabolic mirror along the axis of collimated beam propagation, which then reflect at 90 degrees and focus at the reflected focal length (RFL). Image courtesy of Thorlabs, USA [71].

Another advantage of using the parabolic mirrors is that they can accommodate a much wider range of wavelengths¹⁴ and therefore do not need to be changed as a result of installing a different light source. This makes the system easier to modify since fewer components need to be changed, which also reduces the cost. A detailed analysis of using parabolic mirrors will be presented in this chapter, and how they can be used to significantly improve the output of the SS. Suggestions that could improve this design further will also be discussed in Section 6.6.

6.3 Zemax™ Simulation Methods

The parabolic mirrors were initially simulated in Zemax™ to explore their potential. They were constructed using the dimensions of commercially available products from Thorlabs, USA. A variety of mirror diameters and RFLs were available but the final choice was made after several considerations. Large-diameter mirrors with a long RFL, whilst perfectly operable, would unnecessarily increase the overall footprint of the experimental setup. Smaller mirrors with a short RFL would decrease the footprint and be more suitable since it is still preferable to minimise the spectral filter's free-space laser cavity length (Section 2.3.2.2) in order to minimise the amount of beam divergence (Section 3.3). Therefore, the smallest parabolic mirrors were initially considered, which had a half-inch diameter (12.7 mm) and a RFL of 15 mm (MPD00M9-M03, Thorlabs).

However, it quickly became apparent that these parabolic mirrors would be difficult to align correctly in the real-life experimental setup because the components' mounting stages would physically restrict them from being positioned in such close proximity to one another. The half-inch diameter of this mirror means that it would have to be positioned less than 43 mm from the high density (1145 l/mm) diffraction grating in order to capture the whole of the diverging spectrum, without over-illuminating the mirrors' surface and losing light at the margins. This close proximity, whilst allowed by the size of the mirror itself, is difficult to achieve when taking into account the precision alignment mounting stages needed for both parabolic mirrors, which would position the second mirror just 30 mm from the first due to their combined RFLs. The bulk of the mechanical mounts, including that of the PM also, does not accommodate this particular

¹⁴ Within manufacturing specifications, >97% reflectance between 800 nm – 20 µm [79]

geometrical arrangement. If a diffraction grating with a line/groove density higher than 1145 l/mm were to be used, providing a finer spectral resolution (Section 3.4), an engineering solution would need to be found to achieve the correct arrangement.

It was also preferable to select parabolic mirrors that were compatible with the mounting stages already available in the laboratory, as this would help to reduce the number of components that needed to be ordered and therefore lower the cost. As a result, one inch (25.4 mm) diameter mirrors with a two inch (50.8 mm) RFL were chosen for the simulations (MPD129-M01, Thorlabs). Another condition of the spectral filter design was that the converging spectrum must be fully accommodated by the acceptance angle of the PM. When the properties of both parabolic mirrors are identical, there will be no magnification applied to the beam width and no change to the divergence angle when the spectrum converges onto the PM. Therefore, if the divergence angle from the grating is too wide ($> 5^\circ$ for an on-axis PM or $> 10^\circ$ for an off-axis PM), light will again be lost from the margins of the spectrum.

6.3.1 On-Axis Simulation Setup

The parabolic mirrors were built into the spectral filter simulation, which was initially set up with the PM placed on-axis (Figure 6.2). Since the selected pair of mirrors, P_1 and P_2 , were identical, they would have no impact on the final beam width or the convergence angle. Therefore, as discussed in Chapter 4, for a symmetrical (1:1) telescope, the beam diameter emerging from the collimator (W_0) needed to be less than or equal to the width of a single PM facet ($W_0 \leq L = 2.77 \text{ mm}$), and the diffraction grating needed to produce a divergence angle ($\Delta\delta$) that was less than or equal to the acceptance angle of the on-axis PM ($\Delta\delta \leq \Phi = 5^\circ$). This was necessary to avoid primary vignetting and light loss at the margins of the spectrum respectively¹⁵. To accommodate these conditions, the simulation used a 1.5 mm beam diameter collimator, C , (F240-APC-C, Thorlabs) and a blazed (ruled) reflective diffraction grating, RG , with a line density, $G = 600 \text{ l/mm}$, a blaze wavelength, $\lambda_B = 1250 \text{ nm}$, and a blaze angle, $\gamma_B = 22.0167^\circ$ (GR25-0613, Thorlabs).

¹⁵ Primary vignetting can only be avoided for the central wavelength when the beam diameter is equal to the width of the PM facets. To avoid primary vignetting for every wavelength requires using a smaller beam diameter and/or applying additional techniques that were presented earlier in Section 5.8.

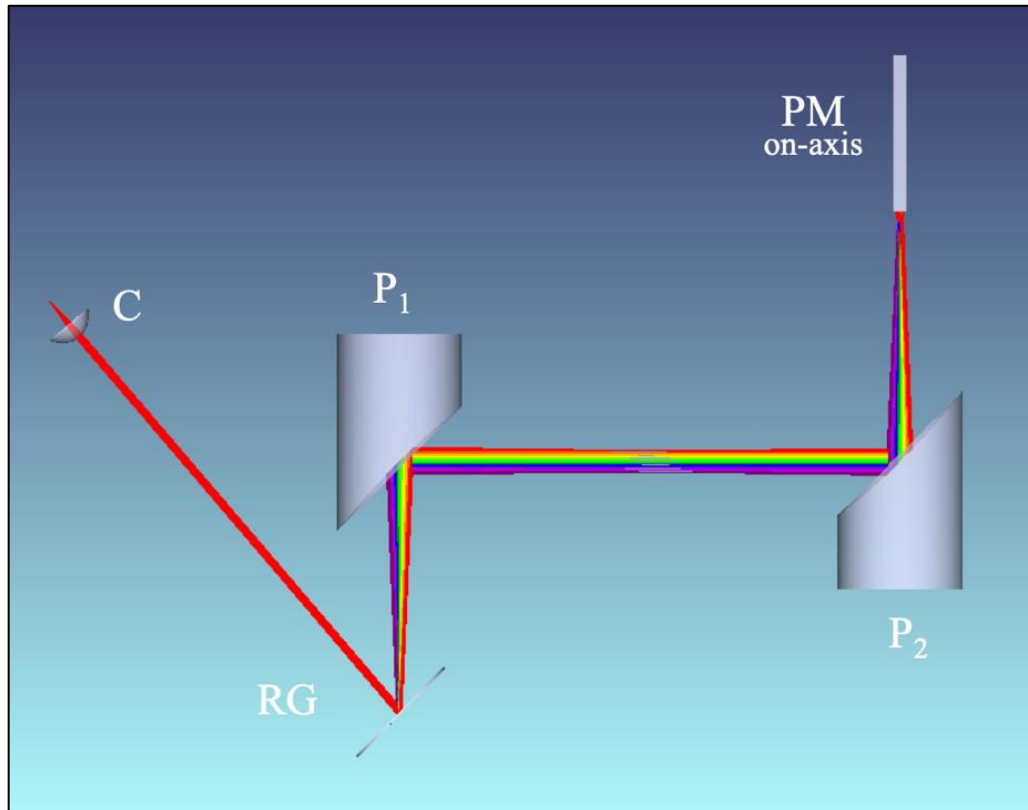


Figure 6.2. Zemax simulation layout using a collimator, C, diffraction grating, RG, two parabolic mirrors, P_1 and P_2 , and a polygon mirror, PM. The different wavelengths used are coloured according to their order in the spectrum, where the red and blue rays represent the longest and shortest wavelengths respectively.

The smaller line density on the new reflection grating creates a narrower divergence angle. This was more suitable than the previous transmission grating, which had a divergence angle ($\Delta\delta = 16.88^\circ$) that was over three times the acceptance angle of the on-axis PM ($\varphi = 5^\circ$). The previous grating would therefore suffer significant losses at the margins of the spectrum and result in a reduction to the TSB. The magnitude of the divergence angle created by the new reflection grating could also be adjusted by changing the incidence angle of the beam emerging from the collimator. This conveniently provides a method to match the convergence angle to the acceptance angle of the on-axis PM and therefore allows a 100% duty cycle to be achieved.

Unfortunately, the new reflection grating distributes the spectrum in more than one order, meaning that only 60-80% of the light will propagate in the first order ($m = 1$) [72]. This was not an issue with the previous transmission grating, which, despite some reflection and zero order transmission losses, only guided the transmitted light in the first diffraction order ($m = 1$) and had a specific operating incidence angle that maximised the optical

power transmission (Section 3.4). The maximum optical power output of the reflection grating is not necessarily going to occur for the incidence angle that provides the optimum divergence angle, and therefore unavoidable power loss should be expected. This reinforces the need to maximise the overall performance of the spectral filter.

The incident beam angle on the reflection grating must be selected to create a divergence angle that meets the acceptance angle condition in order for the on-axis PM to successfully sweep through the whole spectrum, i.e. $\Delta\delta \leq 5^\circ$. The incidence angle that meets this condition can be found by inserting the minimum and maximum wavelength values into Eq. 3.4 and exploring the output as a function of incidence angle. The simulation initially used a 100 nm bandwidth, centred on 1330 nm, with minimum and maximum wavelength values of $\lambda_{min} = 1280 \text{ nm}$ and $\lambda_{max} = 1380 \text{ nm}$ respectively. These values were used to generate the diffraction and divergence angles shown in Figure 6.3 a) and b) respectively.

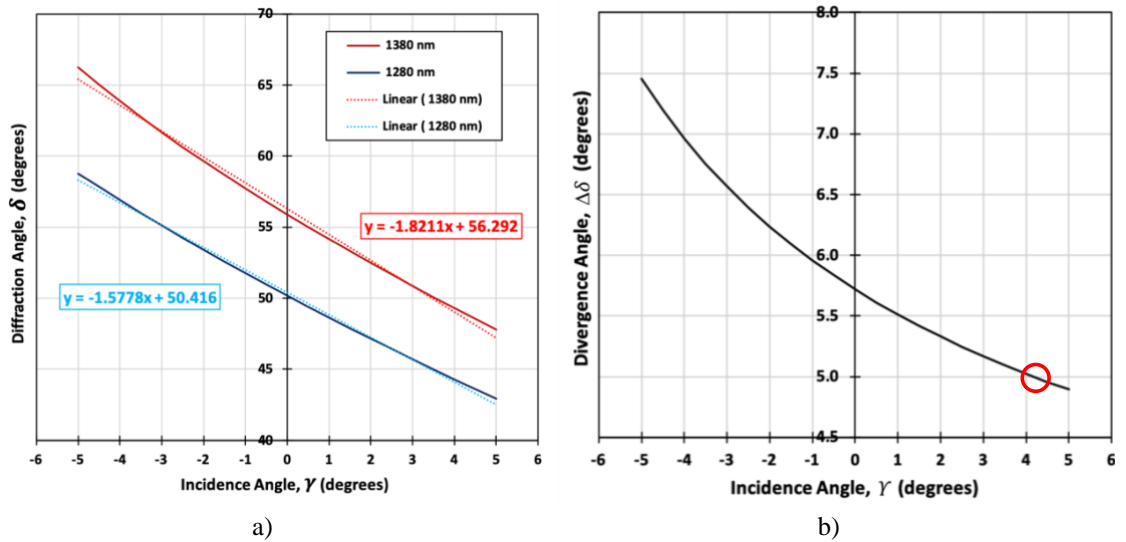


Figure 6.3. **a)** Diffraction angle, δ , as a function of incidence angle, γ , for the two marginal wavelengths in the simulated spectrum - $\lambda_{min} = 1280 \text{ nm}$ (blue) and $\lambda_{max} = 1380 \text{ nm}$ (red). Dissimilar gradient values from the trendlines demonstrate the increasing divergence angle with decreasing incidence angle. **b)** Divergence angle, $\Delta\delta$, as a function of incidence angle, γ , between the two marginal wavelengths. The on-axis PM acceptance angle of 5° is met when the incidence angle is set to 4.2° (red circle).

The two curves in Figure 6.3 a) were generated using the grating equation (Eq. 3.2) and inserting the two marginal wavelength values – 1250 nm (blue curve) and 1380 nm (red curve). The difference between the diffraction angles of the two marginal wavelengths gives the divergence angle as a function of incidence angle, $\Delta\delta(\gamma) = \delta_{max}(\gamma) - \delta_{min}(\gamma)$. The dissimilar gradient values of the linear trendlines from each curve

demonstrate that a wider divergence angle is produced for increasing negative incidence angles. The divergence angle curve in Figure 6.3 b) shows that a $+4.2^\circ$ incidence angle is required (red circle) to meet the 5° acceptance angle condition of the on-axis PM. If this incidence angle is selected, the spectral filter can be expected to return filtered light, back to the optical fibre tip, from all regions of the available spectrum. If the incidence angle is less than this value the TSB should decrease.

6.3.2 On-Axis Simulation Results

The simulation was set up twice to explore two different incidence angles: -5° and $+5^\circ$. Adding the extra 0.8° of incidence angle to the $+4.2^\circ$ allows for the non-symmetrical distribution of the spectrum in the divergence angle (Section 3.4.3), which had a larger angular displacement above the telescope optical axis ($\delta_+ = 2.50^\circ$) than below ($\delta_- = 2.12^\circ$). If the $+4.2^\circ$ incidence angle were used, some of the marginal rays at the longer wavelength region of the spectrum would not be accommodated by the spectral filter. The negative incidence angle (-5°) gives a divergence angle of 7.45° , which is larger than the acceptance angle of the on-axis PM and should therefore only filter through a fraction of the total spectral range, given by $5^\circ/7.45^\circ \sim 67\%$. Since a 100 nm spectral range was used, the TSB should therefore be close to 67 nm . Alternatively, the positive incidence angle ($+5^\circ$) creates a divergence angle of 4.89° , which is less than the acceptance angle of the PM, and therefore rays from the entire 100 nm bandwidth should be swept by the filter.

The total percentage of rays captured for each wavelength at the optical fibre tip is shown in Figure 6.4. The results indicate that only $\sim 64\%$ of the 100 nm bandwidth is filtered when using the negative incidence angle, while 100% of the bandwidth is filtered when using the positive incidence angle, which supports the results from the graphs in Figure 6.3. Light is lost to primary vignetting at the margins for both incidence angles but an extra 18% of the spectrum is captured entirely (100% of the rays in each wavelength) when using the positive incidence angle for the wavelengths 1300 nm and 1360 nm .

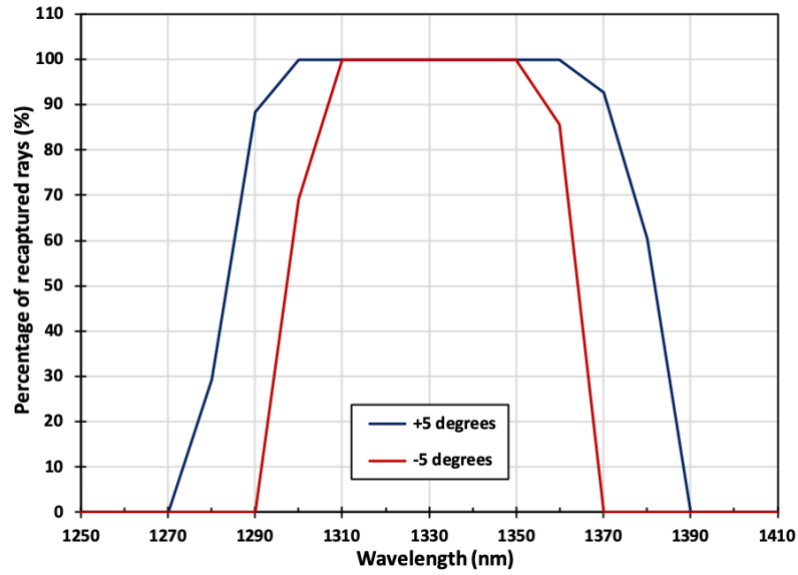


Figure 6.4. On-axis PM simulation results. The percentage of recaptured rays at the entrance aperture of the optical fibre tip as a function of wavelength for two different incidence angles on the diffraction grating. The -5° incidence angle (red curve) only retuned light rays from 7 of the 11 wavelengths in the simulated spectrum (67%) whilst the $+5^\circ$ incidence angle (blue curve) returned light rays from all 11 wavelengths and successfully recaptured an additional 18% of the simulated spectrum in its entirety (100% of rays from 1300 nm to 1360 nm). Evidence of primary vignetting is also seen at the margins of the spectrum by the reduced percentage of recaptured rays for 1290 nm and 1370 nm.

Figure 6.5 a) and b) are both footprint diagrams of the entrance aperture optical fibre tip. They compare the results from using the -5° and the $+5^\circ$ incidence angles respectively and show the spot profile of each beam (coloured by wavelength) as they strike the optical fibre surface. The large black circles on the grid represents the $9\ \mu\text{m}$ entrance aperture of the optical fibre tip.

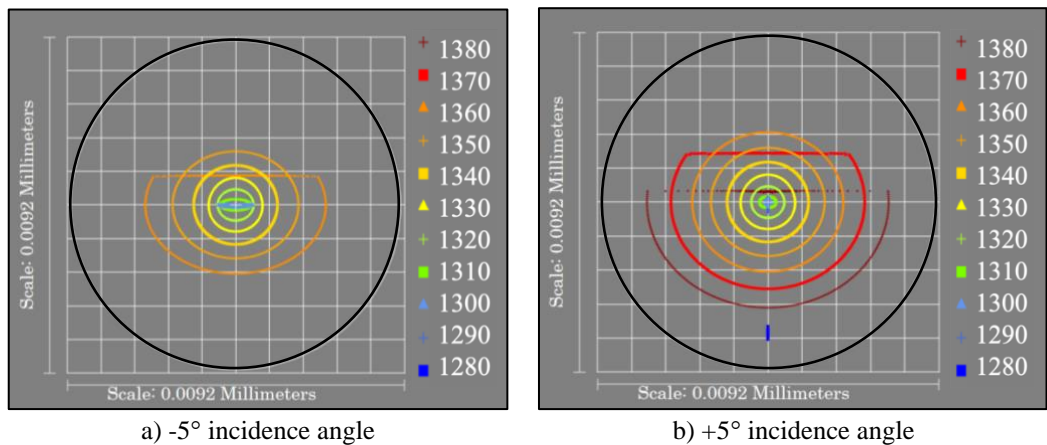


Figure 6.5. On-axis simulation results. Footprint diagrams of the $9\ \mu\text{m}$ entrance aperture optical fibre tip (black circles) for two different incidence angles. **a)** -5° incidence angle: spot profiles for 7 out of 11 wavelengths are visible on the optical fibre tip. **b)** $+5^\circ$ incidence angle: all 11 wavelengths are visible and primary vignetting is also evident by the horizontal cuts across the top of the near circular spots. No secondary vignetting is visible.

In Figure 6.5 a), only 7 out of 11 wavelengths make it back to the optical fibre tip when the negative incidence angle is used. As predicted, the four missing wavelengths are lost at the margins - two from either side of the spectrum. Primary vignetting is also clearly visible on the third wavelength (1360 nm), demonstrated by the horizontal cut across the top of its elliptical spot profile. In Figure 6.5 b), the positive incidence angle allows all eleven wavelengths to successfully return to the optical fibre tip. The diagram also includes more evidence of primary vignetting, although in this case it is only clearly seen on the two longest wavelengths (1380 nm and 1370 nm).

No evidence of secondary vignetting is seen in either diagram, which is demonstrated by all of the rays returning within the entrance aperture of the optical fibre tip (black circles). Another significant feature is that both results show nearly circular spot profiles for the majority of the wavelengths. The shortest wavelengths experience the greatest distortion to their beam footprint shape. In Figure 6.5 a) the spot profiles of the two shortest wavelengths captured (1300 nm and 1310 nm) become horizontally stretched ellipses, whilst in Figure 6.5 b), the three shortest wavelengths captured (1280 nm, 1290 nm and 1300 nm) become vertically stretched ellipses, the last of which (1280 nm) also deviates away from the central location of the optical fibre tip. After some consideration, it is expected that this behaviour is indicative of oblique astigmatism, whereby the focal point of the beam in the sagittal plane is in a different location to the focal point of the beam in the tangential plane, and unlikely to be caused by an error in the simulation.

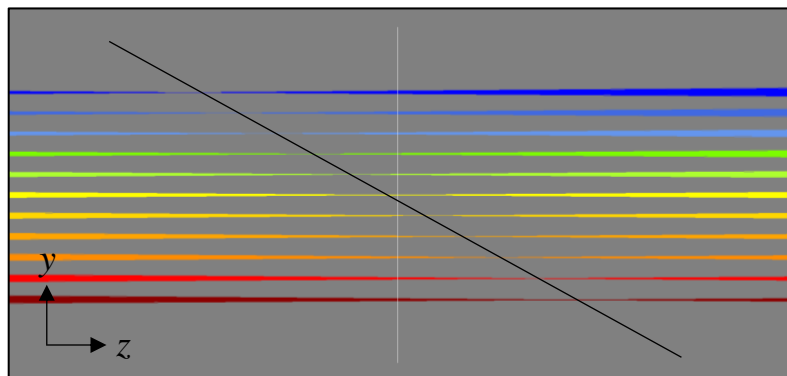


Figure 6.6. Zemax simulation image showing the focal plane between the two parabolic mirrors (black line). The minimum waist point for each wavelength is located at a different distance from the first parabolic mirror. This is a consequence of each wavelength striking the first parabolic mirror after travelling a different distance to reach it.

Figure 6.6 shows that the surface described by the minimum waist of each beam across the spectral range is close to a planar surface but it is also not orthogonal to the optical

axis. This is suspected to be a consequence of each wavelength beam travelling along a different path length before reaching the curved surface of the first parabolic mirror. These different path lengths have been illustrated in Figure 6.7 for the three most significant wavelengths in the spectrum; λ_{min} , λ_c and λ_{max} . In this diagram, the shortest wavelength, λ_{min} , travels the shortest distance, r_{min} , before striking the first parabolic mirror surface and is therefore focused before the RFL.

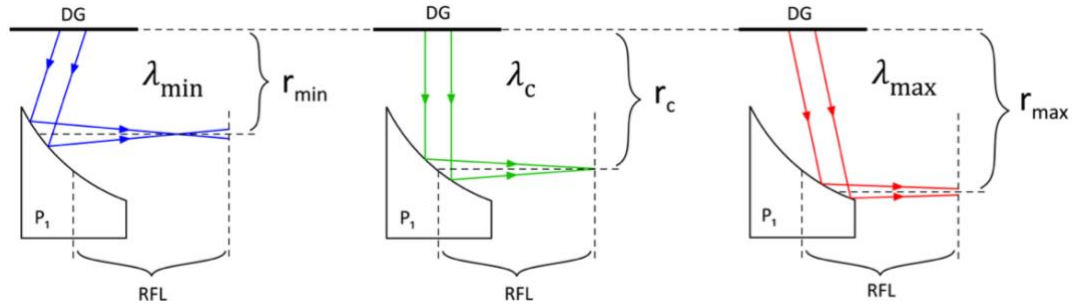


Figure 6.7. Path length difference, r_n , between the diffraction grating, DG, and the first parabolic mirror, P_1 , for the shortest (λ_{min}), central (λ_c) and longest (λ_{max}) wavelengths. The focal point of each wavelength occurs at a different distance from the parabolic mirror and not at the RFL.

The opposite is experienced by the longest wavelength, λ_{max} , which has to travel a longer distance, r_{max} , before striking the parabolic mirror surface and is therefore focused after the RFL. This explains the slope of the focal plane seen in Figure 6.6. This slope will also be affected by the diverging spectrum leaving the surface of the diffraction grating since each wavelength has a different beam width caused by the geometry of their individual diffraction angles, i.e. larger diameter beams (e.g. λ_{max}) will focus later than smaller beams (e.g. λ_{min}) and this introduces the slight non-linearity to the slope that can be seen in Figure 6.6.

The results from simulating the parabolic mirrors have successfully demonstrated their viability as an alternative method to using the two-lens telescope design. They achieve the desired effect of reducing the majority of aberrations (spherical, chromatic, coma and field curvature all appear to have been removed or reduced), as shown by the near circular spot profiles for the majority of wavelengths in Figure 6.5, as well as zero evidence of secondary vignetting occurring over the tested spectral range. Additional aberrations (e.g. oblique astigmatism) appear to have been introduced, which were not detrimental to the performance in this instance but may need to be addressed in subsequent alignments. The next step was to simulate the spectral filter with an off-axis PM to double the acceptance angle and achieve a wider TSB.

6.3.3 Off-Axis Simulation Results

The simulation was modified to accommodate an off-axis PM with a RM (Figure 6.8). This modification doubles the acceptance angle of the PM and allows a wider divergence angle to be used. The eccentricity of the PM was minimised by placing the RM relatively close to the second parabolic mirror, P_2 , but without being so close that it might introduce simultaneous tuning or jeopardise the ability to align the real-life setup. In reality these two components and their mounting stages would be placed as close as possible but the exact location cannot be represented accurately in the simulations since the software does not account for the bulk of the mounting stages. The simulation also used the -5° incidence angle on the diffraction grating since it produced a larger divergence angle (7.45°) that was still smaller than the new acceptance angle of the off-axis PM (10°) and should therefore accommodate the whole of the converging spectrum.

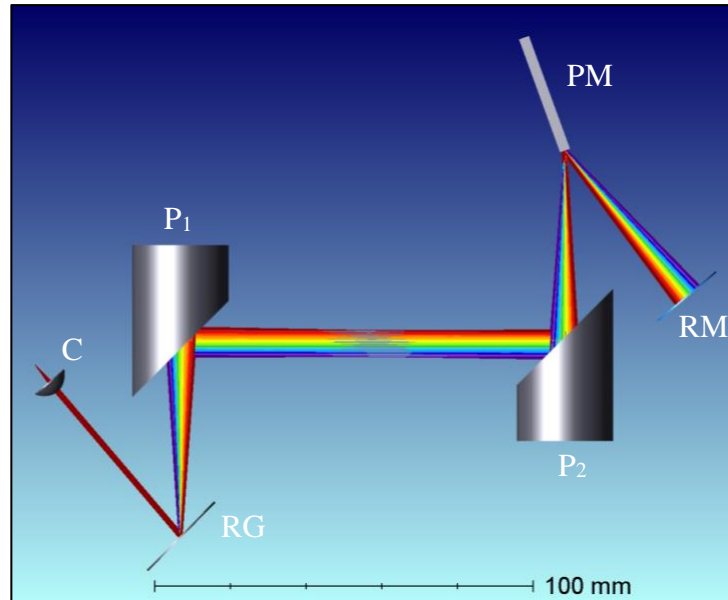


Figure 6.8. Zemax simulation – Collimator, C, reflection grating, RG, parabolic mirrors, P_1 & P_2 , Off-axis polygon mirror, PM, and retroreflector mirror, RM. The off-axis PM doubles the acceptance angle to 10° , allowing a larger divergence angle to be used.

Footprint diagrams were generated again for the number of rays striking the final surface in the simulation. Figure 6.9 is a comparison between using the parabolic mirrors (a) and the two achromatic lenses (b). Figure 6.9 a) show all of the beams successfully returning within the entrance aperture of the optical fibre tip and that the majority of wavelengths have approximately circular spot profiles. The same transformation is seen as before on the shortest wavelengths, which eventually make a departure from circular spots and change into vertically stretched out narrow ellipses (1280 nm , dark blue). However, this

time there is no displacement away from the centre and neither is there any evidence of primary vignetting. The removal of the primary vignetting is due to the PM operating off-axis and tuning through the spectrum in half the previous rotational angle. This produces a full sweep of the spectrum before the boundary of the TF makes contact with the marginal rays of the incident beams. The result is that 100% of a 100 nm bandwidth is successfully swept by the spectral filter and recaptured by the optical fibre tip. However, the unequal pairing of the convergence angle and the acceptance angle means that the duty cycle was 74.5%. The entire spectrum would also be recaptured if the positive incidence angle were used ($+5^\circ$) although the duty cycle would decrease to 48.9%.

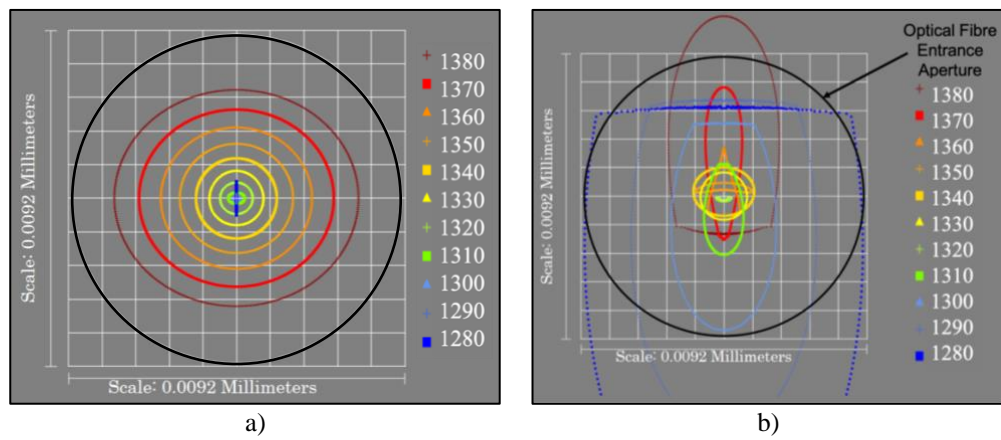


Figure 6.9. Zemax simulation results – **a)** spot diagram on the optical fibre tip for an off-axis polygon. 100% of rays are successfully filtered by the system. Near circular spot profiles are seen with the exception of the shortest wavelength, which is a vertically stretched ellipse. No primary vignetting is seen occurring. **b)** comparative spot diagram from the two-lens telescope design taken from Section 5.5.3. This result demonstrates high degrees of ellipticity for the majority of the beams as well as evidence of primary and secondary vignetting.

Although this result is promising, it does not accurately represent the real life spectral range produced by the SOA, which is approximately 60 nm wider than the 100 nm bandwidth being used in the simulation. Hence calculations were carried out again on the same setup to model a 160 nm bandwidth by activating six extra wavelengths, to give a total of 17 spanning from 1250 nm to 1410 nm, with a separation between each one of 10 nm. However, the wider spectral range increases the divergence angle of the diffraction grating, which may not necessarily be accommodated by the new acceptance angle of the off-axis PM. An analysis of the diffraction angles and their associated divergence angle was carried out again to investigate the impact of the larger bandwidth and to establish the most suitable incidence angle (Figure 6.10).

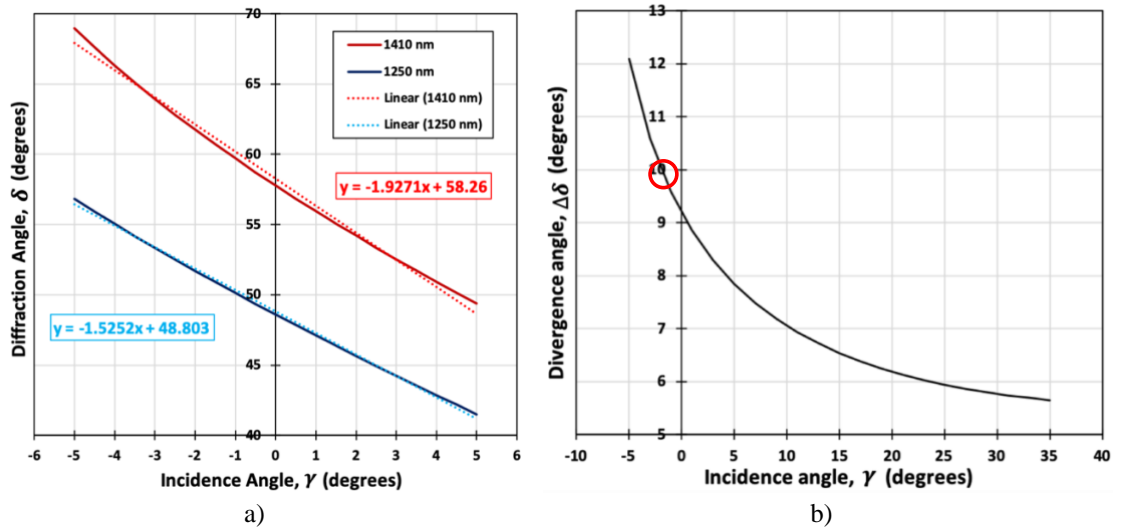


Figure 6.10. Divergence angle versus incidence angle using a 160 nm bandwidth. **a)** The difference between the shortest (blue curve) and the longest (red curve) wavelengths diffraction angles gives the divergence angle as a function of incidence angle. **b)** The maximum divergence angle accommodated by an off-axis polygon is 10° , which allows for an incidence angle of approximately -1.9° (red circle) before the marginal wavelengths will be cut off at the edges of the spectrum.

The two curves in Figure 6.10 a) have been moved further apart by the wider bandwidth and have a greater difference between the gradient values of their trendlines, indicating again that larger, negative incidence angles produce a wider divergence angle. Figure 6.10 b) indicates that even the $+5^\circ$ incidence angle, used earlier for the on-axis PM, would be insufficient to accommodate the new, wider spectral range ($\varphi < \Delta\delta = 7.85^\circ$). In fact, the incidence angle needed to produce the required 5° divergence angle does not exist under these conditions and can only be approached by using a large angle of incidence ($\sim 53^\circ$). This would benefit the spectral resolution by increasing the number of illuminated lines on the grating but could also potentially make the beam diameter too wide to be accommodated by the PM facets. However, since the new acceptance angle of the off-axis PM has now doubled to 10° , a negative incidence angle of approximately -1.9° (red circle, $\Delta\delta = 9.99^\circ$) can be used to accommodate the full 160 nm bandwidth, which was therefore employed in the simulation.

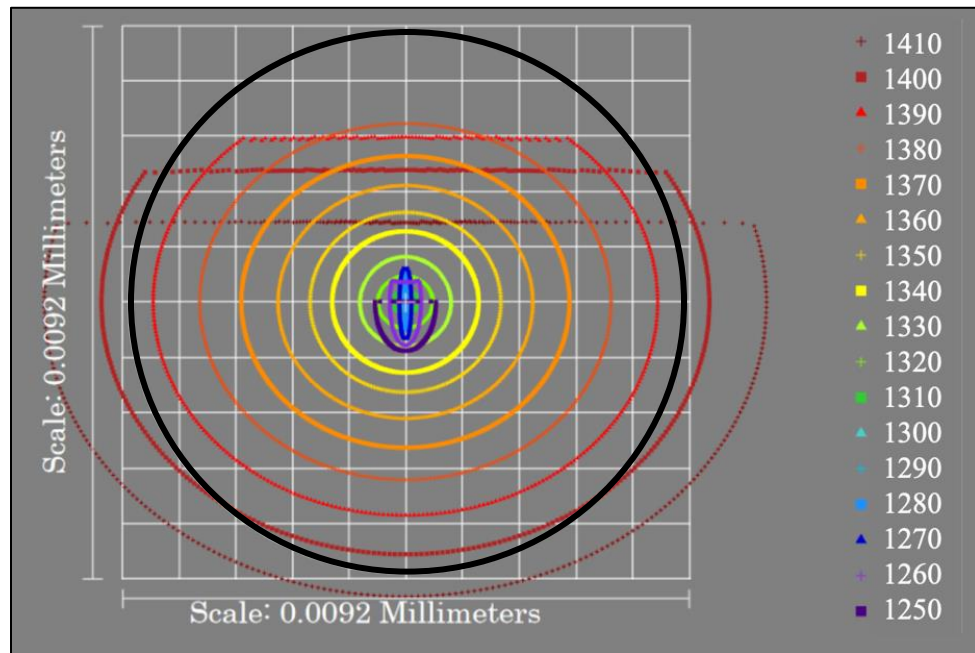


Figure 6.11. Zemax simulation results – footprint diagram on the optical fibre tip. All 17 wavelengths, over the 160 nm bandwidth, manage to land back onto the fibre tip. Near circular spot profiles are seen for the majority of wavelengths. Again, the shortest wavelengths are misshapen into elongated ellipses. Primary vignetting is seen occurring for the marginal wavelengths and secondary vignetting occurs for the longest wavelengths as demonstrated by the largest spots overlapping the boundary of the optical fibre tip (black circle).

The footprint diagram in Figure 6.11 shows the spot profiles for each wavelength beam falling incident on the optical fibre tip (black circle). A similar set of concentric circular beam profiles are seen as well as a more distinctive change in their elongation, which starts with small vertical ellipses for the shortest wavelengths, gradually becoming circular across the central region of the spectrum, and then transforming into large horizontal ellipses for the longest wavelengths. Primary and secondary vignetting are also both seen in the diagram, evidenced by the horizontal cuts and the overlapping spots on the fibre tip respectively. The secondary vignetting is only problematic for the two longest wavelengths (1403 nm and 1413 nm), which only just breach the outline of the optical fibre entrance aperture. Again, this is suspected to be the consequence of different wavelengths travelling along different path lengths through the filter and is supported by the new observation of the horizontal broadening to the longer wavelengths. This observation will be discussed again in Section 7.7.2 where an alternative filter assembly method is suggested that could reduce these effects.

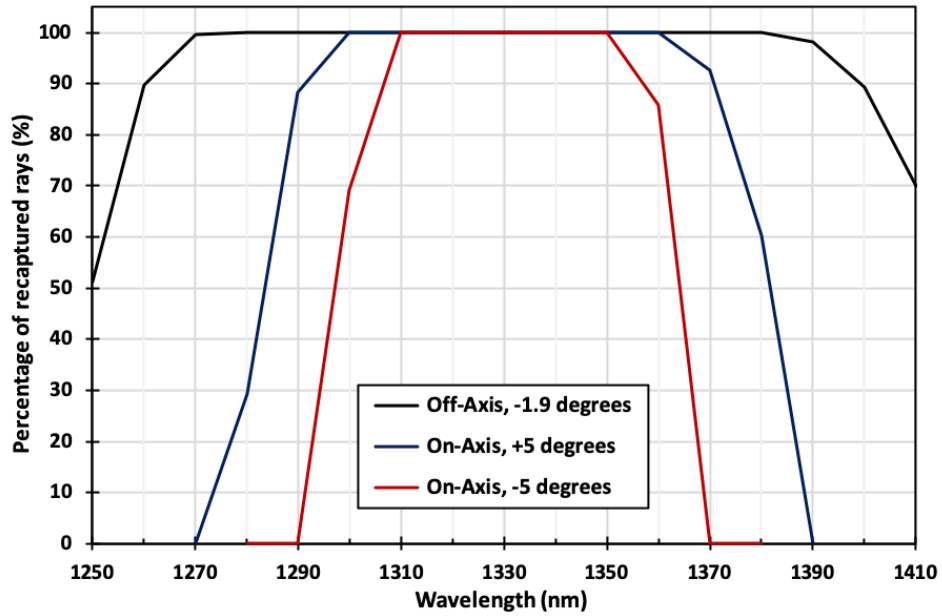


Figure 6.12. Zemax simulation results – Percentage of rays returned to the optical fibre over the range of wavelengths used in the simulation. An optical range of over 100 nm returns 100 % of rays to the fibre. The losses at the margins are caused by primary and secondary vignetting.

The graph in Figure 6.12 shows the percentage of rays successfully returned to the optical fibre tip using the off-axis PM with the new 160 nm bandwidth and the -1.9° incidence angle (black curve). The improved output clearly demonstrates the advantage of using the off-axis PM with the wider spectral range when compared to the previous on-axis designs; $+5^\circ$ (blue) and -5° (red) incidence angles. 100% of the rays from within a 100 nm central region (1280 nm to 1380 nm) are seen returning to the optical fibre tip, which is a 67% improvement over the on-axis PM design with the $+5^\circ$ incidence angle (blue). The results indicate that more light rays were lost at the shorter wavelength region (1250 – 1260 nm) compared to the equivalent longer wavelength region (1400 – 1410 nm), despite the fact that the longer wavelengths suffered from both primary and secondary vignetting. Therefore, the secondary vignetting had less impact than the primary vignetting in this particular spectral filter design.

The parabolic mirror simulation results show a significant improvement in the spectral filter's overall performance. The footprint diagrams demonstrate that the beam profiles are circular at a majority of the wavelengths considered and that the effects of secondary vignetting have also been reduced in comparison with the two-lens telescope. This is due to the light rays experiencing less distortion from aberration, which therefore allows them to follow their intended paths more closely through the spectral filter. This permits more

rays to fall within the boundary of the optical fibre entrance aperture, increasing the number of successfully recaptured rays and improving the optical power output. These observations reinforce the viability of using parabolic mirrors and encouraged their exploration in the experimental study, where the findings could be tested on the real-life system.

6.4 Experimental Setup

The one inch diameter (25.4 *mm*), two inch RFL (50.8 *mm*), parabolic mirrors (MPD129-M01, Thorlabs) and their precision alignment mounting stages (KS1, Thorlabs) were tested to establish the best method of performing the installation and the alignment. The same rigorous approach was employed as before, where the correct height of each component needed to be carefully measured to avoid introducing unwanted tilts to the plane of light propagation. This was more difficult without the aid of a cage assembly to fix the two mirrors in place and the individual post mounts that were used instead were more sensitive to misalignment. As anticipated, the necessity to place the components in close proximity to one another presented its own challenge that needed to be tackled whilst simultaneously satisfying the other alignment conditions. The presentation of results in this section follows the same chronological order as the simulation studies, whereby the on-axis PM is explored first (Section 6.4.1), followed by the off-axis PM (Section 6.4.2).

The final, off-axis, experimental setup can be seen in Figure 6.13 and represents the configuration that gave the best results (shown later in Section 6.4.3). The green line is the path of the central wavelength as it propagates through the filter and the red line is the path of the trigger laser, TL. It was necessary to mount the off-axis PM and the RM directly onto the optics bench, on top of thick rubber sheets to reduce the unwanted transmission of vibrations to the other components.

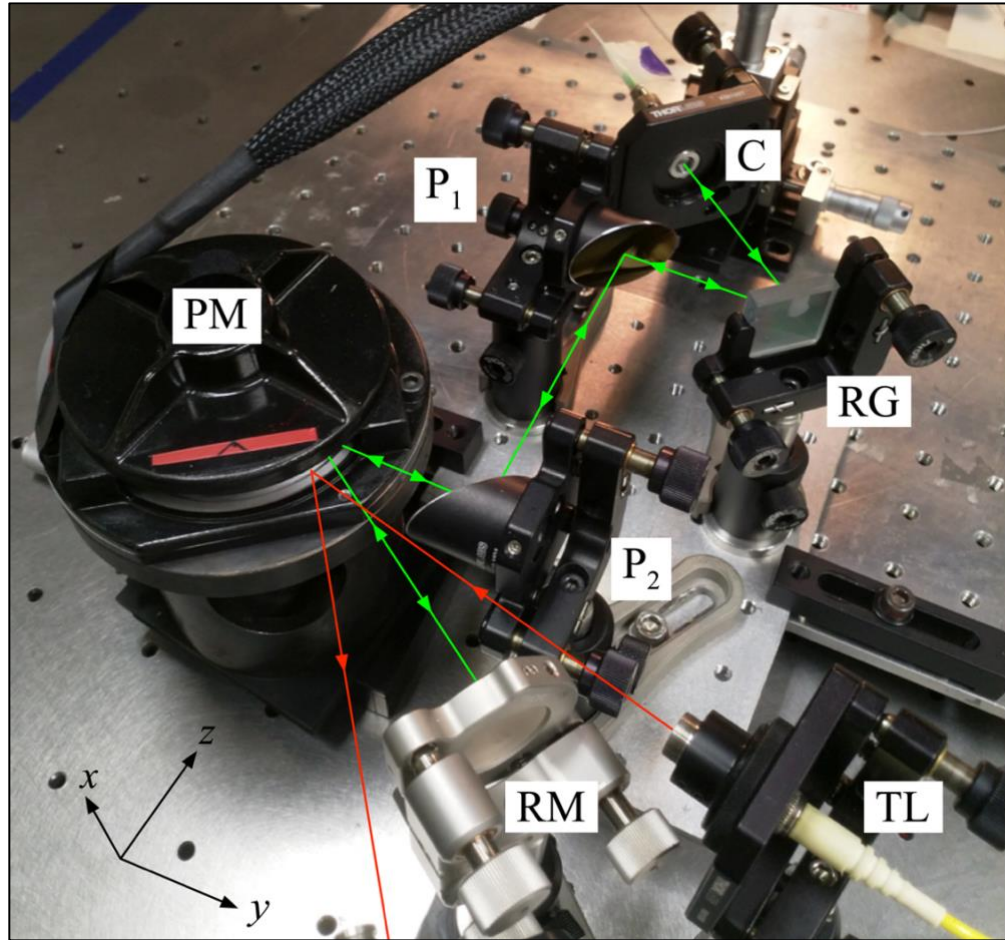


Figure 6.13. Final, parabolic mirror experimental setup employing all of the alignment techniques learned, including the negative incidence angle. Components; collimator, C, reflection grating, RG, parabolic mirrors, P_1 and P_2 , polygon mirror, PM, retroreflector mirror, RM, and trigger laser, TL. Vibrations were minimised by mounting the components on their own optical breadboard with soft rubber feet and the light was directed through the right-hand side of the PM access window where the least turbulent air was detected. The trigger laser photodetector is out of frame at the bottom of the image.

The collimator, C, reflection grating, RG, and parabolic mirrors, P_1 and P_2 , were all placed on top of a single optical breadboard with rubber feet on the bottom to isolate them from the PM. The orientation of the PM allows light from P_2 and the TL to interact with the PM through the right-hand side of the access window, which was identified as the region with the least turbulent air flow (Section 2.3.4.1). Unfortunately, only the PM and the collimator could be mounted on translation stages due to the difficulty of placing the components so close together, as explained earlier in Section 6.3. This limited the amount of freedom, making the task of aligning the setup significantly more difficult to achieve. However, due to the knowledge and experience gained from all the previous experimental work, an operable system was successfully constructed and tested.

6.4.1 On-Axis Experimental Results

The experimental work began with the PM positioned on-axis. The reflection grating was aligned by observing the amount of light transmitted into the various diffraction orders. The highest power output in the first order was seen when the beam incident on the grating had a small, negative angle of incidence. Unfortunately, this angle could not be measured to any high degree of accuracy with the equipment available but was estimated to be approximately $-5^\circ \pm 2^\circ$. Conveniently, this angle was tested earlier in the simulations (Section 6.3.1) and therefore could be used to compare the results. However, this angle of incidence was shown to produce a convergence angle that is larger than the acceptance angle of the on-axis PM, and therefore will not allow the PM to sweep through the entire spectral range. The TSB can still be inferred from the simulation, using discrete wavelengths, which results in a value of 70 nm with an uncertainty of 5 nm.

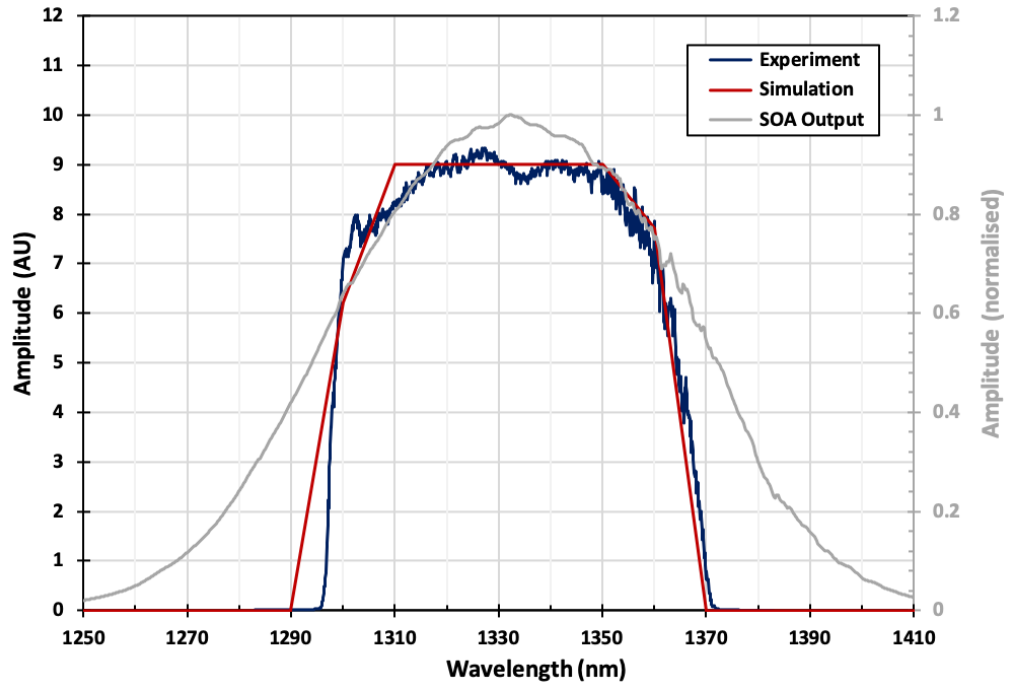


Figure 6.14. Experimental vs. simulated result for the filtered spectrum using an on-axis PM and an incidence angle of -5° . The SOA output is also shown to highlight the available spectrum and therefore the regions that are not capable of being filtered by this particular setup. The FWHM of the blue trace is approximately 68 nm. For a -5° incidence angle, the simulation predicted a 70 nm filtered region.

Figure 6.14 shows the experimental measurements of the filtered spectrum compared with the simulation result and the spectral output produced by the SOA. The simulation result fits well to the experimental curve, which had a FWHM of 68 nm, and therefore

supports the techniques being used to align the filter and confirms that the estimation of the incidence angle on the reflection grating was approximately correct.

The experimental measurements show an almost vertical edge on either side of the spectrum, rather than a smooth Gaussian shaped transition, which is caused by the on-axis PM abruptly cutting through the convergence angle and leaving an extra 70 – 80 nm of bandwidth still available to be filtered. This means that the duty cycle of the filter should be 100% and can be examined in the fringe signal output on the oscilloscope.

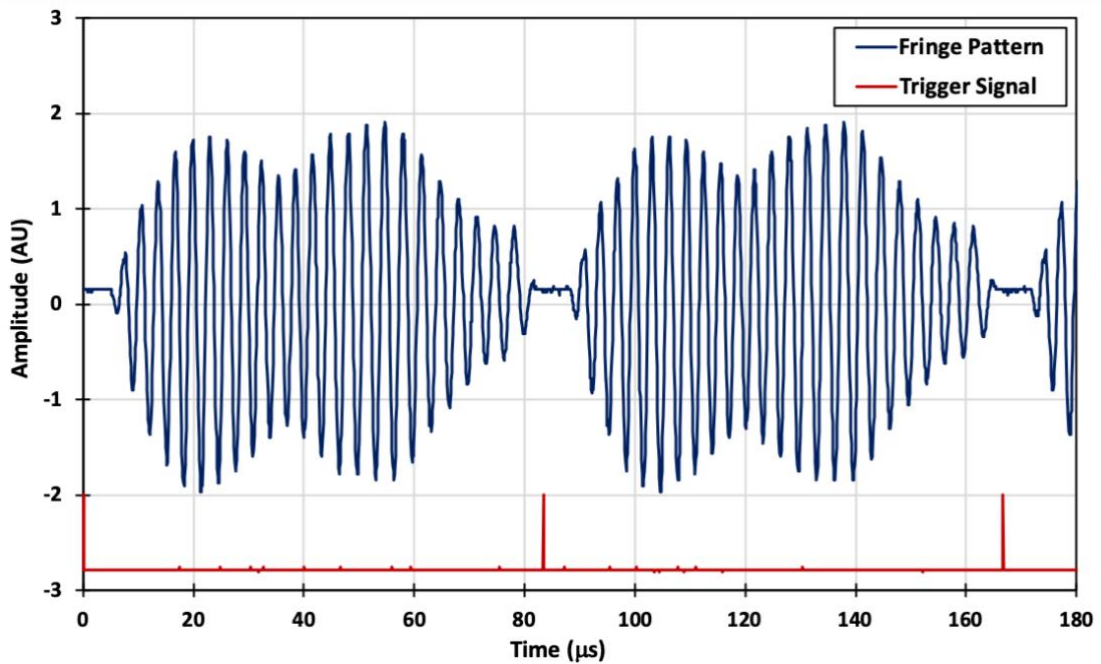
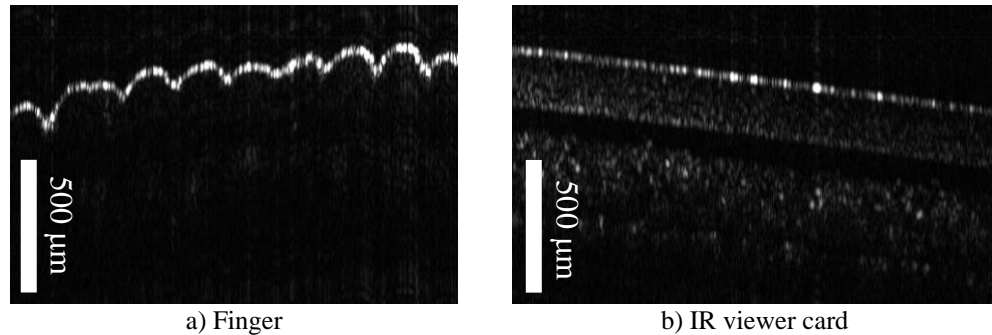


Figure 6.15. Oscilloscope trace of the fringe pattern (blue) and the trigger signal (red) highlighting the period of each facet sweep and therefore the duty cycle of the filter. A near 100% duty cycle is shown demonstrating that the convergence angle is approximately equal to the acceptance angle of the polygon.

The blue trace in Figure 6.15 is the fringe signal observed by the balanced photodetector described in Section 2.4. The red trace is the trigger signal, detected once for every facet sweep. The PM was operating at 12 kHz and gave a facet period of 83.33 μs . The minimal spacing between each fringe pattern indicates that a high duty cycle has been achieved, which was expected from having a convergence angle (7.5°) that is 50% bigger than the acceptance angle of the on-axis PM (5°).

Several images were taken using the output of the spectral filter with the on-axis PM. Figure 6.16 a) shows a B-scan image at the surface of a finger and Figure 6.16 b) shows a B-scan image at the surface of an infra-red (IR) viewing card.

Apart from the surface ridges, no significant details are visible below the epidermis in the image of the finger but some layering is visible in the IR viewing card – the fluorescent material is clearly distinguishable from the top plastic layer.



*Figure 6.16. B-scan images obtained using the parabolic mirrors and a swept bandwidth of 68 nm for an on-axis PM and an incidence angle on the grating of approximately -5° . **a)** shows the contours of a human finger while **b)** shows the various layers of an infra-red viewing card. The axial resolution is poor due to the narrow bandwidth used (68 nm) and the axial scanning range is short due to the poor spectral resolution produced by the reflection grating (600 l/mm).*

The axial resolution (Section 1.5.2) and the axial scanning range (Section 1.4.3) are less than ideal due to the narrow bandwidth (68 nm) and the poor spectral resolution of the reflection grating respectively. The axial scanning range (penetration depth) depends upon the narrow width of the laser linewidths (determined by the resolution of the grating), which in this case were wider because the grating had a line density that is almost half the value of the previous transmission grating (600 l/mm versus 1145 l/mm). Regardless of the image quality, the parabolic mirrors were successful at producing a usable SS output and providing images that were comparable to those produced earlier using the two-lens telescope design. This success encouraged the research to progress with the off-axis PM design.

6.4.2 Off-Axis Experimental Results

The experimental setup was modified to accommodate the off-axis PM and the RM. The initial alignment produced a swept spectral region that was only slightly larger than the previous setup with the on-axis PM (70 nm) and indicated that the filter was not correctly aligned. The spectral filter was rebuilt and realigned multiple times before an appropriate sweeping range was achieved that approached the spectral width of the SOA output. The final assembly (shown in Figure 6.13) employed various vibration dampening techniques and considered the air turbulence surrounding the PM, which was consequently

positioned to allow the rays to travel through a region of free space with the least amount of disturbance (Section 2.3.4.1).

The graph in Figure 6.17 shows the experimental result (blue trace) of the final spectral filter alignment (shown in Figure 6.13) compared with the simulation result (red trace) and the SOA output bandwidth (grey trace). The experimental TSB had a span of 138 nm (1255 nm – 1393 nm), which is 86% of the SOA output (160 nm), and had a FWHM of 113 nm, making it the widest swept bandwidth achieved in this entire body of work.

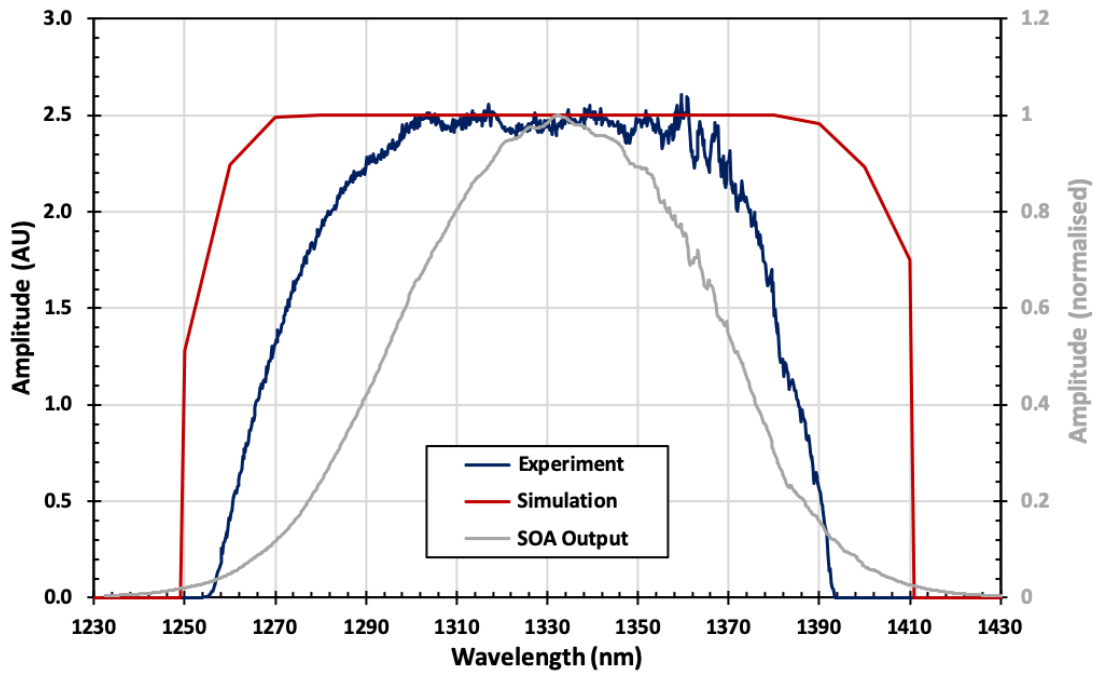


Figure 6.17. Experimental result (blue) versus simulated result (red) for the filtered spectrum using an off-axis PM (the exact setup can be seen in Figure 6.13). The normalised SOA output (grey) is also shown to highlight the available spectrum and the regions that are not being filtered by this particular setup, which is approximately an extra 20 nm. The TSB was measured at 138 nm with a FWHM of 113 nm, which constitutes the widest TSB achieved in this research.

However, the simulation results suggest that there is still an additional 20 nm of bandwidth available to be swept by the filter. This apparent loss was investigated by exploring the duty cycle of the SS, which is shown in Figure 6.18. The time span of the fringe pattern on the oscilloscope was $\sim 58.00 \mu\text{s}$, which is approximately 70% of the total facet period ($83.33 \mu\text{s}$) and demonstrates that 30% of the facet rotation is unaccounted for. This could either be caused by the alignment of the filter, which still might not be optimised, or it could be caused by an unequal pairing of the convergence angle and the acceptance angle ($\psi < \varphi$).

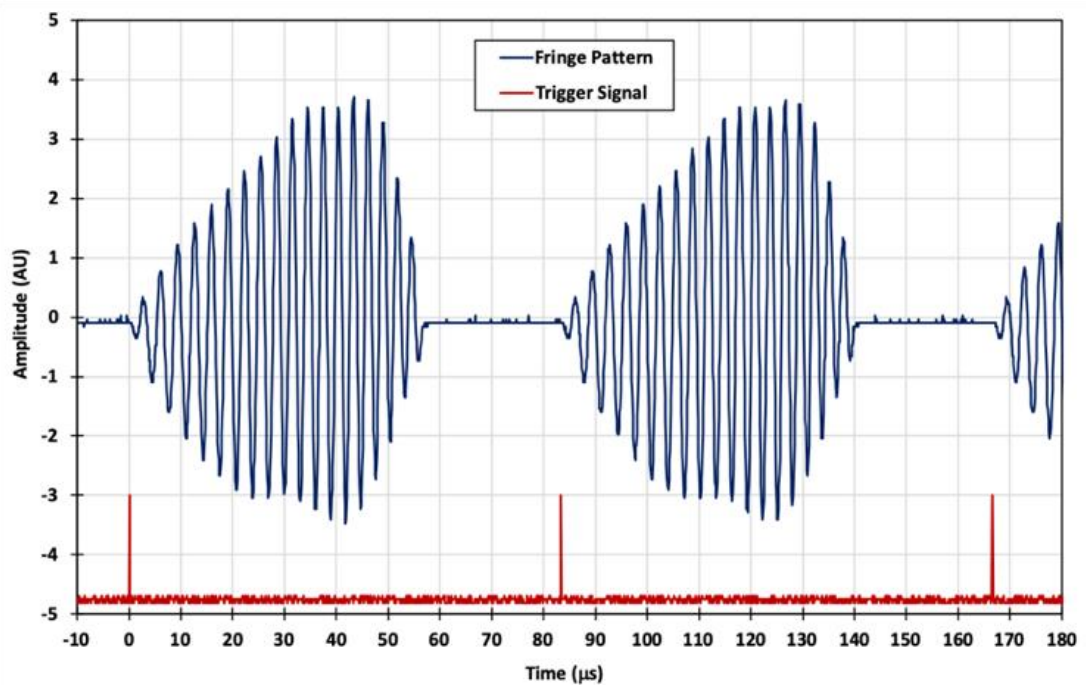


Figure 6.18. Fringe pattern and trigger signal for the widest spectral bandwidth filtered by the off-axis PM using parabolic mirrors. The duty cycle was measured to be ~70%, indicating that 30% of the facet rotation is unused.

Using the results from Figure 6.17 and assuming that the entire spectrum is propagating correctly through the filter with no light loss, the incidence angle on the reflection grating would have to be approximately $+10^\circ$ to produce a divergence angle $\Delta\delta \sim 7^\circ$ (Figure 6.10 b) in order for no light to be swept for 30% of the facet rotation. Naturally selecting this angle during the alignment process is entirely plausible and could simply be a consequence of observing the system's maximum output, which would have considered both the optical power and the spectral bandwidth shown on the spectrum analyser. Although this was not explored further after this work, there is no obvious reason why the spectral filter could not be realigned again to provide the same TSB but with a 100% duty cycle if the correct incident angle on the grating is achieved.

The swept spectrum produced by the parabolic mirrors was compared with the widest swept output achieved with the two-lens telescope design. The telescope design used a 1.5 mm beam diameter collimator, 1145 l/mm transmission grating, 75 mm × 100 mm telescope with 2-inch (50.8 mm) diameter lenses and an off-axis PM. The results in Figure 6.19 show that the TSB (138 nm) and the FWHM (113 nm) of the parabolic mirror setup were larger than the telescope design by 20% and 37% respectively, which had a TSB of 115 nm and a FWHM of 82 nm.

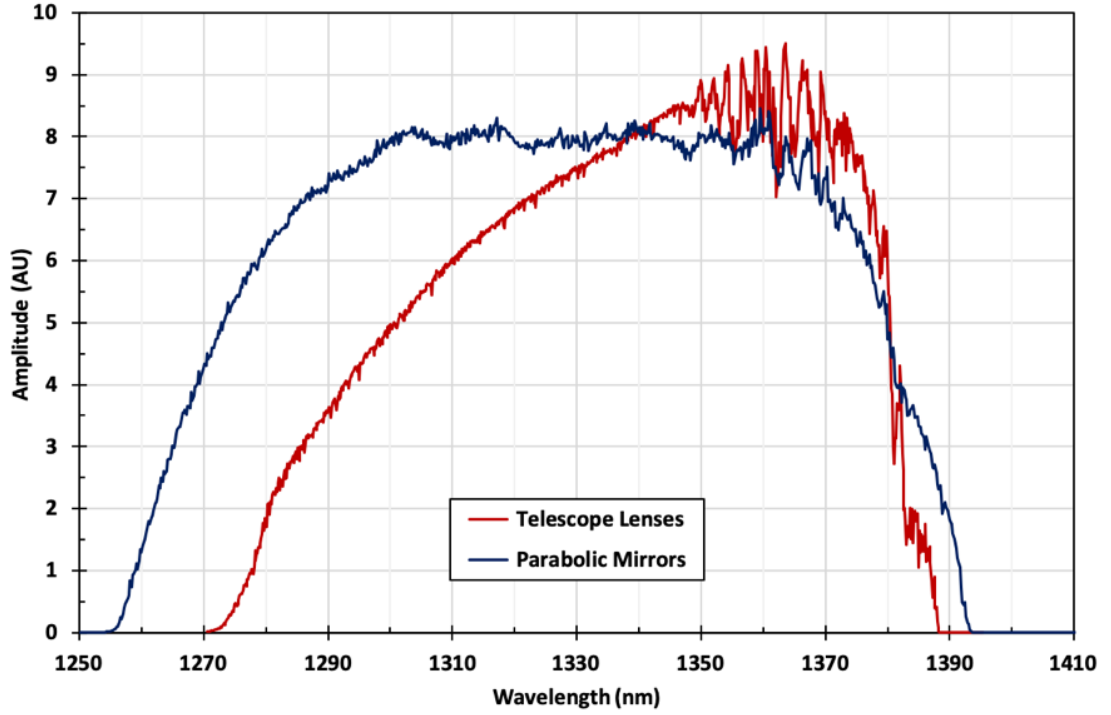


Figure 6.19. Comparison between using parabolic mirrors and a two-lens telescope design. Telescope TSB = 115 nm, FWHM = 82 nm. Parabolic mirrors TSB = 138 nm, FWHM = 113 nm. The TSB is larger by 23 nm (20%) and the FWHM is larger by 31 nm (37%). The predicted TSB of the lenses is 126 nm (Eq. 4.26) due to the 12.66° convergence angle.

The shape of the spectral envelope also has a more uniform and horizontal power distribution across a greater width of the spectrum (~ 60 nm) compared with the output produced by the two-lens telescope design, which peaks at 1360 nm and then slopes down on either side. Although the results do show a significant improvement over the two-lens telescope design, it cannot be considered a true comparison since it was necessary to change the diffraction grating in order to align the system correctly and accommodate the full spectrum (Section 6.3). Changing the diffraction grating has a direct impact on the spectral resolution of the filter, due to the line/groove density (Section 3.4), but the TSB depends upon the combination of components and their successful alignment and therefore does not necessarily increase by changing the grating alone. The flatter spectral shape can be attributed to a reduction in system aberrations but the wider spectral range can be attributed to a better match between the convergence angle and the acceptance angle of the off-axis PM. The setup of the two-lens telescope design is predicted to sweep through no more than 128 nm, according to the TSB equation (Eq. 4.26), whilst the choice of reflection grating combined with the parabolic mirrors allows the entire SOA output to be swept by the filter (depending on the incidence angle – Section 6.3.3).

Figure 6.20 shows the experimental measurement of the signal sensitivity drop-off of the system. These measurements were obtained using a mirror (instead of a physical sample) in the object arm and then increasing the path length in the reference arm by 0.1 mm. The signal amplitude reduces by approximately 44 % over a millimeter of scanning depth.

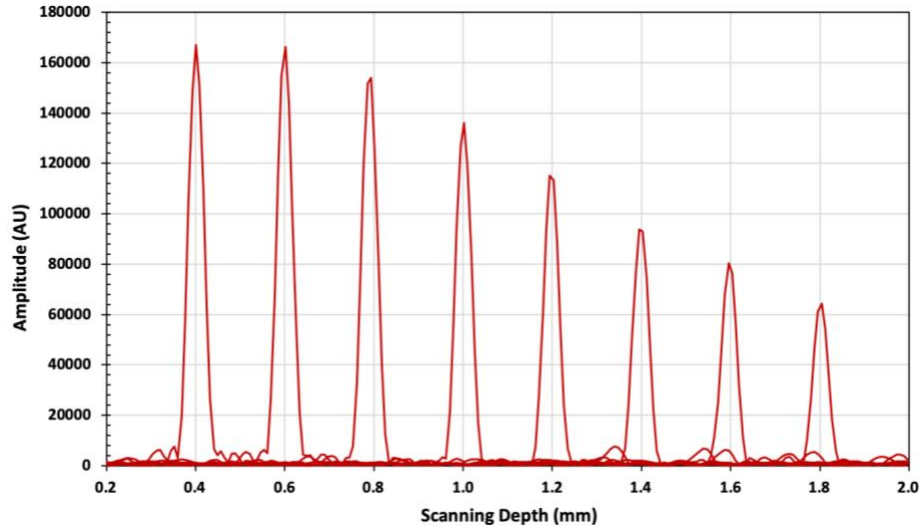


Figure 6.20. Sensitivity signal drop-off measurements for the spectral filter using the parabolic mirrors. The signal amplitude reduces by approximately 44% over a millimeter of scanning depth.

Figure 6.21 shows an arbitrary instantaneous laser linewidth measurement recorded from approximately the center of the SS output ($\lambda = 1332.967 \text{ nm}$). The FWHM of the linewidth was measured to be 0.048 nm . Using a central wavelength of 1330 nm and a double pass on the grating results in a theoretical maximum scanning range (Eq. 1.9) of approximately 18.4 mm .

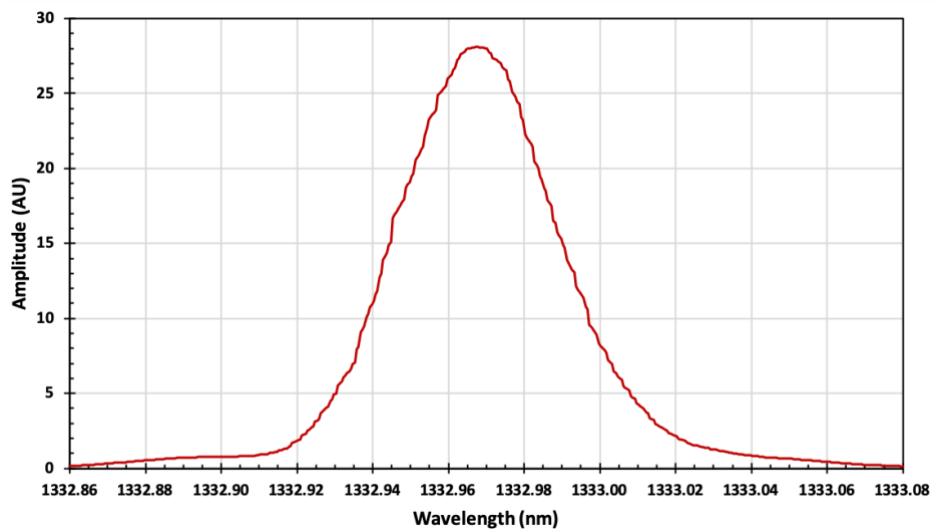


Figure 6.21. Instantaneous laser linewidth measurement at approximately the center of the TSB (1332.967 nm). The FWHM was measured to be 0.048 nm , when using $W_0 = 1.5 \text{ mm}$ incident beam diameter, $G = 1145 \text{ l/mm}$ grating and an incidence angle $\gamma = 48.6^\circ$.

6.4.3 Experimental Images

Several images were taken using the parabolic mirrors setup with the 138 nm TSB. Figure 6.22 a) is a B-scan image of a thin piece of plastic on top of a sheet of paper. This was an ideal target for visually examining the axial resolution of the system since it shows no detail within the material and only highlights the apparent thickness of each surface boundary.

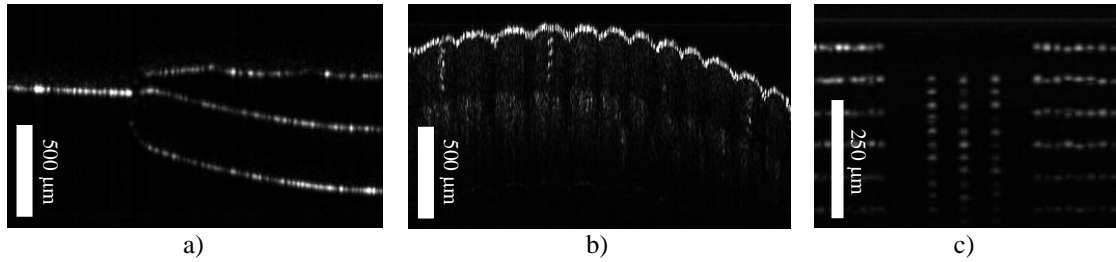


Figure 6.22. B-scan images of **a)** a piece of plastic, **b)** a thumb, and **c)** the Arden Photonics lateral resolution test pattern.

Figure 6.22 b) is a B-scan image of a thumb. The fingerprint ridges in the surface layer are clearly identifiable as well as some layered structure beneath it containing several visible sweat ducts. Figure 6.22 c) is a B-scan image of the Arden Photonics lateral resolution test pattern [60]. The smallest, consistently resolvable separation between lateral points occurs in the third group on the right-hand side of the image, which indicates a lateral resolution of $23\ \mu\text{m}$, although some of the lines on the left-hand side are resolvable down to $\sim 16\ \mu\text{m}$.

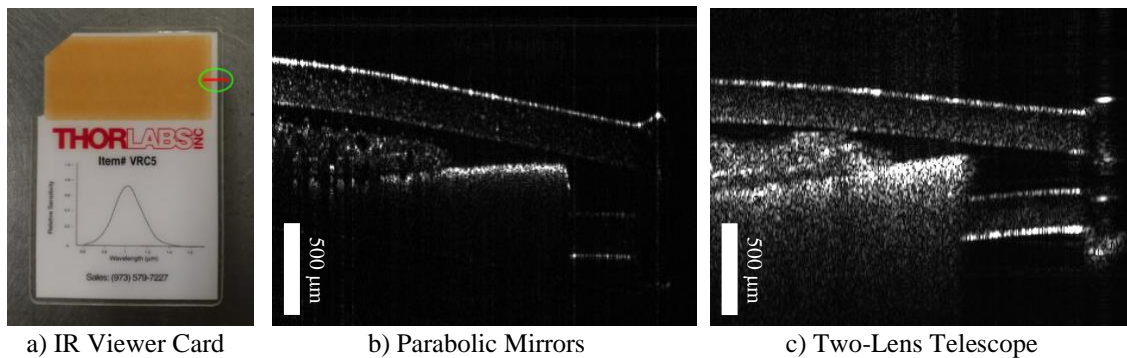


Figure 6.23. **a)** Picture of an infra-red viewing card (VRC5, Thorlabs) indicating the location of the B-scans shown in images **b)** and **c)** (red horizontal line inside the green ellipse, $\sim 4\ \text{mm}$ long). **b)** B-scan image using the parabolic mirrors. **c)** B-scan image using the two-lens telescope. The axial resolution in image **b)** appears to be greater than in image **c)**, as indicated by the structural detail that is not so visible in image **c)**. However, the axial scanning range in image **c)** is arguably better for the two-lens telescope setup, which clearly identifies the lower structures and the thickness of the IR viewing card.

Figure 6.23 compares two B-scan images taken with the two setups discussed above. Figure 6.23 a) is a picture of an infra-red (IR) viewing card (VRC5, Thorlabs) and shows the approximate location of the B-scans, indicated by the red horizontal line inside the green ellipse. The IR florescent material (orange) is situated on top of a layer of white paper, and both of these layers are sandwiched between a transparent plastic material. The location of the B-scan was selected to view all three of these layers simultaneously. Figure 6.23 b) is the B-scan image using the parabolic mirrors with the 138 nm TSB (FWHM = 113 nm) and Figure 6.23 c) is the B-scan image using the two-lens telescope with the 115 nm TSB (FWHM = 82 nm). The image produced by the parabolic mirrors appears to have a greater axial resolution, which is demonstrated by the greater structural detail visible within the fluorescent material. The image produced by the two-lens telescope shows less detail in this area but does demonstrate a much deeper axial scanning range. These observations can be expected from having a larger swept bandwidth and a higher spectral resolution given by the parabolic mirrors and the two-lens telescope setups respectively. The axial scanning range is greater for the two-lens telescope setup because the transmission grating had a line density that was almost two times larger (~ 1.91) than the groove density on the reflection grating (600 l/mm versus 1145 l/mm). The line/groove density directly affects the instantaneous laser linewidth produced by the spectral filter (Eq. 3.3) and therefore the axial scanning range (Eq. 1.10). Both setups could have been improved by illuminating their gratings with a larger beam diameter (Section 3.3) but the parabolic mirror setup would then over illuminate the PM facets and suffer more from primary vignetting as a result.

6.5 Discussion

Earlier simulation results, using the two-lens telescope design (Section 5.5.3), suggested that the effects of aberration could be reduced by using 90 degree off-axis parabolic mirrors. The parabolic mirrors would achieve the same spectral inversion as the two-lens telescope but without the refractive properties of the lenses that cause the majority of aberrations to occur. Additional benefits came from their relatively short total track and their ability to accommodate any wavelength range, making them an attractive option in a future commercial system where the efficient use of space and overall cost and size are likely to be a concern.

The advantage of using the parabolic mirrors was demonstrated in the simulation when the spot profiles on the optical fibre imaging surface became more circular for the majority of wavelengths in the spectrum (Figure 6.5). The parabolic mirrors successfully removed the chromatic, coma and field curvature aberrations that were causing dramatic changes to the shape and size of almost every spot profile and allowing some of the rays to miss the entrance aperture of the optical fibre tip as a consequence (Figure 6.9 a & b). Evidence of primary vignetting was seen, although this can be attributed to the properties of the other components and was not a direct cause of using the parabolic mirrors themselves. Secondary vignetting was only observed for the two longest wavelengths in the off-axis PM simulation when using the wider, 160 nm bandwidth (Figure 6.11). The spot profiles of these longer wavelengths became slightly larger than the diameter of the optical fibre tip, but the impact was less than expected since the beam had a Gaussian distribution ($1/e^2$) with fewer rays out towards the edge of the spot radius. Despite these difficulties, a significantly larger bandwidth was achieved in the experimental setup (TSB = 138 nm and FWHM = 113 nm), although the simulations also showed that it should have been possible to obtain an even wider bandwidth, which indicated that the alignment of the system was still less than ideal.

The wider swept bandwidth produced by the parabolic mirror's setup improved the axial resolution of the images but the axial scanning range was clearly shorter than that produced by the two-lens telescope design (Figure 6.23). The line density of the previously used transmission grating was almost double the groove density of the reflection grating (600 l/mm versus 1145 l/mm), which created an instantaneous laser linewidth that was 1.91 times wider and therefore approximately halved the axial scanning range (Eq. 1.10). Maximising the spectral resolution of the diffraction grating and minimising the instantaneous laser linewidth requires a wide beam to illuminate a large number of lines on a high line/groove density grating, however the beam width needed to be smaller than the size of the PM facet to avoid primary vignetting, and the divergence angle needed to be equal to or less than the acceptance angle of the PM to avoid restricting the TSB.

A matching pair of parabolic mirrors will perform the same task as a two-lens telescope (with no magnification) but without the drawback of lens induced aberrations. Removing

the magnification in either case reduces the number of variables in the system and forces the design to focus on the properties (and the combination) of the other components. The component selection hierarchy still begins with the choice of light source and PM (steps 1 & 2 respectively in Table 4.2, Section 4.9.1), but is no longer influenced by the parameters of the spectral inversion process (step 5, telescope), which previously had to consider all of the previous steps (1 – 4). This means that only the diffraction grating (step 3) and the collimator (step 4) need to be selected carefully to meet the requirements of the light source and the PM respectively, e.g. the divergence angle versus the acceptance angle, and the beam diameter versus the facet width.

Ideally, the beam width produced by the collimator should be as large as possible without over illuminating the facets of the PM and causing unwanted primary vignetting. This will maximise the number of lines/grooves illuminated on the diffraction grating, increasing the spectral resolution and minimising the instantaneous laser linewidth, although the Gaussian light intensity distribution will contribute towards minimising the impact of primary vignetting if the beam width happened to be larger. The divergence angle of the emerging spectrum can be changed by adjusting the incidence angle on the diffraction grating. This has a direct consequence on the TSB, which can either be cut short at the margins, when the convergence angle is too large ($\psi > \varphi$), or it could insufficiently fill the acceptance angle of the PM, producing a poor duty cycle ($\psi < \varphi$). The divergence angle will have a certain magnitude when the light propagating in the first diffraction order is maximised (or when light in the zeroth order is minimised). It is unlikely that the divergence angle and the power transmission will both be optimised simultaneously since the maximum optical power output of the reflection grating is not necessarily going to occur for the incidence angle that provides the optimum divergence angle for the rest of the system (Section 6.3.1). Therefore, unavoidable power loss should be expected unless a custom-built diffraction grating is used that has been specifically designed to operate with the properties and parameters of the other components.

6.6 Further Work

The biggest challenge in the experimental study came from the difficulty of correctly aligning the parabolic mirrors, which possess an additional orientation parameter that is asymmetric about the axis of collimated beam propagation. Lenses are (ideally) perfectly symmetrical about their central optical axis, and therefore do not need to take axial

rotation into consideration, whilst parabolic mirrors must be correctly rotated to accommodate for the perpendicular change in the direction of light propagation. This was carried out by eye in the experimental setup, which does not guarantee the correct alignment is achieved. A more suitable method with axial rotation controls should be employed in future designs to avoid this complication.

The post-mount stages used to hold each parabolic mirror were also more susceptible to vibration and misalignment – the spectral output could be dramatically reduced (or even permanently lost) simply by pressing lightly on the mounts. This was unlike the telescope cage assembly, which typically returned to its original position when touched and maintained its power output after doing so. Using a cage assembly to mount the parabolic mirrors would significantly reduce the risk of introducing unwanted tilts into the propagation plane and would also fix the path length between them, removing the necessity for realignment if a different experimental setup is explored. This method should also accommodate the axial rotation control described above and both should be considered an essential part of any future designs.

It can be envisaged that an ideal setup might be achieved by using the smallest 90 degree, off-axis parabolic mirrors available (half inch diameter (12.7 mm), RFL = 15 mm, MPD00M9-M01, Thorlabs) and a bespoke diffraction grating that has been specifically designed to produce the correct divergence angle for the intended light source. This would allow the convergence angle to match the acceptance angle of the PM and therefore maximise the TSB and the duty cycle. These components would also require mounting stages that can accommodate the minimal space between the components and still allow every plane and axis to be finely adjusted. This could simultaneously optimize the performance and minimise the free-space cavity length. However, this level of specificity can only be realistically justified when designing a commercial system, since the additional cost of producing highly customised opto-mechanical components would not result in significant gains. Of course, the overall engineering and design process must also take into consideration the size of the components and their proximity to one another in order to be successful, which again would present its own challenges. One way to mitigate this problem might be to employ parabolic mirrors with a reflection angle that differs from 90 degrees, which are available from various sources and are also easily customisable [73].

CHAPTER 7

DISCUSSION AND CONCLUSIONS

7.1 Chapter Introduction

The goal of this research project was to establish viable optimisation routes for the performance of a PM-based spectral filter for SS-OCT. In order to achieve this goal, the SS system was examined and tested both theoretically and experimentally whilst also employing ray tracing simulation software to explore different spectral filter designs. The performance of the SS depends upon the ability of the spectral filter to maintain a sufficient level of optical power whilst producing narrowband, instantaneous laser linewidths from a broadband, TSB. The optical power transmission is important for maintaining the image quality and reducing noise, while the linewidths and the bandwidth are essential for maximising the axial scanning range and the axial resolution of the OCT images respectively.

There are four key ways that the performance of the PM-based spectral filter can be affected. These are;

- Un-swept light – resulting in a narrowing of the total swept bandwidth (TSB), which affects the axial resolution of the OCT images.
- Simultaneous tuning – achieving the tuning condition for two separate wavelengths at the same time, misrepresenting them as a single tuning event and therefore introducing ambiguity in the location of the scatterers in the sample and lowering the quality of the OCT images.
- Primary vignetting – caused when the light interacts with the polygon mirror and reduces the total optical power transmission.
- Secondary vignetting – caused when the light attempts to exit the spectral filter but falls outside of the optical fibre entrance aperture.

The un-swept light and the simultaneous tuning are both consequences of the spectral filter design and have been shown to depend on the choice of the components and their various parameters. This concluding chapter reiterates the key parameters of each component that are generally considered to benefit the spectral filter and the OCT

imaging system, and then provides a detailed discussion of their combined operation and how these parameters can be selected and set up to optimise the performance.

One of the primary objectives was to maximise the optical power transmission. As light propagates through the filter, unavoidable power losses occur through back reflections on a number of components. Anti-reflection surface coatings on the lenses and the diffraction grating (working in transmission), as well as using FC/APC optical fibre joining connectors, help minimise these losses, however the majority of optical power loss comes from the two instances of mechanical vignetting, which occur when the light interacts with the PM (primary vignetting) and when the light attempts to exit the filter through the aperture of the optical fibre (secondary vignetting). Although primary and secondary vignetting are independent from one another, they are often both effected whenever the spectral filter is modified and therefore can only be mitigated through a judicious design process. Vignetting must be considered throughout the design process, alongside the first two points, if the spectral filter is to be optimised correctly.

7.2 Specifications For Individual Components In The Spectral Filter

The following sections provide a summary of each component in the spectral filter, starting with the light source and ending with the PM. Each section highlights the key parameters of the components that were considered beneficial to the system's overall performance. These parameters were established through observations in the experiments and the simulations as well as the general properties determined by the theoretical work and they are presented irrespective of the potential disadvantages that can arise as a result of the components combined operation, which is the topic of Section 7.4.

7.2.1 Light Source – Semiconductor Optical Amplifier

Selecting the operating wavelength is achieved through the choice of light source, which also determines the maximum TSB since it cannot be larger than the extent of the bandwidth it produces. The wider the bandwidth of the light source, the greater the opportunity to maximise the theoretical axial resolution (Eq. 1.13), and therefore large bandwidth sources are the most desirable. The SOA used in this research project came with an external power supply that allowed multi-parameter adjustment. It was found that the spectral bandwidth of the light source could be maximised by operating the SOA at a low temperature (9°C) and a high current setting (600 mA) (Section 2.3.2.3). These settings established the central and marginal wavelength values that give the total spectral

range ($\sim 160\text{ nm}$). These values were then used throughout the research, in the simulations and the theoretical analysis, to help find the optimum setup.

7.2.2 Collimators

The collimator is responsible for delivering light from the optical fibre into the free space region of the spectral filter. The same collimator must also collect and reinject the returning swept light back into the optical fibre, the aperture of which being only $9\text{ }\mu\text{m}$ in diameter. Therefore, in order to maximise the total optical power transmission, it is important to select a collimator that can maintain accurate beam propagation, with minimal beam divergence, along the total back and forth path length through the spectral filter. It was shown in Section 3.3 that larger beam diameter collimators experience less beam divergence than smaller beam diameter collimators (based on the available collimators from Thorlabs, Figure 3.3). A large beam diameter collimator should therefore guide a larger proportion of light back to the optical fibre tip, minimising the amount of secondary vignetting and increasing optical power transmission. Furthermore, a large beam diameter collimator will illuminate a greater number of lines/grooves on the diffraction grating, which is key to increasing the theoretical axial scanning range (see Section 7.2.3 below).

7.2.3 Diffraction Grating

The diffraction grating is responsible for spatially distributing the spectrum over a range of angles in preparation for the sweeping process, carried out through angular selection by the rotating PM. It is preferable to use a high line/groove density diffraction grating ($> 1000\text{ l/mm}$) in order to increase the spectral resolution of the filter. This creates narrower instantaneous laser linewidths (Eq. 3.3), which therefore increases the theoretical axial scanning range of the OCT system (Eq. 1.9). Gratings can operate either in transmission or reflection. Transmission grating generally produce high spectral resolutions whilst reflection grating tend to provide higher efficiency since they remove the power loss caused through back reflections and zero order transmission.

7.2.4 Two-Lens Telescope

The two-lens telescope is responsible for inverting the diverging spectrum, emerging from the diffraction grating, into a converging spectrum, incident on the PM. The design of the telescope is largely dependent on the parameters of the other components in the

spectral filter (see Section 7.5) but several features were identified that are considered to be beneficial to the system's performance.

Building and pre-aligning the two telescope lenses into a single cage assembly, rather than using individual post mounts, was shown to improve the system's performance by creating a more robust structure that is more resilient to vibration. Although this modification was not rigorously tested (since it was beyond the scope of the project), this simple design consideration improved both the TSB and the optical power output (Figure 2.13). Future designs could benefit from adding an extension to the cage assembly that includes the collimator and the diffraction grating, which would increase the structural rigidity and could also help with the alignment process.

The experiment carried out in Section 5.5 compared the performance of different lens diameters in the telescope and showed that larger diameter lenses decreased the amount of ray deflection (caused by aberration) experienced by the marginal rays in the spectrum. This allowed more of the light to return to the optical fibre and therefore reduced the amount of secondary vignetting and increased the optical power transmission. The results showed that 2-inch diameter lenses, when compared directly with 1-inch diameter lenses, increased both the TSB and the optical power by roughly 30% (Figure 5.13). Short focal length lenses are also desirable in order to minimise the telescope track length (Section 5.4.1), which should help to reduce the effects of beam divergence as well as decrease the total footprint of the spectral filter.

7.2.5 Polygon Mirror

The PM is one of the key components of the SS. It is placed second on the design hierarchy list and has an impact on every other component in the spectral filter due to the limitations that are set by its parameters (Section 3.6.1). Its rotational speed and facet count fundamentally control the bandwidth sweeping frequency of the spectral filter. Higher sweeping frequencies will increase the data acquisition rate of the OCT system and reduce motion artefacts when performing real-time imaging. Therefore, a high-speed PM with a number of facets larger than 50 is generally considered to be the most suitable for producing SS-OCT images.

Placing the PM off-axis is known to double the acceptance angle, but it will only increase the TSB when the convergence angle is already wider than the on-axis PM's acceptance

angle (Section 4.2). Ideally, the convergence angle should match the acceptance angle, $\psi = \varphi$, in order to sweep through the whole spectrum and maximise the duty cycle. This could be achieved using a specific combination of component parameters, however, prioritising the duty cycle in this way can also introduce further complications that could be difficult to mitigate (discussed shortly in Section 7.4).

Changing the orientation of the PM from below-axis to above-axis (Figure 4.2) was thought to improve the signal output by aligning the observed, sloped focal plane of the converging beams to the slope of the off-axis PM facets (Figure 5.20). It was hypothesised that this alignment would guide the light rays along a more homogenised path through the filter, but the simulation and the experimental results showed almost no difference between the two orientations (Figure 5.23). However, there is still a preference to orientate the PM above-axis, which is due to the variation in beam widths produced by the diffraction grating and shall be discussed in relation to the visible facet width in Section 7.3.3.

Translating the PM along the optical axis, closer to the second lens in the telescope, was shown to provide a better alignment between the incident beam and the TF at the correct moments during the sweeping process (Section 5.8). The simulations showed that only 10 mm of translation was needed to remove primary vignetting entirely. A disadvantage is that this has the potential to introduce significant amounts of simultaneous tuning if the convergence angle is equal to or greater than the acceptance angle, $\psi \geq \varphi$ (Section 4.6).

7.2.6 Summary

The following is a summary of the key properties and parameters of each component in the SS spectral filter that can be considered beneficial to the general operation of the spectral filter and the OCT imaging system. However, these considerations do not take into account their combined operation and therefore some of their properties may not be so desirable when considering the grand optimisation that follows in Section 7.4.

Light Source

- Optimise the settings of the light source to maximise the power output and the spectral range, and determine the central wavelength and the marginal wavelength values needed for the theoretical analysis by selecting $\sim 5\%$ of the maximum intensity.

Collimator

- Select a wide beam diameter collimator, rather than a narrow beam diameter collimator, to minimise the amount of beam divergence and maximise the number of illuminated lines/grooves on the diffraction grating.

Diffraction Grating

- Select a high line/groove density grating, working in reflection, to maximise the spectral resolution and increase the maximum theoretical axial scanning range.

Telescope

- Construct the telescope using a cage assembly (or similar) to increase structural rigidity and minimise the effects of vibration caused by the active PM.
- Select large diameter lenses (e.g. 2-inch diameter or 24.5 mm) to reduce the effects of aberration and minimise ray deflection.
- Short focal lengths are preferable for minimising the footprint of the spectral filter.

Polygon Mirror

- Using a high-speed PM with a large number of facets will increase the bandwidth sweeping frequency and therefore the A-scan acquisition rate of the OCT imaging system.
- Place the PM off-axis and install a RM to increase the acceptance angle. The PM should also be positioned above axis to maximise the visible facet width to accommodate the largest beam diameter in the converging spectrum.
- Translate the PM along the optical axis, closer to the second lens in the telescope, to better align the converging spectrum with the sweeping facet.

7.3 Further Steps On The Path To Optimisation

Additional aspects of the spectral filter that should be considered when designing and constructing a PM-based SS are discussed in this section. A common element among these further steps is the maximisation of the optical power transmission which can be achieved in several ways.

7.3.1 Wavelength Dependent Path Lengths

The PM-based spectral filter produces non-linear spectral sweeping. This is caused by several features working simultaneously. Firstly, the diffraction grating distributes the wavelengths over an angular range (divergence angle) with a spectral gradient according

to the grating equation (Eq. 3.2). The timing signal of the swept wavelengths are linked to the instantaneous rotational angle of the PM, as discussed for the particular design described in Section 4.7. This causes the angular rate of change of the instantaneously swept wavelengths to either speed up or slow down, depending on the wavelength sweeping direction. The difference in the rate of change between the beginning and the end of each sweep of the spectrum was calculated using Eq. 4.20 to be approximately 14%.

Secondly, dispersion effects are introduced due to the different optical paths travelled by each ray through the filter. These differences in the optical path are not necessarily caused by the apparent increase in length experienced by the marginal rays, which propagate through the telescope at large radial displacements (rather than paraxial propagation), and instead depend on the wavelength of each light ray and the glass paths travelled through the telescope. Usually, these path length and time of flight differences are relatively small, and are typically dealt with during the data processing stage (in this case using complex Master-Slave). However, these effects will become more prominent in any future designs that incorporate extra-large bandwidths and would most likely need to be considered for true optimisation.

7.3.2 General Design and Construction Methods for the Spectral Filter

The PM-based spectral filter must be designed and constructed carefully in order to prevent unnecessary light loss. The construction method was demonstrated to be an important part of the design process and showed how the signal strength and the TSB could both be improved by considering the operation of the PM and taking appropriate action to minimise the negative effects caused by its mechanical nature. The spectral filter is susceptible to vibrations (Section 2.3.4) and was also suspected to suffer from the effects of windage created by turbulent air flow surrounding the active PM (Section 2.3.4.1). The windage and vibrations are both undesirable features since they prevent the rays from following their intended path through the filter and contribute towards secondary vignetting, which lowers the optical power transmission.

Isolating the PM from the rest of the components by installing them onto their own optical breadboard, with soft rubber dampening feet, as well as introducing more robust mounting stages, was essential for maintaining the correct alignment of the system and maximising the amount of successfully transmitted light. The effects from windage were

reduced by guiding the light rays through the least turbulent region surrounding the viewing window, which was loosely determined using streamers to examine the air flow.

These features have a significant impact on the performance of the PM-based spectral filter and they should be given an appropriate amount of consideration in order to truly optimise any future design. Investigating this in a higher level of detail was beyond the scope of this project but reasonable efforts were made to minimise these effects wherever possible.

7.3.3 Maximising The Visible Facet Width

Introducing eccentricity, by moving the PM off-axis, doubles the acceptance angle and allows a wider convergence angle to be used. However, it also reduces the facet width, L , from the perspective of the incident beams, which decreases more quickly as the eccentricity increases. As discussed in Section 4.8, the final beam width, W_2 , should ideally be controlled by the combination of components to match the visible facet width, l_v , to prevent light loss through primary vignetting. Fortunately, only the slightest amount of eccentricity is needed to double the acceptance angle and the reduction to the visible facet width is small when using eccentricity values $< 20\%$ of the PM radius (Figure 4.6), which preserves the majority of the facet width and only a fractional loss will occur as a consequence (assuming that $W_2 = L$). However, the minimum eccentricity value is also restricted by the need to incorporate the RM, whose retro-angle, Ω , should not be less than a certain critical angle in order to prevent the secondary form of simultaneous tuning (discussed shortly in Section 7.3.4). The results from the theoretical analysis in Section 4.5.2 showed that a wider visible facet width is produced when the PM sweeps above (rather than below) the telescope optical axis (using a below-axis PM design) (Figure 4.9). Since the beam width changes throughout the spectrum, due to the properties and the interaction with the diffraction grating, the PM should ideally be placed above-axis to provide the largest visible facet width for the largest incident beam, which occurs for the shortest wavelength in the converging spectrum¹⁶.

¹⁶ Assuming the same arrangement used throughout this research, whereby the longest wavelength in the spectrum propagates above the telescope optical axis and the shortest wavelength propagates below.

7.3.4 Simultaneous Tuning

The theoretical analysis in Section 4.6 described how simultaneous tuning occurs whenever $\psi \geq \varphi$. This happens regardless of whether the PM is positioned on-axis or off-axis. However, whenever the PM is positioned off-axis, the eccentricity must be above a certain threshold value in order to avoid the secondary form of simultaneous tuning (Section 4.6.1). The analysis was carried out from two perspectives but both assumed that $\psi = \varphi$. The eccentricity was first considered from the PM's point of view (Eq. 4.18), which established the condition that the eccentricity value must give a PM rotation angle (for the central wavelength) that is greater than half the acceptance angle, $\theta_E > \frac{\varphi}{2}$ to avoid SST. This minimum value of eccentricity was calculated to be $E_{min} = 2.765 \text{ mm}$.

The amount of eccentricity was then considered from the point of view of the wavelength with the largest converging angle, ψ_+ , measured from the optical axis (Eq. 4.19). This was due to the non-linear wavelength distribution in the converging spectrum, which forces the convergence angle to misalign with the acceptance angle and prevents some of the marginal wavelengths from being swept by the spectral filter (see the following section). The minimum eccentricity value, E_{min} , is therefore larger in this instance and was subsequently calculated to be 3.83 mm , which is 12% of the PM radius. This value was also used to find the retro-angle, $\Omega = 13.87^\circ$, and the visible facet width, $l_v = 2.764 \text{ mm}$, which was a reduction of only 0.2% from the true facet width. Using this value of eccentricity (on the PM used in this research) will maximise the visible facet width and therefore help minimise the amount of primary vignetting.

7.3.5 Realignment of the Non-Linear Wavelength Distribution

Section 4.3.1 considered the choice of wavelength assigned to propagate along the telescope optical axis. This was due to the non-linear distribution of the wavelengths in the diverging spectrum (Section 3.4.3) and the desire to match the convergence angle with the acceptance angle. When $\psi = \varphi$ and the central wavelength, λ_c , is selected to propagate along the telescope optical axis, the longest wavelength, λ_{max} , will be forced to converge onto the PM at an angle that is larger than half the acceptance angle, $\psi_+ > \frac{\varphi}{2}$. This will cause a percentage of marginal rays from the longer wavelength region of the spectrum to fall outside of the polygon's sweeping range and will therefore not become

part of the SS output. Deliberately placing a longer wavelength in alignment with the telescope optical axis, such that the diverging spectrum is distributed evenly on either side of the telescope optical axis, will give each wavelength in the converging spectrum the opportunity to be swept by the spectral filter. Using the parameters of the light source and the diffraction grating (Table 3.1), the wavelength needed to correctly redistribute the converging spectrum was calculated to be 1337.38 nm , which is 7.38 nm larger than the central wavelength of the light source. Although this modification is recommended whenever the condition $\psi = \varphi$ is met, it also relies on having the ability in the experimental setup to precisely align the diffraction grating with the telescope, which demands careful calibration and positioning equipment with micron scale accuracy.

It is also speculated that the ratio $\frac{\psi}{\varphi}$ may be partly responsible for the size of the instantaneous laser linewidths. When $\psi < \varphi$, the wavelength tuning speed will be high but the spectrum will be distributed over a small range of angles, suggesting that a wider range of wavelength may be able to translate back through the spectral filter. If $\psi > \varphi$ the spectrum will be spread out over a large angle and the range of wavelengths that successfully translate back through the spectral filter may decrease. It might be expected therefore to produce much narrower laser linewidths when $\psi \gg \varphi$, which could easily be tested experimentally by using a suitable telescope magnification.

7.3.6 Summary

The following is a summary of the key design considerations for the spectral filter:

- The design of the spectral filter must consider the effects of vibration and windage in order to maximise the optical power transmission.
- The ring laser cavity length must be kept short to maximise the amplification of the instantaneous laser linewidths.
- Simultaneous tuning can be prevented by ensuring that $\psi < \varphi$. Ideally though, ψ should be only fractionally smaller than φ in order to maximise the TSB and the duty cycle.
- Secondary simultaneous tuning (SST) can also be prevented by ensuring the eccentricity is in a range between a minimum threshold value (Eq. 4.18) and a maximum that ensures the largest visible facet width is obtained.

- If precision alignment mounting stages are available, a longer wavelength should be assigned to align with the optical axis. This will distribute the divergence angle (and the convergence angle) evenly on either side of the telescope optical axis and allow the whole spectrum to be swept by the filter.
- Future designs may wish to consider the non-linear sweep of the spectrum and attempt to correct this through the design process, although this would be challenging since it is a fundamentally inherent property of the diffraction grating.

7.4 Grand Optimisation And Component Interconnectivity

A component dependent hierarchy was created to help guide the design of the spectral filter (Section 4.9.1). The choice of light source and the PM were established as the two most significant decisions since every other component must be chosen as a function of these two components due to their restrictions and limitations.

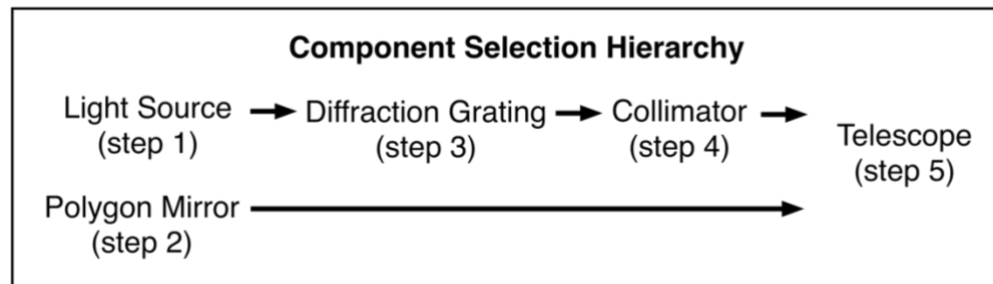


Figure 7.1. Component selection hierarchy. The choice of telescope design depends on the chain of decisions made for the light source (step 1), diffraction grating (step 3) and collimator (step 4) combined with the choice of PM (step 2).

The design hierarchy simplifies the component selection process in the quest to optimise the performance of the PM-based spectral filter (Table 4.2). The choice of light source (step 1) depends upon the properties of the sample intended to be imaged, while the choice of PM (step 2) is generally chosen as a function of its operating speed. These two components can be selected independently from each other but the choice of every other component that follows must consider their properties first. In general, a broadband laser source ($> 150\text{ nm}$) and a high-speed PM ($> 50\text{ kHz}$) should be employed.

Aside from the fact that the majority of optical components are bandwidth limited and cannot accommodate an infinitely broad spectrum, the properties of the components can influence these features and potentially worsen the filter's performance (either by

lowering the optical power or by widening the linewidths and narrowing the TSB). At the same time, the combination of components can also prevent some of the light from traveling correctly through the filter, causing them to be lost through vignetting.

However, satisfying all of the requirements to maximise the efficiency in all areas of the spectral filter is unlikely to be achieved since there are certain parameters that will be affected as a consequence of optimising others. As is frequently the case with competing design criteria, the most advantageous solution involves finding an acceptable balance between all of the parameters.

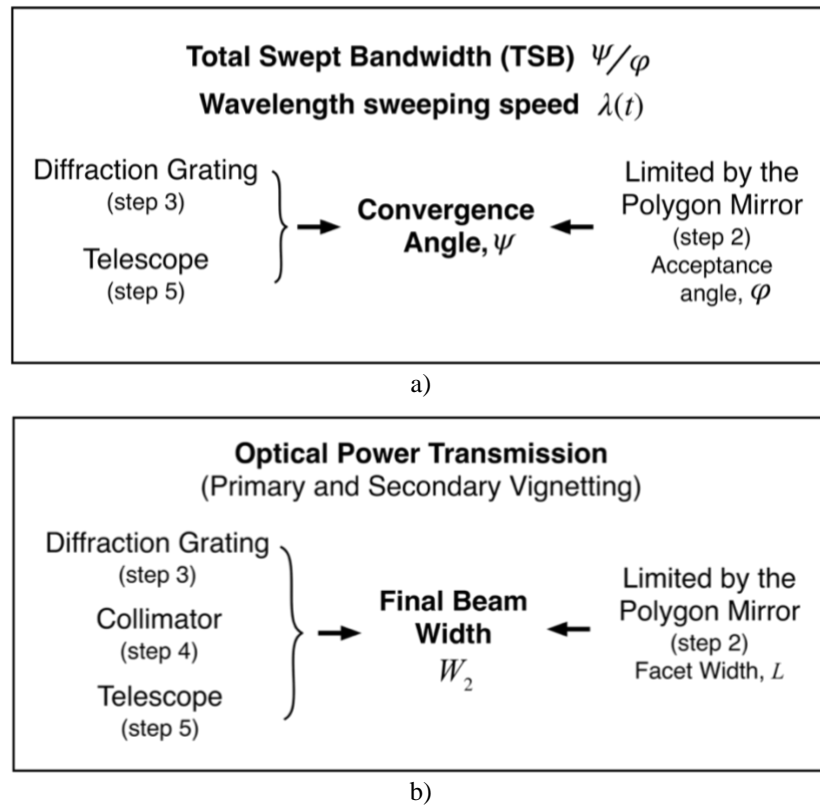


Figure 7.2. Component interconnectivity. **a)** The TSB and the wavelength sweeping speed are determined by the convergence angle, ψ , given by the choice of diffraction grating and telescope but it is limited by the choice of PM due to the acceptance angle, φ . **b)** The optical power transmission (w.r.t. vignetting) is partially determined by the final beam width, W_2 , given by the choice of diffraction grating, collimator and telescope but it is limited again by the choice of PM due to the facet width, L . The extent of the effects from aberration also determine the amount of secondary vignetting.

7.4.1 Polygon Mirror Constraints

Both the radius and the number of facets on the PM together establish the maximum beam width that can be successfully accommodated by a single facet without lowering the

optical power output through primary vignetting¹⁷. These same parameters also establish the acceptance angle, which will limit the TSB whenever the convergence angle is wider than the acceptance angle ($\psi > \varphi$). The acceptance angle can be doubled by placing the PM off-axis and installing the RM, but this also creates the potential to introduce SST if the locations of these two components are positioned carelessly. To avoid this, Eq. 4.19 and Eq. 4.4 should be used to determine the minimum value of eccentricity and the correct retro-angle respectively.

The wavelength sweeping speed is a function of the PM's rotational frequency and is proportional to the ratio between the convergence angle and the acceptance angle, ψ/φ . The duty cycle is also determined by this ratio, which will be 100% whenever $\psi/\varphi \geq 1$. The wavelength sweeping speed can be increased by having $\psi/\varphi < 1$ but the duty cycle will lower as a consequence. If $\psi/\varphi > 1$, the wavelength sweeping speed will decrease and the duty cycle will be 100%, but at the cost of reducing the TSB and introducing simultaneous tuning. This is a complex and challenging problem since it relies on finding the optimal combination of light source, diffraction grating and telescope magnification to satisfy the constraints of the PM. Custom made components could be employed to achieve this but this will increase the cost. It would be more convenient to search for a specific combination of components that produce a convergence angle which is slightly less than the acceptance angle (on-axis or off-axis). This will prevent the initial form of simultaneous tuning from occurring and maximise the duty cycle (depending on ψ/φ , which will be < 1). The wavelength sweeping speed can only be successfully increased by deliberately making $\psi/\varphi < 1$ and employing additional methods that buffer and stack the output sweeps to effectively maximise the duty cycle. Maximising the TSB comes from the desire to improve the axial resolution of the OCT imaging system. Maximising the duty cycle will deliver the most efficient scanning method on the sample, which will improve the data acquisition rate and the speed of real-time imaging, although this will only have a significant impact on the system when the duty cycle is particularly low (e.g. $< 75\%$).

¹⁷ However, primary vignetting still occurs as the PM rotates and sweeps across the path of the beam.

7.4.2 Collimator Constraints

The facet width and the eccentricity of the PM limit the choice of collimator. This is because the final beam width, W_2 , must be smaller than the facet width, L , to prevent over illuminating its surface and causing excess power loss through primary vignetting (Section 4.8). This problem can be mitigated by employing a telescope with a certain magnification to reduce the size of the beam. However, the theoretical analysis carried out in Section 4.8.1 showed that larger beam diameter collimators require more powerful magnification than smaller beam diameter collimators, and that the shortest wavelengths have the largest beam diameter after emerging from the diffraction grating (Figure 4.19), which should therefore be prioritised in the design process. This is problematic though because a higher magnification (or in this case, demagnification) will increase the convergence angle as a consequence, which could be detrimental to the TSB (Eq. 4.26). Furthermore, in order to achieve the highest sweeping frequencies, the PM would ideally have a high facet count, which reduces the size of the facets and decreases the acceptance angle. Maximising the speed of the OCT imaging system therefore places significant constraints on the other component's parameters, which can then have a detrimental effect on the optical power transmission and the axial resolution. Aside from this, the choice of collimator determines the number of illuminated lines/grooves on the grating, as discussed in Section 7.4.3 below.

7.4.3 Diffraction Grating Constraints

Using a diffraction grating with a high line/groove density achieves a wider divergence angle and therefore a higher spectral resolution (Section 3.4). However, a wider divergence angle is not always compatible with the intended telescope design. If the divergence angle is too wide for the NA of the first lens (that is, if the focal length is too long or the lens diameter is too small), the marginal rays will pass around the lens, escaping from the filter, and the TSB will decrease. This risk can be reduced by selecting a grating with a less powerful spectral resolution to produce a smaller divergence angle. The spectral resolution could then be improved by redesigning the filter so that the light is forced to undergo multiple interactions with the diffraction grating. A system designed in this way could deliver a sufficiently narrow linewidth even though it uses a low line/groove density diffraction grating, and/or a narrow beam collimator, since the theoretical linewidth can be approximately halved ($2\sqrt{\ln 2}/\pi \sim 0.53$) for each interaction

with the grating (Section 3.4.1). In any case, the divergence angle must be considered again, after the telescope inversion, due to the necessity to meet the acceptance angle constraint set by the PM. When the divergence angle is very large (high resolution grating) the convergence angle must be reduced to avoid limiting the TSB. When the divergence angle is very small (low resolution grating) the convergence angle must be increased to maximise the duty cycle.

Assuming the PM and the light source have already been selected (as directed by the design hierarchy), the simplest solution to optimise the spectral filter would be to use a diffraction grating which produces a divergence angle (for the selected light source) that perfectly matches the acceptance angle of the PM (although ideally, fractionally less to avoid simultaneous tuning). In this way, the telescope would not require any magnification (or demagnification in this case) and the collimator can then be selected as a function of the facet width only¹⁸. This allows more freedom in the design of the telescope, which now only has the responsibility of collecting the diverging spectrum and delivering it to the PM.

7.4.4 Telescope Constraints

Although the telescope is the final component to be selected in the design hierarchy (step 5), it can also be considered the most important since it offers the greatest opportunity for optimisation. This is because the telescope connects the light source (step 1) to the PM (step 2). The telescope is simultaneously (but not exclusively) responsible for maintaining the TSB, the duty cycle and the wavelength sweeping speed, carried out through controlling the convergence angle. The telescope also affects the optical power transmission by controlling the final beam width on the PM (primary vignetting).

Unless a specific design is being employed, maximising the duty cycle and the TSB requires the convergence angle to closely approach the acceptance angle of the PM. The telescope magnification must be appropriately selected to ensure that both angles are correctly paired, however this also introduces a change in the beam width that can cause primary vignetting and lower the optical power. If the beam width is prioritised, in favour

¹⁸ Although the beam width (or collimator choice) must also consider the visible facet width with respect to the eccentricity and the change in beam width due to the geometry of interacting with the diffraction grating.

of minimising the primary vignetting and maximising power transmission, the convergence angle may exceed the acceptance angle of the PM and both the duty cycle and the TSB will decrease from introducing simultaneous tuning, lowering the axial resolution of the OCT images. If the duty cycle and the TSB are prioritised, favouring to optimise the convergence angle and therefore maximise the axial resolution, the optical power could reduce from excess primary vignetting.

The telescope also plays a significant role in the amount of aberration experienced by the light rays. Spherical, chromatic, coma, astigmatism and field curvature aberration all contribute towards increasing the amount of ray deflection. Aberrations therefore reduce the ability of the filter to effectively guide the light rays back to the optical fibre, which increases the amount of secondary vignetting and lowers the optical power transmission. This also effects the instantaneous laser linewidths, which can be widened by having stray light rays from neighbouring portions of the spectrum enter the optical fibre at the wrong moment during the sweeping process. It is therefore important to minimise the amount of aberration in order to maximise the optical power transmission, since the design of the spectral filter should prioritise the TSB and the duty cycle to maximise the axial resolution and provide sharper OCT images.

Since the desired, high spectral resolution of the diffraction grating produces a wide divergence angle, the spectral filter would appear to favour the use of high NA's on the first lens in the telescope. However, it was shown in Section 5.5.1 that the marginal rays in the spectrum experience increasing amounts of deflection when incident on the lenses at normalised pupil coordinate values close to 1 and -1 (i.e. in the least paraxial fashion). The optical power at the margins of the spectrum subsequently decrease as a result of the increased amount of secondary vignetting. Selecting the properties of the first lens in the telescope (specifically its focal length and lens diameter) is therefore guided by the motivation to make the rays propagate closer to paraxial, but this is governed by the combined properties of the light source (giving the bandwidth) and the diffraction grating (giving the divergence angle). A large bandwidth light source and a high-density grating produce a wider divergence angle, which requires a high NA on the first lens in the telescope in order to successfully capture the entire diverging spectrum. For a fixed divergence angle, a larger diameter (e.g. 2-inch or 50.8 mm) or a shorter focal length on the first lens can help reduce the effects of aberration and allow close to paraxial ray

propagation. This is equivalent to deliberately under filling the aperture of the first lens. The shorter focal length will also reduce the total track length and help minimise the effects of beam divergence. Both of these telescope properties will assist with guiding the rays along their intended path through the filter, allowing more of the light to return to the optical fibre and increasing the optical power transmission. Lenses with a large diameter and a high NA (short focal length) or custom designed F-theta lenses with a wide achromatic response (e.g. camera lenses) would be the most effective here but are less common and significantly more complex and expensive when available. A much simpler and cheaper solution is to use parabolic mirrors, which are discussed shortly in Section 7.6.

Long focal length telescope designs should be accompanied by a wide beam diameter collimator to lower the effects of beam divergence (as well as increasing the spectral resolution by illuminating more lines/grooves on the grating), however the size of the PM's facets will ultimately limit the choice of collimator. A custom-made collimator with a beam width that matches the facet width (after the grating) could be used with a 1:1 telescope, although this would increase the cost. It is also unlikely that the exact combination of light source and diffraction grating can be found without further customisation (specifically the grating), which again would add more specialisation and cost to the final setup. Since the cost is typically a concern, the only option is to follow the spectral filter design hierarchy and select readily available components with parameters that suit the needs of the system and the specifications of the light source and the PM.

7.5 Example Using The Design Hierarchy

The following example is an attempt to use the design hierarchy (Section 4.9.1) to select the correct combination of collimator and two-lens telescope for a given light source and PM. For simplicity, the properties of these components shall remain the same as they have throughout the thesis. The choice of diffraction grating (step 3) follows the selection of the light source (step 1), due to the optical properties it must adhere to, and is not fundamentally restricted by the choice of PM (step 2). Various gratings are available, although in the following example the properties of the 1145 *l/mm* transmission grating (Wasatch Photonics) shall be used to establish the most suitable collimator/telescope

combination. Together with the properties of the light source ($\Delta\lambda = 160 \text{ nm}$ and $\lambda_c = 1330 \text{ nm}$), this diffraction grating produces a divergence angle $\Delta\delta = 16.88^\circ$ (Eq. 3.4).

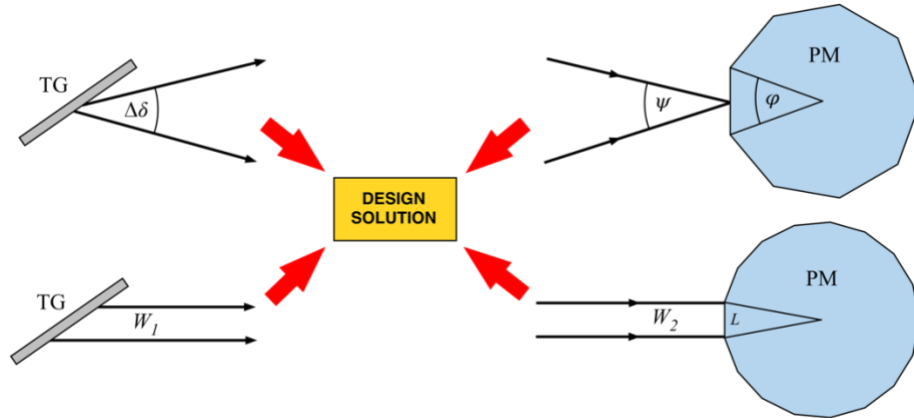


Figure 7.3. Finding the best design solution for the constraints imposed by the PM. Components: transmission grating, TG, polygon mirror, PM, divergence angle, $\Delta\delta$, convergence angle, ψ , acceptance angle, ϕ , initial beam width (after grating), W_1 , final beam width, W_2 , and facet width, L .

The collimator and telescope combination must conform to several criteria in order to achieve an optimised spectral filter design (Figure 7.3). Ideally, the convergence angle should be fractionally less than the acceptance angle ($\psi < \phi = 10^\circ$) in order for the off-axis PM to accommodate all of the wavelengths in the converging spectrum without introducing simultaneous tuning. The final beam width should also be equal to or less than the width of the polygon facets ($W_2 \leq 2.77 \text{ mm}$) in order to remove (or at least minimise) primary vignetting. Further consideration is given to the track length of the telescope and minimising the amount of aberration, which should therefore prioritise shorter focal lengths and large diameter lenses respectively.

Using $\Delta\delta = 16.88^\circ$ specified above, a table can be generated to list the convergence angles for every available focal length combination (Figure 7.4a). Alternatively, the focal length ratio can be calculated for any desired convergence angle and the most suitable lenses can then be selected (in this case, $f_1 \sim 0.6f_2$). However, the use of a table offers the freedom to explore a range of options, which is more beneficial since the combination also needs to satisfy the final beam width condition. Using the initial beam width of the collimator and the parameters of the diffraction grating in Eq. 4.22 (for the central wavelength), a second table can be generated that lists the final beam width for the same set of focal length combinations (Figure 7.4b). However, a separate table must be constructed for each collimator in order to fully compare every available option and look

for any suitable telescope magnifications that satisfy both conditions simultaneously (see Appendix C).

2) List available focal lengths for the second lens

1) List available focal lengths for the first lens

4) Yellow values identify when $\psi < \varphi$

3) Red values identify when $\psi > \varphi$

5) Black box identifies 2-inch diameter lenses

F1	F2									
	30	35	40	50	60	75	80	100	150	200
30	16.88	14.47	12.66	10.13	8.44	6.75	6.33	5.06	3.38	2.53
35	19.69	16.88	14.77	11.82	9.85	7.88	7.39	5.91	3.94	2.95
40	22.51	19.29	16.88	13.50	11.25	9.00	8.44	6.75	4.50	3.38
50	28.13	24.11	21.10	16.88	14.07	11.25	10.55	8.44	5.63	4.22
60	33.76	28.94	25.32	20.26	16.88	13.50	12.66	10.13	6.75	5.06
75	42.20	36.17	31.65	25.32	21.10	16.88	15.83	12.66	8.44	6.33
80	45.01	38.58	33.76	27.01	22.51	18.01	16.88	13.50	9.00	6.75
100	56.27	48.23	42.20	33.76	28.13	22.51	21.10	16.88	11.25	8.44
150	84.40	72.34	63.30	50.64	42.20	33.76	31.65	25.32	16.88	12.66
200	112.53	96.46	84.40	67.52	56.27	45.01	42.20	33.76	22.51	16.88

a) Table of convergence angles (degrees)

2) List available focal lengths for the second lens

1) List available focal lengths for the first lens

3) Red values identify when $W_2 > L$

4) Yellow values identify when $W_2 < L$

5) Black box identifies 2-inch diameter lenses

F1	F2									
	30	35	40	50	60	75	80	100	150	200
30	1.20	1.40	1.60	2.00	2.40	3.00	3.20	3.99	5.99	7.99
35	1.03	1.20	1.37	1.71	2.05	2.57	2.74	3.42	5.13	6.85
40	0.90	1.05	1.20	1.50	1.80	2.25	2.40	3.00	4.49	5.99
50	0.72	0.84	0.96	1.20	1.44	1.80	1.92	2.40	3.59	4.79
60	0.60	0.70	0.80	1.00	1.20	1.50	1.60	2.00	3.00	3.99
75	0.48	0.56	0.64	0.80	0.96	1.20	1.28	1.60	2.40	3.20
80	0.45	0.52	0.60	0.75	0.90	1.12	1.20	1.50	2.25	3.00
100	0.36	0.42	0.48	0.60	0.72	0.90	0.96	1.20	1.80	2.40
150	0.24	0.28	0.32	0.40	0.48	0.60	0.64	0.80	1.20	1.60
200	0.18	0.21	0.24	0.30	0.36	0.45	0.48	0.60	0.90	1.20

b) Table of final beam widths (mm)

Figure 7.4. **a)** Convergence angles produced by every available focal length combination for the initial divergence angle (16.88°). **b)** Final beam width produced by every available focal length combination for the F110 collimator (1.15 mm initial beam diameter). Red values are larger than the specified conditions and yellow values are less than the conditions. The black square in the bottom right of each table highlights the available 2-inch diameter lenses. The green values are the pair that were selected in this discussion.

For illustration, it was found that an $80 \times 150 \text{ mm}$ focal length telescope and a F110 collimator (1.15 mm beam diameter, Thorlabs) produce a convergence angle $\psi = 9^\circ$ and a final beam width $W_2 = 2.25 \text{ mm}$, as highlighted by the green values in tables a) and b) of Figure 7.4. This combination satisfies both conditions and has the shortest telescope track when using the 2-inch diameter lenses. All other combinations had a longer telescope track or sacrificed one of the conditions. However, although the final beam width is smaller than the polygon facets, it was produced by a relatively small beam

diameter collimator (lowering the spectral resolution), and the telescope track length is still relatively long (460 mm). Both of these properties increase the effects from beam divergence, which could potentially decrease the optical power output by causing larger amounts of secondary vignetting. The duty cycle of this design will also suffer slightly as a result of the smaller convergence angle, which, for a perfectly aligned system, should achieve $\sim 90\%$.

In this example, using 10 different focal lengths, there are 100 possible focal length combinations but only 27 that satisfy the first condition, $\psi < \varphi = 10^\circ$. The number of suitable options for the choice of collimator gradually reduces as the beam diameter increases and is limited further when only considering 2-inch diameter lenses. The result is that the number of available options that satisfy both conditions eventually becomes zero, which emphasises the fact that it isn't possible to optimise every parameter simultaneously and that once a decision has been made to satisfy one condition, it will substantially narrow the number of available design pathways that can be followed.

7.6 Parabolic Mirrors

In Chapter 5, the performance of the spectral filter was shown to benefit from increasing the telescope lens diameters. This was in response to understanding the negative impact caused by aberrations and an attempt to reduce the amount of ray deflection at the marginal regions of the spectrum. These ray deflections prevent some of the light from returning correctly to the optical fibre, which lowers the optical power transmission and degrades the OCT images. This solution improved the performance of the spectral filter but it could not remove all of the various forms of aberration that were effecting the path of the rays.

A better solution was found by employing two 90 degree, off-axis parabolic mirrors in the telescope, replacing the two-lens design. These were shown to significantly outperform the lenses, producing a 20% increase in the TSB and a 37% larger FWHM when compared with the best result from using the two-lens telescope design (Figure 6.19). Their ability to carry out the same role as the lenses, without the detrimental effects of spherical aberration, and the experimentally observed performance increase makes them an attractive alternative that should be considered in any future spectral filter designs.

Parabolic mirrors offer an additional advantage from their ability to operate at any wavelength range (within reasonable limits), which allows extra-broadband sources to be used without any fundamental limitations. The spectral filter design simply needs to ensure that the parabolic mirrors are capable of capturing all of the diverging spectrum from the diffraction grating, otherwise light could still be lost at the margins of the spectrum which would therefore reduce the TSB.

The available range of reflected focal lengths (RFL) for the parabolic mirrors is relatively limited when compared to the wide range of available focal lengths for the telescope lenses. From this perspective, lenses might be considered more effective at finding a sufficient magnification to match the divergence angle, at the grating, to the acceptance angle of the PM. However, the parabolic mirrors can easily be custom-made to produce the exact magnification needed to perfectly match these two angles, since the manufacturing process only requires programming in the correct paraboloid to machine out the desired RFL. This could potentially increase the cost, although the benefits gained from doing this would certainly make it a worthwhile investment. The reflection angle does not necessarily need to be 90 degrees either. Shallower or wider angles could be employed that may improve the alignment process by providing more space to adjust the components. A shallower angle may even help to reduce the footprint of the setup. The collimator could also be replaced with a parabolic mirror which would improve the beam divergence and guide more of the light along the correct path. This component would then no longer be dependent on the light source (due to the anti-reflection surface coating) and would therefore not need to be changed as a result of experimenting with different operating wavelengths, making the system even more versatile.

7.7 Final Design Considerations

This thesis has discussed the most important aspects of the PM-based spectral filter design with a focus on optimising its performance. However, the results have shown that it is not entirely possible to optimise every aspect simultaneously. The final conclusion is that it will always come down to a trade-off between maximising the TSB and minimising the instantaneous laser linewidths (to achieve the grating imposed linewidth limit). When the system is designed to sweep through a very large bandwidth, maximising the TSB and the duty cycle, it will inevitably reduce the ability of the system to minimise the linewidths. This means that the design of the spectral filter comes down to deciding

whether to prioritise the axial resolution or the axial scanning range of the accompanying OCT system. If the axial scanning range of the OCT system is prioritised, by designing the spectral filter to produce narrow instantaneous laser linewidths, the TSB and the duty cycle can be expected to decrease, lowering the axial resolution.

The following is a breakdown of the recommended steps to follow to optimise the PM-based spectral filter when the axial resolution is prioritised over the axial scanning range. These recommendations assume that the light source and the PM have already been selected, which ideally should be chosen for their wide spectral bandwidth and high rotational speed respectively. They are divided into two groups depending on the specific areas they attempt to optimise.

Optimisation path favouring the TSB and the Duty Cycle

- Place the PM off-axis and install a retro-reflector mirror to increase the acceptance angle, making sure to use the optimum value of eccentricity to prevent SST. Placing the PM above-axis will maximise the visible facet width for the widest beam widths in the converging spectrum.
- Using the properties of the light source, select a custom-made diffraction grating that produces a divergence angle which is fractionally smaller than the acceptance angle of the off-axis PM. This will allow the system to use a 1:1 telescope magnification whilst also removing simultaneous tuning and maximising the duty cycle. If a custom-made grating is not an option, the next closest alternative should be used.

Maximising the Optical Power Transmission

- Shorten the ring laser cavity length as much as possible to maximise the linewidth amplification process.
- Replace the collimator and the two-lens telescope with parabolic mirrors to reduce the effects of aberration. Employ custom-made RFLs to create the optimum magnification if necessary. This will minimise the amount of ray divergence and therefore reduce the amount of secondary vignetting.

- Primary vignetting can be effectively mitigated by translating the PM axially, towards the telescope, to optimise the active facet position with respect to the object plane of the converging spectrum.

It is preferable to maximise the axial resolution of the OCT imaging system, which in turn requires maximising the TSB. Whilst optical power output is a concern and should not be ignored, if the TSB is narrow, the axial resolution of the accompanying OCT system will be low. Maximising the TSB of the PM-based SS can afford to be prioritised over the power output since there are methods that can be used to amplify the optical signal. Several suggestions for further development now follow that are considered to be advantageous in any future spectral filter designs.

7.7.1 Ring Laser Cavity Modular Design

Section 2.3.2.2 discussed the instantaneous laser linewidth amplification process and suggested that the power could be increased by reducing the path length of the ring laser cavity. The optical track length of the components in the spectral filter cannot be reduced by any significant amount but the optical fibres, which contribute the longest path lengths, can be shortened greatly. A simple solution to this problem would be to build all of the optical fibre sections of the cavity (fibre optic circulator and coupler) into a single unit with a minimal footprint, as shown in Figure 7.5. This unit could also be designed to minimise the number of fibre couplings, which would improve the optical power transmission, and could even be incorporated into the optical fibre-based interferometer array. Using this approach, it is estimated that the ring laser cavity length could be significantly reduced to less than a meter in total, however this custom modification may increase the cost and might therefore be more applicable when upscaling to a commercial system.

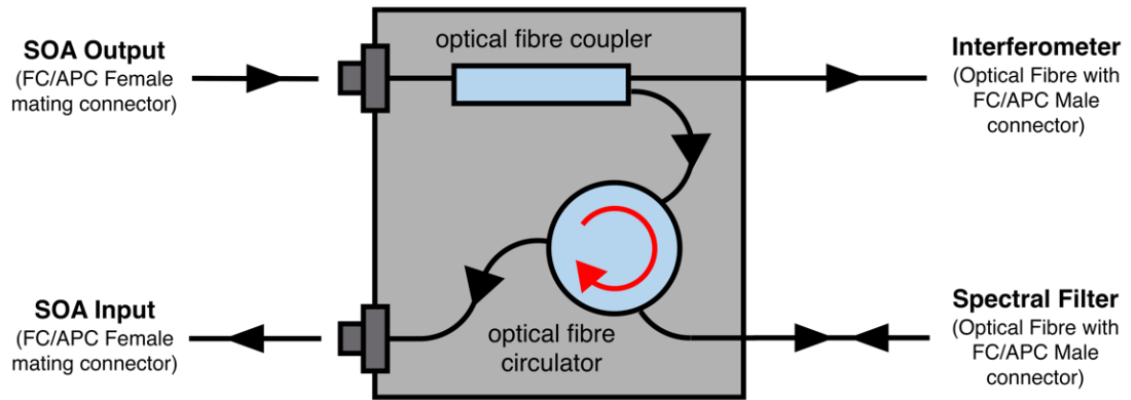


Figure 7.5. A simple example of a custom-built box to contain the optical fibre components of the ring laser cavity. The input/output ports of the SOA use female FC/APC connectors mounted to the outside of the box while optical fibres of a specified length connect to the interferometer and the spectral filter using male FC/APC connectors.

7.7.2 Parabolic Mirrors With A Twist

The combination of experimental results and observations made in the simulations from Chapter 6 suggest that the performance of the spectral filter might be improved by changing the layout of its construction. This was realised after observing the axial location of each beam's minimum waist point between the two parabolic mirrors (Figure 6.6) and by considering the way that each wavelength interacts with the first parabolic mirror surface (Figure 6.7). The two-lens telescope design was affected by aberrations and produced a curved focal plane at the midpoint (Figure 5.9) but when larger diameter lenses were used, the curvature of the focal plane was reduced and the performance of the spectral filter improved (Section 5.5). The sloped focal plane produced by the parabolic mirrors (Figure 6.6) showed virtually no curvature and it is suspected that the system might be improved if this slope were aligned vertically at the midpoint between the two parabolic mirrors.

The solution to this problem could be as simple as rotating the first parabolic mirror by 90 degrees about the axis of collimated beam propagation (see Figure 6.1). Using Figure 6.7 as a reference, this rotation would make all of the rays propagate either out of the page or into the page (depending on the direction of rotation). Since the spectrum is mostly operating in the sagittal plane, this new orientation would significantly even-out the distance that each light ray travels to reach the surface of the first parabolic mirror and allow each reflected wavelength beam to focus at approximately the same distance from its surface, at the midpoint between the two mirrors. A hypothesis that can be followed

up in future work is that this design modification could improve the performance of the spectral filter by reducing the amount of secondary vignetting caused by astigmatism.

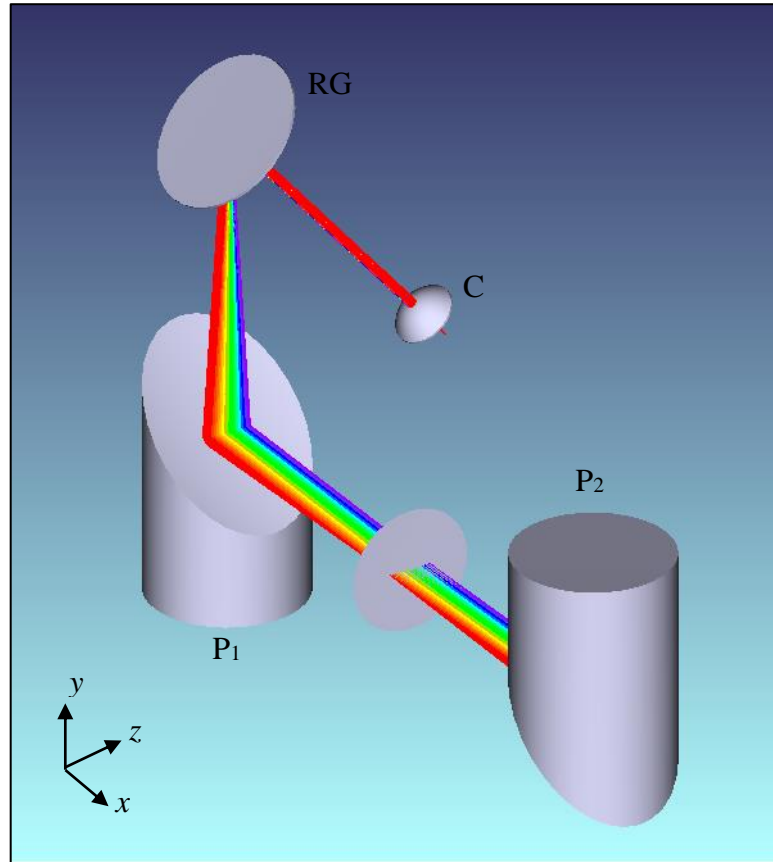


Figure 7.6. Suggested alternative filter alignment with laser light propagating in all three planes. In this design, the chief rays of each wavelength start in the y-z plane and then change into the x-z plane when travelling through the telescope, between the two parabolic mirrors. Collimator lens, C, Reflection Grating, RG and Parabolic mirrors, P₁ and P₂.

One potential issue with this modification is that the second parabolic mirror and all subsequent components would also have to be orientated to accommodate this change, which would therefore introduce a vertical aspect to the filter, sending light into the x-direction instead of propagating (almost) exclusively in the y-z plane (Figure 7.6). This configuration would potentially be more difficult to align, since the filter would now be operating in three dimensions instead of just two, and the extra degree of freedom in the alignment could present additional challenges when dealing with any vibrations produced by the active PM.

REFERENCES

- [1] G. J. Tearney, B. E. Bouma and J. G. Fujimoto, "High-speed phase- and group-delay scanning with a grating-based phase control delay line," *Optics Letters*, vol. 22, no. 23, pp. 1811-1813, 1 December 1997.
- [2] K. K. Lee, A. Mariampillai, J. X. Yu, D. W. Cadotte, B. C. Wilson, B. A. Standish and V. X. Yang, "Real-time speckle variance swept-source optical coherence tomography using a graphics processing unit," *Biomedical Optics Express*, vol. 3, no. 7, pp. 1557-1564, 2012.
- [3] S. M. Moaghianezam, D. Koos and S. E. Fraser, "Differential phase-contrast, swept-source optical coherence tomography at 1060 nm for in vivo human retinal and choroidal vasculature visualization," *Journal of Biomedical Optics*, vol. 17, no. 2, pp. 0260111-0260115, 2012.
- [4] A.-Q. K. Muhammad and T. Akkin, "Swept-source polarisation-sensitive optical coherence tomography based on polarization-maintaining fiber," *Optics Express*, vol. 18, no. 4, pp. 3392-3403, 15 February 2010.
- [5] M. K. K. Leung, A. Mariampillai, B. A. Standish, K. K. Lee, I. A. Vitkin and V. X. Yang, "Simultaneous 6-channel optical coherence tomography using a high-power telescope-less polygon-based swept laser in dual-amplifier configuration," in *Optical Coherence Tomography and Coherence Domain Optical Methods in Biomedicine XIV*, 2010.
- [6] Y. Chen, L. D. Burnes, M. de Bruin and J. F. de Boer, "Three-dimensional pointwise comparison of human retinal optical property at 845 and 1060 nm using optical frequency domain imaging," *Journal of Biomedical Optics*, vol. 14, no. 2, pp. 0240161-0240165, 2009.
- [7] E. C. Lee, J. F. de Boer, M. Mujat, H. Kim and S. H. Yun, "In vivo optical frequency domain imaging of human retina and choroid," *Optical Express*, vol. 14, no. 10, pp. 4403-4411, 15 May 2006.
- [8] C. Boudoux, S. H. Yun, W. Y. Oh, W. M. White, N. V. Iftimia, M. Shishkov, B. E. Bouma and G. J. Tearney, "Rapid wavelength-swept spectrally encoded confocal microscopy," *Optics Express*, vol. 13, no. 20, pp. 8214-8221, 3 October 2005.
- [9] W. Y. Oh, B. J. Vakoc, M. Shishkov, G. J. Tearney and B. E. Bouma, ">400 kHz repetition rate wavelength-swept laser and application to high-speed optical frequency domain imaging," *Optics Letter*, vol. 35, no. 17, pp. 2919-2921, 1 September 2010.
- [10] B. Bräuer, N. Lippok, S. G. Murdoch and F. Vanholsbeeck, "Simple and versatile long range swept source for optical coherence tomography applications," *Journal of Optics*, vol. 17, no. 2015, p. 125301, 2015.
- [11] Y. Mao, S. Chang, E. Murdock and C. Flueraru, "Simultaneous dual-wavelength-band common-path swept-source optical coherence tomography with single polygon mirror scanner," *Optics Letters*, vol. 36, no. 11, pp. 1990-1992, 1 June 2011.
- [12] S. M. R. Motaghian Nezam, "High-speed polygon-scanner-based wavelength-swept laser source in the telescope-less configuration with application in optical coherence tomography," *Optics Letters*, vol. 33, no. 15, pp. 1741-1743, 1 August 2008.
- [13] A. Morosawa, C. Chong and T. Sakai, "Wide tuning range wavelength-swept laser with single semiconductor optical amplifier for OCT," in *Optical Coherence Tomography and Coherence Techniques III*, 2007.
- [14] W. Y. Oh, S. H. Yun, G. J. Tearney and B. E. Bouma, "Wide Tuning Range Wavelength-Swept Laser With Two Semiconductor Optical Amplifiers," *IEEE Photonics Technol Lett*, vol. 17, no. 3, pp. 678-680, March 2005.

- [15] M. Tokurakawa, J. M. Daniel, C. S. Chenug, H. Liang and W. A. Clarkson, "Ultra-broadband wavelength-swept Tm-doped fiber laser using wavelength-combined gain stages," *Optics Express*, vol. 23, no. 1, pp. 471-476, 2015.
- [16] S.-W. Lee, H.-W. Song, M.-Y. Jung and S.-H. Kim, "Wide tuning range wavelength-swept laser with a single SOA at 1020 nm for ultrahigh resolution Fourier-domain optical coherence tomography," *Optics Express*, vol. 19, no. 22, pp. 21227-21237, 24 October 2011.
- [17] Precision Laser Scanning, "Blog: Road Runner 70,000 RPM polygon scanner solves the noise problem," Precision Laser Scanning, 16 March 2016. [Online]. Available: <https://precisionlaserscanning.com/2016/03/road-runner-70000-rpm-polygon-scanner-solves-the-noise-problem/>. [Accessed 17 January 2018].
- [18] W. Y. Oh, S. H. Yun, G. J. Tearney and B. E. Bouma, "115 kHz tuning repetition rate ultrahigh-speed wavelength-swept semiconductor laser," *Optics Letter*, vol. 30, no. 23, pp. 3159-3161, 1 December 2005.
- [19] B. Johnson, A. Walid, K. Mark, G. D. Brian, W. Peter and F. C. Dale, "Long-to-short wavelength swept source," *Optics Express*, vol. 26, no. 26, pp. 34909-34918, 2018.
- [20] R. Huber, D. C. Adler and J. G. Fujimoto, "Buffered Fourier domain mode locking: unidirectional swept laser sources for optical coherence tomography imaging at 370,000 lines/s," *Optics Letters*, vol. 31, no. 20, pp. 2975-2977, 2006.
- [21] Y. Mao, C. Flueraru, S. Sherif and S. Chang, "High performance wavelength-swept laser with mode-locking technique for optical coherence tomography," *Optics Communications*, vol. 282, no. 2009, pp. 88-92, 19 September 2008.
- [22] R. Huber, M. Wojtkowski, K. Taira and J. G. Fujimoto, "Amplified, frequency swept lasers for frequency domain reflectometry and OCT imaging: design and scaling principles," *Optics Express*, vol. 13, no. 9, 2nd May 2005.
- [23] S. Elahi, L. Thrane, A. M. Rollins and M. W. Jenkins, "Extended dynamic range of Doppler OCT by application of a new method to high density B-scans using a MHz FDML swept laser source," in *Optical Coherence Tomography and Coherence Domain Optical Methods in Biomedicine XXI*, 2017.
- [24] "Santec Tunable Lasers," Santec, 30th March 2021. [Online]. Available: <https://www.santec.com/en/products/instruments/tunablelaser/>. [Accessed 30th March 2021].
- [25] J. Jayaraman, B. B. Christopher, J. Carter, I. Borova, N. Bramham, C. Lindbald and A. Cazabat, "Widely tunable electrically pumped 1050nm MEMS-VCSELs for optical coherence tomography," in *SPIE OPTO*, San Francisco, 2020.
- [26] G. F. Marshall and G. E. Stutz, *Handbook of Optical and Laser Scanning*, 2nd Edition ed., London: CRC Press, 2012.
- [27] S.-W. Lee, H.-W. Song, B.-K. Kim, M.-Y. Jung, S.-H. Kim and J.-D. Cho, "Fourier domain optical coherence tomography for retinal imaging with 800-nm swept source: Real-time resampling in k-domain," *Journal of the Optical Society of Korea*, vol. 15, no. 3, pp. 293-299, 2011.
- [28] V. F. Duma, "Scanning in biomedical imaging: from classical devices to handheld heads and micro-systems.," in *Fifth International Conference on Lasers in Medicine*, Timisoara, 2014.
- [29] S. Moon and Z. Chen, "Phase-stability optimization of swept-source optical coherence tomography," *Biomedical Optics Express*, vol. 9, no. 11, pp. 5280-5295, 2018.
- [30] S. H. Yun, C. Boudoux, G. J. Tearney and B. E. Bouma, "High-speed wavelength swept semiconductor laser with a polygon-scanner-based wavelength filter," *Optics Letters*, vol. 28, no. 20, pp. 1981-1983, 15 October 2003.

- [31] M. Everson, V. F. Duma and G. Dobre, "Optical power transmission in a polygon mirror-based swept source optical coherence tomography system," in *Digital Optical Technologies 2017*, Munich, 2017.
- [32] M. Everson, V. F. Duma and G. Dobre, "Aspects of vignetting in a polygon mirror-based spectral filter for swept source optical coherence tomography (SS-OCT)," in *Seventh International Conference on Lasers in Medicine*, Timisoara, 2018.
- [33] M. Everson, V. F. Duma and G. Dobre, "Geometric & radiometric vignetting associated with a 72-facet, off-axis, polygon mirror for swept source optical coherence tomography (SS-OCT)," in *AIP Conference Proceedings*, Timisoara, 2017.
- [34] D. Huang, E. A. Swanson, C. P. Lin, J. S. Schuman, W. G. Stinson, W. Chang, M. R. Hee, T. Flotte, K. Gregory, C. A. Puliafito and J. G. Fujimoto, "Optical Coherence Tomography," *Science*, vol. 254, no. 5035, pp. 1178-1181, 22 November 1991.
- [35] H. Liang, M. Gomez Cid, R. Cucu, G. Dobre, B. Kudimov, J. Pedro, D. Saunders, J. Cupitt and A. Podoleanu, "Optical Coherence Tomography: a non-invasive technique applied to conservation of paintings," in *Optical Methods for Arts and Archaeology*, 2005.
- [36] T. C. Chen, A. Hoguet, A. K. Junk, K. Nouri-Mahdavi, S. Radhakrishnan, H. L. Takusagawa and P. P. Chen, "Spectral-domain OCT: helping the clinician diagnose glaucoma," *American Academy of Ophthalmology*, vol. 125, no. 11, pp. 1817-1827, November 2018.
- [37] W. Drexler and J. G. Fujimoto, "Optical coherence tomography: technology and applications," in *Biological and Medical Physics, Biomedical Engineering*, Berlin, Springer Science & Business Media, 2008, p. 3.
- [38] P. Hariharan, "Basics of Interferometry," in *Basics of Interferometry*, Sydney, Elsevier, 2007, p. 4.
- [39] A. F. Fercher, C. K. Hitzenberger, G. Kamp and S. Y. El-Zaiat, "Measurements of intraocular distances by backscattering spectral interferometry," *Optics Communications*, vol. 117, no. 1-2, pp. 43-48, 15 May 1995.
- [40] M. A. Choma, M. V. Sarunic, C. Yang and J. A. Izatt, "Sensitivity advantage of swept source and Fourier domain optical coherence tomography," *Optics Express*, vol. 11, no. 18, pp. 2183-2189, 2003.
- [41] J. F. d. Boer, R. Leitgeb and M. Wojtkowski, "Twenty-five years of optical coherence tomography: the paradigm shift in sensitivity and speed provided by Fourier domain OCT," *Biomedical Optics Express*, vol. 8, no. 7, pp. 3248-3280, 2017.
- [42] S. R. Chinn, E. A. Swanson and J. G. Fujimoto, "Optical coherence tomography using a frequency-tunable optical source," *Optics Letters*, vol. 22, no. 5, pp. 340-342, 1 March 1997.
- [43] B. Golubovic, B. E. Bouma, G. J. Tearney and J. G. Fujimoto, "Optical frequency-domain reflectometry using rapid wavelength tuning of a Cr⁴⁺: forsterite laser," *Optics Letters*, vol. 22, no. 22, pp. 1704-1706, 15 November 1997.
- [44] F. C. Lexer, C. K. Hitzenberger, A. F. Fercher and M. Kulhavy, "Wavelength-tuning interferometry of intraocular distances," *Applied Optics*, vol. 36, no. 25, pp. 6548-6553, 1 September 1997.
- [45] I. S. I. 60825-1, *Safety of laser products: PART 1 - Equipment classification, requirements and user's guide*, 1.2 ed., Geneva: IEC, 2014.
- [46] A. G. Podoleanu, "Optical Coherence Tomography," *Journal of Microscopy*, pp. 209-219, 18 June 2012.
- [47] C. K. Hitzenberger, "Low-coherence interferometry," in *Handbook of Visual Optics*, Boca Raton: CRC Press, 2017, pp. 37-57.

- [48] H. C. Hendargo, R. P. McNabb, A.-H. Dhalla, N. Shepherd and J. A. Izatt, "Doppler velocity detection limitations in spectrometer-based versus swept-source optical coherence tomography," *Biomedical Optics Express*, vol. 2, no. 8, pp. 2175-2188, 2011.
- [49] L. V. Wang and H. I. Wu, "Optical Coherence Tomography," in *Biomedical Optics: Principals and Imaging*, John Wiley & Sons, 2012, pp. 181-215.
- [50] M. Pircher, E. Götzinger and C. K. Hitzenberger, "Dynamic focus in optical coherence tomography for retinal imaging," *Journal of biomedical optics*, vol. 11, no. 5, p. 054013, 2006.
- [51] E. N. Morel, N. A. Russo, J. R. Torga and R. Duchowics, "Interferometric system based on swept source-optical coherence tomography scheme applied to the measurement of distances of industrial interest," *Optical Engineering*, vol. 55, no. 1, p. 014105, 2016.
- [52] J. Cao, P. Wang, Y. Zhang, G. Shi and Y. Liu, "Experimental and theoretical investigation of polygon-based swept source with continuous adjustable free spectral range," *Optics Communications*, vol. 478, no. 2021, p. 126401, 2021.
- [53] NKT Photonics, "Supercontinuum white light lasers," NKT Photonics, [Online]. Available: <https://www.nktphotonics.com/lasers-fibers/product-category/supercontinuum-lasers/>. [Accessed 11 April 2021].
- [54] X. Zhang, L. Zhongliang, N. Nan and W. Xiangzhao, "An optimized depth-resolved dispersion compensation method in optical coherence tomography signal processing," in *Fourth International Conference on Photonics and Optical Engineering*, Xi'an, 2020.
- [55] A. Bradu, M. Maria and A. Podoleanu, "Demonstration of tolerance to dispersion of master/slave interferometry," *Optics Express*, vol. 23, no. 11, pp. 14148-14161, 2015.
- [56] W. Tai-Ang, C. Ming-Che, L. Hsiang-Chien, L. Cheng-Yu and T. Meng-Tsan, "Ultrahigh-resolution optical coherence tomography/angiography with an economic and compact supercontinuum laser," *Biomedical Optics Express*, vol. 10, no. 11, pp. 5687-5702, 2019.
- [57] Thorlabs, "Fixed Focus Collimator Packages: FC/APC Connectors," Thorlabs, USA, [Online]. Available: https://www.thorlabs.de/newgrouppage9.cfm?objectgroup_id=1696&pn=F240APC-C. [Accessed 20th September 2018].
- [58] J. Cao, P. Wang, Y. Zhang, G. Shi, B. Wu, S. Zhang and Y. Liu, "Methods to improve the performance of the swept source at 1.0 μm based on a polygon scanner," *Photonics Research*, vol. 5, no. 3, pp. 245-250, June 2017.
- [59] M. G. Littman and H. J. Metcalf, "Spectrally narrow pulsed dye laser without beam expander," *Applied Optics*, vol. 17, no. 14, pp. 2224-2227, 1978.
- [60] Arden Photonics, "Arden Photonics/Products/APL-OP01," August 2016. [Online]. Available: <https://www.ardenphotonics.com/products/apl-op01/>. [Accessed 10th September 2018].
- [61] A. Podoleanu and A. Bradu, "Master-slave interferometry for parallel spectral domain interferometry sensing and versatile 3D optical coherence tomography," *Optics Express*, vol. 21, no. 16, pp. 19324-19338, 2013.
- [62] A. Bradu and A. Podoleanu, "Calibration-free B-scan images produced by master-slave optical coherence tomography," *Optics Letters*, vol. 39, no. 3, pp. 450-453, 2014.
- [63] S. Rivet, M. Maria, A. Bradu, T. Feuchter, L. Leick and Podoleanu A, "Complex master slave interferometry," *Optics Express*, vol. 24, no. 3, pp. 2885-2904, 2016.
- [64] A. Bradu and A. Podoleanu, "Imaging the eye fundus with real-time en face spectral domain optical coherence tomography," *Biomedical Optics Express*, vol. 5, no. 4, pp. 1233-1249, 2014.

- [65] X. Attendu, R. Guay-Lord, M. Strupler, N. Godbout and C. Boudoux, "Combined optical coherence tomography and hyper-spectral imaging," in *Proc. SPIE 10057, Multimodal Biomedical Imaging XII*, San Francisco, 2017.
- [66] C. Palmer, *Diffraction Grating Handbook*, sixth edition ed., New York, Rochester: Newport Corporation, 2005.
- [67] S. H. Yun, C. Boudoux, G. J. Tearney and B. E. Bouma, "High-speed wavelength-swept semiconductor laser with a polygon-scanner-based wavelength filter," *Optics Letters*, vol. 28, no. 20, pp. 1981-1983, 15 October 2003.
- [68] S. H. Yun, C. Boudoux, G. J. Tearney and B. E. Bouma, "High-speed wavelength-swept semiconductor laser with a polygon-scanner-based wavelength filter," *Optics Letters*, vol. 28, no. 20, pp. 1981-1983, 15 October 2003.
- [69] M. Everson, V. F. Duma and G. Dobre, "Optimisation of a polygon mirror-based spectral filter for swept source optical coherence tomography (SS-OCT)," in *2nd Canterbury Conference on OCT with Emphasis on Broadband Optical Sources*, Canterbury, 2018.
- [70] M. Everson, V. F. Duma and G. Dobre, "Performance enhancements from telescope optics in a polygon mirror-based, spectral filter for Swept Source-Optical Coherence Tomography (SS-OCT)," in *Optical Instruments Science, Technology, and Applications*, Frankfurt, 2018.
- [71] Thorlabs, "Off-Axis Parabolic Mirrors, Unprotected Gold Coating (0.8 - 20 μm)," Thorlabs, Inc, 21 September 2017. [Online]. Available: https://www.thorlabs.de/newgrouppage9.cfm?objectgroup_id=12395. [Accessed 21 September 2017].
- [72] Thorlabs Inc., "Near-IR Ruled Reflective Diffraction Gratings," Thorlabs, 13 September 2018. [Online]. Available: https://www.thorlabs.de/newgrouppage9.cfm?objectgroup_id=8627&pn=GR25-0613#3741. [Accessed 13 September 2018].
- [73] Edmund Optics, "Off-Axis Mirrors," Edmund Optics, 8th April 2021. [Online]. Available: https://www.edmundoptics.com/c/off-axis-mirrors/1198/#27458=27458_s%3AMzA1. [Accessed 8th April 2021].
- [74] J. Cao, P. Wang, Y. Zhang, G. Shi and Y. Liu, "Experimental and theoretical investigation of polygon-based swept-source with continuous adjustable free spectral range," *Optics Communications*, vol. 478, no. 2021, p. 126401, 20 August 2021.
- [75] R. G. Cucu, A. G. Podoleanu, J. A. Rogers, J. Pedro and R. B. Rosen, "Combined confocal/en face T-scan-based ultrahigh-resolution optical coherence tomography in vivo retinal imaging," *Optics Letters*, vol. 31, no. 11, pp. 1684-1686, 1 June 2006.
- [76] M. Wang, C. Wu, D. Sinefeld, B. Li, F. Xia and C. Xu, "Comparing the effective attenuation lengths for long wavelength in vivo imaging of the mouse brain," *Biomedical Optics Express*, vol. 9, no. 8, pp. 3534-3542, 2018.
- [77] K. O. Varughese and K. Siva Rama Krishna, "Flattening the field of postobjective scanners by optimum choice and positioning of polygons," *Applied Optics*, vol. 32, no. 7, pp. 1104-1108, 1993.
- [78] M. P. Dierking and W. S. McCormick, "High-bandwidth laser-pulse generator using continuous-wave lasers," *Applied Optics*, vol. 33, no. 24, pp. 5657-5664, 20 August 1994.
- [79] Y. Li and J. Katz, "Asymmetric distribution of the scanned field of a rotating reflective polygon," *Applied Optics*, vol. 36, no. 1, pp. 342-352, 1997.
- [80] L. Beiser, "Design equations for a polygon laser scanner," in *Beam Deflection and Scanning Technologies*, 1991.

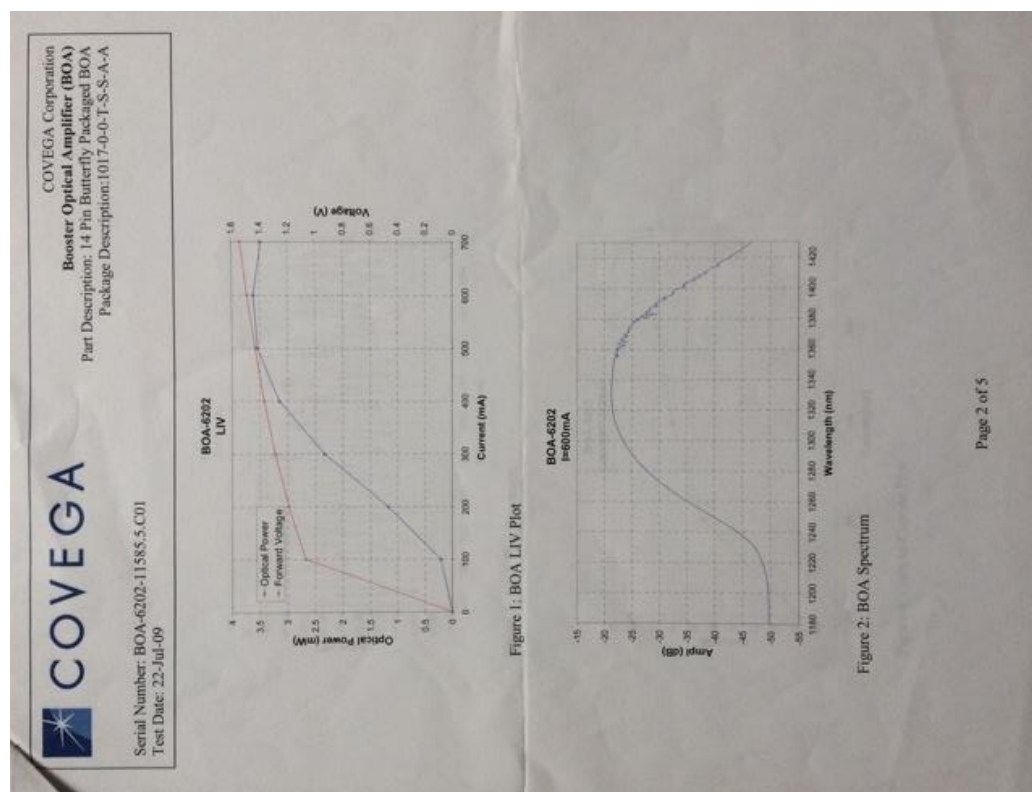
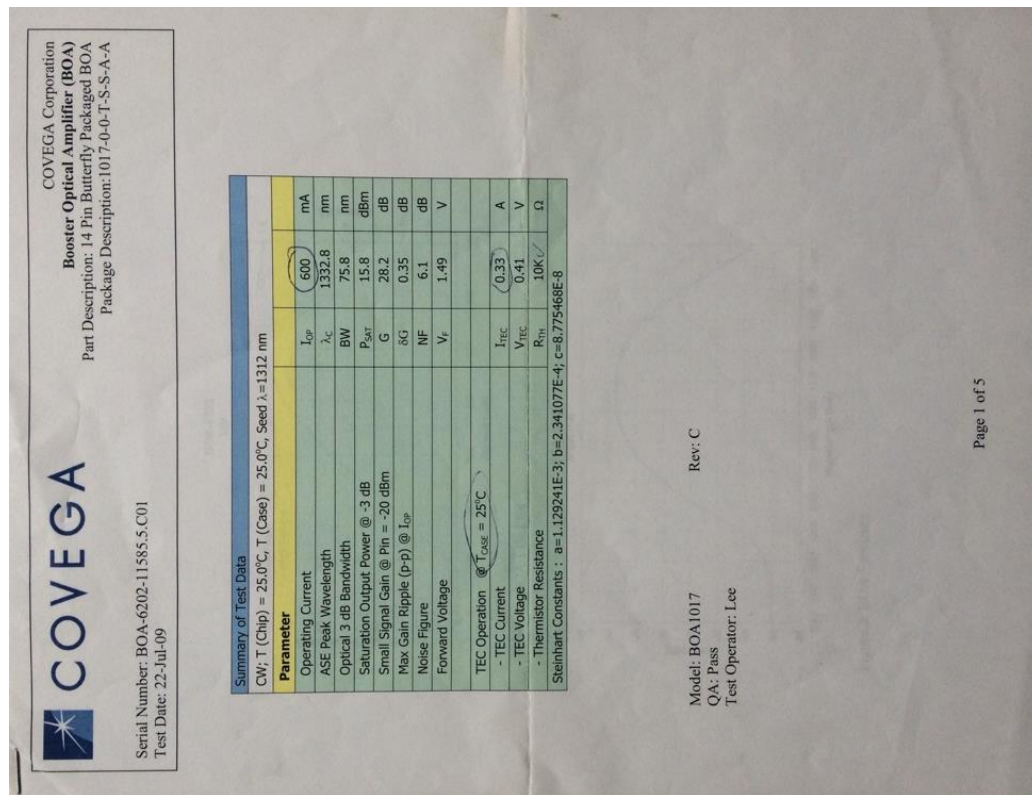
- [81] V.-F. Duma and A. G. Podoleanu, "Polygon mirror scanners in biomedical imaging: a review," in *Optical Components and Materials X*, 2013.
- [82] C. T. Walters, "Flat-field postobjective polygon scanner," *Applied Optics*, vol. 34, no. 13, pp. 2220-2225, 1 May 1995.
- [83] L. Liu, N. Chen and C. J. Sheppard, "Double-reflection polygon mirror for high-speed optical coherence microscopy," *Optics Letters*, vol. 32, no. 24, pp. 3528-3530, 2007.
- [84] A. L. Oldenberg, J. J. Reynolds, D. L. Marks and S. A. Boppart, "Fast-Fourier-domain delay line for in vivo optical coherence tomography with a polygonal scanner," *Applied Optics*, vol. 42, no. 22, pp. 4606-4611, 1 August 2003.
- [85] N. Guang Chen and Q. Zhu, "Rotary mirror array for high-speed optical coherence tomography," *Optics Letters*, vol. 27, no. 8, pp. 607-609, 15 April 2002.
- [86] J. Mansik, J. Unsang, S. Jae-Won and K. Jeehyun, "Frequency swept laser at 1300 nm using a wavelength scanning filter based on a rotating slit disk," *Journal of the Optical Society of Korea*, vol. 13, no. 3, pp. 330-334, September 2009.
- [87] W. Y. Oh, S. H. Yun, G. J. Tearney and B. E. Bouma, "Wide tuning range wavelength-swept laser with two semiconductor optical amplifiers," *IEEE Photonics Technol Lett*, vol. 17, no. 3, pp. 678-680, March 2005.
- [88] X. Attendu, C. Crunelle, M. Poinsinet se Sivry-Houle, B. Maubois and J. Urbain, "Towards combined optical coherence tomography and hyper-spectral imaging for gastrointestinal endoscopy," in *Multimodal Biomedical Imaging XIII*, San Francisco, 2018.
- [89] K. F. Kwong, D. Yankelovich, K. C. Chu, J. P. Heritage and A. Dienes, "400-Hz mechanical scanning optical delay line," *Optics Letters*, vol. 18, no. 7, pp. 558-560, 1993.
- [90] S. H. Yun, D. J. Richardson, D. O. Culverhouse and B. Y. Kim, "Wavelength-swept fiber laser with frequency shifted feedback and reonantly swept intra-cavity acoustooptic tunable filter," *Journal of selected topics in quantum electronics*, vol. 3, no. 4, pp. 1087-1096, 1997.
- [91] T. Mitsui, "Dynamic range of optical reflectometry with spectral interferometry," *Japanese Journal of Applied Optics*, vol. 38, no. 1999, pp. 6133-6137, 1999.
- [92] S. H. Yun, C. Bourdoux, C. Pierce, J. F. de Boer, G. J. Tearney and B. E. Bouma, "Extended-cavity semiconductor wavelength-swept laser for biomedical imaging," *Photonics Technology Letters*, vol. 16, no. 1, pp. 293-295, 2004.
- [93] S. H. Yun, G. J. Tearney, J. F. de Boer and B. E. Bouma, "Removing depth-degeneracy in optical frequency domain imaging with frequency shifting," *Optics Express*, vol. 12, no. 20, pp. 4822-4828, 2004.
- [94] R. Huber, M. Wojtkowski and J. G. Fujimoto, "Fourier domain mode locking (FDML): A new laser operating regime and application for optical coherence tomography," *Optics Express*, vol. 14, no. 8, pp. 3225-3237, 2006.
- [95] S.-W. Lee, C.-S. Kim and B.-M. Kim, "External line-cavity wavelength-swept source at 850 nm for optical coherence tomography," *Photonics Technology Letters*, vol. 19, no. 3, pp. 176-178, 2007.
- [96] Y. Mao, S. Chang, S. Sherif and C. Flueraru, "Graded-index fibre lens proposed for ultrasmall probes used in biomedical imaging," *Applied Optics*, vol. 46, no. 23, pp. 5887-5894, 2007.
- [97] C. Chong, T. Suzuki, A. Morasawa and T. Sakai, "Spectral narrowing effect by quasi-phase continuous tuning in high-speed wavelength-swept light source," *Optics Express*, vol. 16, no. 25, pp. 21105-21118, 2008.

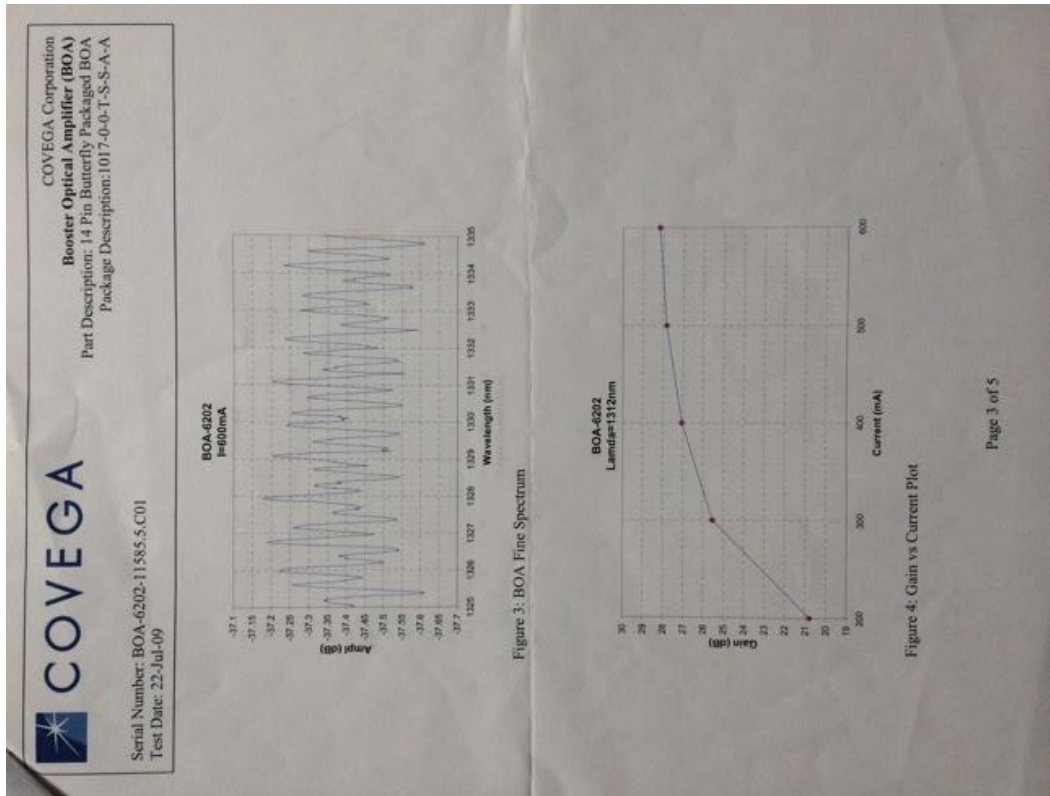
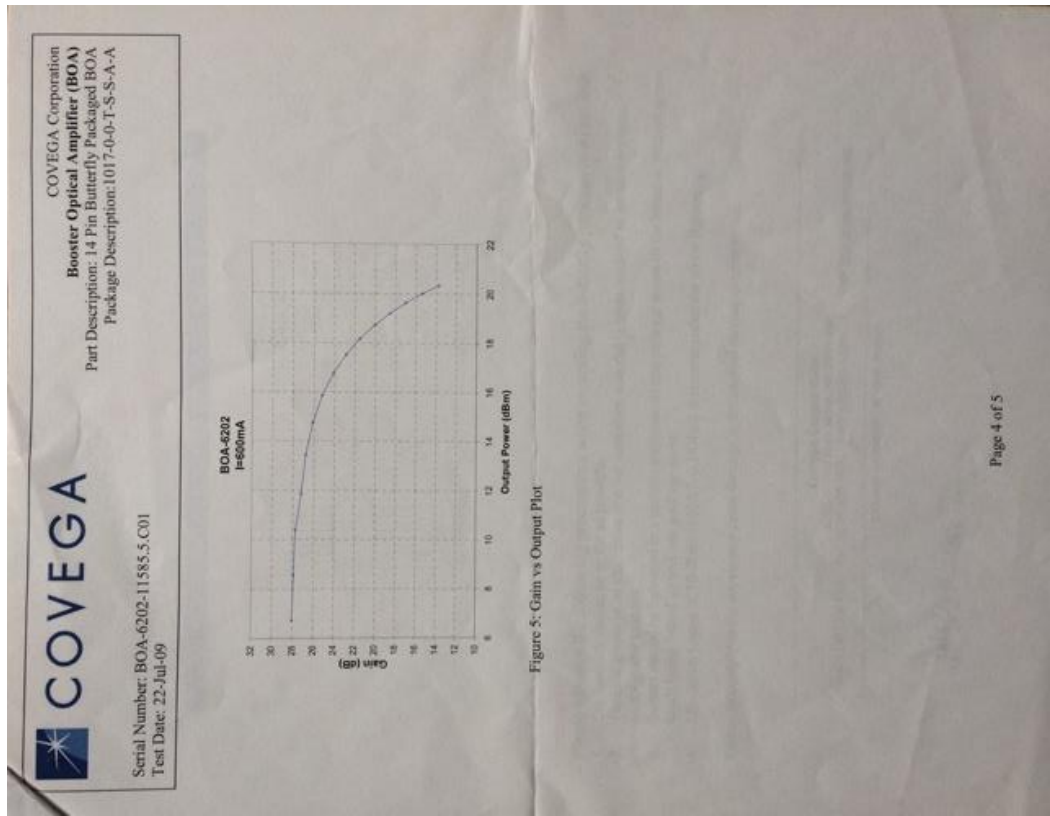
- [98] G. Y. Liu, A. Mariampillai, B. A. Standish, N. R. Munce, X. Gu and I. Alex Vitkin, "High power wavelength linearly swept mode locked fiber laser for OCT imaging," *Optics Express*, vol. 16, no. 18, pp. 14095-14105, 2008.
- [99] M. K. Leung, A. Mariampillai, B. A. Standish, K. K. Lee, N. R. Munce, I. Alex Vitkin and V. X. Yang, "High-power wavelength-swept laser in Littman telescope-less polygon filter and dual-amplifier configuration for multichannel optical coherence tomography," *Optics Letters*, vol. 34, no. 18, pp. 2814-2816, 2009.
- [100] V. F. Duma, "Radiometric versus geometric, linear, and non-linear vignetting coefficient," *Applied Optics*, vol. 48, no. 32, pp. 6355-6364, 2009.
- [101] D. Hunger, T. Steinmetz, Y. Colombe, C. Deutsch, T. W. Hänsch and J. Reichel, "A fiber Fabry-Perot cavity with high finesse," *New Journal of Physics*, vol. 12, no. 2010, p. 65038, 2010.
- [102] W. Weiser, B. R. Biedermann, T. Klein, C. M. Eigenwillig and R. Huber, "Multi-megahertz OCT: High quality 3D imaging at 20 million A-scans and 4.5 GVoxels per second," *Optics Express*, vol. 18, no. 14, pp. 14685-14704, 2010.
- [103] V. F. Duma, K.-s. Lee, P. Meemon and J. P. Rolland, "Experimental investigations of the scanning functions of galvanometer-based scanners with applications in OCT," *Applied Optics*, vol. 50, no. 29, pp. 5735-5749, 2011.
- [104] B. Baumann, W. Choi, B. Potsaid, D. Huang, J. S. Duker and J. G. Fujimoto, "Swept source/Fourier domain polarization sensitive optical coherence tomography with a passive polarization delay unit," *Optics Express*, vol. 20, no. 9, pp. 10229-10241, 2012.
- [105] X. Mu, G. Zhou, H. Yu, Y. Du, H. Feng, J. Ming Lin Tsai and F. S. Chau, "Compact MEMS-driven pyramidal polygon reflector for circumferential scanned endoscopic imaging probe," *Optics Express*, vol. 20, no. 6, pp. 6325-6339, 2012.
- [106] C. D. Lu, M. F. Kraus, B. Potsaid, J. J. Liu, W. Choi, V. Jayaraman, A. E. Cable, J. Hornegger, J. S. Duker and J. G. Fujimoto, "Handheld ultrahigh speed swept source optical coherence tomography instrument using a MEMS scanning mirror," *Biomedical Optics Express*, vol. 5, no. 1, pp. 293-311, 2013.
- [107] Y. S. Kwon, M. O. Ko, M. S. Jung, I. G. Park, N. Kim, S.-P. Han, H.-C. Ryu, K. H. Park and M. Y. Jeon, "Dynamic sensor interrogation using wavelength-swept laser with polygon-scanner-based wavelength filter," *Sensors*, vol. 2013, no. 13, pp. 9669-9678, 2013.
- [108] B. Johson, W. Atia, M. Kuznetsov, B. D. Goldberg, P. Whitney and D. C. Flanders, "Analysis of a spinning polygon wavelength swept laser," Axsun Technologies, Billerica, 2015.
- [109] J. Fan, P. Wang, F. Gao, Z. Hu, W. Kong, H. Li and G. Shi, "Phase and amplitude correction in polygon tunable laser-based optical coherence tomography," *Journal of Biomedical Optics*, vol. 22, no. 9, pp. 0960131-0960139, 2017.
- [110] V. F. Duma, "Polygon mirror laser scanning heads: Characteristic functions," in *Proceedings of the Romanian Academy, Series A*, Timisoara, 2017.
- [111] A. G. Podoleanu, "Unbalanced versus balanced operation in an optical coherence tomography system," *Applied Optics*, vol. 39, no. 1, pp. 173-182, 2000.
- [112] M. Münter, M. Pieper, T. Kohlfaerber, E. Bodenstorfer, M. Ahrens, C. Winter, R. Huber, P. König, G. Hüttman and H. Schulz-Hildebrandt, "Microscopic optical coherence tomography (mOCT) at 600 kHz for 4D volumetric imaging and dynamic contrast," *Biomedical Optics Express*, vol. 12, no. 10, pp. 6024-6039, 2021.

Appendix A

Covega, Semiconductor Optical Amplifier (SOA) data sheets

SOA data sheets, (pages 1-5)





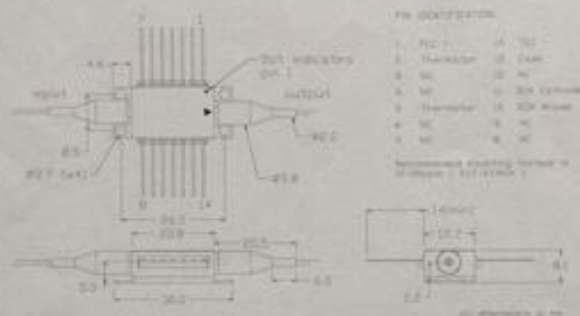


COVEGA

COVEGA Corporation
Booster Optical Amplifier (BOA)
 Part Description: 14 Pin Butterfly Packaged BOA
 Package Description: 1017-0-0-T-S-S-A-A

Serial Number: BOA-6202-11585.5.C01
 Test Date: 22-Jul-09

Packaging



Attention:

Please observe the following precautions when mounting the butterfly package to a heatsink:

1. The heatsink should be as flat as possible.
2. Thermal grease or an alternative thin but compliant material is recommended to be used between package and heatsink.
3. Screws should be tightened in a suitable sequence so that package mates to the heatsink without screw heads being forced up and into package snout.
4. Maximum torque of 10-20oz-in (0.07-0.14Nm) is recommended for screw tightening.

Failure to comply to the above may cause damage to the internal thermo-electric cooler.

Covega Corporation

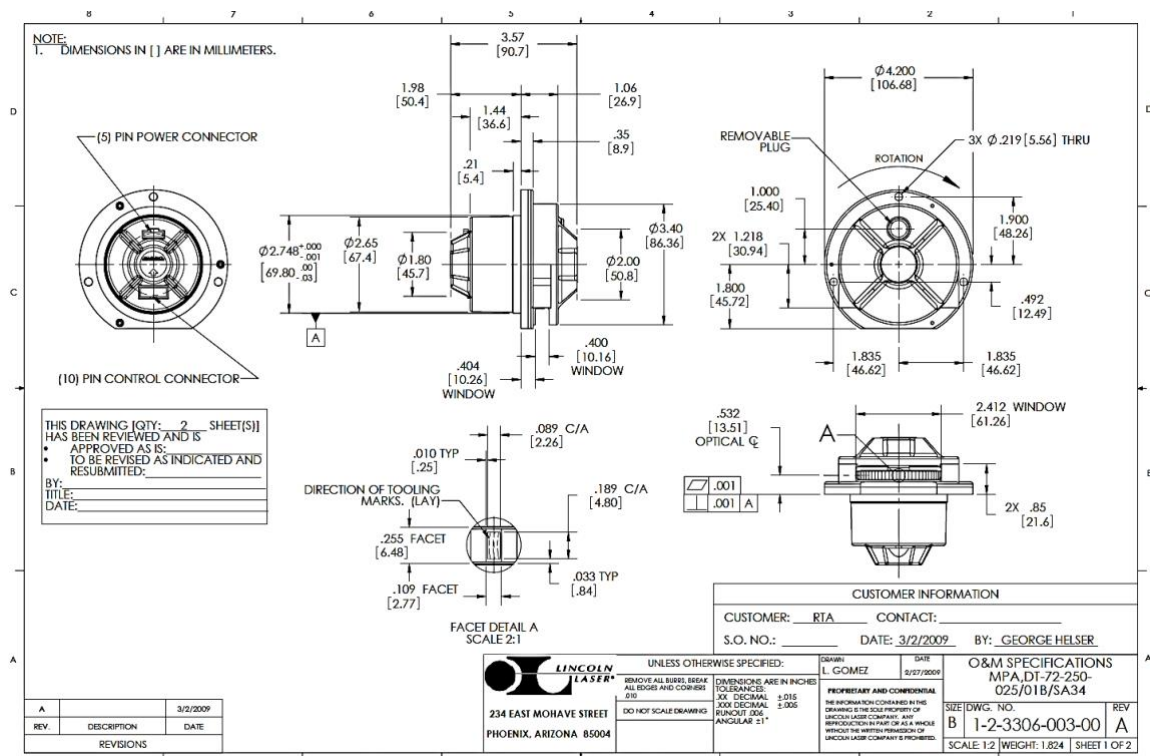
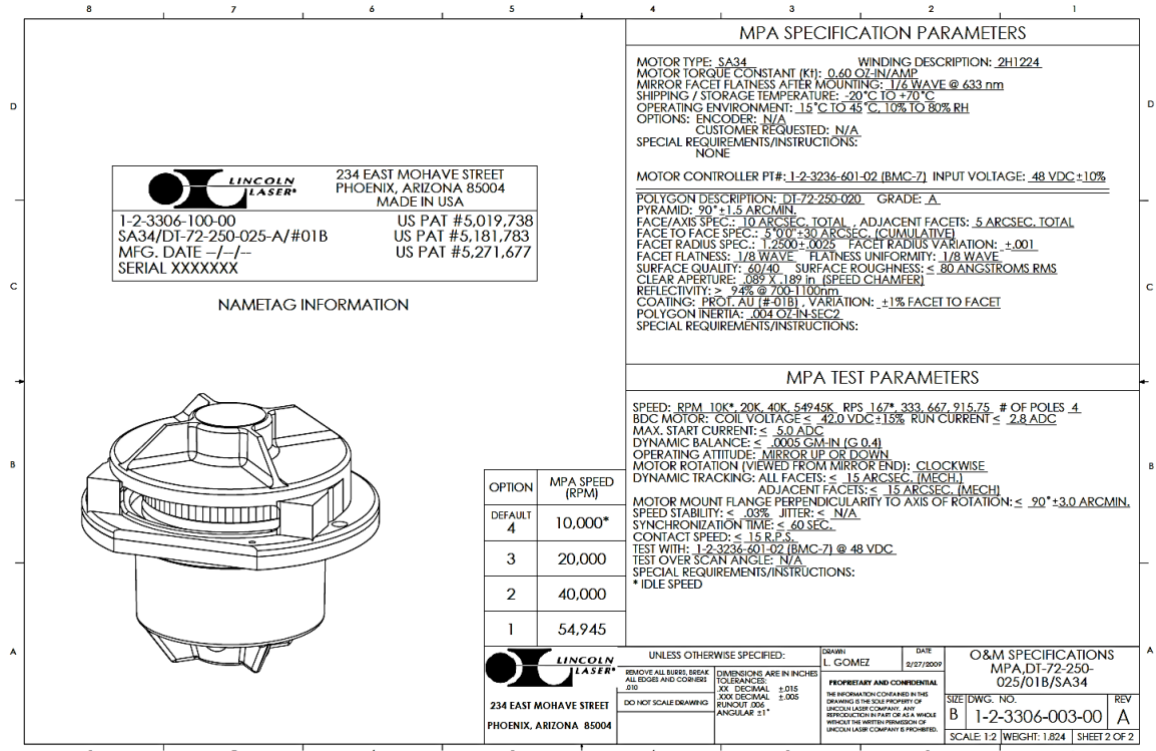
10335 Guilford Road, Jessup, MD 20794, USA
 Phone: +1 877.226.8342 Fax: +1 240.456.7200 Email: sales@covega.com Web: <http://www.covega.com>

© Covega Corporation - All rights reserved

JWEI@therlabs.com

APPENDIX B

Polygon Mirror specifications



APPENDIX C

Tables for selecting the focal lengths (magnification) in the two-lens telescope to meet the requirements of the Polygon Mirror – Acceptance angle and Facet Width.

Convergence Angle, $\psi = \Delta\delta \frac{f_1}{f_2} < 10^\circ$ (off-axis Polygon Mirror)

Using a Divergence angle $\Delta\delta = 16.88^\circ$

F1 = f_1 = focal length of first lens, F2 = f_2 = focal length of second lens

Convergence Angle < Acceptance Angle (10 degrees)										
F1	F2									
	30	35	40	50	60	75	80	100	150	200
30	16.88	14.47	12.66	10.13	8.44	6.75	6.33	5.06	3.38	2.53
35	19.69	16.88	14.77	11.82	9.85	7.88	7.39	5.91	3.94	2.95
40	22.51	19.29	16.88	13.50	11.25	9.00	8.44	6.75	4.50	3.38
50	28.13	24.11	21.10	16.88	14.07	11.25	10.55	8.44	5.63	4.22
60	33.76	28.94	25.32	20.26	16.88	13.50	12.66	10.13	6.75	5.06
75	42.20	36.17	31.65	25.32	21.10	16.88	15.83	12.66	8.44	6.33
80	45.01	38.58	33.76	27.01	22.51	18.01	16.88	13.50	9.00	6.75
100	56.27	48.23	42.20	33.76	28.13	22.51	21.10	16.88	11.25	8.44
150	84.40	72.34	63.30	50.64	42.20	33.76	31.65	25.32	16.88	12.66
200	112.53	96.46	84.40	67.52	56.27	45.01	42.20	33.76	22.51	16.88

Final Beam Width, Eq. 4.21, $W_2(\lambda_n) = W_0 \frac{f_2}{f_1} \frac{\cos \gamma}{\cos \delta(\lambda_n)} < 2.77 \text{ mm}$

Collimators

F230, W1 = 0.83 mm, W2 < 2.77 mm Final Beam Width										
F1	F2									
	30	35	40	50	60	75	80	100	150	200
30	0.86	1.01	1.15	1.44	1.73	2.16	2.31	2.88	4.32	5.77
35	0.74	0.86	0.99	1.24	1.48	1.85	1.98	2.47	3.71	4.94
40	0.65	0.76	0.86	1.08	1.30	1.62	1.73	2.16	3.24	4.32
50	0.52	0.61	0.69	0.86	1.04	1.30	1.38	1.73	2.59	3.46
60	0.43	0.50	0.58	0.72	0.86	1.08	1.15	1.44	2.16	2.88
75	0.35	0.40	0.46	0.58	0.69	0.86	0.92	1.15	1.73	2.31
80	0.32	0.38	0.43	0.54	0.65	0.81	0.86	1.08	1.62	2.16
100	0.26	0.30	0.35	0.43	0.52	0.65	0.69	0.86	1.30	1.73
150	0.17	0.20	0.23	0.29	0.35	0.43	0.46	0.58	0.86	1.15
200	0.13	0.15	0.17	0.22	0.26	0.32	0.35	0.43	0.65	0.86

F110, W1 = 1.15 mm, W2 < 2.77 mm Final Beam Width										
F1	F2									
	30	35	40	50	60	75	80	100	150	200
30	1.20	1.40	1.60	2.00	2.40	3.00	3.20	3.99	5.99	7.99
35	1.03	1.20	1.37	1.71	2.05	2.57	2.74	3.42	5.13	6.85
40	0.90	1.05	1.20	1.50	1.80	2.25	2.40	3.00	4.49	5.99
50	0.72	0.84	0.96	1.20	1.44	1.80	1.92	2.40	3.59	4.79
60	0.60	0.70	0.80	1.00	1.20	1.50	1.60	2.00	3.00	3.99
75	0.48	0.56	0.64	0.80	0.96	1.20	1.28	1.60	2.40	3.20
80	0.45	0.52	0.60	0.75	0.90	1.12	1.20	1.50	2.25	3.00
100	0.36	0.42	0.48	0.60	0.72	0.90	0.96	1.20	1.80	2.40
150	0.24	0.28	0.32	0.40	0.48	0.60	0.64	0.80	1.20	1.60
200	0.18	0.21	0.24	0.30	0.36	0.45	0.48	0.60	0.90	1.20

F240, W1 = 1.5 mm, W2 < 2.77 mm Final Beam Width										
F1	F2									
	30	35	40	50	60	75	80	100	150	200
30	1.56	1.82	2.08	2.60	3.13	3.91	4.17	5.21	7.81	10.42
35	1.34	1.56	1.79	2.23	2.68	3.35	3.57	4.47	6.70	8.93
40	1.17	1.37	1.56	1.95	2.34	2.93	3.13	3.91	5.86	7.81
50	0.94	1.09	1.25	1.56	1.88	2.34	2.50	3.13	4.69	6.25
60	0.78	0.91	1.04	1.30	1.56	1.95	2.08	2.60	3.91	5.21
75	0.59	0.73	0.83	1.04	1.25	1.56	1.67	2.08	3.13	4.17
80	0.63	0.68	0.78	0.98	1.17	1.47	1.56	1.95	2.93	3.91
100	0.47	0.55	0.63	0.78	0.94	1.17	1.25	1.56	2.34	3.13
150	0.31	0.36	0.42	0.52	0.63	0.78	0.83	1.04	1.56	2.08
200	0.23	0.27	0.31	0.39	0.47	0.59	0.63	0.78	1.17	1.56

F220, W1 = 2.04 mm, W2 < 2.77 mm Final Beam Width										
F1	F2									
	30	35	40	50	60	75	80	100	150	200
30	2.13	2.48	2.83	3.54	4.25	5.31	5.67	7.08	10.63	14.17
35	1.82	2.13	2.43	3.04	3.64	4.55	4.86	6.07	9.11	12.15
40	1.59	1.86	2.13	2.66	3.19	3.99	4.25	5.31	7.97	10.63
50	1.28	1.49	1.70	2.13	2.55	3.19	3.40	4.25	6.38	8.50
60	1.06	1.24	1.42	1.77	2.13	2.66	2.83	3.54	5.31	7.08
75	0.85	0.99	1.13	1.42	1.70	2.13	2.27	2.83	4.25	5.67
80	0.80	0.93	1.06	1.33	1.59	1.99	2.13	2.66	3.99	5.31
100	0.64	0.74	0.85	1.06	1.28	1.59	1.70	2.13	3.19	4.25
150	0.43	0.50	0.57	0.71	0.85	1.06	1.13	1.42	2.13	2.83
200	0.32	0.37	0.43	0.53	0.64	0.80	0.85	1.06	1.59	2.13

F260, W1 = 2.8 mm, W2 < 2.77 mm Final Beam Width										
F1	F2									
	30	35	40	50	60	75	80	100	150	200
30	2.92	3.40	3.89	4.86	5.83	7.29	7.78	9.72	14.59	19.45
35	2.50	2.92	3.33	4.17	5.00	6.25	6.67	8.34	12.50	16.67
40	2.19	2.55	2.92	3.65	4.38	5.47	5.83	7.29	10.94	14.59
50	1.75	2.04	2.33	2.92	3.50	4.38	4.67	5.83	8.75	11.67
60	1.46	1.70	1.94	2.43	2.92	3.65	3.89	4.86	7.29	9.72
75	1.17	1.36	1.56	1.94	2.33	2.92	3.11	3.89	5.83	7.78
80	1.09	1.28	1.46	1.82	2.19	2.73	2.92	3.65	5.47	7.29
100	0.88	1.02	1.17	1.46	1.75	2.19	2.33	2.92	4.38	5.83
150	0.58	0.68	0.78	0.97	1.17	1.46	1.56	1.94	2.92	3.89
200	0.44	0.51	0.58	0.73	0.88	1.09	1.17	1.46	2.19	2.92

F280, W1 = 3.4 mm, W2 < 2.77 mm Final Beam Width										
F1	F2									
	30	35	40	50	60	75	80	100	150	200
30	3.54	4.13	4.72	5.90	7.08	8.86	9.45	11.81	17.71	23.62
35	3.04	3.54	4.05	5.06	6.07	7.59	8.10	10.12	15.18	20.24
40	2.66	3.10	3.54	4.43	5.31	6.64	7.08	8.86	13.28	17.71
50	2.13	2.48	2.83	3.54	4.25	5.31	5.67	7.08	10.63	14.17
60	1.77	2.07	2.36	2.95	3.54	4.43	4.72	5.90	8.86	11.81
75	1.42	1.65	1.89	2.36	2.83	3.54	3.78	4.72	7.08	9.45
80	1.33	1.55	1.77	2.21	2.66	3.32	3.54	4.43	6.64	8.86
100	1.06	1.24	1.42	1.77	2.13	2.66	2.83	3.54	5.31	7.08
150	0.71	0.83	0.94	1.18	1.42	1.77	1.89	2.36	3.54	4.72
200	0.53	0.62	0.71	0.89	1.06	1.33	1.42	1.77	2.66	3.54

APPENDIX D

Zemax: Lens Data Editor example

Surface No.	Type	Comment	Curvature	Thickness	Glass	Semi-Diameter	Conic	Parameter 0	Parameter 1	Parameter 2	Parameter 3	Parameter 4	Parameter 5	Parameter 6	Parameter 7	Parameter 8	Parameter 9	Parameter 10	Parameter 11	Parameter 12	TCE	Coating
0	STANDARD		0.00E+00	0.00E+00		0.00E+00	0.00E+00	0.00E+00	0.00E+00	0.00E+00	0.00E+00	0.00E+00	0.00E+00	0.00E+00	0.00E+00	0.00E+00	0.00E+00	0.00E+00	0.00E+00	0.00E+00	0.00E+00	
1	STANDARD	Fiber	0.00E+00	5.94E+00		0.00E+00	0.00E+00	0.00E+00	0.00E+00	0.00E+00	0.00E+00	0.00E+00	0.00E+00	0.00E+00	0.00E+00	0.00E+00	0.00E+00	0.00E+00	0.00E+00	0.00E+00	0.00E+00	
2	F240APC-C		0.00E+00	3.43E+00	D-ZK3M	4.97E+00	0.00E+00	0.00E+00	0.00E+00	0.00E+00	0.00E+00	0.00E+00	0.00E+00	0.00E+00	0.00E+00	0.00E+00	0.00E+00	0.00E+00	0.00E+00	0.00E+00	0.00E+00	
3	EVENASPH	F240APC-C	-2.18E-01	5.00E+01		4.97E+00	-9.26E-01	0.00E+00	0.00E+00	-4.79E-04	-3.13E-08	6.50E-10	0.00E+00	0.00E+00	0.00E+00	0.00E+00	0.00E+00	0.00E+00	0.00E+00	0.00E+00	0.00E+00	
4	COORDRBK		0.00E+00	0.00E+00		0.00E+00	0.00E+00	0.00E+00	0.00E+00	0.00E+00	0.00E+00	0.00E+00	0.00E+00	0.00E+00	0.00E+00	0.00E+00	0.00E+00	0.00E+00	0.00E+00	0.00E+00	0.00E+00	
5	DGRATING	Gamma = 5	0.00E+00	0.00E+00	MIRROR	0.00E+00	0.00E+00	0.00E+00	0.00E+00	6.00E-01	1.00E+00	0.00E+00	0.00E+00	0.00E+00	0.00E+00	0.00E+00	0.00E+00	0.00E+00	0.00E+00	0.00E+00	0.00E+00	
6	COORDRBK		0.00E+00	0.00E+00		0.00E+00	0.00E+00	0.00E+00	0.00E+00	0.00E+00	0.00E+00	0.00E+00	0.00E+00	0.00E+00	0.00E+00	0.00E+00	0.00E+00	0.00E+00	0.00E+00	0.00E+00	0.00E+00	
7	STANDARD	Parabolic Mirror	1.97E-02	5.08E+01	MIRROR	1.27E+01	-1.00E+00	0.00E+00	0.00E+00	4.55E+01	0.00E+00	0.00E+00	0.00E+00	0.00E+00	0.00E+00	0.00E+00	0.00E+00	0.00E+00	0.00E+00	0.00E+00	0.00E+00	
8	STANDARD		0.00E+00	0.00E+00		1.00E+01	0.00E+00	0.00E+00	0.00E+00	0.00E+00	0.00E+00	0.00E+00	0.00E+00	0.00E+00	0.00E+00	0.00E+00	0.00E+00	0.00E+00	0.00E+00	0.00E+00	0.00E+00	
9	STANDARD	Parabolic Mirror	-1.97E-02	-7.63E+01	MIRROR	1.27E+01	0.00E+00	0.00E+00	0.00E+00	0.00E+00	0.00E+00	0.00E+00	0.00E+00	0.00E+00	0.00E+00	0.00E+00	0.00E+00	0.00E+00	0.00E+00	0.00E+00	0.00E+00	
10	STANDARD		0.00E+00	0.00E+00		0.00E+00	0.00E+00	0.00E+00	0.00E+00	0.00E+00	0.00E+00	0.00E+00	0.00E+00	0.00E+00	0.00E+00	0.00E+00	0.00E+00	0.00E+00	0.00E+00	0.00E+00	0.00E+00	
11	COORDRBK		0.00E+00	3.18E+01		0.00E+00	0.00E+00	0.00E+00	0.00E+00	0.00E+00	0.00E+00	0.00E+00	0.00E+00	0.00E+00	0.00E+00	0.00E+00	0.00E+00	0.00E+00	0.00E+00	0.00E+00	0.00E+00	
12	COORDRBK		0.00E+00	3.18E+01		0.00E+00	0.00E+00	0.00E+00	0.00E+00	0.00E+00	0.00E+00	0.00E+00	0.00E+00	0.00E+00	0.00E+00	0.00E+00	0.00E+00	0.00E+00	0.00E+00	0.00E+00	0.00E+00	
13	STANDARD	Polygon	0.00E+00	3.18E+01	MIRROR	1.39E+00	0.00E+00	0.00E+00	0.00E+00	0.00E+00	0.00E+00	0.00E+00	0.00E+00	0.00E+00	0.00E+00	0.00E+00	0.00E+00	0.00E+00	0.00E+00	0.00E+00	0.00E+00	
14	COORDRBK		0.00E+00	0.00E+00		0.00E+00	0.00E+00	0.00E+00	0.00E+00	0.00E+00	0.00E+00	0.00E+00	0.00E+00	0.00E+00	0.00E+00	0.00E+00	0.00E+00	0.00E+00	0.00E+00	0.00E+00	0.00E+00	
15	COORDRBK		0.00E+00	5.00E+01		1.00E+01	0.00E+00	0.00E+00	0.00E+00	0.00E+00	-7.00E+01	0.00E+00	0.00E+00	0.00E+00	0.00E+00	0.00E+00	0.00E+00	0.00E+00	0.00E+00	0.00E+00	0.00E+00	
16	STANDARD	Retro Mirror	0.00E+00	-5.00E+01	MIRROR	1.00E+01	0.00E+00	0.00E+00	0.00E+00	0.00E+00	0.00E+00	0.00E+00	0.00E+00	0.00E+00	0.00E+00	0.00E+00	0.00E+00	0.00E+00	0.00E+00	0.00E+00	0.00E+00	
17	COORDRBK		0.00E+00	-3.18E+01		0.00E+00	0.00E+00	0.00E+00	0.00E+00	0.00E+00	0.00E+00	0.00E+00	0.00E+00	0.00E+00	0.00E+00	0.00E+00	0.00E+00	0.00E+00	0.00E+00	0.00E+00	0.00E+00	
18	COORDRBK		0.00E+00	3.18E+01		0.00E+00	0.00E+00	0.00E+00	0.00E+00	0.00E+00	0.00E+00	0.00E+00	0.00E+00	0.00E+00	0.00E+00	0.00E+00	0.00E+00	0.00E+00	0.00E+00	0.00E+00	0.00E+00	
19	STANDARD	Polygon	0.00E+00	-3.18E+01	MIRROR	1.39E+00	0.00E+00	0.00E+00	0.00E+00	0.00E+00	0.00E+00	0.00E+00	0.00E+00	0.00E+00	0.00E+00	0.00E+00	0.00E+00	0.00E+00	0.00E+00	0.00E+00	0.00E+00	
20	COORDRBK		0.00E+00	3.18E+01		0.00E+00	0.00E+00	0.00E+00	0.00E+00	0.00E+00	0.00E+00	0.00E+00	0.00E+00	0.00E+00	0.00E+00	0.00E+00	0.00E+00	0.00E+00	0.00E+00	0.00E+00	0.00E+00	
21	COORDRBK		0.00E+00	0.00E+00		0.00E+00	0.00E+00	0.00E+00	0.00E+00	0.00E+00	0.00E+00	0.00E+00	0.00E+00	0.00E+00	0.00E+00	0.00E+00	0.00E+00	0.00E+00	0.00E+00	0.00E+00	0.00E+00	
22	STANDARD		0.00E+00	7.63E+01		0.00E+00	0.00E+00	0.00E+00	0.00E+00	0.00E+00	0.00E+00	0.00E+00	0.00E+00	0.00E+00	0.00E+00	0.00E+00	0.00E+00	0.00E+00	0.00E+00	0.00E+00	0.00E+00	
23	STANDARD	Parabolic Mirror	-1.97E-02	-5.08E+01	MIRROR	1.27E+01	-1.00E+00	0.00E+00	0.00E+00	0.00E+00	0.00E+00	0.00E+00	0.00E+00	0.00E+00	0.00E+00	0.00E+00	0.00E+00	0.00E+00	0.00E+00	0.00E+00	0.00E+00	
24	STANDARD	Focal Point	0.00E+00	0.00E+00		1.00E+01	0.00E+00	0.00E+00	0.00E+00	0.00E+00	0.00E+00	0.00E+00	0.00E+00	0.00E+00	0.00E+00	0.00E+00	0.00E+00	0.00E+00	0.00E+00	0.00E+00	0.00E+00	
25	STANDARD	Parabolic Mirror	1.97E-02	7.63E+01	MIRROR	1.27E+01	-1.00E+00	0.00E+00	0.00E+00	-4.55E+01	0.00E+00	0.00E+00	0.00E+00	0.00E+00	0.00E+00	0.00E+00	0.00E+00	0.00E+00	0.00E+00	0.00E+00	0.00E+00	
26	COORDRBK		0.00E+00	0.00E+00		0.00E+00	0.00E+00	0.00E+00	0.00E+00	0.00E+00	0.00E+00	0.00E+00	0.00E+00	0.00E+00	0.00E+00	0.00E+00	0.00E+00	0.00E+00	0.00E+00	0.00E+00	0.00E+00	
27	DGRATING	Gamma = 5	0.00E+00	0.00E+00	MIRROR	1.27E+01	0.00E+00	0.00E+00	0.00E+00	6.00E-01	1.00E+00	0.00E+00	0.00E+00	0.00E+00	0.00E+00	0.00E+00	0.00E+00	0.00E+00	0.00E+00	0.00E+00	0.00E+00	
28	COORDRBK		0.00E+00	-5.00E+01		0.00E+00	0.00E+00	0.00E+00	0.00E+00	0.00E+00	0.00E+00	0.00E+00	0.00E+00	0.00E+00	0.00E+00	0.00E+00	0.00E+00	0.00E+00	0.00E+00	0.00E+00	0.00E+00	
29	EVENASPH	F240APC-C	-2.18E-01	-3.43E+00	D-ZK3M	4.97E+00	-9.26E-01	0.00E+00	0.00E+00	-4.79E-04	-3.13E-08	6.50E-10	0.00E+00	0.00E+00	0.00E+00	0.00E+00	0.00E+00	0.00E+00	0.00E+00	0.00E+00	0.00E+00	
30	STANDARD		0.00E+00	-5.94E+00		0.00E+00	0.00E+00	0.00E+00	0.00E+00	0.00E+00	0.00E+00	0.00E+00	0.00E+00	0.00E+00	0.00E+00	0.00E+00	0.00E+00	0.00E+00	0.00E+00	0.00E+00	0.00E+00	
31	STANDARD	Fiber	0.00E+00	-1.00E+00		4.50E+03	0.00E+00	0.00E+00	0.00E+00	0.00E+00	0.00E+00	0.00E+00	0.00E+00	0.00E+00	0.00E+00	0.00E+00	0.00E+00	0.00E+00	0.00E+00	0.00E+00	0.00E+00	
32	STANDARD		0.00E+00	0.00E+00		4.50E+03	0.00E+00	0.00E+00	0.00E+00	0.00E+00	0.00E+00	0.00E+00	0.00E+00	0.00E+00	0.00E+00	0.00E+00	0.00E+00	0.00E+00	0.00E+00	0.00E+00	0.00E+00	